Surface wrinkling of elastic supported membranes: Controlling defects and upscaling

D I S S E R T A T I O N

zur Erlangung des akademischen Grades eines

Doktors der Naturwissenschaften (Dr. rer. Nat.)

an der Fakultät für Biologie, Chemie und Geowissenschaften der Universität Bayreuth

UNIVERSITÄT BAYREUTH

vorgelegt von

Bernhard Alexander Glatz

geboren in Karlsruhe

Mai 2019

Die vorliegende Arbeit wurde in der Zeit von November 2013 bis August 2015 in Bayreuth am Lehrstuhl Physikalische Chemie II sowie von September 2015 bis Mai 2019 in Dresden am Leibniz-Institut für Polymerforschung Dresden e.V. in der Abteilung Polymergrenzflächen unter Betreuung von Herrn Prof. Dr. Andreas Fery angefertigt.

Vollständiger Abdruck der von der Fakultät für Biologie, Chemie und Geowissenschaften der Universität Bayreuth genehmigten Dissertation zur Erlangung des akademischen Grades eines Doktors der Naturwissenschaften (Dr. rer. nat.)

Dissertation eingereicht: 08.05.2019

Zulassung durch die Promotionskommission: 22.05.2019

Wissenschaftliches Kolloquium: 22.07.2019

Amtierender Dekan: Prof. Dr. Stefan Peiffer

Prüfungsausschuss:

Prof. Dr. Andreas Fery	(Gutachter)
Prof. Dr. Hans-Werner Schmidt	(Gutachter)
Prof. Dr. Josef Breu	(Vorsitz)
Prof. Dr. Markus Retsch	

"There is much pleasure to be gained from useless knowledge."

Bertrand Russell

Table of Contents

List of Abbreviations

2D-FT	Two-dimensional Fourier transformation
3W-VSI	Three-Wavelength Vertical Scanning Interferometry
AP-P	Atmospheric-pressure plasma
A	Wrinkling amplitude
AFM	Atomic force microscope
CLSM	Confocal Laser Scanning Microscopy
CVD	Chemical vapor deposition
DFTB	Density-functional based tight binding
DOS	Density of state
ε_c	Critcal strain to induce wrinkling
EPDM	Ethylene propylene diene monomer rubber
eUV-iL	Extreme ultraviolet interference lithography
FIB	Focused ion beam
HMDSO	Hexamethyldisiloxane
HER	Hydrogen evolution reaction
HNBR	Hydrated nitrile butadiene rubber
λ	Wrinkling wavelength
LP-P	Low-pressure plasma
LiL	Laser interference lithography
µcP	Micro-contact printing
MSL	Multilayer soft lithography
NBR	Nitrile butadiene rubber
OM	Optical microscope
PDMS	Poly(dimethyl) siloxane
PF-QNM	Peak-force quantitative nanomechanical mapping
PEDOT:PSS	Poly(3,4-ethylenedioxythiophene) polystyrene sulfonate polymer mixture
PEEK	Polyether ether ketone
PEM	Polyelectrolyte multilayer
PPS	Polyphenylene sulfide

PSD	Power spectral density
PTFE	Polytetrafluoroethylene
PVD	Physical vapor deposition
PVMS	Poly(vinylmethyl) siloxane
QNM	see PF-QNM
SAED	Selected area electron diffraction
SEM	Scanning electron microscope
SIEBIMM	Strain-induced buckling instability for mechanical measurements
SiO_x	Glass-like / SiO2-like
SNOM	Scanning Near-Field Optical Microscopy
TEM	Transmission electron microscope
TEOS	Tetraethyl orthosilicate
TMDSO	1,1,3,3-Tetramethyldisiloxane
TPU	Thermoplastic urethane
UV	Ultraviolet light
UVO	Ultraviolet/Ozone-treatment
WLI	White Light Interferometry
XPS	X-ray photoelectron spectroscopy

Zusammenfassung

Die vorliegende Arbeit befasst sich mit der Mikro- und Nanostrukturierung von Oberflächen mittels kontrollierter Faltenbildung. Natürlich Vorbilder hierfür sind die menschliche Haut, Oberflächen von Pflanzen sowie Faltengebirge. In der kontrollierten Faltenbildung wird ein dickes, elastisches Substrat uniaxial gestreckt, dann wird unter Dehnung eine dünne, inelastische Schicht aufgebracht, und schließlich wird das neu entstandene Zweischichtsystem relaxiert. Die dünne Schicht wird hierbei derart gestaucht, dass sie sich faltet. Bedingt durch ihre feste Verbindung mit dem elastischen Substrat, sind diese Falten jedoch sehr klein. Meist besitzen sie die Form sinusförmiger Wellen und befinden sich im Größenbereich von einigen nm bis hin zu hunderten µm.

Diese Arbeit gliedert sich in drei Hauptteile. Im ersten Teil wurden Defektstrukturen von gefalteten Oberflächen untersucht. Im zweiten Teil wurde die Skalierbarkeit von gefalteten Oberflächen hin zu Maßstäben > 1 m^2 untersucht. Zudem wurden neue plasmagestützte Verfahren getestet, um inelastische Schichten auf organischen Elastomeren aufbringen zu können. Und im dritten Teil wurde das Prinzip der kontrollierten Faltenbildung angewendet, um molekulare 2D-Polymerschichten < 1 nm Dicke auf ihre Elastizität hin zu untersuchen.

Der Fokus im ersten Teil der Arbeit lag auf den zwei häufigsten Defektarten. Dies sind einerseits Liniendefekte der Wellen und anderseits Querrisse in der Oberfläche. Liniendefekte entstehen, wenn sich zwei kleinere Wellen in einer großen vereinen. Die Gründe hierfür sind meist lokale Inhomogenitäten der Schicht- oder Substratelastizität, der Schichtdicke oder der mechanische Spannung im Zweischichtsystem. Um sie zu verstehen, wurden Liniendefekte gezielt erzeugt, analysiert sowie mechanisch simuliert. Hierfür wurde ein Polydimethylsiloxan- (PDMS) Substrat mit gradientartig ansteigender Elastizität an einer gemeinsamen Grenzfläche mit einem homogenen PDMS per Ultraviolett/Ozon- (UVO) Behandlung *in-situ* oxidiert, was die dünne, inelastische Schicht erzeugte. Die unterschiedlichen Substratelastizitäten verursachen unterschiedlich große Wellen und somit Liniendefekte. Während sich vielfach ungeordnete Liniendefekte zeigten, bildeten sich an wenigen Abschnitten bestimmter Elastizitätsverhältnisse von Substrat zu Film geordnete, repetitive Defektmuster. Diese entsprechen ganzzahligen Verhältnissen der lokalen Wellenlängen auf beiden Seiten der Grenzfläche. Zudem blieben die nahen Bereiche entlang der Grenzfläche liniendefektfrei.

Querrisse entstehen, da das elastische Substrat unter Dehnung Querkontraktion erfährt. In diesem quer zur Dehnungsrichtung gestauchten Zustand wird der inelastische Film aufgebracht. Bei der anschließenden Relaxation des Zweischichtsystems reißt der dünne Film aufgrund seiner niedrigen Elastizität meist parallel zur Dehnungsrichtung auf, während das elastische Substrat generell unbeschadet bleibt. Zur Untersuchung dieses Verhaltens wurde auf 60 % vorgedehntes PDMS *in-situ* via Niederdruckplasma oxidiert und anschließend

relaxiert, um Faltenbildung zu induzieren. Dazu wurden gezielt zwei Plasma-Parameter – Kammerdruck und Nennleistung – so variiert, dass innerhalb einer Parameterreihe sowohl rissfreie als auch gerissene Faltenstrukturen entstanden. Von allen Proben wurde je ein Querschnitt der oxidierten Schicht angefertigt, um diese auf deren Elastizität und Dicke *via* Quantitativer Nanomechanischer Analyse (PF-QNM) zu untersuchen. Alle untersuchten Schichten wiesen eine ähnliche Dicke und einen gradientartigen Verlauf der Elastizität auf; lediglich die jeweilige exponentielle Steigung des Gradienten unterschied sich. Schließlich wurden alle behandelten Proben via Finite Element Methode (FEM) simuliert, um die maximalen Spannungen innerhalb der jeweiligen gradientartigen Schichten zu berechnen. Es zeigte sich, dass in beiden Parameterreihen eine kritische Spannung von σ_{crit} = 14 MPa zwischen rissfreien und gerissenen Schichten auftritt. Im Ergebnis lassen sich so gezielt rissfreie Faltenstrukturen herstellen.

Im zweiten Teil dieser Arbeit wurden kontrollierte Faltensysteme skaliert. Hierzu wurden zwei plasmagestützte Systeme verwendet – eine Dielektrische Barriereentladung (DBD) und ein Plasma Jet – sowie eine selbst gebaute Rolle-zu-Rolle-Streckapparatur. Letztere erlaubte es, PDMS-Folien während des Wickelprozesses unter gleichbleibender Dehnung zu halten und in diesem Zustand *in-situ* zu oxidieren, sodass bei der anschließenden Relaxation der Folien gleichmäßige Falten entstanden. Weiterhin war eine Prozessführung mit organischen Elastomeren wie bspw. Ethylen-Propylen-Dien-Kautschuk (EPDM) möglich, da sowohl in der DBD als auch im Plasma-Jet glasbildende Prekursoren-Moleküle wie bspw. Hexamethyldisiloxan (HMDSO) in die Plasmaflamme eingebracht werden konnten. Diese setzten sich als dünne, steife Glasschicht auf dem Elastomer ab. Gleichzeitig ionisierte das Plasma die Oberfläche des Elastomers und ermöglichte dadurch eine kovalente Anbindung der Glasschicht. Im Rahmen dieser Arbeit konnten so große Flächen verschiedenster vorgedehnter Elastomere > 1 m^2 auf unterschiedliche Arten mit dünnen Schichten überzogen werden, die durch Relaxation Faltenmuster bildeten.

Im dritten Teil der Arbeit wurde eine 2-Dimensionale Polyimin-Schicht auf PDMS aufgebracht, die eine Dicke von 700 pm hat und damit genau eine molekulare Lage umfasst. Durch anschließende Dehnung faltete sich die Polyimin-Schicht. Da eine direkte Proportionalität zwischen Schichtdicke, Schicht- und Elastomer-Elastizität, sowie der Faltenwellenlänge besteht, war eine Berechnung unbekannter Werte möglich. Im vorliegenden Fall waren die Schichtdicke sowie die Elastomer-Elastizität bekannt, sodass die Schicht-Elastizität direkt berechnet werden konnte. Diese lag bei 267 ± 30 GPa, und damit vergleichbar hoch zu Graphen.

Insgesamt wurde in dieser Arbeit sowohl die Möglichkeit demonstriert, Defektstrukturen in Faltenbildungssystemen zu kontrollieren oder sogar zu vermeiden, als auch Faltenbildungssysteme in Größenordnungen > 1 m^2 zu skalieren – letzteres mit diversen Elastomeren und schichtbildenden Materialien.

Außerdem wurde an einer molekularen Polyimin-Schicht auf PDMS gezeigt, dass es möglich ist, dünnste Schichten < 1 nm Dicke mittels Faltenbildung mechanisch zu charakterisieren.

Summary

This thesis is on the subject of controlled wrinkling for micro- and nanostructuring of surfaces. Natural examples of wrinkles are human skin, plant surfaces and folding mountains. In controlled wrinkling, a thick, elastic substrate is stretched uniaxially and a thin, inelastic layer is applied to it. Eventually, the bilayer is relaxed, leading to sinusoidal wrinkles of the layer in the size range of a few nm to hundreds of µm.

This work is divided into three main parts. In the first part, defect structures of wrinkled surfaces are investigated. In the second part the scalability of wrinkled surfaces > 1 m^2 is investigated and new plasma-assisted methods are tested in order to apply inelastic layers to organic elastomers. In the third part, the principle of controlled wrinkle formation is applied to investigate the elasticity of molecular 2D polymer layers < 1 nm thickness.

The focus in the first part is on the two most common types of defects. These are on the one hand line defects of the wrinkles and on the other hand transversal cracks in the surface. Line defects occur when two smaller waves merge into a large one. The reasons for this are local inhomogeneities of layer and substrate elasticity, layer thickness or mechanical stress in the bilayer. In order to understand those, line defects are specifically generated, analyzed and mechanically simulated. For this purpose, a polydimethylsiloxane (PDMS) substrate with gradually increasing elasticity is casted next to a homogeneous PDMS substrate. Both get *in-situ* oxidized by ultraviolet/ozone (UVO) treatment, which creates the stiff, thin layer. The different substrate elasticities cause waves of different periodicity and thus line defects. While they are often disordered along the substrate interface, repetitive line defect patterns are observed on a few sections. These correspond to whole-number ratios of the local wavelengths on both sides of the interface. In addition, the adjacent areas along the interface remain line defect free.

Transversal cracks occur since the elastic substrate is laterally contracted under strain. The inelastic layer is applied in this compressed state. During the subsequent relaxation of the bilayer, the thin layer usually tears parallel to the direction of elongation due to its low elasticity, while the elastic substrate generally remains undamaged. To investigate this behavior, PDMS at a pre-strain of 60 % is oxidized *in-situ* via low-pressure plasma (LP-P) and then relaxed to induce wrinkling. For this purpose, two plasma parameters - chamber pressure and nominal power - are varied in order that both crack-free and cracked wrinkle surfaces form within a parameter screening. A cross-section of the oxidized layer is prepared from each sample to examine its elasticity and thickness via Quantitative Nanomechanical Analysis (PF-QNM). All investigated layers show a similar thickness and a gradual profile in elasticity; only the slope of the exponential gradient differs in each case. Eventually, all treated samples are simulated using Finite Element Method (FEM) to calculate the maximum stresses within each gradient layer. It turns out that in both parameter screenings a critical stress of σ_{crit} = 14 MPa separates crack-free from cracked layers. As a result, crack-free wrinkled surfaces can be generated specifically.

In the second part, controlled wrinkled surfaces are scaled. For this, two plasma-assisted systems are applied - a dielectric barrier discharge (DBD) and a plasma jet - as well as a custom-built roll-to-roll stretching device. The latter allows for *in-situ*-oxidation of PDMS at constant strain, so that uniform wrinkles are formed subsequently. Furthermore, processes with organic elastomers such as ethylene-propylene-diene rubber (EPDM) are also possible, since glass-forming precursor molecules such as hexamethyldisiloxane (HMDSO) can be introduced into the plasma both in DBD and in the plasma jet. These are deposited as a thin, stiff glass layer on the elastomer surface. At the same time, the plasma ionizes the elastomeric surface and thus enables covalent bonding of the glass layer. This work therefore allows for large-area wrinkling of various pre-stretched elastomers > 1 m^2 with diverse layer materials.

In the third part of the work, a 2-dimensional polyimine layer was applied to PDMS, which has a height of 700 pm, so one molecular layer. Subsequent stretching leads to wrinkling of the layer. Since there is a direct proportionality between layer thickness, layer and elastomer elasticity, as well as wrinkle wavelength, unknown parameters can be calculated therefrom. In here, layer thickness and elastomer elasticity are known, allowing the calculation of layer elasticity. One gets 267 ± 30 GPa, which is comparable to graphene.

Summarizing, this thesis demonstrates the possibility of controlling or avoiding defect structures in wrinkled systems, as well as scaling those to sizes > 1 m^2. In the latter case various elastomers and layer materials are successfully applied. Additionally, a molecular polyimine layer on PDMS shows that it is possible to mechanically characterize thin layers < 1 nm by wrinkle formation.

List of Publications and Awards

Structure of the thesis

This thesis is constituted of the publications **II.**, **III.** and **V.** as well as the patent application **VII.** A brief overview as well as a general synopsis is given in chapter 3.

Publications

I. M. Tebbe, M. Mayer, B.A. Glatz, C. Hanske, P.T. Probst, M.B. Müller, M. Karg, M. Chanana, T.A. König, C. Kuttner and A. Fery: "Optically anisotropic substrates via wrinkle-assisted convective assembly of gold nanorods on macroscopic areas", **2015**; *Faraday Discussions*, 181, 243 – 260

II. B.A. Glatz, M. Tebbe, B. Kaoui, R. Aichele, C. Kuttner, A.E. Schedl, H.W. Schmidt, W. Zimmermann and A. Fery: "Hierarchical line-defect patterns in wrinkled surfaces", **2015**; *Soft Matter*, 11 – 17, 3332 – 3339

III. H. Sahabudeen, H. Qi, B.A. Glatz, D. Tranca, R. Dong, Y. Hou, T. Zhang, C. Kuttner, T. Lehnert, G. Seifert, U. Kaiser, A. Fery, Z. Zheng and X. Feng: "Wafer-sized multifunctional polyimine-based two-dimensional conjugated polymers with high mechanical stiffness", **2016**; *Nature Communications*, 7, 13461

IV. Y. Park, J. Berger, P.-A. Will, M. Soldera, B. A. Glatz, L. Müller-Meskamp, K. Taretto, A. Fery, A.F. Lasagni, K. Vandewal and K. Leo: "Light trapping for flexible organic photovoltaics", **2016**; *SPIE Organic Photonics + Electronics*, 9942 – 9949

V. B.A. Glatz and A. Fery: "The influence of plasma treatment on the elasticity of the in-situ oxidized thin layer: Towards crack-free wrinkling", **2019**, *Soft Matter*, 2019, 15 – 1, 65 – 72

VI. R. Pratapan, B.A. Glatz, A. K. Ghosh, S. Michel, A. Fery A. Garnier and R. Tabor: "Enhancing printing resolution on hydrophobic polymer surfaces using patterned coatings of cellulose nanocrystals", **2019**, *Langmuir*, 35 – 22, 7155 – 7160

Patents

VII. B.A. Glatz, A. Knapp and A. Fery: "Surface-structured polymer bodies and method for the fabrication thereof", Patent application, DE 10 **2017** 218 363 A1, EP 3470 456 A1, US **2019**/0111610 A1

1. Introduction

"Nature does not create without a meaning."

Aristoteles

1.1. Lattice structures - from nature into the lab

The repetitive structuring in the micro- and nano-scale is widely spread in nature. Indications of the first structures date back to roughly half a billion years ago. [1] Such structures are most likely sensitive to environmental changes that has been taking place innumerable times ever since. Well-known examples are the leaf surface of lotus flowers, [2] the flow-optimized shark skin (Fig. 1 **a** and **d**), [3-5] the brick-and-mortar structure of nacre (Fig. 1 **b** and **e**), [6, 7] or the colored wings of butterflies (Fig. 1 **c** and **f**). [8, 9] Beyond, there are lots of other animals [10-12] and plants [13, 14] that have a colorful appearance caused by lattice structures on their skins as well.

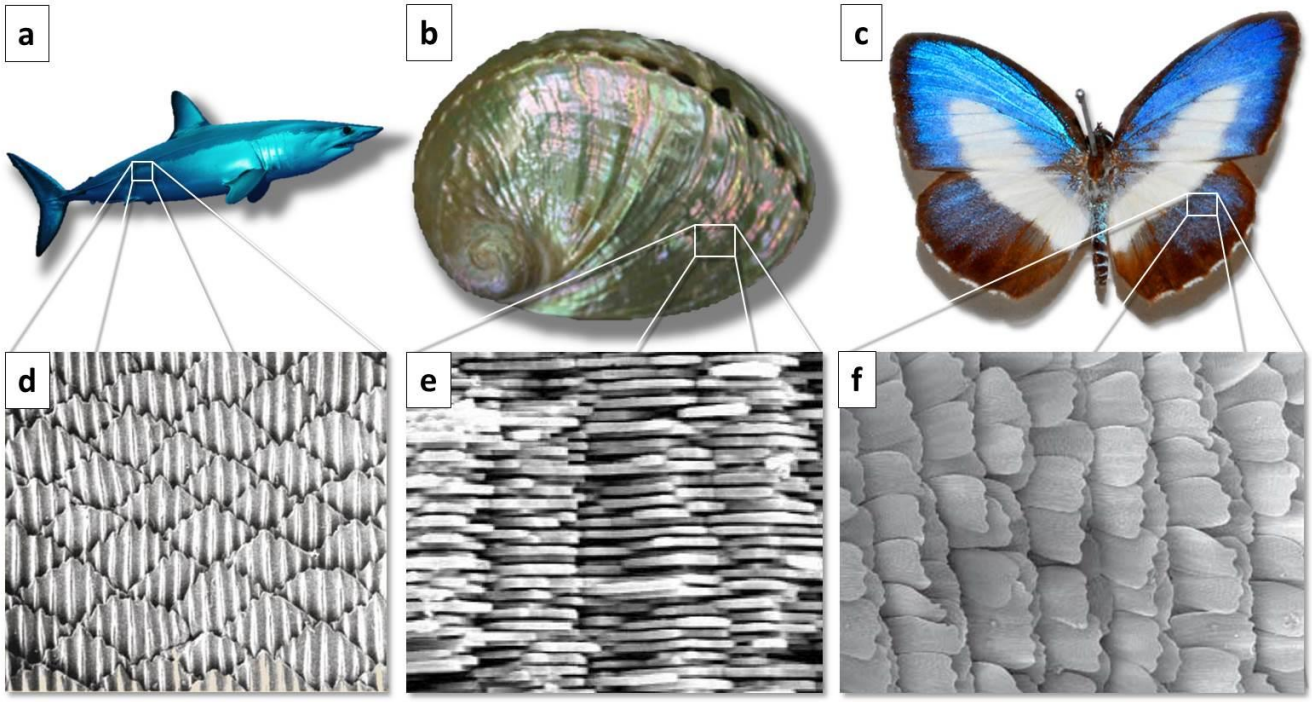

*Figure 1 | (**a**) Shortfin mako shark "Isurus oxyrinchus"; [15](**b**) Shell of mollusk "Haliotis glabra"; [16] (**c**) "Danis danis" from the butterfly family of lycaenidae; [17] (**d**) SEM image of the roof tile-like scales on shark sin; [3] (**e**) TEM image of the brick- and mortar-structure of nacre; [6] (**f**) SEM image of the dorsal wing scales on a Lycaenidae butterfly; [8] Reproduced with permission from references mentioned above.*

This colorful appearance is caused by the repetitive structural lattice units, since they are in the same length scale as visible light. This is not an absolute precondition; however colored lattices are probably best explored, since they are simple to find in nature due to their striking look. Nevertheless, some lattices have also been found to be most effective in the UV-range. [18] The physics behind natural lattices is well-understood, [19] so consequentially there have been efforts to bio-mimic and eventually rebuild such structures semi-artificially. The intention is to imitate the physical effects and to improve or even surpass naturally observable effects. [20-22]

To create similar effects artificially, there are in principal two possible pathways. One is the *top-down* formation of defined and repetitive grating structures, e.g. via Electron beam (e-beam), [23, 24] Focused Ion Beam (FIB), [25] Laser Lithography [26] or Multi-Photon Lithography. [27, 28] Closely related are direct writing interference processes into soft materials as used e.g. in extreme Ultraviolet interference Lithography (eUV-iL) [29] or Laser interference Lithography (LiL). [30] Multilayer Soft Lithography (MSL) is applied at soft materials as well, however radiation-free. [31] Direct processes without radiation, but with mechanical stamping as the patterning medium are e.g. Nanoimprint Lithography [32] or Scanning Probe Lithography. [33] The other pathway starts in the opposite dimension of the size range, and is therefore called *bottom-up* formation. It is used in many self-assembling processes, when small particles such as molecules, proteins, polymers etc. assemble themselves in a way that a superordinate structure is formed. [34] This structure can gain different microscopic and even macroscopic appearances [35] that can be used for gratings as well. [36] Beyond these two approaches, *wrinkling* processes are regarded as a third approach to micro- and nano-structuring, [37, 38] since it is not a clearly delimitable topic within nano-structuring. It can be regarded either as a bottom-up method [39] or as a combination of bottom-up and tow-down. [40]

1.2. Introduction to wrinkling processes

Wrinkling is a natural buckling instability phenomenon that can be observed in manifold appearances. There are two well-known natural examples for wrinkling that scale over an enormous size range: On a large scale, within the size range of *m* to several hundred *km*, is the folding of stone plates and whole mountain ranges, [41] as also depicted in Fig. 2 **a** – **c**. These processes have been taken place on earth ever since, and are a result of the plate tectonics. During these processes, the various plates and fragments of the lithosphere move slowly over the liquid earth core, where they drift away or towards each other and collide. In the latter case, the huge forces of the lateral movement induced by the underlying liquid core may result in two scenarios: On the one hand one plate pushes on top of another forcing the lower one to descend and to melt partially under the tremendous pressure. This lava is ascending, and eventually volcanoes belts such as the pacific ring of fire are formed. On the other hand both plates compress each other laterally, and thrust in a way that enormous folds and creases arise at the plate's interface, so-called synclines and anticlines. [42, 43] Though in some cases (such as the Andes) a mixture of both cases is observed, they still may be regarded as folding mountains. [44]

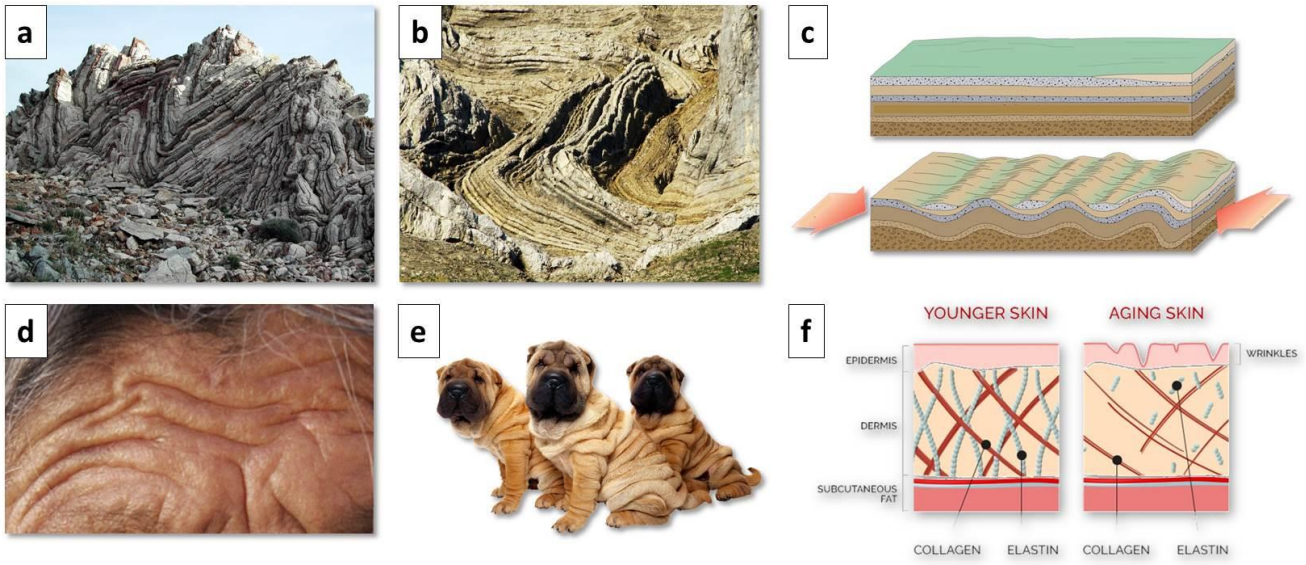

*Figure 2 | (**a**) Folded rock formation „Diplóno pétris", Agios Pavlos (Crete), Greece; [45] (**b**) Folded stone layers „Chrumme Würm" at Glärnisch, Switzerland; [46] (**c**) Schematic of syncline and anticline formation by subterrestrial compression; [47] (**d**) Wrinkled skin on the forehead of an old lady; [48] (**e**) Cantonese Shar-Pei dogs [49] (**f**) Schematic of skin aging due to the loss of collagen and elastin; [50] Reproduced with permission from references mentioned above.*

On a smaller scale it is wrinkling in the µm- up to the cm-range on skin folds as plant surfaces, [51] but also to bigger folds as e.g. on elephant skin. [52] Fig. 2 **d** – **f** show this exemplarily. Here folding and creasing of the surface has more diverse reasons. A very familiar kind of appearance is the well-studied aging of human skin [53-55] that seems to be caused again by different effects, such as habitual positions while sleeping [56] or the creeping glycation of the subcutis. [57] A temporary phenomenon on human skin is the morphological change observed when skin is dipped in water for a long time. It has been shown that the wrinkling of wet skin has some benefits: The macroscopic adhesion becomes increased compared to plain skin and is thus able to compensate for the reduced adhesion due to wetness. [58] Moreover another example for natural wrinkling processes is the entanglement of human brain mass in order to increase its surface area, and so eventually its effectivity. [59] Eventually, all those kinds of wrinkles on different skins have similar physical reasons as the before mentioned geological faults: The hard crust or skin is deformed by forces that act from the gel-like support underneath onto it. Physically or mechanically seen, it is therefore buckling of thin layers supported on compliant substrates.

Based on these principles, wrinkles have been also observed and produced artificially in the history of modern science, however at that time without the investigators realizing it or being able to explain their discovery. For example, in 1960 Cunnigham et al. bombarded gold surfaces with high energetic Ar^+-Ions, forming regularly parallel wrinkles, [60] while in 1982 Martin et al. achieved similar parallel structures on PDMS with Al-layers on top. [61] The first elaborate study with Ti-layers on PDMS was done by Bodö et al. in 1986, [62] however it was not before 1998, when Bowden et al. were able

to explain the underlying mechanisms for the first time. [63, 64] In the following years many publications dealing with the underlying physics and mechanics of wrinkling were published. It did not happen before 2004 that Stafford et al. presented for the first time a direct application for practice: In a bilayer-system they used the direct proportionality of emerging wavelength to the thin layer's thickness. Therefore they were able to calculate the Young's Modulus of the layer, and furthermore by changing this thickness the wavelength changes as well, so eventually they could prove the robustness of this new determination tool which they called "Strain-induced elastic buckling instability for mechanical measurements" (SIEBIMM). [65]

In order to comprehensively cover the subject area of wrinkling, here another type will shortly be introduced, though it is not in the focus of the thesis: The folding of self-supporting, free-standing membranes – so briefly, the wrinkling of single layers. This is in contrast to two- or multi-layer-wrinkling, which this thesis deals solely with. The well-known and also well-studied topic investigates non-supported materials, e.g. thin plates [66] or hanging sheets. [67] The physical and mathematical fundamentals are mainly based on the tension field theory [68] that describes the in-plane stresses of thin panels under shear forces. The arising shear loads precede parallel to the wave directions and are simplified to be uniaxial, with only one load tensor σ_x that has to be considered. The tension field theory allows simple but also reliable analysis of the post-buckling behavior in thin, wrinkled membranes. [69]

1.3. Objective of the thesis

The key objective of this thesis is the understanding and consequential improvement of established bilayer wrinkling systems, so the controlled wrinkling of thin films supported on compliant substrates. This first part can be mainly divided into two large sections, one dealing with surface defect structures and the other with the technical scalability of folded surfaces. And besides, a minor objective investigated in the second part is the application of wrinkled surfaces for the mechanical testing of ultrathin 2D-polymer films.

In order to be able to investigate defect structures in the surface in the first part of the work, for a start it has to be defined in which kind of wrinkle formation system these are considered. In the context of this work only controlled systems are used, which are characterized by a defined mechanical tension as well as direction of the same. In the simplest case of uniaxial mechanical stress, this leads to sinusoidal, parallel and uniform folds that form transversely to the direction of stress introduced. In such systems, defect structures are clearly visible as they disturb the homogeneity of the folded surface and are therefore easy to analyze.

The investigated defect structures are on the one hand so-called line defects, in which two waves unite in an intersection, which is why they are sometimes called Y-defects due to their appearance as well. On the other hand these are cracks, which run parallel to the stress direction and transverse to the wave direction. Line defects are mainly caused by locally limited in homogeneities, e.g. the layer thickness or the modulus of elasticity of both the substrate

and the thin film. Transverse cracks, on the other hand, are caused globally and occur when the elastic substrate is subjected to mechanical stress: The elastomer is compressed across the direction of elongation and then reversibly returns to its original shape. The thin film, on the other hand, cannot carry out this deformation due to its brittle nature and therefore tears parallel to the direction of elongation of the elastomer.

In the first part of this dissertation, wrinkle structures are produced from Polydimethyl siloxane (PDMS) using in-situ Ultraviolet/Ozone- (UVO) oxidation on an elasticity gradient in order to specifically produce line defects. At the interface of the gradient to a stiff embedding, which also consists of PDMS, different elastomer stiffnesses meet, which induces the formation of waves of different periodicity. These are detected by optical incident light microscopy. The waves meet along the boundary surface, which induces line defects. Depending on the ratio of the stiffness of the gradient to the embedding, either irregular or highly ordered line defect structures are formed in which, for example, every 6th large wave splits into two smaller ones (6:7 branching). The smallest branching ratio is observed at the soft end of the gradient with the largest difference in the stiffness ratio between gradient and embedding: Here every 2^{nd} wave splits (2:3 branching). Furthermore, it is observed that near the boundary surface at a distance of a few wave maxima no line defects form, but only along the same. The interface and the resulting defects are thus able to bind local inhomogeneities of the mechanical stress with a limited range. It is therefore possible not only to order line defects, but also to keep the surrounding areas free of defects.

To investigate the transverse cracks, hard elastomers from PDMS pre-stretched by 60 % are oxidized in situ using O_2 low-pressure plasma under various conditions. The result is wrinkle structures of different sizes that show transverse cracks under some conditions and not under others. In subsequent investigations of the mechanics of the oxidized layers, a relationship between oxidation conditions, layer hardness and thickness and crack formation can be established. Quantitative nanomechanical analysis (PF-QNM) of profile cross-sections of individual samples shows that the layer thickness is almost constant across all plasma conditions - only the maximum stiffness changes within a parameter screening. In addition, the stiffness within the oxidized layer changes exponentially perpendicular to the surface. Mechanical simulations using the Finite Element Method (FEM) show that such an exponential gradient has lower stress maxima compared to a discrete layer system. In comparison with the experimentally investigated layers, a threshold in mechanical tension can be derived which distinguishes between cracked and intact layers. In addition, it can be shown that an exponential slope as small as possible contributes to a more uniform distribution of the maximum stresses within the gradient layer. This enables the production of intact layers under conditions under which single-stage layer systems would exhibit transverse cracks.

In the second part of this thesis, the possibility of maximizing the area of folded surfaces and extending it to new, previously unused methods and materials is investigated. In the literature folded areas of a maximum of several cm^2 are known, at the same time in many places a scalability of folded systems is claimed. In this paper two methods are

used which have not been used for the formation of folds before: On the one hand dielectric barrier discharge (DBD) and on the other plasma jet. Both methods generate plasma under atmospheric conditions with which PDMS is oxidized in-situ. This type of processing is very similar to the low-pressure oxidation mentioned in the first part. The difference lies in the pristine surface that can be processed simultaneously, and in the possibility of *in-situ* oxidation in a continuous process. For this purpose, a self-constructed roll-to-roll structure is used in which the area to be processed between two rolls is uniaxially stretched in such a way that the same percentual stretch is permanently maintained - independent of the winding and unwinding speed. This makes it possible to cover surfaces of > 1 m^2 evenly with folds of the order of $\lambda < 1$ µm. In both methods, precursor molecules can also be introduced into the plasma, where they fragment or ionize and thus partially polymerize during deposition on a surface to form a thin, uniform film. In the context of this work, this is applied with glass-forming molecules such as Hexamethyl disiloxane (HMDSO), Tetramethyl disiloxane (TMDSO) or Tetraethyl orthosilicate (TEOS). Using this technique, large areas > 1 m^2 of both PDMS and purely organic elastomers such as ethylene propylene diene methylene rubber (EPDM), nitrile butadiene rubber (NBR), hydrogenated nitrile butadiene rubber (HNBR) and thermoplastic urethanes (TPU) can be coated with a thin layer of glass and wrinkled. In total it is therefore possible to coat a wide variety of elastomers with various glass-forming layers using two similar preparative methods, as well as to produce each of these combinations in a size scale of > 1 m^2 wrinkled surface area. The aforementioned methods are therefore a novelty in the field of wrinkle formation when compared to the state of the art in literature. This includes all partial methods of this thesis part, such as wrinkling of silicone polymers under atmospheric conditions via plasma jet or DBD, the plasma-assisted wrinkling with glass-forming precursors and the scaling of wrinkled surface from cm^2 to m^2-areas.

In the third and last part of this work, the formation of wrinkles is applied for characterization purpose. A molecular 2D polyimine film is applied to a PDMS substrate and folded. Since the thickness of the film is measured beforehand and the modulus of elasticity of the PDMS substrate is also known, the modulus of elasticity of the 2D film can be determined from the wavelength of the pleat pattern by simple conversion. This method, called SIEBIMM (Strain Induced Elastomer Buckling Instability for Mechanical Measurements), is known from literature, nevertheless for thicker layers. This film has a height of h_f = 700 pm and is thus the thinnest film ever measured via SIEBIMM. In order to validate the accuracy of the measurement, chemically similar films of comparable height (2 - 3 nm) and known elasticity (E_f = 14 GPa) are measured in the same way via SIEBIMM and compared with the literature values which show a deviation of $\sigma < 5$ %.

Overall, this work shows possibilities to reduce the number of defect structures in existing wrinkle formation systems or to reduce them to certain areas of the folded surface. Furthermore, various methods are presented to implement wrinkle formation on a large scale > 1 m^2. A combination of defect structure analysis and the resulting optimization, as well as scaling to large areas, opens up a wide range of new possibilities for technical application. These are, for example, optical functional surfaces in solar cells or LEDs, layers with reduced friction for various technical processes,

such as large-area anti-fouling foils in shipping or automotive industry, or as cost-effective and non-toxic adhesion protection in medical technology, which protects against virus, bacteria or cell adhesion to surfaces. Finally, this thesis demonstrates the possibility of investigating the mechanical properties of even the thinnest film under $h_f < 1$ nm by means of wrinkling on elastic substrates. In combination, it can be deduced that the wrinkle surfaces presented in this thesis have a wide range of possible applications, as their functionality extends over several orders of magnitude both in terms of the total area and the periodicity of the structure.

References

[1] P. Andrew Richard: 515 million years of structural colour, **2000**; *J. Opt. A: Pure Appl. Opt.*, 2 – 6, R15

[2] Y.-T. Cheng and D.E. Rodak: Is the lotus leaf superhydrophobic?, **2005**; *Appl. Phys. Lett.*, 86 – 14, 144101

[3] P. Ball: Engineering Shark skin and other solutions, **1999**; *Nature*, 400, 507 – 509

[4] X. Pu, G. Li and H. Huang: Preparation, anti-biofouling and drag-reduction properties of a biomimetic shark skin surface, **2016**; *Biol. Open*, 5 - 4, 389 – 396

[5] S.B. Creager and M.E. Porter: Stiff and tough: a comparative study on the tensile properties of shark skin, **2018**; *Zoology*, 126, 154 – 163

[6] F. Song, A.K. Soh and Y.L. Bai: Structural and mechanical properties of the organic matrix layers of nacre, **2003**; *Biomat.*, 24 – 20, 3623 – 3631

[7] R.Z. Wang, Z. Suo, A.G. Evans, N. Yao and I.A. Aksay: Deformation mechanisms in nacre, **2011**; *J. Mater. Res.*, 16 – 9, 2485 – 2493

[8] A.L. Ingram and A.R. Parker: A review of the diversity and evolution of photonic structures in butterflies, incorporating the work of John Huxley (The Natural History Museum, London from 1961 to 1990), **2008**; *Phil. Trans. Roy. Soc. B: Biol. Sci.*, 363 – 1502, 2465 – 2480

[9] B.D. Wilts, P. Pirih and D.G. Stavenga: Spectral reflectance properties of iridescent pierid butterfly wings, **2011**; *J. Compar. Physiol. A*, 197 – 6, 693 – 702

[10] E. Shevtsova, C. Hansson, D.H. Janzen and J. Kjærandsen: Stable structural color patterns displayed on transparent insect wings, **2011**; *Proceed. Nat. Acad. Sci.*, 108 – 2, 668 – 673

[11] J. Zi, X. Yu, Y. Li, X. Hu, C. Xu, X. Wang, X. Liu and R. Fu: Coloration strategies in peacock feathers, **2003**; *Proceed. Nat. Acad. Sci.*, 100 – 22, 12576 – 12578

[12] P. Vukusic and J.R. Sambles: Photonic structures in biology, **2003**; *Nature*, 424, 852 – 855

[13] H.M. Whitney, M. Kolle, P. Andrew, L. Chittka, U. Steiner and B.J. Glover: Floral Iridescence, Produced by Diffractive Optics, Acts As a Cue for Animal Pollinators, **2009**; *Science*, 323 – 5910, 130 – 133

[14] B. Prüm, H. Florian Bohn, R. Seidel, S. Rubach and T. Speck: Plant surfaces with cuticular folds and their replicas: Influence of microstructuring and surface chemistry on the attachment of a leaf beetle, **2013**; *Acta Biomater.*, 9 – 5, 6360 – 6368

[15] Patrick Doll: Shortfin mako shark “Isurus oxyrinchus"

[16] S. Tadepalli, J.M. Slocik, M.K. Gupta, R.R. Naik and S. Singamaneni: Bio-Optics and Bio-Inspired Optical Materials, **2017**; *Chem. Rev.*, 117 – 20, 12705 – 12763

[17] Civico Museo di Storia Naturale di Trieste: Shell of mollusk "Haliotis glabra"

[18] R. Maia, O. Caetano João Victor, N. Báo Sônia and H. Macedo Regina: Iridescent structural colour production in male blue-black grassquit feather barbules: the role of keratin and melanin, **2009**; *J. Roy. Soc. Interf.*, 6, S203 – S211

[19] S. Kinoshita, S. Yoshioka and J. Miyazaki: Physics of structural colors, **2008**; *Rep. Prog. Phys.*, 71 – 7, 076401-1 – 076401-30

[20] I. Brodie and J.J. Muray: The Physics of Micro/Nano-Fabrication, **1992**, Springer US; P. 26 – 33, 418, 522 – 538

[21] Z. Tang, N.A. Kotov, S. Magonov and B. Ozturk: Nanostructured artificial nacre, **2003**; *Nat. Mat.*, 2, 413 – 418

[22] A. Finnemore, P. Cunha, T. Shean, S. Vignolini, S. Guldin, M. Oyen and U. Steiner: Biomimetic layer-by-layer assembly of artificial nacre, **2012**; *Nat. Comm.*, 3, 966-1 – 966-6

[23] T. Fujita, H. Nishihara and J. Koyama: Blazed gratings and Fresnel lenses fabricated by electron-beam lithography, **1982**; *Opt. Lett.*, 7 – 12, 578 – 580

[24] M. Altissimo: E-beam lithography for micro-/nanofabrication, **2010**; *Biomicrofluidics*, 4 – 2, 026503-1 – 026503-6

[25] S. Cabrini, A. Carpentiero, R. Kumar, L. Businaro, P. Candeloro, M. Prasciolu, A. Gosparini, C. Andreani, M. De Vittorio, T. Stomeo and E. Di Fabrizio: Focused ion beam lithography for two dimensional array structures for photonic applications, **2005**; *Microelectron. Eng.*, 78 – 79, 11 – 15

[26] J. Fischer and M. Wegener: Three-dimensional optical laser lithography beyond the diffraction limit, **2013**; *Las. & Phot. Rev.*, 7 – 1, 22 – 44

[27] A.M. Kasko and D.Y. Wong: Two-photon lithography in the future of cell-based therapeutics and regenerative medicine: a review of techniques for hydrogel patterning and controlled release, **2010**; *Fut. Med. Chem.*, 2 – 11, 1669 – 1680

[28] M.P. Stocker, L. Li, R.R. Gattass and J.T. Fourkas: Multiphoton photoresists giving nanoscale resolution that is inversely dependent on exposure time, **2011**; *Nat. Chem.*, 3, 223 – 227

[29] B. Päivänranta, A. Langner, E. Kirk, C. David and Y. Ekinci: Sub-10 nm patterning using EUV interference lithography, **2011**; *Nanotech.*, 22 – 37, 375302-1 – 375302-7

[30] Q. Xie, M.H. Hong, H.L. Tan, G.X. Chen, L.P. Shi and T.C. Chong: Fabrication of nanostructures with laser interference lithography, **2008**; *J. Alloys Compd.*, 449 – 1, 261 – 264

[31] M.A. Unger, H.-P. Chou, T. Thorsen, A. Scherer and S.R. Quake: Monolithic Microfabricated Valves and Pumps by Multilayer Soft Lithography, **2000**; *Science*, 288 – 5463, 113 – 116

[32] L.J. Guo: Nanoimprint Lithography: Methods and Material Requirements, **2007**; *Adv. Mater.*, 19 – 4, 495 – 513

[33] R. Garcia, A.W. Knoll and E. Riedo: Advanced scanning probe lithography, **2014**; *Nat. Nanotech.*, 9, 577 – 587

[34] Y. Xue and M.B. Zimmt: Patterned Monolayer Self-Assembly Programmed by Side Chain Shape: Four-Component Gratings, **2012**; *J. Am. Chem. Soc.*, 134 – 10, 4513 – 4516

[35] R.D. Kamien: Topology from the Bottom Up, **2003**; *Science*, 299 – 5613, 1671 – 1673

[36] Y. Pennec, W. Auwärter, A. Schiffrin, A. Weber-Bargioni, A. Riemann and J.V. Barth: Supramolecular gratings for tuneable confinement of electrons on metal surfaces, **2007**; *Nat. Nanotech.*, 2, 99 – 103

[37] Y. Xia and G.M. Whitesides: Soft Lithography, **1998**; *Angew. Chem. Int. Ed.*, 37 – 5, 550 – 575

[38] D. Qin, Y. Xia and G.M. Whitesides: Soft lithography for micro- and nanoscale patterning, **2010**; *Nat. Protoc.*, 5, 491 – 502

[39] R. Li, H. Yi, X. Hu, L. Chen, G. Shi, W. Wang and T. Yang: Generation of diffraction-free optical beams using wrinkled membranes, **2013**; *Sci. Rep.*, 3, 2775-1 – 2775-6

[40] A. Schweikart and A. Fery: Controlled wrinkling as a novel method for the fabrication of patterned surfaces, **2009**; *Microchim. Acta*, 165 – 3, 249 – 263

[41] P. Yamato, B.J.P. Kaus, F. Mouthereau and S. Castelltor: Dynamic constraints on the crustal-scale rheology of the Zagros fold belt, Iran, **2011**; *Geology*, 39 – 9, 815 – 818

[42] M.J. Fleuty: The description of folds, **1964**; *Proc. Geol. Associ.*, 75 – 4, 461 – 492

[43] F.M. Gradstein: The Geologic Time Scale – *Chapter 1 Introduction*, **2012**, In: F.M. Gradstein, J.G. Ogg, M.D. Schmitz and G.M. Ogg, editor, Boston: Elsevier; 1 – 29

[44] V.A. Ramos, V.D. Litvak, A. Folguera and M. Spagnuolo: An Andean tectonic cycle: From crustal thickening to extension in a thin crust (34°–37°SL), **2014**; *Geosci. Front.*, 5 – 3, 351 – 367

[45] Dieter Müller: „Diplóno pétris", Agios Pavlos (Crete), Greece, retrieved: 03/**2019**

[46] Hanspeter Fritsch: Chrumme Würm“, Glärnisch, Switzerland, retrieved: 03/**2019**

[47] © Pearson Prentice Hall Inc.: Schematic of syncline and anticline formation, **2005**

[48] Tomas Castelazo: Wrinkled skin on the forehead of an old lady, retrieved: 03/**2019**

[49] pngimg.com: Cantonese Shar-Pei dogs, retrieved: 03/**2019**

[50] © New York Presbyterian Hospital: Schematic of skin aging, **2019**

[51] P. Prusinkiewicz and P. Barbier de Reuille: Constraints of space in plant development, **2010**; *J. Exp. Bot.*, 61 – 8, 2117 – 2129

[52] A.F. Martins, N.C. Bennett, S. Clavel, H. Groenewald, S. Hensman, S. Hoby, A. Joris, P.R. Manger and M.C. Milinkovitch: Locally-curved geometry generates bending cracks in the African elephant skin, **2018**; *Nat. Comm.*, 9, 3865-1 – 3865-8

[53] Y. Wu, P. Kalra, L. Moccozet and N. Magnenat-Thalmann: Simulating wrinkles and skin aging, **1999**; *Vis. Comp.*, 15 – 4, 183 – 198

[54] S. Pillai, C. Oresajo and J. Hayward: Ultraviolet radiation and skin aging: roles of reactive oxygen species, inflammation and protease activation, and strategies for prevention of inflammation-induced matrix degradation – a review, **2005**; *Int. J. Cosmetic Sci.*, 27 – 1, 17 – 34

[55] J.W. Choi, S.H. Kwon, C.H. Huh, K.C. Park and S.W. Youn: The influences of skin visco-elasticity, hydration level and aging on the formation of wrinkles: a comprehensive and objective approach, **2013**; *Skin Res. Technol.*, 19 – 1, e349 – e355

[56] M.A.C. Kane, V. Lambros and G. Anson: Sleep Wrinkles: Facial Aging and Facial Distortion During Sleep, **2016**; *Aesth. Surg. J.*, 36 – 8, 931 – 940

[57] P. Gkogkolou and M. Böhm: Advanced glycation end products – Key player in skin aging?, **2012**; *Derm.-Endocrin.*, 4 – 3, 259 – 270

[58] K. Kareklas, D. Nettle and V. Smulders Tom: Water-induced finger wrinkles improve handling of wet objects, **2013**; *Biol. Lett.*, 9 – 2, 20120999-1 – 20120999-3

[59] R. Toro: On the Possible Shapes of the Brain, **2012**; *Evol. Biol.*, 39 – 4, 600 – 612

[60] R.L. Cunningham, P. Haymann, C. Lecomte, W.J. Moore and J.J. Trillat: Etching of Surfaces with 8-Kev Argon Ions, **1960**; *J. Appl. Phys.*, 31 – 5, 839 – 842

[61] G.C. Martin, T.T. Su, I.H. Loh, E. Balizer, S.T. Kowel and P. Kornreich: The metallization of silicone polymers in the rubbery and the glassy state, **1982**; *J. Appl. Phys.*, 53 – 1, 797 – 799

[62] P. Bodö and J.E. Sundgren: Titanium deposition onto ion-bombarded and plasma-treated polydimethylsiloxane: Surface modification, interface and adhesion, **1986**; *Thin Solid Films*, 136 – 1, 147 – 159

[63] N. Bowden, S. Brittain, A.G. Evans, J.W. Hutchinson and G.M. Whitesides: Spontaneous formation of ordered structures in thin films of metals supported on an elastomeric polymer, **1998**; *Nature*, 393, 146 – 149

[64] N. Bowden, W.T.S. Huck, K.E. Paul and G.M. Whitesides: The controlled formation of ordered, sinusoidal structures by plasma oxidation of an elastomeric polymer, **1999**; *Appl. Phys. Lett.*, 75 – 17, 2557 – 2559

[65] C.M. Stafford, C. Harrison, K.L. Beers, A. Karim, E.J. Amis, M.R. VanLandingham, H.-C. Kim, W. Volksen, R.D. Miller and E.E. Simonyi: A buckling-based metrology for measuring the elastic moduli of polymeric thin films, **2004**; *Nat. Mat.*, 3, 545 – 550

[66] F.P.J. Rimrott and M. Cvercko: Wrinkling in Thin Plates due to In-plane Body Forces, Berlin, Heidelberg, Springer, 1986, 19 – 48

[67] H. Vandeparre, M. Piñeirua, F. Brau, B. Roman, J. Bico, C. Gay, W. Bao, C.N. Lau, P.M. Reis and P. Damman: Wrinkling Hierarchy in Constrained Thin Sheets from Suspended Graphene to Curtains, **2011**; *Phys. Rev. Lett.*, 106 – 22, 224301-1 – 224301-4

[68] H. Wagner: Ebene Blechwandtraeger mit sehr duennem Stegblech (Flat sheet metal girders with very thin metal web), **1931**; *Zeitschrift fuer Flugtechnik und Motorluftschiffahrt*, 20 – 8, 200 – 207 (20 – 9, 227 – 231)

[69] D.J. Steigmann: Tension-field theory, **1990**; *Proc. Roy. Soc. London. A. Math. Phys. Sci.*, 429 – 1876, 141 – 173

2. Theory and Status of the Field

"Physics is a weird subject. The first time you look at it, you don't understand anything about it. The second time you work through it, you think you've understood everything, except one or two small details. The third time you work through the material, you notice that you understand almost nothing about it, but you've gotten so used to it that you don't mind it anymore."

adapted from Arnold Sommerfeld

2.1. Wrinkling of stiff layers on compliant substrates

Controlled wrinkling in the framework of this thesis is defined as buckling of a thin, rigid layer on a compliant, elastic support. In this controlled formation, the applied compression is of defined manner, and so the load is not randomly distributed, but well-defined with a distinct direction. This oriented compression eventually leads to an out-of-place-displacement of the thin, rigid layer that has a sinusoidal shape. Fig. 3 schematically shows the process of controlled wrinkle formation in a bilayer system. The phenomenon is caused by a minimization of the deformation energy of the compound that can be interpreted as a mechanical compromise between the hard layer and the soft substrate with minimized load along the layer-substrate-interface.

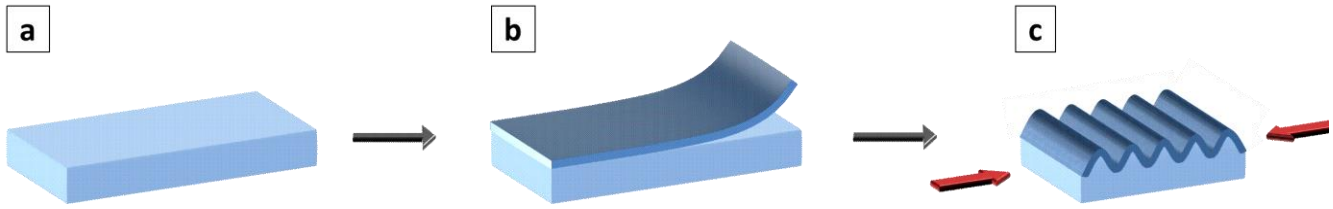

*Figure 3 | Schematic of controlled, uniaxial wrinkling: A thick slab of elastomer (**a**) is adhesively coated to a thin, rigid layer (**b**). The compound sample eventually becomes compressed uniaxially (**c**), which causes parallel wrinkles to form.*

Since the first experiments were published that had been able to conclusively explain wrinkle formation in bilayer systems, countless works on the subject were published. It was soon discovered that the application of a mechanical pre-strain influences the morphology of the resulting wrinkles, depending on its intensity and directions. By this, it is possible to gain control not just over the main wrinkle orientation, but also on their size. The simplest case is a uniaxial load, where the pre-strain is only applied in one direction onto the bilayer system (Fig. 4 **a**). This is also the case for all experiments conducted within this work, but there are still numbers of other morphologies. The second case is the isotropic load onto a bilayer system, which is very common in literature besides the aforementioned uniaxial load (**Fig.** 4 **b**). [1-5] In here, the compression points orthogonal onto the edges of the sample; or rather on all, and not only on one exterior side. Since the compression is therefore isotropic, no preferred direction of wrinkles can be observed, hence the morphology is random. Wrinkling in this way often happens in thermal processes, when the substrate becomes heated and therefore increases isotropic, with a subsequent isotropic compression. The third case that is more related to the first mentioned is biaxial load / compression that leads to zig-zag-like morphologies, often referred to as Chevron- or Herringbone-structures (Fig. 4 **c**). [2, 6-9] It can be regarded as a mechanical and also morphological hybrid between the first and the second case, which both represent the extreme cases of stress-induced patterning. Fourthly, a special morphology shows up when the uniaxial load is significantly increased beyond a certain threshold: Then the previously sinusoidal

waves split into two dissimilar amplitudes (Fig. 4 **d**). [10-12] This behavior is more detailed explained later in chapter 2.2.4. Eventually, the fifth and sixth cases are two rather more specific morphologies: In the fifth case the waves emerge from radial strain out of a center spot (Fig. 4 **e**), [13-15] in the sixth from radial compression towards a center spot (Fig. 4 **f**). [9, 16-18] In opposite to the aforementioned these structures can only be created and observed on local spots and not globally over the entire surface. Other morphologies are possible as well, however they are mostly crossovers or hybrids of the six cases described here. [14]

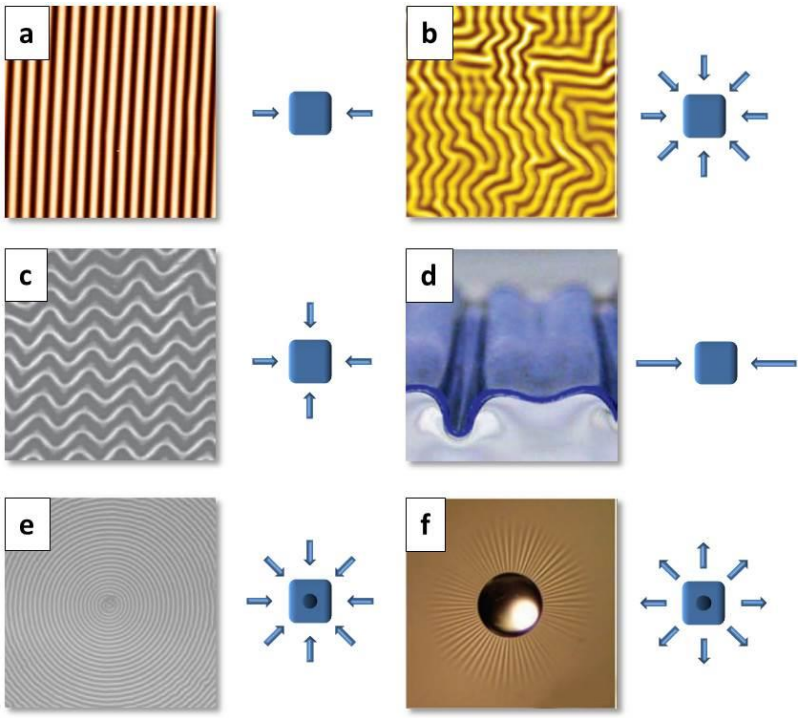

*Figure 4 | Overview of the different wrinkle morphologies: (**a**) parallel waves via uniaxial compression (sinusoidal wrinkles), (**b**) random waves via isotropic compression, [4] (**c**) parallel waves, iterative displaced at a certain angle via orthogonal, biaxial strain (Chevron / Herringbone structure), [7] (**d**) parallel waves with dissimilar amplitudes via large uniaxial compression (bi-sinusoidal wrinkles) [11] (**e**) circular waves via radial strain pointing away from a center point (target structure), [14] (**f**) radial waves via radial compression towards a center point (spoke structure). [16] Reproduced with permission from references mentioned above.*

Another important aspect is the method of producing wrinkles on compliant bilayer systems, so how to create a thin, rigid film that is adhesively or covalently bound onto a comparably soft, elastomeric substrate. A widely used method is the deposition of metals on an elastic foundation, which was used to gain the first insights into wrinkled surfaces. For this purpose elastomeric PDMS was metallized by depositing Ti or Al, [19, 20] later also the first systematic descriptions on surface wrinkling were obtained similarly. [21] In general, a widely used combination of metal and elastomer is Ti/PDMS (alternatively: TiO_2/PDMS), since Ti/TiO_2 both have excellent

adhesion properties on PDMS, [22] furthermore the covalent binding of Ti to Si- or SiO_2-surfaces has already be proven experimentally. [23, 24] Also Aluminum, [25] Chromium, [26] Indium, [27] Tantalum [28] and Gold [29] have shown decent adhesion properties on PDMS. Another common preparation method is the adhesion or covalent linkage of hard, rigid polymer films onto soft elastomeric ones, so that the eventual bilayer system is entirely polymeric. Here a much-used polymer for the film is high-molecular polystyrene. [14, 28, 30, 31] Besides PS, also wrinkled surfaces with PMMA, [32] PTFE, [33] PEDOT:PSS, [34, 35] Polydopamine [36] and even with hydrogels [37] have been reported. Besides the selective wrinkle generation, folding in technical PEEK- and PPS-composites has been observed as well. [38] A preparation methodology that is substantially different is the wrinkling of highly dense polymer brush layers, whose property as a rigid layer is created only by the compression of the underlying soft elastomeric substrate. [39] This can be even applied to mechanically characterize those dense brush layers. [40] Moreover also layers of actually independent particles can be wrinkled that however necessarily need to have a decent in-plane-adhesion. Such particle layers are capable for mechanical analysis as well. [41] Apart from that, even on the surface of single spherical hollow particles, or within such, buckling is possible. [8, 18]

A further methodology is the in-situ creation of the thin, rigid film within the elastomeric substrate. This can be done by oxidizing silicone-based polymers such as PDMS. There are various methods known, of which most utilize physical treatment such as bombardment processes with e-beam, [42, 43] Focused Ion Beam (FIB), [44, 45] but also radiation process with lasers [46, 47] or plasmas, [1, 3, 48-50] with the latter being one focus of this work (see chapters 2.4.2. as well as 2.4.3.). Related to radiation, but in a stricter sense a chemical method, is the treatment with UVO [51-54] that represents another focus of this work (see chapter 2.4.1.). Eventually, chemical treatment is possible with strong acids such as H_2SO_4 or HNO_3. [55] Besides, there are many more reported preparation techniques. [5, 56, 57]

2.2. Physical and mathematical fundamentals of surface wrinkling

Bilayer wrinkling can be regarded as a mechanical mismatch of at thin, rigid layer on a thick, elastic substrate underneath, when both layers are strongly bond to each other. If such a bilayer system becomes strained, the thin layer tries to bend in a single bow; however this out-of-plane bending is restricted by the substrate's support. Resultantly, the mechanical compromise of both layers manifests as a repetitive, sinusoidal deflection of the thin layer along the interface to the soft substrate. To understand such bilayer systems, there are basically two ways to approach the fundamental physics and their consequences. The one is to consider the involved forces necessary to induce wrinkling, the other deals with the involved energies in the bilayer system. Both approaches are similar; nevertheless they result in slightly different equations. Since the force-equilibrium ansatz is applied both, in most cases in literature and in the publications this works presents, it will be explained in detail.

Subsequently, the energy-equilibrium ansatz is briefly discussed and its differences to the force-equilibrium ansatz are explained in short.

2.2.1. Force-equilibrium ansatz

In the first approach the competing forces are taken into account to describe the opposing mechanisms. [58-62] It is basically the sum of two competing mechanisms, so the bending forces F_B that are necessary to bend the bilayer out of its neutral plane, as well as the stretching forces F_S that the bilayer experiences while being strained.

$$F_{total} = F_S + F_B \tag{1.1}$$

Inserting for F_S and F_B yiels in Eq. 1.2 that describes the total forces for bending and stretching: [61, 63, 64]

$$\bar{E}_l \, I_l \, \frac{d^4 z(x)}{dx^2} + F \, \frac{d^2 z(x)}{dx^2} + kz = 0 \tag{1.2}$$

In Eq. 1.2, the first term corresponds to the Euler-Bernoulli beam theory, [61, 65, 66] and the second one represents the applied deformation force. In the third term, *k* is the elastic half-circular force regime along the z-direction, as suggested by Winkler, Wieghardt and Biot. [67-69]

In the Euler-Bernoulli term, *I* is the Moment of Inertia (Eq. 1.3), with *w* and *h* being the width and the height of the layer. And in the deformation term, *F* is the force exerted by the substrate that affects the thin layer from below.

$$I_l = \frac{wh^3}{12} \tag{1.3}$$

As mentioned above, *k* is the elastic half-circular force regime. *E* and *v* represent the Young's Modulus and the Poisson's ratio of the rigid layer or the elastic substrate, respectively.

$$k = \frac{\bar{E}_s w \pi}{\lambda} \tag{1.4}$$

Furthermore, $\bar{E}_l$ in Eq. 1.2 as well as $\bar{E}_s$ in Eq. 1.4 represent the in-plane modulus $\bar{E}$ in the thin layer according to Eq. 1.5.

$$\bar{E} = \frac{E}{1 - \nu^2} \tag{1.5}$$

Figuratively said, the rigid layer favors a vertical deformation with a preferably large mode, in order to keep the sum consisting of moment of inertia *I* for the whole layer and the torsion forces of the each half-space of the layer *k* to the smallest feasible value. On the other side, since the restoring forces for a bulk elastomer are

isotropic while the deformation length is smallest for a lateral distance, the elastic substrate favors the lateral deformation. Furthermore, the high resilience of the rigid layer in comparison to the elastic substrate causes just a minimal lateral deformation of it, resulting in a nearly constant length of the layer along its centroidal axis. [70]

The next step is to consider how the displacement of the surface wrinkles morphologically appears, which will be described with a sinusoidal shape. One possibility is to regard the force from the elastic substrate onto the rigid layer as infinitesimal springs on the substrate along the interface, leading to the aforementioned sum of half-circular force regimes called "Neo-Hookean Half-Space": [67-69] This enables the substitution of *z(x)* as in Eq. 1.2, resulting in Eq. 1.6:

$$z(x) = A_n \sin\left(\frac{m\pi}{\lambda}\right) \tag{1.6}$$

Moreover, *m* will be set to *m = 1* in order to satisfy the condition that the deformation force is the smallest possible. This corresponds to the first buckling mode. Inserting this in Eq. 1.2 gives Eq. 1.7:

$$\bar{E}_l\, I_l\, \frac{d^4 A_n \sin\left(\frac{\pi}{\lambda}\right)}{dx^2} + k\, A_n \sin\left(\frac{\pi}{\lambda}\right) + F\, \frac{d^2 A_n \sin\left(\frac{\pi}{\lambda}\right)}{dx^2} = 0 \tag{1.7}$$

Deriving Eq. 1.7 for the Force *F* gives:

$$F = 4\bar{E}_l I_l \left(\frac{\pi}{\lambda}\right)^2 + \frac{\omega \bar{E}_s}{4}\left(\frac{\pi}{\lambda}\right)^{-1} = \left(\frac{h^3 \omega \pi^2 \bar{E}_l}{3\lambda^2}\right) + \left(\frac{\lambda \omega \bar{E}_s}{4\pi}\right) \tag{1.8}$$

The force *F* now needs to be differentiated with respect to λ, thus the force minimizes to *F = 0*, giving:

$$0 = \frac{\delta F}{\delta \lambda} = \frac{\omega \bar{E}_s}{4\pi} - \frac{2h^3 \pi^2 \bar{E}_l \omega}{3\lambda^3} \tag{1.9}$$

Deriving Eq. 1.9 for λ leads to the force-equilibrium wrinkling equation:

$$\lambda = 2\pi h \left(\frac{\bar{E}_l}{3\bar{E}_s}\right)^{1/3} \tag{1.10}$$

Eq. 1.10 does not depend on the pre-strain, as in the force-equilibrium ansatz the assumption is made that the out-of-place displacement of the thin layer has a periodic, sinusoidal shape. In reality this is adequate in a lot of cases; nevertheless there are systems that require adapted calculation methods, as shown via the force-equilibrium ansatz for high strains in chapter 2.2.2.

With Eq. 1.10 the force-equilibrium ansatz now also allows for the calculation of the critical strain ε_c that is necessary to induce a periodic buckling structure after all. If ε_c is recognized as an extrinsic value, independent of the sample properties, the calculation inevitably needs for a definition of boundary conditions, such as sample size and material properties. This is possible via the definition of the critical stress σ_c (Eq. 1.11) as well as the critical force F_c (Eq. 1.12), beyond which the bilayer starts to buckle. [61]

$$\sigma_c = \bar{E}_l \varepsilon_c = \frac{F_c}{A} = \frac{F_c}{hw} \tag{1.11}$$

$$F_c = \bar{E}_l \varepsilon_c hw \tag{1.12}$$

In 1.12, F_c depends on the input variables *h* representing the height and *w* the width of the layer. Defining the calculated force as $F = F_c$, and inserting Eq. 1.10 into Eq. 1.8, gives the critical force F_c that eventually can be equated with Eq. 1.12:

$$\bar{E}_l \varepsilon_c hw = \frac{h\omega}{4} (\bar{E}_l)^{1/3} (\bar{E}_s)^{2/3} \tag{1.13}$$

Solving this for ε yields in: [59, 61, 71]

$$\varepsilon_c = \frac{1}{4} \left(\frac{3\bar{E}_s}{\bar{E}_l} \right)^{2/3} \tag{1.14}$$

Eq. 1.14 is the critical strain ε_c that defines the threshold between an intact, flat surface and a wrinkled morphology.

Finally, via force-equilibrium it is also possible to gain the amplitude *A* of the buckling instability. It is important to note that this calculation only works for the assumption that the buckling wavelength λ is independent of the applied strain ε. Then the assumption that the strain above ε_c is equal to the tensile strain in the layer can be made, giving:

$$\varepsilon - \varepsilon_c = \varepsilon_{eff} = \frac{\sigma}{\bar{E}_l} \tag{1.15}$$

With this, one can calculate: [59, 61]

$$\varepsilon_{eff} = \frac{1}{\lambda} \int_0^{\lambda} \left[1 + \left(\frac{dz}{dx} \right)^2 \right]^{1/2} - 1 \tag{1.16}$$

This integral represents one wrinkling period λ within Eq. 1.10 along the x-axis and with the deformation vertical to it in the z-axis. For solving it, the assumption is made that $\frac{dz}{dx}$ is small, meaning that in reality the amplitude *A* (z-direction) is much smaller than the wavelength λ (x-direction). This simplifies the integral term $u = \left[1 + \left(\frac{dz}{dx} \right)^2 \right]^{1/2}$ in Eq. 1.16 to: [59, 61]

$$u = 1 + \frac{1}{2} \left(\frac{dz}{dx} \right)^2 \tag{1.17}$$

Eventually, with this assumption the effective strain calculates as follows:

$$\varepsilon_{eff} = \frac{1}{\lambda} \int_0^{\lambda} 1 + \frac{1}{2} \left(\frac{dz}{dx} \right)^2 - 1 \tag{1.18}$$

If now the elastic half-space $z(x) = A_n \sin\left(\frac{m\pi}{\lambda}\right)$ (Eq. 1.6) is inserted for *z*, one gets: [61, 71]

$$\varepsilon - \varepsilon_c = \left(\frac{A\pi}{\lambda}\right)^2 \tag{1.19}$$

Inserting $\varepsilon_c = \frac{1}{4}\left(\frac{\bar{E}_s}{3\bar{E}_l}\right)^{2/3}$ (Eq. 1.14) and $\lambda = 2\pi h\left(\frac{\bar{E}_l}{3\bar{E}_s}\right)^{1/3}$ (Eq. 1.10) into Eq. 1.19 gives eventually:

$$A = h\left(\frac{\varepsilon - \varepsilon_c}{\varepsilon_c}\right)^{1/2} \tag{1.20}$$

It must be noted that at large values of ε this equation is not valid anymore, since the assumption $A << \lambda$ made for Eq. 1.17 is no longer true as well.

Fig. 5 **a** – **d** show the relationship of the overall force in the system F_{total} and the emerging wrinkle amplitude *A*, resulting in the two cases of a flat surface on the one side and a wrinkled surface on the other side. The general relationship of wavelength and amplitude to the thickness ratio of substrate/film *H/h* as well as to the film/substrate-ratio E/E_s is exemplarily shown in Fig. 5 **e** – **f**. It becomes obvious that for high *H/h*-values, both λ and *A* are limited by a maximum threshold, beyond which they cannot increase. In Fig. 5 **e**, a large E/E_S is able to shift the threshold to higher λ, while in Fig. 5 **f** the threshold is independent of E/E_S.

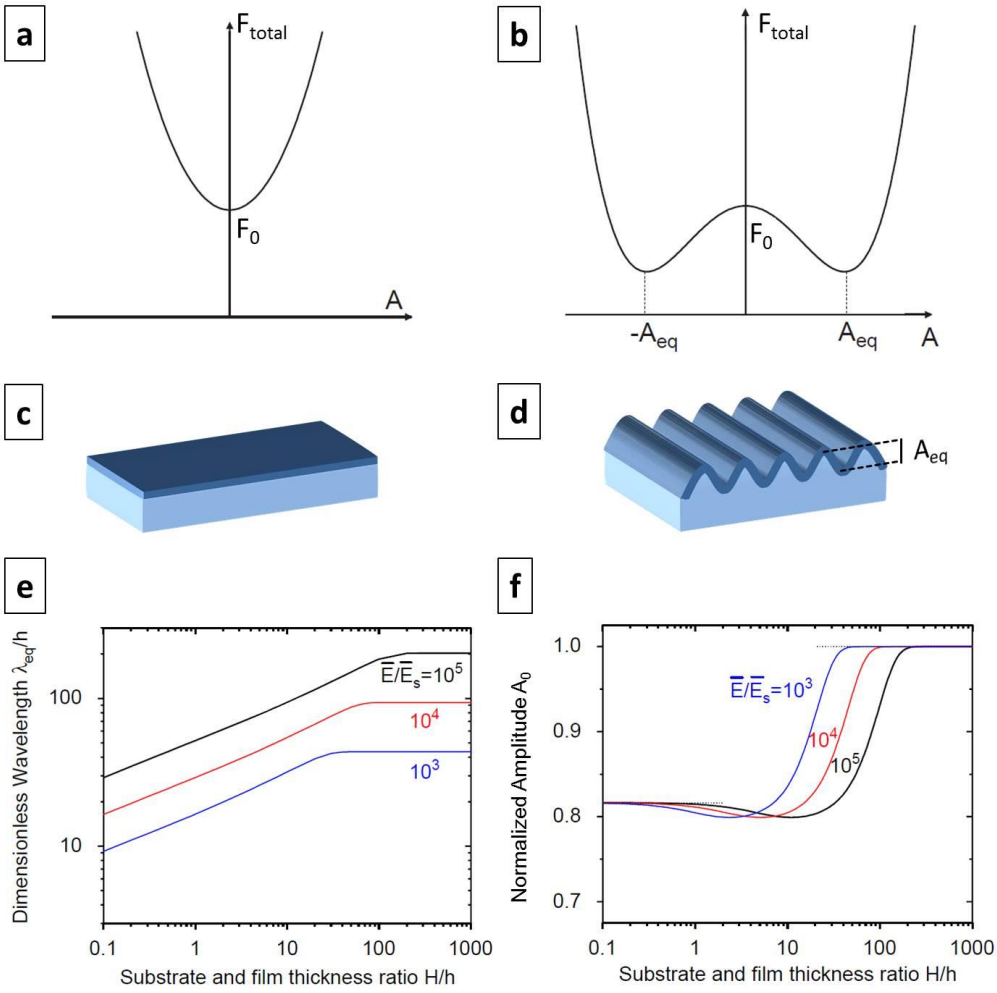

*Figure 5 | Total force in the bilayer system F_{total} vs. equilibrium wrinkle amplitude A_{eq}: If the applied mechanical load is small or zero (**a**), the minimum in F_{total} matches a parable with its minimum at A = 0, [59] so a flat surface (**c**). In case of a large mechanical load (**b**), F_{total} develops a symmetric double-well shape with two minima at A ≠ 0, [59] giving a wrinkled film with a specific amplitude A_{eq} (**d**), since the negative amplitude $-A_{eq}$ does not exist in reality. Calculation of the dimensionless wavelength λ_{eq}/h (**e**) [59] and the normalized amplitude A_0 (**f**) [59] vs. substrate/film thickness ratio H/h, for 3 different film/substrate moduli ratios E/E_S. Reproduced with permission from references mentioned above.*

2.2.2. Force-equilibrium at high pre-strains

As mentioned before, the calculation of the wavelength has one big disadvantage. As can be seen in Eq. 1.10, it ignores the effective influence of the pre-strain ε_{pre} on the wrinkles, since only the initial wavelength can be calculated. Before the critical wrinkling wavelength (Eq. 1.14) is reached, this influence onto the resulting morphology but also dimensions may be neglected, nevertheless beyond in the post-buckling regime with $\varepsilon_{effective} = \varepsilon_{applied} - \varepsilon_{cricital}$ this simplification becomes inaccurate for values that are distinctly larger than $\varepsilon_{applied} - \varepsilon_{cricital}$. To avoid deviations for large pre-strains, there are several solutions in literature known. Jiang et al. developed an

empirical model that takes into account the pre-strain, and expands the existing force-equilibrium ansatz calculations by a simple term: [71]

$$\lambda = \frac{\lambda_c}{(1+\varepsilon)\left(1+\frac{5\varepsilon(1+\varepsilon)}{32}\right)^{1/3}} \tag{1.21}$$

In here, λ_c is the same λ as for Eq. 1.10, however at the point of ε_c (Eq. 1.14), when the wrinkles are just forming and the vertical deflection exactly matches a sinusoidal shape, as for the initial presumption made in Eq. 1.6. With the same method, a large-strain approximation for the amplitude *A* can be made as well, leading to a similarly result:

$$A = \frac{A_c}{(1+\varepsilon)^{1/2}\left(1+\frac{5\varepsilon(1+\varepsilon)}{32}\right)^{1/3}} \tag{1.22}$$

Another approach to the post-buckling wavelength was published by Béfahy et al. [72] They described this regime as a linear function in dependency of the applied pre-strain as:

$$\lambda = -\lambda_c \varepsilon_{pre} + \lambda_c \left[1+\left(\frac{\pi h}{\lambda_c}\right)^2\right] \tag{1.23}$$

Still these calculations only describe another regime in a phase-diagram of involved wrinkling parameters. [73, 74] Beyond wrinkling with deformed structures of originally sinusoidal shape there is another buckling phenomenon, where the formation and calculation of wavelength λ and amplitude A becomes decoupled. This is described in the following chapter 2.2.4.

2.2.3. Energy-equilibrium ansatz

Another solution to describe the buckling behavior in bilayer wrinkling is the examination of the total deformation energy involved in the system. [61, 75-80] The basic assumptions made for this are similar to the force-equilibrium ansatz, meaning there are two opposing energy contributions to U_{total} as well. Also the vertical deformation is assumed to have a sinusoidal shape according to the Neo-Hookean Half Space model. Eventually the transformation results in Eq. 1.24 for the wavelength and Eq. 1.25 for the amplitude. [77, 79]

$$\lambda = 2\sqrt{\pi}\left(\frac{wEh^4}{12(1-\nu^2)F}\right)^{1/4} l^{1/2} \tag{1.24}$$

$$A = \frac{\sqrt{2}}{\pi}\left(\frac{wEh^4}{12(1-\nu^2)F}\right)^{1/2} \lambda^{1/2} \tag{1.25}$$

It is noteworthy that Eq. 1.25 and Eq. 1.25 consider the width *w*, height *h* and length *l* of the film, unlike the comparable Eq. 1.10 $\lambda = 2\pi h \left(\frac{\bar{E}_l}{3\bar{E}_s}\right)^{1/3}$ in the force-equilibrium ansatz that only takes into account the film height *h*. That is because in the energy-equilibrium ansatz, a Lagrange Multiplier $\mathcal{L}$ confines the geometry of the examined bilayer by an inextensibility condition; so its width, height and length have to be defined and < ∞. This condition is missing in the force-equilibrium ansatz. And secondly, different derivation approaches lead to different powers for the calculation of the wavelength λ and the amplitude *A* as well. Both approaches deliver reliable values, [51, 71, 76] however in literature mainly the force-equilibrium approach is used, making it the standard model for wrinkling calculations. Therefore all calculations performed within this work were made with force-equilibrium as well.

2.2.4. Bi- and- quadro-sinusoidal wrinkling, folding and delamination

At low pre-strains, where the substrate is still in the elastic deformation regime or just above it, the buckling deformation in bilayer systems appears in a sinusoidal shape, as it has been described in detail in the chapters before. Nevertheless, when it comes to large mechanical pre-strains, the sinus-shape evolves into different repetitive wave structures. The well-known initial sinusoidal modification turns at increasing pre-strains into bi-sinusoidal / bi-furcale wrinkles, as shown in Fig. 6 **a** experimentally as well as in Fig. 6 **b** by simulations. This phenomenon is also known as period doubling. It has first been described by Pocivavsek et al. [10] in 2008, when they tried to close the gap in understanding between wrinkling, folding and delamination of thin sheets. Bi-sinusoidal wrinkles are characterized by a division of one sinusoidal wave with distinct amplitude into two different amplitudes that however still follow the same wavelength, so breaking the up-down-symmetry typically observed in wrinkled surfaces. Moreover there is a parity of sinusoidal and bi-sinusoidal wavelength close to the threshold of amplitude splitting. Several attempts have been made ever since to approach a solution to this, mostly realizing that multimodal behavior can only be computed via nonlinearity. One method that delivers promising results is the introduction of a subharmonic mode additional to the harmonic ground state sinus by Brau et al. [11, 81] Beyond a critical threshold in pre-strain, the subharmonic dominates the harmonic and determines the wrinkle morphology with further increasing strain. This implies for the calculation of such systems that the basic equations have to be expanded. Both, Eq. 1.2 and Eq. 1.6 in the force-equilibrium ansatz, describe a sinus-shaped repetitive deformation of the thin stiff layer that follows the Neo-Hookean half space model. [67-69] By adding another phase-shifted sinus to the first one, one gets the following ansatz:

$$z(x) = A_n \cos\left(\frac{m\pi}{\lambda}x\right) + B_n \cos\left(\frac{m\pi}{2\lambda}x\right) \qquad (1.26)$$

From this it also can be seen that $\frac{A}{2} \sim B$, which is consistent with the experimental observations of a single wavelength even after the bifurcation event. Inserting *z(x)* in Eq. 1.2. $\left(\bar{E}_l\, I_l\, \frac{d^4 z(x)}{dx^2} + F\, \frac{d^2 z(x)}{dx^2} + kz = 0\right)$, results in two equations with two unknown parameters. In the simplest solution, one of those parameters is set to zero, resulting in the known description of an invariant sinusoidal deformation. If both parameters are unequal to zero, the subharmonic mode will show up beyond a distinct threshold that can be calculated via: [11, 81]

$$\varepsilon_{bi} = \left(\frac{5}{32\left(\frac{K_2}{K}\right)} \right)^2 \tag{1.27}$$

with

$$K = \frac{2E(1-\sigma)}{(1+\sigma)(3-4\sigma)} \tag{1.28}$$

$$K_2 = \frac{(1-2\sigma)(13-16\sigma)}{2(1+\sigma)(3-4\sigma)^2} \tag{1.29}$$

ε_{bi} in Eq. 1.27 therefore defines the critical threshold in pre-strain, beyond which bisinusoidal wrinkling appears. Here the invariant amplitude A from the sinusoidal regime splits into two amplitudes A_1 and A_2 that with increasing ε further grow or shrink, respectively. In Fig. 6 **c**, ε_c is marked with the first magenta line at $\delta \sim 0.17$, in d it is along the line where the blue marked wrinkle-regime turns into the red marked period-double-regime.

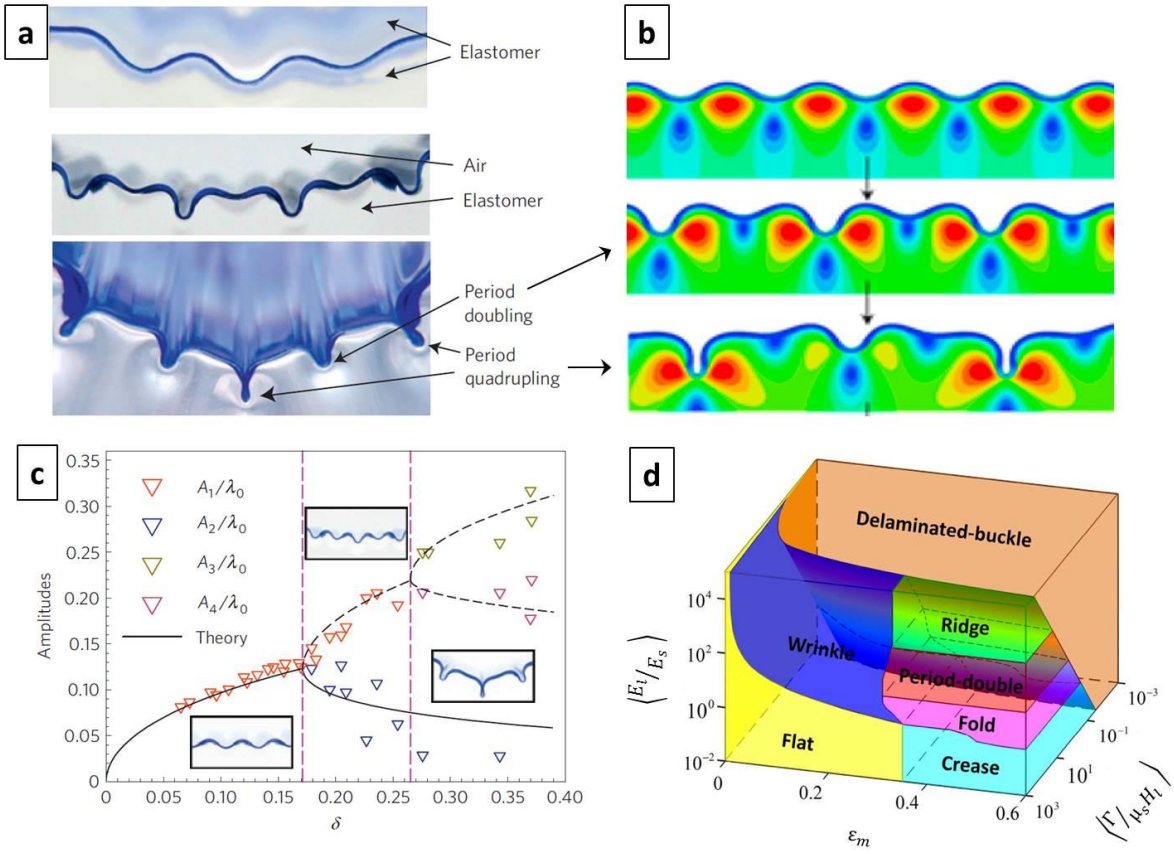

*Figure 6 | (**a**) Experimental [11] and (**b**) simulated data [74] of the evolution from sinusoidal over bisinusoidal (period doubling) to quadrosinusoidal (period quadrupling) wrinkles. (**c**) 2D-Diagram of the amplitude splitting on the y-axis in dependency of the compression ratio δ on the x-axis; [11] (**d**) 3D-Diagram of the Young's Modulus ratio $\frac{E_l}{E_s}$ on the z-axis and the normalized adhesion energy $\frac{\Gamma}{\mu_s H_l}$ on the y-axis in dependency of the compression ratio ε_m on the x-axis. [73] In (**c**) and (**d**) the applied values for the calculations are dimensionless. Reproduced with permission from references mentioned above.*

This is just the first step of a splitting cascade that might follow afterwards. [82] Nevertheless, in literature so far only the second splitting to quadro-sinusoidal / period quadrupling has been shown. [10, 11, 83] As this happens, the previously doubled periodicity becomes a quadrupled periodicity, so the repetitive unit now extends over four waves. The calculation expands by another summand as in Eq. 1.30.

$$z(x) = A_n \cos\left(\frac{m\pi}{\lambda}x\right) + B_n \cos\left(\frac{m\pi}{2\lambda}x\right) + C_n \cos\left(\frac{m\pi}{4\lambda}x\right) \qquad (1.30)$$

Inserting this again in Eq. 1.2 gives three equations with three unknown parameters, so eventually three different amplitudes A_1, A_2 and A_3. In Fig. 6 **a** and **b** this case is depicted in the lower line each, in **c** the transformation

point is marked with the second magenta-colored line. The phase diagram of d does not recognize this case, here only period doubling is recorded. Theoretically this splitting cascade will go on until a chaotic regime superimposes the formation of repetitive structures. [82] Nevertheless, for real mechanical systems, a threshold around the period quadrupling up to the so-far not observed period eightfold increase seems to be likely. [11] Experiments could only show that at even higher pre-strains folding and eventually delamination of the thin layer from the compliant substrate will follow. As Fig. 6 **d** illustrates, in systems with very low $\frac{E_l}{E_s}$ -ratios the interim state of creasing layers has been observed, in contrast to this at high $\frac{E_l}{E_s}$ -ratios the folding of layers into the substrate turns around and shows characteristic ridge-structures protruding off the surface. [73]

2.2.5. Multi-layer-systems

Besides the common case of a bi-layer-system, wrinkling may also happen in systems consisting of three or more layers. Such multi-layers can be e.g. polyelectrolyte multi-layers, [84] 2D-film-multi-layers, [85] polymers such as PDMS [86] or combinations of the aforementioned. [87] Also replica of thus prepared hierarchical wrinkle patterns have been reported. [86]

For three-layer-systems, consisting of a thin hard layer on top, an intermediate layer and a soft, thick substrate underneath, there are different known models to describe the buckling behavior. Fig. 7 **a** illustrates this exemplarily. The first was introduced by Stafford et al. [88] They invoke the bi-layer method based on the Neo-Hookean Half-Space as originally introduced by Winkler, Wieghardt and Biot [67-69] (see chapter 2.2.1.) and refined it according to the sandwich beam theory [89] to calculate the effective Young's Modulus E_{eff} that includes both, hard top layer and intermediate layer:

$$E_{eff} = \frac{1 + m^2 n^4 + 2mn(2n^2 + 3n + 2)}{(1+n)^3(1+mn)} E_l \qquad (1.31)$$

E_l denotes the Young's Modulus of the top layer (with E_i being the according Modulus for the intermediate layer), and so $m = \frac{E_i}{E_l}$. In the same notation the height for both layers is defined, giving $n = \frac{h_i}{h_l}$. As a consequence, the prediction of wrinkle wavelength and height is simple, if the thickness values and Young's Moduli for both layers are known and if an entire attachment of top layer, intermediate layer and substrate can be taken for granted. Fig. 7 **b** illustrates why it is so important to know the mechanical parameters of all participating materials: Depending on the elasticity and thickness of the layers, the entire system is able to wrinkle, or just parts of it. Also the model of Lejeune et al. [90, 91] requires not only an entire attachment but also the folding of all participating layers as granted. In the simplest case of a three layer system it introduces a theoretical intermediate layer, which has a theoretical Young's Modulus that calculates from the degree of attachment between the real top

layer and substrate. Therefore it may have extreme values reaching from zero to full attachment, so $0 \leq \frac{E_i}{E_s} \leq 1$ with E_i and E_s being the Young's Moduli of the intermediate layer and the substrate, respectively. Their ansatz is rather simple to solve for the critical strain ε_c to induce wrinkling, however not for the wavelength λ:

$$\varepsilon_c = \frac{1}{12\lambda^2} h_l^2 + \frac{2E_s}{E_l h_l} \left[\frac{1}{\frac{3-4\nu_s}{(1-\nu_s)^2 \lambda} + 2h_i \frac{E_s \lambda^2}{E_i - 1}} \right] \tag{1.32}$$

h_l and h_i correspond to the height of the top layer and the intermediate layer, respectively. As can be seen in Fig. 7 **c**, it is however unable to predict the wrinkling behavior beyond the critical strain ε_c to induce wrinkling, which is nevertheless highly important for the prediction of experimental results. Since here the model of Stafford et al. produces reliable results, a mixed model that combines both afore introduced ones is stated, therefore called *comprehensive three-layer-model*, [90] as depicted in Fig. 7 **d**. In the first place it is grounded on the force-equilibrium ansatz, regarding the total force of bending and stretching of layer and substrate, as plotted in Eq. 1.2 (described in chapter 2.2.1.). In here, the first summand $\bar{E}_l \, I_l \, \frac{d^4 z(x)}{dx^2}$ describes the bending of the layer, and the second one $F \, \frac{d^2 z(x)}{dx^2}$ sums up layer and substrate together. The comprehensive layer model expands this by an intermediate layer that is added to the first summand. This results in the following strain-dependency:

$$\varepsilon_c = \frac{E_{eff,F}}{E_{eff,A} \, \lambda^2} + \frac{\left[\frac{2E_s \lambda}{\frac{3-4\nu_s}{(1-\nu_s)^2} + 2h_i \frac{E_s}{(E_i - 1)\lambda}} \right]}{E_{eff,A}} \tag{1.33}$$

with $E_i I_i + E_l I_l = E_{eff,F}$ representing the effective stiffness of top and intermediate layer, as well as $E_i I_i + E_l I_l + E_s I_s = E_{eff,A}$ being the effective stiffness of all layers and substrate combined. This way of calculation allows for the expansion to more than just two top layers, if to both $E_{eff,F}$ and $E_{eff,A}$ the individual effective moduli of any additional layers are added. At the same time, the calculation of each moment of Inertia *I* becomes also more complex as well. [90]

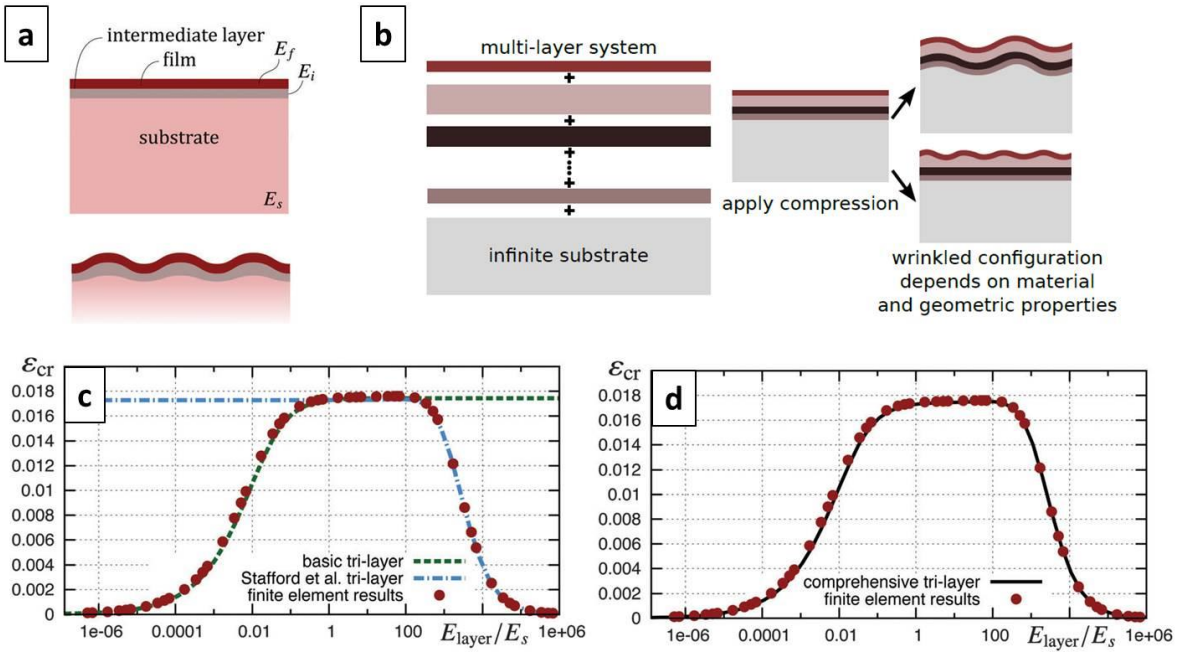

*Figure 7 | Schematic definition of a tri-layer-system (**a**) [90] and a multi-layer-system (**b**), [90] with according behavior under compression. (**c**) shows the calculation limits for the aforementioned tri-layer model of Stafford et al as well as for the basic tri-layer model, [90] while in (**d**) the comprehensive tri-layer model covers the whole range. [90] The parameters used for the sample calculation are h_f = 1 nm, h_i = 0.1 nm, E_f = 100 MPa and E_s = 1 MPa. Reproduced with permission from references mentioned above.*

2.2.6. Strain-induced elastic buckling instability for mechanical measurements (SIEBIMM)

A significant advantage of controlled wrinkling is the predictability of experimental results regarding the topological features such as corrugation wavelength and height. As described in the chapters above, with known parameters such as layer or substrate elasticity and the applied mechanical strain, the emerging surface corrugations are well-predictable. Wavelength λ, amplitude A and critical strain ε_c are the most common characteristic values determined. For example the wavelength is most commonly determined via $\lambda = 2\pi h \left(\frac{\bar{E}_l}{3\bar{E}_s}\right)^{1/3}$ (Eq. 1.10). Nevertheless, it becomes apparent as well that a simple transposition of Eq. 1.10 may turn around this strategy: When taking into account that $\bar{E} = \frac{E}{1-\nu^2}$ (Eq. 1.5), and furthermore by solving Eq. 1.10 for the Young's Modulus of the thin layer E_l, one gets:

$$E_l = \frac{3E_s(1-\nu_l^2)}{(1-\nu_s^2)}\left(\frac{\lambda}{2\pi h_l}\right)^3 \qquad (1.34)$$

The transposition solves for the Young's modulus of the thin layer E_l, regarding all other sufficient parameters for wrinkling, and therefore allows for the estimation of it *via* the determination of the corrugation wavelength

λ. Hence it is the fundamental equation of the so-called "strain-induced buckling instability for mechanical measurements"-method, abbreviated as SIEBIMM. It was originally introduced by Stafford et al. in 2004 [92] as one of the first practical applications of controlled wrinkling. From the outset Stafford et al. considered it as a metrology tool for very thin, uniform films and layers, where up to this point of time only nano-indentation was able to provide reliable results, nevertheless with an elaborate effort to prepare and eventually measure the samples. In the experiments, Stafford used translucent materials with different batches of PS being the thin layer, and PDMS being the soft substrate. The curved bilayer structure can act as a diffraction grating with its dominant corrugation periodicity, and so allows for determining the 1st order diffraction pattern of a monochromatic ray of light. This analysis method is however only applicable if all bound materials are translucent, and if the analyzed surface has periodicities not lower than $\frac{\lambda}{2}$ of the incident monochromatic light. [93] Other methods used for SIEBIMM analysis are optical microscopy, SEM or AFM (see chapter 2.6)

SIEBIMM ever since has found multiple usages in the survey of thin films, e.g. in polyelectrolyte multilayers, [84, 94-96] 2D polymer films, [34, 97] nano-clays, [98, 99] polymer brush layers, [40] in nanowires, when they are fully embedded in an elastomeric matrix [100] and even as a real-time tool to investigate the changing modulus of drying salt films. [41] In the case of an unidentified substrate Modulus, but with known layer mechanics, it is also possible to determine the Modulus of the substrate as well. This approach has been tested and verified in the group of Stafford as well by Wilder et al. [101] They recalculated Eq. 1.34 and solved it for E_s:

$$E_S = \frac{E_l(1-\nu_s^2)}{3(1-\nu_l^2)}\left(\frac{\lambda}{2\pi h_l}\right)^{-3} \qquad (1.35)$$

Both methods have one major issue in common: In SIEBIMM it is crucial to have a proper fixation of the thin layer with the soft substrate, to ensure a uniform stress distribution at the interface of layer and substrate at the same time. On the one hand an insufficient fixture may lead to delamination of the layer, [31, 90, 102] and so eventually to noticeably larger wavelengths than for firmly attached films. Inserting wavelengths thus measured in Eq. 1.34 imply a distinctly higher Young's Modulus of the film than e.g. for comparable nano-indentation measurements. This might pass unnoticed, as first of all a slight delamination does not lead to the typical occurrence of deep channel-like patterns, [102] and second of all the determined Modulus may still be in a reasonable size range. Only if the value exceeds valid size ranges, the error can be acknowledged. [103] On the other hand the fixation needs to be done carefully in order not to destroy the substrate surface. Elastomers with an organic backbone can be degraded by any kind of oxidation process, while inorganic backbones such as PDMS will form a glassy layer on their surface. Though this is partially reversible, [104, 105] a glassy layer of unknown mechanical properties and thickness is formed e.g. in plasma processes even after the shortest feasible treatment times. [106] One way to cope with this intermediate layer can be not only to accept the presence of it,

but to generate it under specific conditions where known mechanical or geometrical properties arise. If these properties are taken for granted, the values can be added to the calculation and the whole system can be calculated via a three-layer-approach (see chapter 2.2.5.). Possible ways are the generation of a defined oxide layer as the hydrophilicity agent [107] or the insertion of an amphiphilic polymer layer. [95] Another way to cope with the intermediate layer is to generate it as a very thin and reversible medium that supports the binding of the actual layer to the substrate, however reversibly disappears after its generation, except for the binding sites. Here PDMS can be applied, as it shows reversible properties in its surface chemistry and physics. Nevertheless, it is elusive to find such fully re-convertible conditions. One way is the gentle chemical treatment, such as by diluted hydrochloric acid. [98]

2.3. Defect formation in wrinkled surfaces

Wrinkled surfaces are the result of a mechanical mismatch between the thin top layer and the elastomeric substrate underneath. Due to the nature of participating materials and mechanics, small instabilities in such a system appear regularly, which manifest as defect structures that eventually disrupt the homogeneous surface morphology. The prediction of such defects in terms of their frequency and localization is difficult, nevertheless methods exist to prevent or at least order such structures. [108-110] Within this work, two main defect structures were investigated, namely the line defects as well as the lateral surface cracks, as depicted in Fig. 8 for different strain release rates.

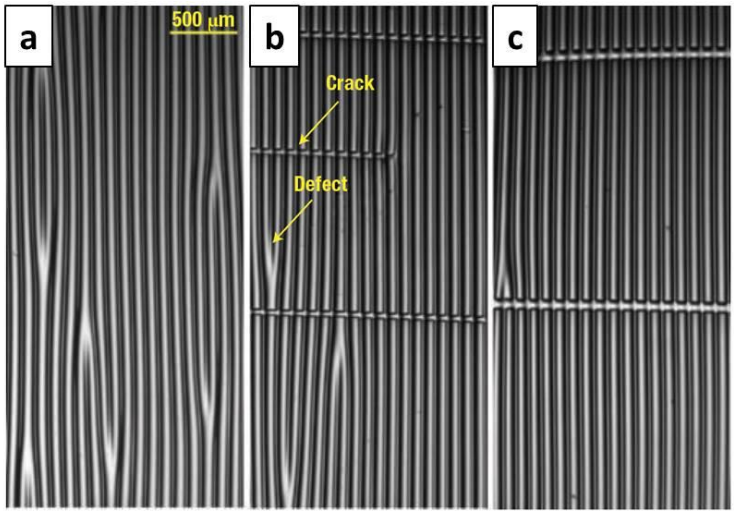

*Figure 8 | Cracks and line defects forming at different strain release rates of (**a**) instantaneously (**b**) 0.9 mm/min and (**c**) 58 µm/min, resulting in different crack/line-defect-ratios. Reproduced with permission from reference [51]*

2.3.1. Line defects

Line defects arise in many wrinkling processes. They form, when two small, adjacent folds of a wrinkled surface combine to one large fold. The origin of such structures trace back to fluctuations of the material parameters along the borderline, such as thickness or elasticity, but also variations of external mechanical forces. For homogeneous systems, each material parameter remains constant resulting in a highly uniform system. Only if uneven external forces are applied, the internal stress fields of each material fluctuate. Heterogeneous system can theoretically vary within each parameter, creating significantly more possibilities for line defects to emerge.

Numerical simulations of both systems have been accomplished, mostly utilizing *Föppl-von-Karman-plates* [60, 111] that describe the bending and deflection behavior of thin flat plates. They have proved that the threshold for the formation of line defects is the persistence length of the layer material. If the local inhomogeneity is longer and wider, respectively, the layer is able to reduce local in-plane stresses by branching one out-of-plane fold into two smaller ones. If the horizontal expansion of $z(x) = A_n \sin\left(\frac{m\pi}{\lambda}\right)$ (Eq. 1.6) is larger than the diameter of the inhomogeneity, branching is likely to occur. [112, 113] This critical coherency persistent length L_C can also be expressed as function dependent on the mechanical properties of both participating materials, so of layer and substrate as well:

$$L_C = \frac{\left(\frac{ß}{\bar{B}}\right)^{1/2}\left(\frac{3\bar{E}_s}{\bar{E}_l}\right)^{1/3}}{(2\pi h)^2}}{\left[1-\alpha^{1/3}\right]^2} \qquad (1.36)$$

with α and *ß* as gradient slope coefficients and B as:

$$B = \left[\frac{(\lambda_2 - \lambda_1)^4}{16}\right] - \Delta U \qquad (1.37)$$

with λ_1 and λ_2 being the both observed corrugation wavelengths as well as ΔU being the potential energy difference along the fault zone. Hence it is possible to simulate the time-depended behavior of bilayer systems with an implemented gradient in the layer or substrate as well. The total potential energy of the system E_{tot} has to be derived for the time, giving:

$$\frac{\partial \zeta}{\partial t} = -\Gamma \frac{\delta E^{tot}}{\delta \zeta} \qquad (1.38)$$

Similar calculations with *Föppl-von-Karman-plates* have been done by Yu et al. [113] They were able to successfully mimic experimental wrinkling results of a gradient Nickel film on top of an isotropic PDMS substrate with numerical simulations (Fig. 9 **a** and **b**). In a different manner, Miquelard-Garnier et al. prepared a thickness

gradient in a PS-film (Fig. 9 **c**) resulting in similar branching patterns. [109] Vandeparre et al. gained related morphologies (Fig. 9 **d**, left side), however by creating the z-gradient within the film via a diffusion-controlled reaction of gaseous toluene with a tri-layer system of Ti/PS/SiO_x. [114] Ni et al. took these results and adapted them to their numerical simulations in order to recreate the branching behavior (Fig. 9 **d**, right side). [112]

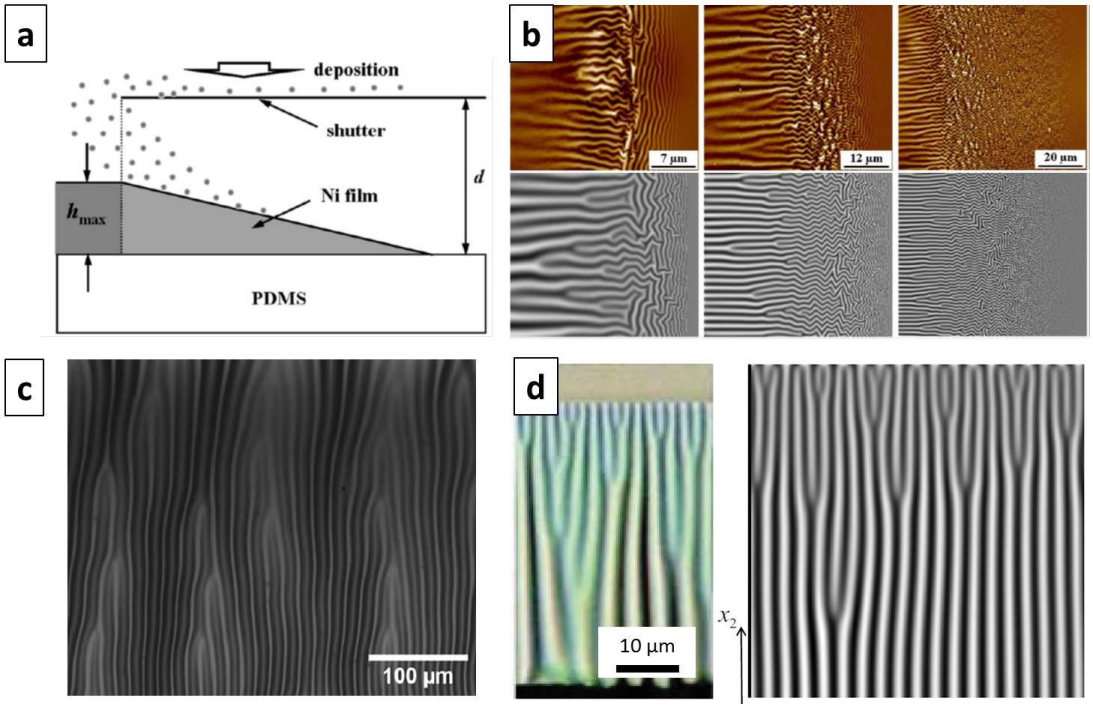

*Figure 9 | (**a**) Schematic setup by Yu e al. to produce gradient films with Nickel on a PDMS substrate [113] as well as (**b**) their experimental results (colored, upper line) and according simulations (black, lower line). [113] (**c**) Experimental layer gradient results by Miquelard-Ganier et al. [109] and (**d**) by Vandeparre et al. (green, left), [114] for the latter with according simulations by Ni et al. (black, right), [112] Reproduced with permission from references mentioned above.*

2.3.2. Lateral surface cracks

The cracking of thin brittle films and layers is a well-known phenomenon in nature [115] as well as in artificial systems [116-120] that has been described already long before the discovery of controlled wrinkling. However, the combination – so cracking of pre-strained thin films that wrinkle – is not very well studied. Efimenko et al. observed that the crack density strongly depends on the release rate of the applied pre-strain, [51] Rand et al. investigated the crack density in wrinkled surfaces in dependency of the applied pre-strain, [108] and Lin et al. found a nearly sinusoidal crack propagation speed in wrinkled surfaces, with a contemporaneous behavior for the energy release rate. [121]

In general, cracking of materials, no matter whether in bulk or in thin layers with mainly 2D-mechanics, always requires an input of material with an included extension of the surface inside the forming crack. This simply can be described as: [122, 123]

$$\frac{d\Gamma}{dt} = -P^* \tag{1.39}$$

Γ is the summarized fracture energy per crack, P^* is the energy transport into the fracture zone. On the other side, the overall energy in the system is the sum of external forces and internal strain and potential energy, so:

$$d\Pi^{int} + d\Pi^{ext} = -d\Gamma \tag{1.40}$$

If both competing energies are in a quasi-equilibirum state, meaning the energy required for fracturing is equal to the energy provided by the system, the crack moves with a constant speed through the material after its initiation. The equilibrium then is given as:

$$\frac{d\Pi^{tot}}{dA} + \frac{d\Gamma}{dA} = 0 \tag{1.41}$$

The constant speed is accompanied by a constant energy release and therefore called *energy release rate* or *Griffith's fracture criterion* and is expressed as *G*. Based on this, Gecit et al., Beuth et al. and Ye et al. [124-126] described different thin-layer-cases, of which Hutchinson et al. developed a model for thin layers on compliant substrates when applied to mechanical stresses. [127, 128] They predict five different types of thin layer cracking, as depicted in Fig. 10. In general, all these five types are subject to cracking of wrinkled layers as well. From literature it is evident that most reported cases in wrinkled surfaces contain the cases of Fig. 10 **b** and **c**, so continuous networks of cracks or quasi-parallel channels systems. In those it is however unidentified, whether the surface cracks stop to spread at the layer-substrate interface **b** or if they protrude further into the material **c**. Therefore both, **b** and **c** are shortly expounded.

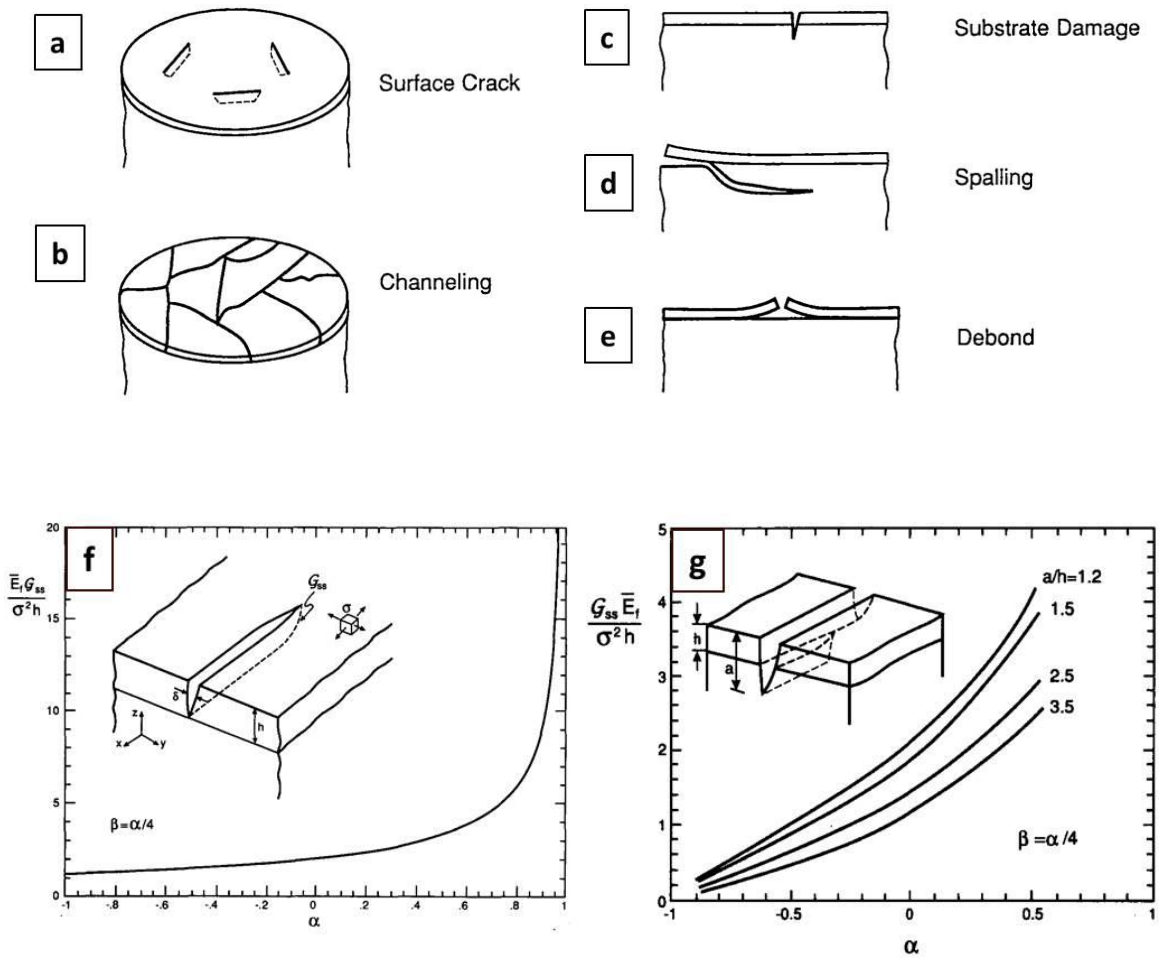

*Figure 10 | (**a** – **e**) The five different surface cracking types of thin films on compliant substrates, [127] with especially (**b**) and also (**c**) being the most frequent observed ones in surface wrinkling. In (**f**), the normalized energy release rate $\omega = \frac{\bar{E}_l G}{(\sigma^2 d)}$ for varying interfacial stresses is depicted, [127] in (**g**) additionally this stress is shown for different $\frac{a}{h}$-ratios as well. [127] Reproduced from references mentioned above.*

When channels are forming, while the substrate stays intact at the same time **b**, the strain energy release rate at the front of each crack can be solved as: [127]

$$G = \frac{(\sigma^2 d)}{\bar{E}_l}\left[2tanh\left(\frac{h}{2d}\right) - tanh\left(\frac{h}{d}\right)\right] \qquad (1.42)$$

With h being the height (or depth) of the crack, d the average distance between two adjacent cracks, σ the applied mechanical stress and $\bar{E}_l$ the in-plane-Modulus of the thin layer (see Eq. 1.5). For reasons of simplification, the height of a crack h is equipollent to the thin layer height h_l, assuming that the surface crack protrudes aground of the thin layer. The calculation also includes the prediction that with increasing mechanical stress the crack density rises as well. It is assumed that freshly formed cracks will always emerge at the point of

highest in-bulk stress, which is right in the middle between two other cracks, so at $\frac{d}{2}$. Moreover, the second dimensionless part of Eq. 1.42 is sometimes called *normalized strain energy release rate* and stated as:

$$\omega = \frac{G\bar{E}_l}{(\sigma^2 d)} = 2tanh\left(\frac{h}{2d}\right) - tanh\left(\frac{h}{d}\right) \qquad (1.43)$$

In addition, ω is important in the second likely case of wrinkling: Such as in Fig. 10 **c**, when the cracks are also protruding into the underlying substrate, the energy release rate is more complex to derive: [126]

$$\omega = \frac{4\pi}{\pi^2 - 4}\left(\frac{\bar{E}_l}{\bar{E}_s}\eta_s[sin^{-1}\tau\right)^2 \qquad (1.44)$$

With $\bar{E}_l$ and $\bar{E}_s$ representing the in-plane-Moduli of layer and substrate, respectively. Furthermore:

$$\tau = \left(\frac{1}{\eta_s}\right)\left(1 - {\eta_s}^{-1}\right)^{0,5\,-s}\left(\frac{1+\lambda_1}{\eta_s}\right) \qquad (1.45)$$

with τ representing a material- and stress-field dependent constant. It calculates via the variable *s*, which is again derived via the so-called *Dundur's parameters* α and β that are often interrelated via $= \frac{\alpha}{4}$. [129] Moreover, η_s and λ_1 are fitting parameters to a full numerical solution. Consequently, the calculation of channel-structures is less complex compared to cracks protruding into the substrate (see Fig. 10 **b** and **c**). All parameters for channel-structures such as crack-interdistance d, height of a crack *h* and mechanical properties of the fractured layer $\bar{E}_l$ can be derived from experimental data directly, while for simultaneous cracks in layer and substrate additional data have to be acquired and calculations have to be made.

2.4. Preparation Techniques

A widely used method to produce bilayer systems for wrinkling is the *in-situ* oxidation of silicone-type polymers. Principally for such a process there are many manufacturing approaches, such as Focused Ion Beam (FIB), [130, 131] electron-beam, [42] laser irradiation, [46] wet-chemical treatment with acids, [55, 132] Ultraviolet Radiation with Ozone (UVO) and different Plasma-Techniques. However in this work only the two last-mentioned approaches were applied and will therefore shortly be introduced.

2.4.1. Ultraviolet-Radiation with Ozone (UVO)

The treatment of UVO has been multiply described to flat PDMS surfaces. [133-137] The treatment process differs significantly from comparable UV-processes, where no oxygen is present in the system. Depending on the wavelength and intensity of the UV lamp, the atmospheric material as well as the density and composition of the irradiated material, the light may protrude nm up to cm into it. The strongest restriction is imposed by the optical transmission of the material in the UV range, which again traces back to the interaction of UV-light with chemical

bonds and functional groups. As no π–bonds are present, the interactions happen mostly with the weakest σ–bonds in the polymer. The Si-O bond is quite strong at 798 $\frac{kJ}{mol}$, especially when compared to a C-C bond in alkanes, oligomers or polymers at ~ 365 $\frac{kJ}{mol}$. [138] A high-energetic UV-light of λ < 150 nm (E > 8.27 eV) would be necessary to induce an excitation, which is however beyond the practical limit of UV irradiation at atmospheric conditions that is situated around 210 nm. On the other side, the Si-CH_3 bond is weaker at 535 $\frac{kJ}{mol}$ (E = 5.54 eV / λ = 224 nm) [139] and so just as excitable for gas discharge UV lamps, whose two main bands are at 185 and 254 nm. [140] To induce a bond break, the pathway is nevertheless not efficient enough. Therefore the atmospheric conditions are utilized to insert a process gas, in the simplest case molecular oxygen. It is dissociated by the 185 nm band into two triplet state oxygen atoms. They may recombine with triplet state oxygen molecules in the ground state to O_3, after they have lost potential energy via kinetic collisions. The formed, but instable O_3 again is dissociated by the second UV band at 254 nm. Here again molecular oxygen is formed, however by setting free one highly reactive singlet oxygen atom O(^{1}P) as well. In general this is perceived as the reactive species, unlike the name UVO process may suggest it to be O_3. [141] Its ability to oxidize the bulk material and so to break bonds is larger than that of UV irradiation at 185 and 254 nm, respectively. However, the diffusion of O_3 and especially of the singlet atomic oxygen into the bulk material is restricted by various parameters. Both tend to react or decay quickly, also non-reactive collision processes may contribute to a transformation of the quantum state in less energetic species. In case, a singlet oxygen atom hits a methyl-group of the $Si(CH_3)_2O_2$-network, a reaction cascade is started, which leads to glazing of the uppermost layers. Nevertheless, only a few percent of the methyl groups on the surface are oxidized (provided that the elasticity of the layer material shows a linear dependence on its chemical composition), in the underlying layers the percentage is even lower.

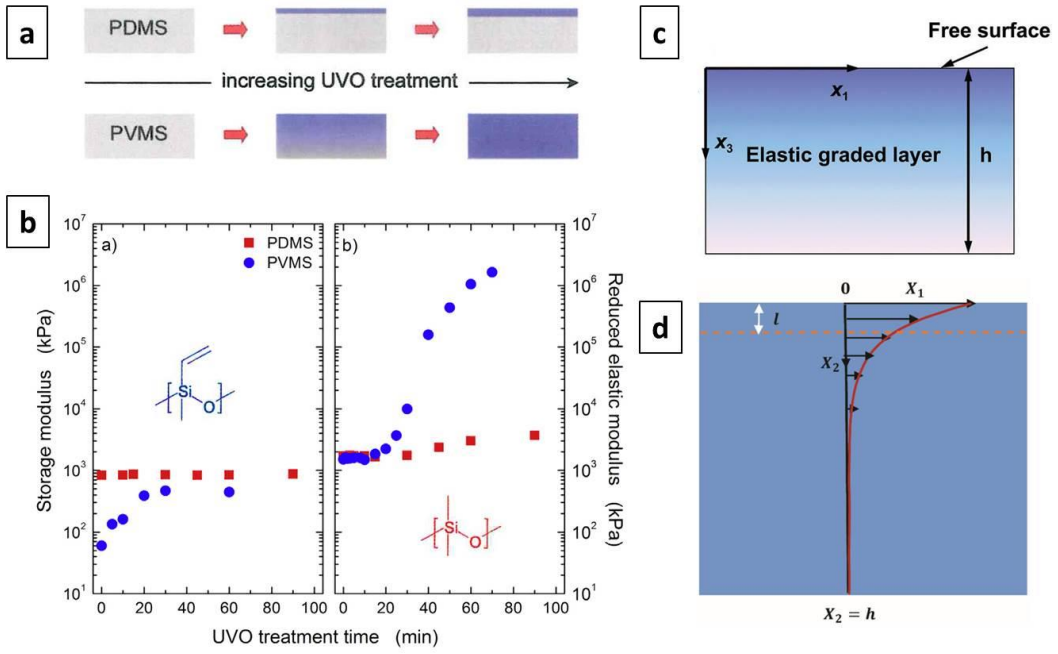

*Figure 11 | (**a**) schematic depiction of PDMS and (PVMS) being treated via UVO; [142] (**b**) E' vs. $t_{ox,UVO}$ / E_r vs. $t_{ox,UVO}$ for both PDMS and PVMS, showing a distinct difference in plasma-induced macroscopic hardening; [53, 142] (**c**) schematic depiction of the gradient layer structure in an UVO-treated PDMS film [54] as well as (**d**) an exponential description of such a gradient; [143] Reproduced with permission from references mentioned above.*

Depending on the UVO conditions, elasticity values of the top layer from several MPa [144] up to hundreds of MPa [51, 145] can be achieved, which is still far from the value of pure glass at ~ 72 GPa. [146] The underlying layers however drop non-linearly according to diffusion of charged and excited particles in condensed matter. This can be described via a cubic [147] or or an exponential decay function. [143] The overall effect to the surface chemistry is therefore a superposition of UV light absorption on the one side, and protruding O_3 and mainly $O(^1P)$ on the other side. The difference between both processes is illustrated in Fig. 11 **a** and **b**: While PDMS with no UV-active functional groups is treated mainly by diffusion processes of O_3 and $O(^1P)$ in near-surface layers, the vinyl-groups of Poly(vinylmethyl) siloxane (PVMS) are hardened by the UV-light even in deep layers. This eventually leads to a macroscopic hardening of the PVMS due to the deep-reaching UV light, while the comparably thin hardened surface layers in PDMS do not contribute to a quantifiable macroscopic effect. [142] The depth profile of the intruding UV light has just recently been simulated in the form of an exponential decay function (Fig. 11 **c** and **d**), [54, 143] while former investigations have assumed a cubic slope. [147]

2.4.2. Low pressure plasma (LP-P)

Quite similar to UVO, the treatment of flat PDMS surfaces with low pressure plasma has been described manifold. [148-151] The mechanism however differs significantly, though it is a superposition of two contributions as well,

namely the bombardment of ions onto the surface simultaneously with the penetration and absorption of vacuum ultraviolet (VUV) radiation into the surface. In low-pressure plasmas (LP-Ps), the plasma is excited by alternating voltage (AC) via either radio frequency (RF) in capacitive electrical excitation generators or in microwave (MW) generators that operate in the upper kHz to the lower GHz range. Within the field of different plasma types, LP-Ps have a comparable high electron charge carrier density η_e with a simultaneous medium overall charge carrier energy kT_e, as shown in Fig. 12 **a**. First of all, the magnetic field induced by RF generators has to be powerful enough to ignite a plasma, so to split neutral gas molecules into positively and negatively charged species beyond a critical threshold proportion. This threshold highly depends on the environmental conditions as well as the internal gas parameters. However, LP-Ps can be ignited already at 0.1 % conversion rate to charge carrier particles, and exhibit a nearly full conductivity at ~ 1 % conversion. [152] An undesirable side effect is that the converted gas redistributes itself in such a way that most of the charged gas is shielded from the field. It tries to escape from the electric field, which is why there is a continuous diffusion process of particles towards the edges. This process, called ambipolar diffusion, is unidirectional for both electrons and cations, which is very unusual for charge carrier diffusion processes. In practice this means that the highest field strength of a LP-P can be found at its edges, so close to the low pressure chamber walls or the electrodes, respectively. If a sample is placed here, it will experience another plasma density than in the middle of the chamber. Another important aspect is that the electric field strength requires the first ionization energy to be reached, which is situated for basic elements in the range of 5 – 15 eV. [152] The ions occurring carry the potential energy in the range of covalent bonds (for more detailed values, see chapter 2.4.1.), so consequently they are able to excite and break them. Under such strong electric field conditions, the electrons heat up to ~ $1.5 \cdot 10^6$ K, [153] while the cations and neutral species remain perceptibly cooler. And secondly, besides the required minimum field strength, the AC generators create an electromagnetic oscillation that is able to excite the charge carrier particles to different speeds, depending on their charge density. Technical LP-P devices work at pressures < 1.0 mbar, in order to achieve a free path way of all species that is distinctly longer than the Debye length. [153] Here, another side effect can be observed: In these pressure ranges the plasma is usually in a non-local thermal equilibrium (non-LTE) state. This means that the individual temperature of electrons and the cationic and neutral species differs significantly, with the small electrons being higher-energetic in comparison to the cations, as also shown by Fig. 12 **b**. [154] Consequently, the energy transfer within the plasma happens primarily via the electrons, since due to their distinctively lower mass and therefore higher diffusion coefficient they can be accelerated way quicker in the AC field, and so eventually cover longer distances. Due to their high speed and number, elastic and inelastic impacts with heavy ions and neutral species often occur. While the inelastic collisions create more ions, the elastic collisions raise the energy level of bound orbital electrons of those ions. If they drop back to lower energy levels, photons are released; in some cases of high energetic excitation, the following energy release is strongly pronounced in the lower VUV range. The spectrum of these so-called VUV photons is located between 100 – 200

nm. Quite similar to ions, this is in the energetic range of strong covalent chemical bonds, consequently VUV is able to excite and break such bonds as well. Depending on the AC frequency to induce the particle oscillation, the difference in particle temperature of electrons and cationic as well as neutral species can differ significantly. As mentioned before, in technical LP-Ps the AC frequency is usually set in the upper kHz- to lower GHz-range. When it is set to the low to mid GHz-range, the excitation frequency is beyond the plasmon resonance frequency of the specific gas medium. By this, the heavy particles do not oscillate and stay at nearly ambient conditions, only the electrons will be excited and accelerated, [155] consequently reducing the overall plasma temperature drastically and so making it more convenient to sensitive application processes.

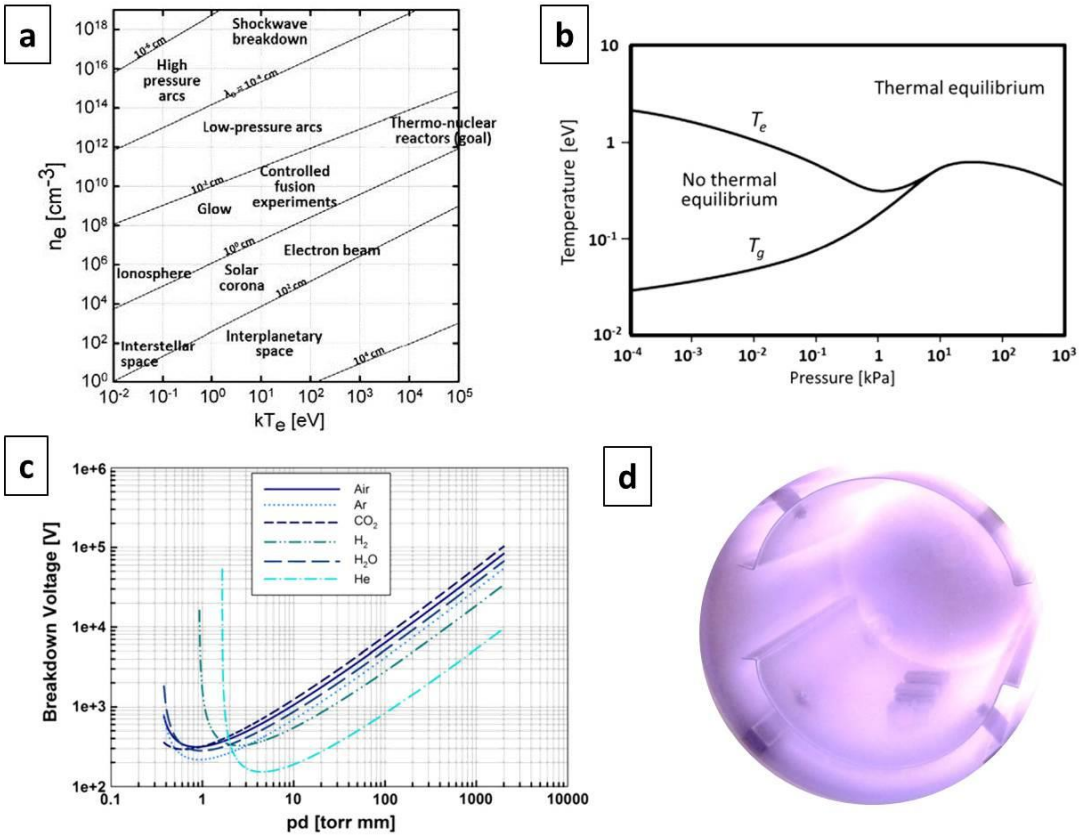

*Figure 12 | (**a**) Categorization of various plasma types, regarding their charge carrier density on the y-axis as well as their overall charge carrier energy on the x-axis. [154, 156] The inclined lines represent different Debye lengths, from short (top) to far (bottom). (**b**) Electron- and Ion-Temperature curves T_e and T_g in plasma in dependency of different pressures (x-axis) and energies (y-axis). [154] Beyond ~ 1 kPa, electrons and ions have the same temperatures, making them an LTE plasma, while below non-LTE plasmas exist. (**c**) Breakdown voltage or so-called "Paschen voltage" for different elements and molecules. [154, 157] (**d**) Appearance of a N_2-plasma at p = 10 kPa and T_g of ~ 300 K, resulting in an estimated degree of polymerization of 0.1 %. Reproduced with permission from references mentioned above.*

The first ionization energy of standard processing gases used mainly in this study is $E_I(O_2)$ = 13.62 eV and $E_I(N_2)$ = 14.53 eV. The utilized plasmas within this thesis are non-LTEs at differing electron temperatures and AC excitations via both RF and MW generators. [152, 153] Yet none of them is operated in the microplasma regime. [155, 158] In practical terms this means, they comprise a comparably mild treatment with a gentle time-dependent temperature increase of the sample surface. The main pathways of treatment used within this work is the bombardment with VUV photons, since O_2 or N_2 -ion species with any charge value will be able to protrude maximal a few nm into condensed matter. Experiments on the breakdown voltage V_B of diverse low molecular gases have furthermore revealed strong differences in the choice of operating gas and pressure, which is exemplarily shown in Fig. 12 **c**. For example, O_2 has a minimum in breakdown voltage at V_B = 350 V and p·d ~ 0.5 mbar / 1cm, while N_2 has V_B = 180 V and p·d ~ 0.9 mbar / 1cm. [159-161] Generally one can say that for N_2 the ionization takes places easier than for O_2, and that both offer different optimum electrode gap sizes. Exemplarily, Fig. 12 **d** shows the appearance of a N_2-plasma at ~ 1 mbar.

2.4.3. Atmospheric pressure plasma (AP-P)

In opposite to a LP-P (see chapter 2.4.2.), the atmospheric pressure plasma (AP-P) is in a local thermal equilibrium state (see Fig. 12 **b**). The overall particle density is too high for long pathways to cover, however at the same time this density provokes a lot of particle collisions as well. Since the inelastic collisions are also able to slightly accelerate the heavy cations and so enhance their kinetic energy, it eventually leads to a distinct heating of all plasma particles – electrons as well as cations and neutral species. In order to avoid such heating, which can reach up to 1000 K and more, different approaches have been developed, since it is not applicable to most industrial as well as scientific processes. All approaches have the goal to create a non-LTE with hot electrons and ambient condition ions. The first is – similar to LP-P – to generate a pulsed high energetic RF excitation in the lower upper MHz- to lower GHz-range, in which mainly the electrons will be excited, while the ions remain at lower potential and kinetic energies, respectively. However, under atmospheric conditions the discharge only works with small gap sizes between the electrodes, usually below the mm-range, but also going down to the lowest µm-range. [162, 163] For the latter case, such micrometer-level plasma discharges are called microplasmas, and have been investigated and put into practice just recently. [158, 164] Their primary goal is to avoid a strong kinetic acceleration of ions and electrons in order to minimize the elastic collisions of hot electrons with ions, so to keep the ions as low-energetic as possible. This is possible, as the energy to create a plasma arc in the µm-range is quite low, [165, 166] since the breakdown voltage according to the Paschen law has a shear drop below a gap size of d ~ 3 µm, so minimizing V_B in this size range again drastically. [163, 167] The first case are hereinafter referred to as macroplasmas, in order to distinguish them from microplasmas. They work in the discharge range of mm and are the current state of the art technology in industry, though their comparably large gap sizes require quite harsh

excitation conditions to induce a plasma arc. With reference to sample processing, this means that only robust sample can be processed.

The second approach is to avoid electron acceleration at first place by placing a dielectric barrier between the both electrodes. According to publication numbers this so-called Dielectric Barrier Discharge (DBD) is also the most commonly used method. Often they are referred to as cold plasmas, since the dielectric material blocks the movement of the charge carrier particles, however due to their charge density mainly that of the electrons.

2.5. Layer and substrate materials

For the wrinkling of surfaces, in the simplest case a single thin layer that can bend is already sufficient. This unsupported wrinkling of a free-standing sheet has been widely discussed in literature as well. Nevertheless, for the controlled wrinkling of a bilayer system with a thin layer on a compliant substrate, at least two layers are crucial. For this the thin layer has to be stiff in comparison to the thick substrate, which again needs to have elastic properties.

2.5.1. PDMS, EPDM, HNBR and TPU

The substrate component of the bilayer system basically just has to meet one requirement: It needs to be elastic. Therefore different standard elastomer systems as often used in scientific and industrial applications are utilized within the work of this thesis.

Elastomers differ from other systems in terms of their cross linking density. On the one side, thermoplastics have a nearly nonexistent crosslinking density allowing them to be melted, cast into mold and then cured. The missing crosslinking sites however make thermoplastics also weak materials with a low tensile strength. On the other side, thermosets are highly crosslinked to a dense 3D polymer network and therefore cannot melt but only decompose while being thermally treated. This makes them mechanically resilient, with the drawback that they are not even deformable during the manufacturing process or in any afterwards treatment step. Regarding their cross-linking density, elastomers are in between thermoplastics and thermosets. Their comparably low crosslinking sites allow them to be subjected to mechanical load without leaving any permanent damage behind and so giving them a high tensile strength. [168] For this purpose, Fig. 13 gives an overview to the three main types of polymer cross-linking, while b compares schematically their physical properties.

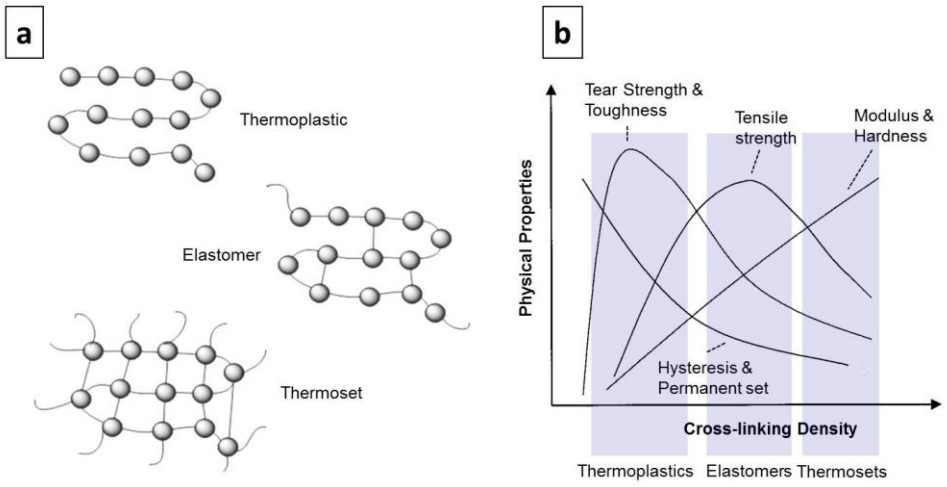

*Figure 13 | (**a**) Schematic comparison of thermoplastics, elastomers and thermosets regarding their cross-linking density, [169] (**b**) Physical and mechanical properties in dependency of the polymer network cross-linking density. [170] Reproduced from references mentioned above.*

The most common used elastomer in scientific nanotechnology is Polydimethyl siloxane (PDMS), since it is not only elastic but offers furthermore the unique property to create in-situ a thin, rigid film on its surface (see chapters 2.4.). This property arises from the nature of PDMS with its backbone consisting of SiO_x-assembled monomer units that can be partly or fully oxidized to become SiO_2 – so glass with its distinctly different mechanics to initial PDMS (E_{SiO2} = 72 GPa [146]). The Young's Modulus of standard PDMS can range from the low KPa-range [171] up to 10 MPa, [172] depending on the exact composition, curing conditions and furthermore techniques that has been used to determine these values. The standard values for the PDMS used within this thesis (Dow Corning Sylgard 182 and 184) are in the range of 2 – 3 MPa, [145, 173] it however also can be prepared to lower values in the range of a few hundred KPa. [174] This mainly depends on the ratio of curing agent to pre-polymer, and – if executed – on the subsequent thermal curing step. Sylgard consists of two components, which become mixed and afterwards cured at ambient conditions or thermally. The first is the pre-polymer solution, consisting of a bisvinyl-terminated dimethylsiloxane as depicted in Fig. 14 **b**, marked as the blue molecule **a**, and besides some additives. The second component is the Curing Agent consisting of at least two chemicals. One is an ordinary dimethylsiloxane (the red molecule b in Fig. 14 **b**) and the second is a platinum complex as the metal catalyst (the green molecule **c** in Fig. 14 **b**). In the case of the catalyst two complexes are possible – the Speier [175] or the Karstedt [176] catalyst. The three mixed chemicals react in a polyinsertion with two possible pathways as schematically depicted in Fig. 14 **a**. The Si-H functional group in **b** activates **c**, which then may insert into **a** to start a continuous cycle that extends the chain (left cycle) or interlinks two chains (right cycle). If the cycles are not stopped by any external intervention, they continue until the contemporaneously rising viscosity of the mixture slows down the reaction and eventually stops it, though the catalyst's reaction sites still stay active. This

is possible, since the catalysts are efficient with turnover numbers normally higher than 10^3 cycles, allowing long chain growths. [176] Once the reaction has stopped, it may only be reactivated via a thermal curing process to enhance monomer movement within the bulk PDMS. It seems to be likely that a sensitive metal like Pt within the Speier and Karstedt catalysts will stay active only for a certain time period after it has been kinetically stopped, since it is highly sensitive to environmental changes and therefore may be terminated by distorting molecules such as O_2.

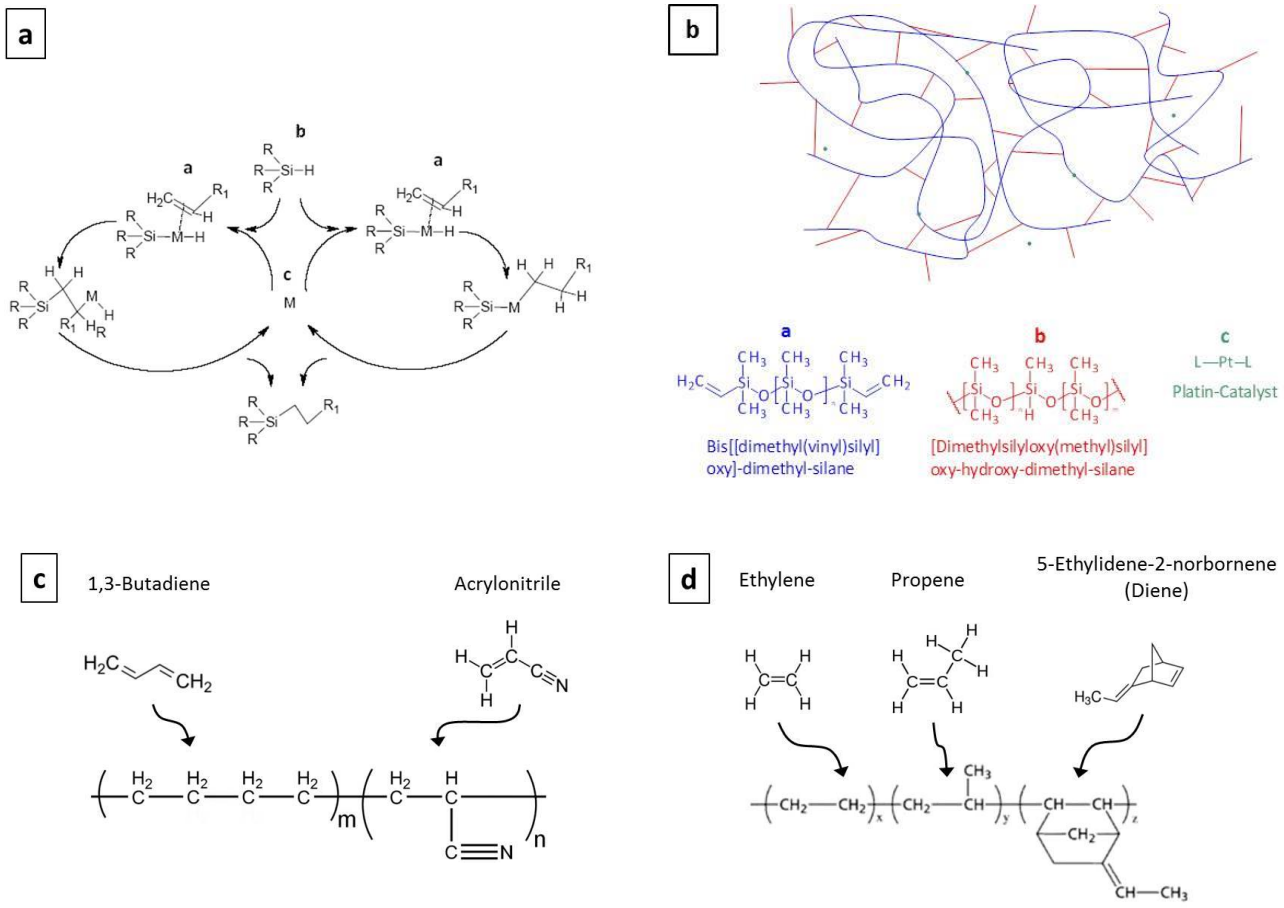

*Figure 14 | (**a**) the insertion cycle for the chaing growth and crosslinking of PDMS as for the Dow Corning Sylgard system: First the catalyst "c" becomes hydrosilated by the dimethylsiloxane "b", followed by a continuous insertion cycle of the bisvinyl species "a" into the "a-c"-bond. [177] (**b**) The insertion from (a) eventually leads to a 3D-cross-linked PDMS network of former bisvinyl species "a" with former dimethylsiloxane species "b", with active catalyst sites "c" both on the bisvinyl chains and freely moving sites within the bulk. (**c**) Chemical formula of HNBR and (**d**) of EPDM. Reproduced with permission from references mentioned above.*

Alternatives to PDMS are organic elastomers. For those, *in-situ*-oxidation as mentioned above in this chapter (see chapter 2.4.) are not possible, since the organic C-C-backbone of the main chain would be degraded into

smaller fragment molecules instead of being oxidized while preserving the main chain at the same time, as this is the case for PDMS. However, they can be utilized differently, if they become activated carefully on the surface only, and subsequently a thin layer is applied to the hydrophilized surface. Within this thesis, three organic elastomer classes are tested under this approach, which are namely hydrogenated nitrile butadiene rubber (HNBR), ethylene propylene diene monomer rubber (EPDM) and thermoplastic urethane rubber (TPU). All three are used as standard elastomers in industrial- and everyday-applications, which makes them suitable materials for various reason: They are robust against utilization and abrasion, their physical, mechanical and chemical properties are well-known and they are easily accessible both as small and large foils, which eventually makes them also applicable for upscaling experiments as well.

First, HNBR (Fig. 14 **c**) is a copolymer of two monomers being 1,3-butadiene (BD) and acrylonitrile (AN). [178-180] It is basically a derivate of an acrylonitrile butadiene rubber (NBR), which simply gets hydrogenated in order to eliminate the double bond in the monomer unit of NBR. This makes NBR chemically and physically more stable, with the downside of a distinctly decreased reactiveness as well. A similar system is the carboxylation of the double bond in order to enable polar and ionic bonds at this sites (XNBR). HNBR is radically polymerized, in case of this thesis Bis(1-methyl-1-phenylethyl)peroxid) (DCM) is used as the radical initiator. It's elongation at break varies is comparable to that of PDMS (ε_{rupt} = 100 - 400 %), the ultimate tensile strength is however slightly higher (σ_{UTS} = 15 MPa). [181, 182]

EPDM (Fig. 14 **d**) is a widely used copolymer consisting of 3 monomers ethylene, propylene and a diene. Unlike HNBR, its structural setup can vary, since the diene is not a pre-specified monomer. In principle, 3 different monomers for the diene come into application, so dicyclopentadiene (DCPD), 5-Ethylidene-2-norbornene (ENB) and 1,4-hexadiene (HX). Within this thesis, only EPDM with ENB as diene is used. Its elongation at break is larger than that of Syl 184 (ε_{rupt} = 280 - 600 %), also the ultimate tensile strength is slightly higher (σ_{UTS} = 15 - 17 MPa). [178, 180, 182, 183] Just as for HNBR, DCM is used as the initiator for the radical polymerization.

TPU is a class of various urethanes. The one used within this project is an aliphatic, thermoplastic TPU. It's elongation at break is even higher than of PDMS, HNBR and EPDM (ε_{rupt} = 480 - 850 %), such as the ultimate tensile strength (σ_{UTS} = 30 - 45 MPa). [180, 182]

2.5.2. Precursor materials

In opposite to the substrate, the layer on top has to be stiff and thin at the same time. The maximum thickness it is allowed to reach depends on the overall thickness of the substrate as well. When taking into account the Young's Moduli of the substrate elastomers discussed in the previous chapter as well as Eq. 1.10, wrinkling

periodicities in the nm- and µm-size become possible with comparably stiff layers in the upper MPa- to lower GPa-range with simultaneous layer thicknesses up to maximum a few µm.

A rather novel method to create such layers on top of polymeric films is the atmospheric plasma-assisted deposition of glass-forming precursor molecules such as HMDSO, TMDSO or TEOS on the polymer surface, from which HMDSO is the best investigated material by far. Under vacuum conditions this method is known for some time, [184, 185] though under atmospheric conditions suitable experimental setups have only been available since around 10 - 15 years. [186] In this method a glass-forming precursor molecule is inserted in the nozzle of a plasma jet in liquid or gaseous state via a carrier gas flow. The plasma immediately fragmentizes the molecules in countless species [185, 187] of which the SiO-containing recombine and eventually deposit as a rather homogeneous film, while the CH-containing fragments may be converted to volatile organic molecules. [188] The latter conversion highly depends on the utilized carrier gas that has a perspicuous influence on the atomic consumption of the emerging film, and therefore presumably also on its cross-link density and mechanical stiffness. In the absence of oxygen in the plasma jet stream, most C-containing fragments are included in the layer while with increasing oxygen concentration within the stream, the C-proportion decreases continuously. [189, 190] A comparable effect on the consumption has been observed for the employed power as well. [191] And as mentioned above, besides the well-investigated HMDSO also other molecules such as TMDSO [192] or TEOS [193] have been tested for the formation of glassy layers. Therefore these molecules were chosen within this work for their ability to form glassy layers that are able to buckle.

2.6. Analysis techniques

For the generation of micro- and nano-structured surfaces, the most important investigation step is the morphological analysis of the recently generated surface. Popular methods are Scanning Electron Microscopy (SEM) [194] or Transmission Electron Microscopy (TEM) [195] Both are able to surmount the diffraction limit of visible light by applying electrons as the information medium. They offer a distinctly smaller diffraction limit, according to the Abbe equation being in the range of a few nm for SEM [196] and even far below 1 nm for TEM. [197] Nevertheless, both methods only allow for 2D images and furthermore SEM requires conducting surfaces, which in turn requires sputtering of the surfaces afore. However, in order to get a 3-dimensional impression of the surface morphology, other methods such as White Light Interferometry (WLI), [198, 199] Confocal Laser Scanning Microscopy (CLSM), [200, 201] Three-Wavelength Vertical Scanning Interferometry (3W-VSI), [202] Scanning Near-Field Optical Microscopy (SNOM) [203, 204] or Atomic Force Microscopy (AFM) have to be used. Within this thesis, mainly AFM was used and therefore will be shortly introduced, with a focus on the determination of mechanical properties but also on topographical analysis.

2.6.1. Atomic Force Microscopy (AFM)

The AFM is an imaging instrument for the analysis of surfaces with nano-scaled morphology. In contrast to optical microscopes and the electron-based SEM and TEM techniques, which enlarge the real images of surfaces by using various lens systems, it creates images indirectly. The functional principle of the AFM is based on interaction forces of a probe and the sample's surface atoms to each other. [205] It allows for measuring position coordinates or mechanical surface properties in relation to a predefined coordinate system within a grid-like scanning system. The pointwise collected values are presented in a false color image representing e.g. the topography or mechanical properties of the surface."

When a leaf spring, the so-called cantilever with an attached tip probe, is guided over a sample surface, forces occur between the tip probe and the sample surface. Both attractive and repulsive forces are able to bend the cantilever, and depending on the probe-to-surface-distance the one or the other forces dominates, leading to an extension or attraction of the cantilever. Consequently this bending needs to be tracked: A laser source is pointed on the metallic back side of the cantilever, and the reflected light then is recorded in a four-field detector. Depending on the bending magnitude and direction of the cantilever, the reflected laser position shifts within the detector array. The position change is measured, and a voltage-operated piezo crystal constantly readapts the average height of the probe while scanning along the surface. After some further conversions, information about the surface topography and mechanics are gained. This principle is depicted in Fig. 15 **a** and **b**.

In fact, there are several operation methods for AFM-type scanning probe microscopes, such as chemical force mapping, [206] magnetic force mapping, [207, 208] atomic force acoustic microscopy [209, 210] or Kelvin probe force microscopy. [211] The two most popular are contact mode and tapping mode, besides there is also non-contact mode. In contact mode, the probe is brought into permanent contact with the sample surface, and then scans along the surface with a constant cantilever deflection, which is permanently re-adjusted in its z-position by the piezo crystal. In tapping mode, the cantilever is excited close to its resonance frequency and consequently brought close to the surface. Due to the resonant vibration it just taps the surface shortly and so preserves the surface from increased mechanical stress, also the probe tip itself becomes spared. Fig. 15 schematically shows the functional principle: In the upper image a cantilever is resonating freely, while in the lower image near a surface the resonance is being damped to lower vibration amplitudes. Since tapping mode is much more material-sparing than contact mode, it might be regarded as the standard operating mode in AFM, especially when the need is only for recording the topography of surfaces that is not on the molecular or atomic level. In such a case, the force-feedback-loop is tried to be kept a constant probe-surface-interaction-force, with z-height adaptions by the piezo crystal. Nevertheless, it is also accompanied by drawbacks, since from the high-frequent oscillations and damping thereof only qualitative mechanical sample parameters can be obtained: At very low

forces a lot of parasitic cantilever motions can occur, triggered by external forces such as impact sound from the environment, viscosity fluctuations in air or fluid of the cantilever-surrounding medium, or setup-depending forces as piezo-induced jerking movements. [212, 213]

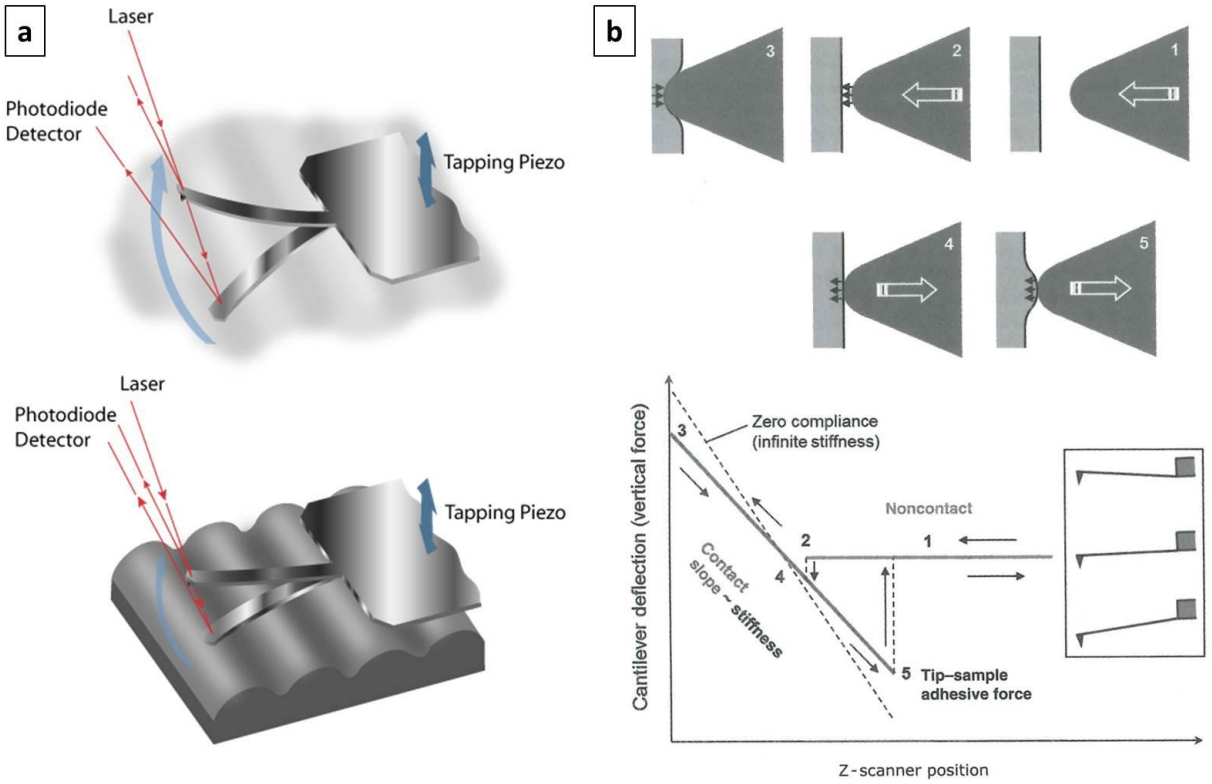

*Figure 15 | (**a**) Schematic of Tapping Mode in AFM: in the upper image the cantilever is excited to oscillate freely while its movement is tracked by a laser signal that points on its upper side, and its reflection is recorded by a 4-field-detector; in the lower image the cantilever approaches to a surface that consequently either damps its oscillation and forces it out of its mean oscillation position. [214] (**b**) Schematic of the 5 stages of the tip-to-surface interaction within one approach cycle: [212] After the tip is approached to the surface in **1**, it experiences sudden negative adhesion force by it in **2** (so-called "jump-on-contact"). With further approach the tip penetrates the surface, resulting now in a positive repulsion force in **3**. While retracting in **4**, the regime changes again from repulsive to adhesive force, with a sudden tip release from the surface in **5** (so-called "jump-off-contact") ; Reproduced with permission from references mentioned above.*

To overcome this issue, different approaches have been developed so far to get precise mechanical data on the one side, while fulfilling the requirements of high-resolution mapping at the same time. The first successful operation mode was Force Volume. [215] It is a contact-mode, in which the topography of a surface is getting mapped, while force curves for each according point are recorded simultaneously. Eventually this leads to a 3-Dimensional surface map, comparable to imaging, but including further depth information from cantilever

deflections in contact, hence a force volume map. It therefore may be compared to optical confocal microscopes. [200, 201] However, it only measures mechanical properties indirectly via the cantilever deflection, and furthermore needs comparably high forces in the nN-range to exceed the parasitic cantilever motions. The latter also hinders this method to be precise e.g. for soft samples such as elastomers, also theoretical models to get accurate absolute values fail for that reason. Nonetheless, the largest drawback is the scan speed, since one single force curve usually needs ~ 1 s for the approach-retract-cycle [216] and even for low resolution images of e.g. 128 x 128 px thousands of force curves need to be recorded, therefore resulting in data acquisition times of at least several hours.

The second operation mode that partially solves these problems is Pulsed Force, sometimes also called Digital Pulsed Force. [217, 218] Similar to Force Volume it is a contact operation mode as well, however with a non-linear but oscillating trajectory above the surface, in which the probe only shortly detaches from the surface. This is realized by a sinusoidal oscillation of the piezo crystal within the range of up to 150 nm, being in contact with the surfaces most of the cycle time. It enables a much quicker data acquisition in the speed range of tapping mode imaging, since the oscillation frequency usually operates in the upper Hz- to lower kHz-range, while the sawtooth-like movement of Force Volume is much slower in the bottom Hz-range. In such a short sine period, similar parameters to Force Volume such as stiffness or adhesion can be acquired. It however also shares the disadvantage of parasitic cantilever movements, wherefore it needs to be run in the nN-range as well.

2.6.2. Peak Force Quantitative Nanomechanical Mapping (PF-QNM) with the Dejarguin-Muller-Toprov (DMT) model

In order to measure accurate values for each data point, but still run with a sufficient speed, the Peak Force Quantitative Nanomechanical Mapping mode (PF-QNM) was invented. [216, 219] It can be regarded as a mixture of Tapping and Pulsed Force mode, with additional digital feedback-loops to control the maximum tapping force (Peak Force) that acts upon the probe tip. Similar to Pulsed Force Mode, PF-QNM operates in a tapping-related mode in the range of several Hz up to the lower kHz-range. Unlike in Pulsed Force, each point measurement on the surface is recorded and the typical force-distance-interaction curve is extracted from this data by special algorithms. This is made to extinguish the typical parasitic movements that accompany each single approach-and-retract cycle of the probe. Subsequently, the extracted data is compared to a second force-time-measurement close to the surface. This cycle suffers less from the parasitic movements and therefore acts as the cross check template to how the individual force-time-curves should look. The extracted data from the first cycle is directly compared with this second one, and eventually a combination of both (not a simple overlay) results in the output force-time-curve. This quite elaborate procedure is applied in order to lower the resolution limit for the force feedback, which drops down into the medium pN-range. [216] On the one side, the lower forces enhance

the accuracy in measurement when compared with normal Force Volume or older Pulsed Force modes, since the linear elastic regime now contributes to a larger, relative share of the overall measurement. Consequently this also allows for more accurate mechanical determination even of soft materials such as polymers or gels. The control-point for the force feedback loop is selected within the second, disturbance-free cycle. As the name of the method suggests, in PF-QNM the maximum force feedback, the Peak Force, is chosen as control-point (see Fig. 16 **a** and **b**). The combination of pN-regime and precise Peak-Force-control furthermore enables the quick measurement of high-resolution images, as Fig. 16 **c** – **f** demonstrate. On the other side, the sinusoidal tapping with precise force control allows for high-speed cycles, which is only comparable to Pulsed Force. Due to modern Hard- and Software equipment, tapping speeds of up to 2 kHz are achievable. [212, 213]

In summary, it is possible to measure not only the tip deflection, but due to the precise force feedback this allows for a calculation of material parameters as well, since the linear elastic force regime contains in principle modulus information of the sample surface. To extract those, some assumptions about the experimental setup need to be taken. First, the probe tip is regarded as a sphere with a specific tip radius. Second, both the tip probe and the plane surface become regarded as isotropic, homogenous and linear elastic materials, however with the tip probe being distinctly harder than the plain surface to be able to assume only an elastic surface deformation. With this, the Young's Modulus of the deformed surface can be calculated relatively easy. Still, it depends whether interfacial forces are neglected or not. When neglected, the reduced Young's Modulus of the sample surface is simply:

$$\bar{E}_{eff} = \frac{3}{4}\frac{F_T}{R^{1/2}{a_0}^{3/2}} \tag{1.46}$$

with

$$\frac{1}{\bar{E}_{eff}} = \frac{1-\nu_S^2}{E_S} + \frac{1-\nu_T^2}{E_T} \tag{1.47}$$

In here, $\bar{E}_{eff}$ is composed of E_S and E_T according to Eq. 1.47, consisting of the Young's Modulus and Poisson ratio of the sample E_S, ν_S and of the probe tip E_T, ν_T. Furthermore, there is the Force F_T acting upon the surface by the tip, the tip radius R and the tip indentation a_0. This classical mechanical model is based on the findings of H. Hertz and therefore called Hertz-model. [220, 221] Nevertheless, its major drawback is in fact the disregard of adhesion forces with their additional contact stress contributions while loading and unloading, especially when considering large tip radii and soft surface materials.

When adhesion is taken into account, the Hertz-model needs to be expanded by a term regarding a defined interaction force. Since this highly depends on mechanical properties and the absolute contact size, two different

models have been developed to approximate two common boundary scenarios. On the one side, there is the so-called Derjaguin-Muller-Toporov-model (DMT) [222-224] based on the Derjaguin-approximation, [225] which is best suited for small tip radii hitting comparably hard surfaces, on the other side the Johnson-Kendall-Roberts model (JKR) [226] that is suitable for large tip radii and soft samples. The difference is mainly based on the assumption whether the adhesion forces are dominated within the contact area or outside. JKR describes the inside case and DMT the outside case. [221, 227] Eventually both models result in more accurate values within their specific boundary conditions than the Hertz model does in general for non-adhesive contact. Nevertheless, Tabor [228] and Maugis [229] found that both models do not result in absolute values, since the parameters in the contact line mechanics are interdependent. In practical terms this means that the adhesion force correction parameter has to be assessed from experience of previous studies with similar materials and geometries, before E_S can be calculated. They therefore introduced specifice correction parameters μ_T (Tabor) for JKR and λ (Maugis) for DMT.

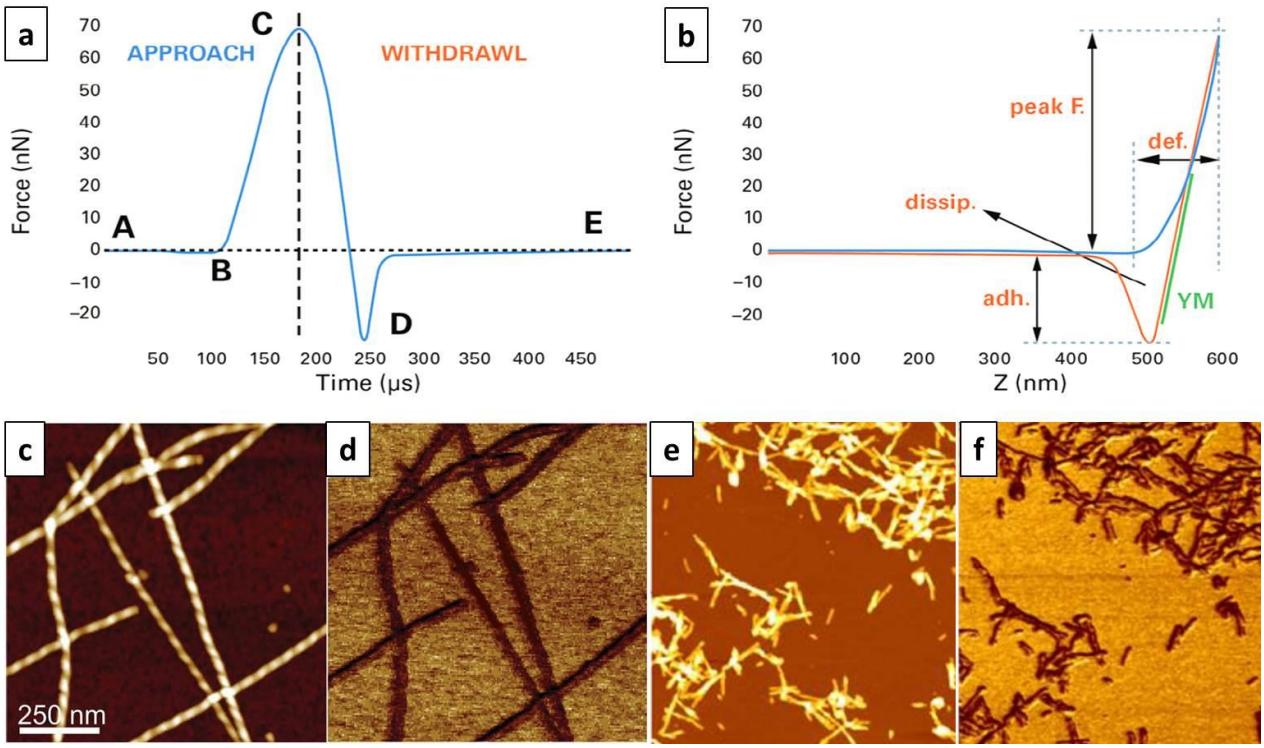

*Figure 16 | (**a**) Force-Time-Curve for the approach (left) and withdraw (right) in Peak-Force-Tapping: The tip is approached at Point A and experiences initial sample contact in point B, gets further approached and not retracted before the pre-defined Peak Force in point C is reached. While withdraw a jump-off with a negative force (due to adhesion between tip and sample) at point D is observed, before the tip levels out at zero force at point E. [219] (**b**) Force-Distance-Curve showing the characteristic physical and mechanical parameters that can be obtained via PF-QNM; The Young's Modulus (marked in green) is extracted from the linear slope in the withdraw regime. [219] (**c**) – (**f**): Topographic (**c** and **e**) as well as DMT-Modulus (**d** and **f**) images of amyloid fibers. [230, 231] Reproduced with permission from references mentioned above.*

Within the PF-QNM analysis of this thesis only the DMT-model is used, wherefore the JKR-model will not be explained further. The DMT model, as mentioned before, is based on the Derjaguin-approximation. It describes the interaction force between two bodies, when they are approximately assumed as two plan-parallel, planar surfaces. In a first approximation it then can also be applied for the approach of two spheres or combinations of two evenly curved objects: [232]

$$F_{Pullout} = -2\pi R_{eff} V \tag{1.48}$$

$$\frac{1}{R_{eff}} = \frac{1}{R_1} + \frac{1}{R_2} \tag{1.49}$$

where $F_{Pulllout}$ describes the pullout force between sphere and planar surface at the point of contact loss, with R_{eff} being the effective radius as described in Eq. 1.49 and V being the interaction potential.

In the DMT-model, the Dejarguin-approximation and the Hertz-model are combined in a way that the contact area is the same as in a Hertz-approach, however with superposed interaction forces according to the Dejarguin-approximation: [223, 224, 233, 234]

$$\bar{E}_{eff} = \frac{3}{4}\frac{F_T - F_{int}}{\left[R_{eff}(a_{def} - a_0)\right]^{2/3}} \tag{1.50}$$

$\bar{E}_{eff}$ is composed just as the Hertz model of E_S and E_T (Eq. 1.47), from which the normal Young's Modulus of the surface E_S can be calculated. Furthermore, F_T, R_{eff} and a_0 are also supposed to be of equal values as used in the Hertz-model. Additionally, the interaction force F_{int} is now regarded according to Eq. 1.48.

References

[1] D.B.H. Chua, H.T. Ng and S.F.Y. Li: Spontaneous formation of complex and ordered structures on oxygen-plasma-treated elastomeric polydimethylsiloxane, **2000**; *Appl. Phys. Lett.*, 76 - 6, 721-723

[2] Y. Shu, K. Krishnacharya and L. Pei-Chun: Harnessing Surface Wrinkle Patterns in Soft Matter, **2010**; *Adv. Funct. Mater.*, 20 - 16, 2550-2564

[3] J.-Y. Park, H.Y. Chae, C.-H. Chung, S.J. Sim, J. Park, H.H. Lee and P.J. Yoo: Controlled wavelength reduction in surface wrinkling of poly(dimethylsiloxane), **2010**; *Soft Matter*, 6 - 3, 677-684

[4] A.B. Croll and A.J. Crosby: Pattern Driven Stress Localization in Thin Diblock Copolymer Films, **2012**; *Macromol.*, 45 - 9, 4001-4006

[5] Z. Chuanyong, Z. Yan, J. Haipeng, H. Xue, X. Jixun, W. Juanjuan, C. Yanping, J. Shichun and L. Conghua: Tuning and Erasing Surface Wrinkles by Reversible Visible-Light-Induced Photoisomerization, **2016**; *Angew. Chem. Int. Ed.*, 55 - 12, 3931-3935

[6] P.-C. Lin and S. Yang: Spontaneous formation of one-dimensional ripples in transit to highly ordered two-dimensional herringbone structures through sequential and unequal biaxial mechanical stretching, **2007**; *Appl. Phys. Lett.*, 90 - 24, 241903

[7] H.D. Choon, P. Minwoo, P. ChooJin, K. Bongsoo, X. Younan, H.J. Hyun, K.J. Min, P.J. Jin and J. Unyong: Ordered Zigzag Stripes of Polymer Gel/Metal Nanoparticle Composites for Highly Stretchable Conductive Electrodes, **2011**; *Adv. Mater.*, 23 - 26, 2946-2950

[8] Q. Li, X. Han, J. Hou, J. Yin, S. Jiang and C. Lu: Patterning Poly(dimethylsiloxane) Microspheres via Combination of Oxygen Plasma Exposure and Solvent Treatment, **2015**; *J. Phys. Chem. B*, 119 - 42, 13450-13461

[9] H. Aharoni, D.V. Todorova, O. Albarrán, L. Goehring, R.D. Kamien and E. Katifori: The smectic order of wrinkles, **2017**; *Nat. Comm.*, 8 - 15809

[10] L. Pocivavsek, R. Dellsy, A. Kern, S. Johnson, B. Lin, K.Y.C. Lee and E. Cerda: Stress and Fold Localization in Thin Elastic Membranes, **2008**; *Science*, 320 - 5878, 912-916

[11] F. Brau, H. Vandeparre, A. Sabbah, C. Poulard, A. Boudaoud and P. Damman: Multiple-length-scale elastic instability mimics parametric resonance of nonlinear oscillators, **2010**; *Nat. Phys.*, 7 - 56

[12] L. Zhuo and Y. Zhang: The mode-coupling of a stiff film/compliant substrate system in the post-buckling range, **2015**; *Int. J. Sol. Struct.*, 53 - 28-37

[13] C. Lu, H. Möhwald and A. Fery: Large-Scale Regioselective Formation of Well-Defined Stable Wrinkles of Multilayered Films via Embossing, **2008**; *Chem. Mater.*, 20 - 22, 7052-7059

[14] J.Y. Chung, A.J. Nolte and C.M. Stafford: Diffusion-Controlled, Self-Organized Growth of Symmetric Wrinkling Patterns, **2009**; *Adv. Mater.*, 21 - 13, 1358-1362

[15] H. Li, B. Sheng, H. Wu, Y. Huang, D. Zhang and S. Zhuang: Ring Wrinkle Patterns with Continuously Changing Wavelength Produced Using a Controlled-Gradient Light Field, **2018**; *Materials*, 11 - 9, 1571

[16] J. Huang, M. Juszkiewicz, W.H. de Jeu, E. Cerda, T. Emrick, N. Menon and T.P. Russell: Capillary Wrinkling of Floating Thin Polymer Films, **2007**; *Science*, 317 - 5838, 650-653

[17] B. Liang, N. Hamila, M. Peillon and P. Boisse: Analysis of thermoplastic prepreg bending stiffness during manufacturing and of its influence on wrinkling simulations, **2014**; *Comp. A: Appl. Sci. Manuf.*, 67 - 111-122

[18] Y. Zhang, Y. Qian, Z. Liu, Z. Li and D. Zang: Surface wrinkling and cracking dynamics in the drying of colloidal droplets, **2014**; *Europ. Phys. J. E*, 37 - 9, 84

[19] G.C. Martin, T.T. Su, I.H. Loh, E. Balizer, S.T. Kowel and P. Kornreich: The metallization of silicone polymers in the rubbery and the glassy state, **1982**; *J. Appl. Phys.*, 53 - 1, 797-799

[20] P. Bodö and J.E. Sundgren: Titanium deposition onto ion-bombarded and plasma-treated polydimethylsiloxane: Surface modification, interface and adhesion, **1986**; *Thin Solid Films*, 136 - 1, 147-159

[21] N. Bowden, S. Brittain, A.G. Evans, J.W. Hutchinson and G.M. Whitesides: Spontaneous formation of ordered structures in thin films of metals supported on an elastomeric polymer, **1998**; *Nature*, 393 - 146

[22] Y. Gao, T. Shi, Z. Tang, S. Jiang and Q. Xia: Silver on nano-wrinkles as a substrate for surface-enhanced Raman scattering, **2014**; *Appl. Surf. Sci.*, 313 - 687-691

[23] J. Yu, Y. Wang, R.L. Moore, J.-Q. Lu and R.J. Gutmann: Low-Temperature Titanium-Based Wafer Bonding: Ti ⁄ Si , Ti ⁄ SiO 2 , and Ti ⁄ Ti, **2007**; *J. Electrochem. Soc.*, 154 - 1, H20-H25

[24] F. Baudin, V. Delaye, C. Guedj, N. Chevalier, D. Mariolle, B. Imbert, J.M. Fabbri, L. Di Cioccio and Y. Bréchet: Evaluation of Titanium Direct Bonding Mechanism, **2013**; *ECS J. Sol. State Sci. Tech.*, 2 - 5, N115-N119

[25] P.J. Yoo and H.H. Lee: Morphological Diagram for Metal/Polymer Bilayer Wrinkling: Influence of Thermomechanical Properties of Polymer Layer, **2005**; *Macromol.*, 38 - 7, 2820-2831

[26] J. Jones, S.P. Lacour, S. Wagner and Z. Suo: Stretchable wavy metal interconnects, **2004**; *J. Vac. Sci. Tech. A*, 22 - 4, 1723-1725

[27] A.E. Schedl, C. Neuber, A. Fery and H.W. Schmidt: Controlled Wrinkling of Gradient Metal Films, **2018**; *Langmuir*, 34 - 47, 14249-14253

[28] J.Y. Chung, J.-H. Lee, K.L. Beers and C.M. Stafford: Stiffness, Strength, and Ductility of Nanoscale Thin Films and Membranes: A Combined Wrinkling–Cracking Methodology, **2011**; *Nano Lett.*, 11 - 8, 3361-3365

[29] C.-C. Fu, A. Grimes, M. Long, C.G.L. Ferri, B.D. Rich, S. Ghosh, S. Ghosh, L.P. Lee, A. Gopinathan and M. Khine: Tunable Nanowrinkles on Shape Memory Polymer Sheets, **2009**; *Adv. Mater.*, 21 - 44, 4472-4476

[30] A. Agrawal, P. Luchette, P. Palffy-Muhoray, S.L. Biswal, W.G. Chapman and R. Verduzco: Surface wrinkling in liquid crystal elastomers, **2012**; *Soft Matter*, 8 - 27, 7138-7142

[31] Y. Ebata, A.B. Croll and A.J. Crosby: Wrinkling and strain localizations in polymer thin films, **2012**; *Soft Matter*, 8 - 35, 9086-9091

[32] S. Schauer, M. Worgull and H. Hölscher: Bio-inspired hierarchical micro- and nano-wrinkles obtained via mechanically directed self-assembly on shape-memory polymers, **2017**; *Soft Matter*, 13 - 24, 4328-4334

[33] J.T. Paci, C.T. Chapman, W.-K. Lee, T.W. Odom and G.C. Schatz: Wrinkles in Polytetrafluoroethylene on Polystyrene: Persistence Lengths and the Effect of Nanoinclusions, **2017**; *ACS Appl. Mat. Interf.*, 9 - 10, 9079-9088

[34] F. Greco, A. Zucca, S. Taccola, A. Menciassi, T. Fujie, H. Haniuda, S. Takeoka, P. Dario and V. Mattoli: Ultra-thin conductive free-standing PEDOT/PSS nanofilms, **2011**; *Soft Matter*, 7 - 22, 10642-10650

[35] Z. Wen, Y. Yang, N. Sun, G. Li, Y. Liu, C. Chen, J. Shi, L. Xie, H. Jiang, D. Bao, Q. Zhuo and X. Sun: A Wrinkled PEDOT:PSS Film Based Stretchable and Transparent Triboelectric Nanogenerator for Wearable Energy Harvesters and Active Motion Sensors, **2018**; *Adv. Funct. Mater.*, 28 - 37, 1803684

[36] R. Wang, Y. Long, T. Zhu, J. Guo, C. Cai, N. Zhao and J. Xu: Fabrication of oriented wrinkles on polydopamine/polystyrene bilayer films, **2017**; *J. Colloid Interface Sci.*, 498 - 123-127

[37] E. Martinez-Campos, A. Gallardo, N. Lujan, A. Santos-Coquillat, H. Reinecke, A.d. Campo and J. Rodriguez-Hernandez: Wrinkled Hydrogel Surfaces with Modulated Surface Chemistry and Topography: Evaluation As Supports for Cell Growth and Transplant, **2019**; *ACS Appl. Bio Mat.*, 2 - 2, 654-664

[38] S.P. Haanappel, R.H.W. ten Thije, U. Sachs, B. Rietman and R. Akkerman: Formability analyses of uni-directional and textile reinforced thermoplastics, **2014**; *Comp. A: Appl. Sci. Manuf.*, 56 - 80-92

[39] M. Wang, J.E. Comrie, Y. Bai, X. He, S. Guo and W.T.S. Huck: Formation of Hierarchically Structured Thin Films, **2009**; *Adv. Funct. Mater.*, 19 - 14, 2236-2243

[40] H. Huang, J.Y. Chung, A.J. Nolte and C.M. Stafford: Characterizing Polymer Brushes via Surface Wrinkling, **2007**; *Chem. Mater.*, 19 - 26, 6555-6560

[41] G.L. Ferretti, M. Nania, O.K. Matar and J.T. Cabral: Wrinkling Measurement of the Mechanical Properties of Drying Salt Thin Films, **2016**; *Langmuir*, 32 - 9, 2199-2207

[42] C. Vieu, F. Carcenac, A. Pépin, Y. Chen, M. Mejias, A. Lebib, L. Manin-Ferlazzo, L. Couraud and H. Launois: Electron beam lithography: resolution limits and applications, **2000**; *Appl. Surf. Sci.*, 164 - 1, 111-117

[43] M.T. Russell, L.S.C. Pingree, M.C. Hersam and T.J. Marks: Microscale Features and Surface Chemical Functionality Patterned by Electron Beam Lithography: A Novel Route to Poly(dimethylsiloxane) (PDMS) Stamp Fabrication, **2006**; *Langmuir*, 22 - 15, 6712-6718

[44] M.-W. Moon, S.H. Lee, J.-Y. Sun, K.H. Oh, A. Vaziri and J.W. Hutchinson: Wrinkled hard skins on polymers created by focused ion beam, **2007**; *Proc. Nat. Acad. Sci.*, 104 - 4, 1130-1133

[45] H.-G. Park, H.-C. Jeong, Y.H. Jung and D.-S. Seo: Control of the wrinkle structure on surface-reformed poly(dimethylsiloxane) via ion-beam bombardment, **2015**; *Sci. Rep.*, 5 - 12356

[46] J. Cong, J. Wang, J. Xie, C. Yang, J. Zhao, L. Li, Y. Cao, A. Fery, X.-Q. Feng and C. Lu: Determinative Surface-Wrinkling Microstructures on Polypyrrole Films by Laser Writing, **2018**; *Langmuir*, 34 - 16, 4793-4802

[47] L. Qi, C. Ruck, G. Spychalski, B. King, B. Wu and Y. Zhao: Writing Wrinkles on Poly(dimethylsiloxane) (PDMS) by Surface Oxidation with a CO2 Laser Engraver, **2018**; *ACS Appl. Mat. Interf.*, 10 - 4, 4295-4304

[48] N. Bowden, W.T.S. Huck, K.E. Paul and G.M. Whitesides: The controlled formation of ordered, sinusoidal structures by plasma oxidation of an elastomeric polymer, **1999**; *Appl. Phys. Lett.*, 75 - 17, 2557-2559

[49] M. Pretzl, A. Schweikart, C. Hanske, A. Chiche, U. Zettl, A. Horn, A. Böker and A. Fery: A Lithography-Free Pathway for Chemical Microstructuring of Macromolecules from Aqueous Solution Based on Wrinkling, **2008**; *Langmuir*, 24 - 22, 12748-12753

[50] F.A. Bayley, J.L. Liao, P.N. Stavrinou, A. Chiche and J.T. Cabral: Wavefront kinetics of plasma oxidation of polydimethylsiloxane: limits for sub-µm wrinkling, **2014**; *Soft Matter*, 10 - 8, 1155-1166

[51] K. Efimenko, M. Rackaitis, E. Manias, A. Vaziri, L. Mahadevan and J. Genzer: Nested self-similar wrinkling patterns in skins, **2005**; *Nat. Mat.*, 4 - 293

[52] C. Bukowsky, J.M. Torres and B.D. Vogt: Slip-stick wetting and large contact angle hysteresis on wrinkled surfaces, **2011**; *J. Colloid Interface Sci.*, 354 - 2, 825-831

[53] A.E. Özçam, K. Efimenko and J. Genzer: Effect of ultraviolet/ozone treatment on the surface and bulk properties of poly(dimethyl siloxane) and poly(vinylmethyl siloxane) networks, **2014**; *Polymer*, 55 - 14, 3107-3119

[54] Z. Chen, X. Zhang and J. Song: Surface wrinkling of an elastic graded layer, **2018**; *Soft Matter*, 14 - 43, 8717-8723

[55] M. Watanabe and K. Mizukami: Well-Ordered Wrinkling Patterns on Chemically Oxidized Poly(dimethylsiloxane) Surfaces, **2012**; *Macromol.*, 45 - 17, 7128-7134

[56] J.R. Serrano, Q. Xu and D.G. Cahill: Stress-induced wrinkling of sputtered SiO2 films on polymethylmethacrylate, **2006**; *J. Vac. Sci. Tech. A*, 24 - 2, 324-327

[57] S. Park and A. Boker: Ceramic nanowrinkles via a facile replication process, **2011**; *J. Mater. Chem.*, 21 - 32, 11734-11736

[58] A.L. Volynskii, S. Bazhenov, O.V. Lebedeva and N.F. Bakeev: Mechanical buckling instability of thin coatings deposited on soft polymer substrates, **2000**; *J. Mat. Sci.*, 35 - 3, 547-554

[59] Z.Y. Huang, W. Hong and Z. Suo: Nonlinear analyses of wrinkles in a film bonded to a compliant substrate, **2005**; *J. Mech. Phys. Sol.*, 53 - 9, 2101-2118

[60] R. Huang: Kinetic wrinkling of an elastic film on a viscoelastic substrate, **2005**; *J. Mech. Phys. Sol.*, 53 - 1, 63-89

[61] C.J. Young, N.A. J. and S.C. M.: Surface Wrinkling: A Versatile Platform for Measuring Thin-Film Properties, **2011**; *Adv. Mater.*, 23 - 3, 349-368

[62] M. Nania: Scalable Soft Matter Patterning From the Macro to the Nanoscale, **2017**, Department of Chemical Engineering, Imperial College London, United Kingdom

[63] B. Audoly and A. Boudaoud: Buckling of a stiff film bound to a compliant substrate—Part II:: A global scenario for the formation of herringbone pattern, **2008**; *J. Mech. Phys. Sol.*, 56 - 7, 2422-2443

[64] W. Hutchinson John: The role of nonlinear substrate elasticity in the wrinkling of thin films, **2013**; *Phil. Trans. Roy. Soc. A: Math. Phys. Eng. Sci.*, 371 - 1993, 20120422

[65] L.D. Landau and E.M. Lifshitz: Theory of elasticity, **1975**, Oxford, Pergamon Press; 58 - 65

[66] O.A. Bauchau and J.I. Craig: Structural Analysis - *Euler-Bernoulli beam theory*, **2009**, In: O.A. Bauchau and J.I. Craig, editor, Dordrecht: Springer Netherlands; 173-221

[67] E. Winkler: Die Lehre von der Elasticitaet und Festigkeit mit besonderer Ruecksicht auf ihre Anwendung in der Technik, **1867**, Prag (Bohemian Kingdom), H. Dominicus Press; 182 - 184

[68] W. K.: Über den Balken auf nachgiebiger Unterlage, **1922**; *ZAMM – J. Appl. Math. Mech. / Zeitschrift für Angewandte Mathematik und Mechanik*, 2 - 3, 165-184

[69] M.A. Biot: Bending of an infinite beam of an elastic foundation, **1937**; *J. Appl. Mech.*, 4 - 1, A1 – A7

[70] I. Szabo: Hoehere Technische Mechanik (Advanced technical mechanics), **2001**, 6th ed, Berlin, Springer Link; 401 - 403

[71] H. Jiang, D.-Y. Khang, J. Song, Y. Sun, Y. Huang and J.A. Rogers: Finite deformation mechanics in buckled thin films on compliant supports, **2007**; *Proc. Nat. Acad. Sci.*, 104 - 40, 15607-15612

[72] S. Béfahy, P. Lipnik, T. Pardoen, C. Nascimento, B. Patris, P. Bertrand and S. Yunus: Thickness and Elastic Modulus of Plasma Treated PDMS Silica-like Surface Layer, **2010**; *Langmuir*, 26 - 5, 3372-3375

[73] Q. Wang and X. Zhao: A three-dimensional phase diagram of growth-induced surface instabilities, **2015**; *Sci. Rep.*, 5 - 8887

[74] R. Zhao, T. Zhang, M. Diab, H. Gao and K.S. Kim: The primary bilayer ruga-phase diagram I: Localizations in ruga evolution, **2015**; *Ext. Mech. Lett.*, 4 - 76-82

[75] J. Groenewold: Wrinkling of plates coupled with soft elastic media, **2001**; *Phys. A: Stat. Mech. Appl.*, 298 - 1, 32-45

[76] E. Cerda, K. Ravi-Chandar and L. Mahadevan: Wrinkling of an elastic sheet under tension, **2002**; *Nature*, 419 - 579

[77] E. Cerda and L. Mahadevan: Geometry and Physics of Wrinkling, **2003**; *Phys. Rev. Lett.*, 90 - 7, 074302

[78] A. Schweikart: Ordering of Nanoparticles by Wrinkle-Assisted Self-Assembly, **2011**, Department of Biology, Chemistry and Geological Sciences, University of Bayreuth

[79] Y. Ebata: Bending, Wrinkling, and Folding of Thin Polymer Film/Elastomer Interfaces, **2013**, Polymer Science and Engineering, University of Massachusetts Amherst

[80] R.V.d. Carvalho: Wrinkling of thin sheets under tension, **2015**, Institutio Superior Tecnico Lisboa, Portugal

[81] F. Brau, P. Damman, H. Diamant and T.A. Witten: Wrinkle to fold transition: influence of the substrate response, **2013**; *Soft Matter*, 9 - 34, 8177-8186

[82] M.J. Feigenbaum: The universal metric properties of nonlinear transformations, **1979**; *J. Stat. Phys.*, 21 - 6, 669-706

[83] J.-Y. Sun, S. Xia, M.-W. Moon, K.H. Oh and K.-S. Kim: Folding wrinkles of a thin stiff layer on a soft substrate, **2012**; *Proc. Roy. Soc. A: Math. Phys. Eng. Sci.*, 468 - 2140, 932-953

[84] A.J. Nolte, M.F. Rubner and R.E. Cohen: Determining the Young's Modulus of Polyelectrolyte Multilayer Films via Stress-Induced Mechanical Buckling Instabilities, **2005**; *Macromol.*, 38 - 13, 5367-5370

[85] C. Androulidakis, E.N. Koukaras, J. Rahova, K. Sampathkumar, J. Parthenios, K. Papagelis, O. Frank and C. Galiotis: Wrinkled Few-Layer Graphene as Highly Efficient Load Bearer, **2017**; *ACS Appl. Mat. Interf.*, 9 - 31, 26593-26601

[86] G. Lin, P. Chandrasekaran, C. Lv, Q. Zhang, Y. Tang, L. Han and J. Yin: Self-similar Hierarchical Wrinkles as a Potential Multifunctional Smart Window with Simultaneously Tunable Transparency, Structural Color, and Droplet Transport, **2017**; *ACS Appl. Mat. Interf.*, 9 - 31, 26510-26517

[87] A.J. Nolte, R.E. Cohen and M.F. Rubner: A Two-Plate Buckling Technique for Thin Film Modulus Measurements: Applications to Polyelectrolyte Multilayers, **2006**; *Macromol.*, 39 - 14, 4841-4847

[88] C.M. Stafford, S. Guo, C. Harrison and M.Y.M. Chiang: Combinatorial and high-throughput measurements of the modulus of thin polymer films, **2005**; *Rev. Sci. Instrum.*, 76 - 6, 062207

[89] D. Zenkert: An Introduction to Sandwich Construction, **1995**, Engineering Materials Advisory Services

[90] E. Lejeune, A. Javili and C. Linder: Understanding geometric instabilities in thin films via a multi-layer model, **2016**; *Soft Matter*, 12 - 3, 806-816

[91] E. Lejeune, A. Javili and C. Linder: An algorithmic approach to multi-layer wrinkling, **2016**; *Ext. Mech. Lett.*, 7 - 10-17

[92] C.M. Stafford, C. Harrison, K.L. Beers, A. Karim, E.J. Amis, M.R. VanLandingham, H.-C. Kim, W. Volksen, R.D. Miller and E.E. Simonyi: A buckling-based metrology for measuring the elastic moduli of polymeric thin films, **2004**; *Nat. Mat.*, 3 - 545

[93] A.N. Boto, P. Kok, D.S. Abrams, S.L. Braunstein, C.P. Williams and J.P. Dowling: Quantum Interferometric Optical Lithography: Exploiting Entanglement to Beat the Diffraction Limit, **2000**; *Phys. Rev. Lett.*, 85 - 13, 2733-2736

[94] C. Lu, I. Dönch, M. Nolte and A. Fery: Au Nanoparticle-based Multilayer Ultrathin Films with Covalently Linked Nanostructures: Spraying Layer-by-layer Assembly and Mechanical Property Characterization, **2006**; *Chem. Mater.*, 18 - 26, 6204-6210

[95] E.D. Cranston, M. Eita, E. Johansson, J. Netrval, M. Salajková, H. Arwin and L. Wågberg: Determination of Young's Modulus for Nanofibrillated Cellulose Multilayer Thin Films Using Buckling Mechanics, **2011**; *Biomacromol.*, 12 - 4, 961-969

[96] E. Johansson and L. Wågberg: Tailoring the mechanical properties of starch-containing layer-by-layer films, **2012**; *Colloids Surf. Physicochem. Eng. Aspects*, 394 - 14-22

[97] H. Yuan, G. Singh, D. Raghavan, A.M. Al-Enizi, A. Elzatahry and A. Karim: Dispersion Morphology and Correlation to Moduli Using Buckling Metrology in Clay–Biopolymer Nanocomposite Thin Films, **2014**; *ACS Appl. Mat. Interf.*, 6 - 16, 13378-13388

[98] D.A. Kunz, J. Erath, D. Kluge, H. Thurn, B. Putz, A. Fery and J. Breu: In-Plane Modulus of Singular 2:1 Clay Lamellae Applying a Simple Wrinkling Technique, **2013**; *ACS Appl. Mat. Interf.,* 5 - 12, 5851-5855

[99] D.A. Kunz, P. Feicht, S. Godrich, H. Thurn, G. Papastavrou, A. Fery and J. Breu: Space-resolved in-plane moduli of graphene oxide and chemically derived graphene applying a simple wrinkling procedure, **2013**; *Adv. Mater.*, 25 - 9, 1337-41

[100] S.Y. Ryu, J. Xiao, W.I. Park, K.S. Son, Y.Y. Huang, U. Paik and J.A. Rogers: Lateral Buckling Mechanics in Silicon Nanowires on Elastomeric Substrates, **2009**; *Nano Lett.*, 9 - 9, 3214-3219

[101] E.A. Wilder, S. Guo, S. Lin-Gibson, M.J. Fasolka and C.M. Stafford: Measuring the Modulus of Soft Polymer Networks via a Buckling-Based Metrology, **2006**; *Macromol.*, 39 - 12, 4138-4143

[102] A.J. Nolte, J. Young Chung, C.S. Davis and C.M. Stafford: Wrinkling-to-delamination transition in thin polymer films on compliant substrates, **2017**; *Soft Matter*, 13 - 43, 7930-7937

[103] S. Schlenkrich: Spannungsinduzierte Wellenbildung in laserdeponierten Polymer/Metall-Systemen, **2014**, Georg-August-University School of Sciences, University of Göttingen, Göttingen, Germany

[104] H. Hillborg and U.W. Gedde: Hydrophobicity recovery of polydimethylsiloxane after exposure to corona discharges, **1998**; *Polymer*, 39 - 10, 1991-1998

[105] D. Hegemann, H. Brunner and C. Oehr: Plasma treatment of polymers for surface and adhesion improvement, **2003**; *Nuc. Instr. Meth. Phys. Res. Sect. B: Beam Inter. Mat. Atoms*, 208 - 281-286

[106] M.J. Owen and P.J. Smith: Plasma treatment of polydimethylsiloxane, **1994**; *J. Adhes. Sci. Technol.*, 8 - 10, 1063-1075

[107] F. Azzam, L. Chaunier, C. Moreau, D. Lourdin, P. Bertoncini and B. Cathala: Relationship between Young's Modulus and Film Architecture in Cellulose Nanofibril-Based Multilayered Thin Films, **2017**; *Langmuir*, 33 - 17, 4138-4145

[108] C.J. Rand, R. Sweeney, M. Morrissey, L. Hazel and A.J. Crosby: Fracture-induced alignment of surface wrinkles, **2008**; *Soft Matter*, 4 - 9, 1805-1807

[109] G. Miquelard-Garnier, A.B. Croll, C.S. Davis and A.J. Crosby: Contact-line mechanics for pattern control, **2010**; *Soft Matter*, 6 - 22, 5789-5794

[110] Y. Xuan, X. Guo, Y. Cui, C. Yuan, H. Ge, B. Cui and Y. Chen: Crack-free controlled wrinkling of a bilayer film with a gradient interface, **2012**; *Soft Matter*, 8 - 37, 9603-9609

[111] X. Chen and J.W. Hutchinson: Herringbone Buckling Patterns of Compressed Thin Films on Compliant Substrates, **2004**; *J. Appl. Mech.*, 71 - 5, 597-603

[112] Y. Ni, D. Yang and L. He: Spontaneous wrinkle branching by gradient stiffness, **2012**; *Phys. Rev. E*, 86 - 3, 031604

[113] S. Yu, Y. Ni, L. He and Q.-L. Ye: Tunable Formation of Ordered Wrinkles in Metal Films with Controlled Thickness Gradients Deposited on Soft Elastic Substrates, **2015**; *ACS Appl. Mat. Interf.*, 7 - 9, 5160-5167

[114] H. Vandeparre, S. Gabriele, F. Brau, C. Gay, K.K. Parker and P. Damman: Hierarchical wrinkling patterns, **2010**; *Soft Matter*, 6 - 22, 5751-5756

[115] G. Korvin: Fractured but not fractal: Fragmentation of the gulf of suez basement, **1989**; *Pure Appl. Geophys.*, 131 - 1, 289-305

[116] M.S. Hu and A.G. Evans: The cracking and decohesion of thin films on ductile substrates, **1989**; *Acta Metall.*, 37 - 3, 917-925

[117] A. Bejan, Y. Ikegami and G.A. Ledezma: Constructal theory of natural crack pattern formation for fastest cooling, **1998**; *Int. J. Heat Mass Transfer*, 41 - 13, 1945-1954

[118] M. Yanaka, Y. Tsukahara, N. Nakaso and N. Takeda: Cracking phenomena of brittle films in nanostructure composites analysed by a modified shear lag model with residual strain, **1998**; *J. Mat. Sci.*, 33 - 8, 2111-2119

[119] Y. Leterrier, D. Pellaton, D. Mendels, R. Glauser, J. Andersons and J.A.E. Månson: Biaxial fragmentation of thin silicon oxide coatings on poly(ethylene terephthalate), **2001**; *J. Mat. Sci.*, 36 - 9, 2213-2225

[120] U.A. Handge: Analysis of a shear-lag model with nonlinear elastic stress transfer for sequential cracking of polymer coatings, **2002**; *J. Mat. Sci.*, 37 - 22, 4775-4782

[121] C.B. Lin, C.C. Lin, S. Lee and Y.T. Chou: The effect of dislocations on crack propagation in wrinkled gold film deposited on polydimethylsiloxane, **2008**; *J. Appl. Phys.*, 104 - 1, 016106

[122] G. Papadopoulos: Fracture Mechanics - The experimental method of caustics and the Det.-Criterion of fracture, **1993**, 1st ed, London, Springer Scientific Publishing; 207 - 219

[123] D. Gross and T. Selig: Fracture Mechanics - With an Introduction to Micromechanics, **2011**, 2nd ed, Heidelberg, Springer Scientific Publishing; 94 - 106

[124] M.R. Gecit: Fracture of a surface layer bonded to a half space, **1979**; *Int. J. Eng. Sci.*, 17 - 3, 287-295

[125] J.L. Beuth: Cracking of thin bonded films in residual tension, **1992**; *Int. J. Sol. Struct.*, 29 - 13, 1657-1675

[126] T. Ye, Z. Suo and A.G. Evans: Thin film cracking and the roles of substrate and interface, **1992**; *Int. J. Sol. Struct.*, 29 - 21, 2639-2648

[127] J.W. Hutchinson and Z. Suo: Advances in Applied Mechanics - *Mixed Mode Cracking in Layered Materials*, **1991**, In: J.W. Hutchinson and T.Y. Wu, editor, Elsevier; 63-191

[128] Z.C. Xia and J.W. Hutchinson: Crack patterns in thin films, **2000**; *J. Mech. Phys. Sol.*, 48 - 6, 1107-1131

[129] A.G. Evans, M. Rühle, B.J. Dalgleish and P.G. Charalambides: The fracture energy of bimaterial interfaces, **1990**; *Mat. Sci. Eng. A*, 126 - 1, 53-64

[130] L.A. Giannuzzi and F.A. Stevie: A review of focused ion beam milling techniques for TEM specimen preparation, **1999**; *Micron*, 30 - 3, 197-204

[131] C.A. Volkert and A.M. Minor: Focused Ion Beam Microscopy and Micromachining, **2011**; *MRS Bull.*, 32 - 5, 389-399

[132] M. Watanabe: Wrinkles with a well-ordered checkerboard pattern, created using dip-coating of poly(methyl methacrylate) on a UV-ozone-treated poly(dimethylsiloxane) substrate, **2012**; *Soft Matter*, 8 - 5, 1563-1569

[133] M. Ouyang, C. Yuan, R.J. Muisener, A. Boulares and J.T. Koberstein: Conversion of Some Siloxane Polymers to Silicon Oxide by UV/Ozone Photochemical Processes, **2000**; *Chem. Mater.*, 12 - 6, 1591-1596

[134] M. Brinkmann, V.Z.H. Chan, E.L. Thomas, V.Y. Lee, R.D. Miller, N. Hadjichristidis and A. Avgeropoulos: Room-Temperature Synthesis of a-SiO2 Thin Films by UV-Assisted Ozonolysis of a Polymer Precursor, **2001**; *Chem. Mater.*, 13 - 3, 967-972

[135] K. Efimenko, W.E. Wallace and J. Genzer: Surface Modification of Sylgard-184 Poly(dimethyl siloxane) Networks by Ultraviolet and Ultraviolet/Ozone Treatment, **2002**; *J. Colloid Interface Sci.*, 254 - 2, 306-315

[136] B. Schnyder, T. Lippert, R. Kötz, A. Wokaun, V.-M. Graubner and O. Nuyken: UV-irradiation induced modification of PDMS films investigated by XPS and spectroscopic ellipsometry, **2003**; *Surf. Sci.*, 532–535 - 0, 1067-1071

[137] Y.-J. Fu, H.-z. Qui, K.-S. Liao, S.J. Lue, C.-C. Hu, K.-R. Lee and J.-Y. Lai: Effect of UV-Ozone Treatment on Poly(dimethylsiloxane) Membranes: Surface Characterization and Gas Separation Performance, **2009**; *Langmuir*, 26 - 6, 4392-4399

[138] B.d. Darwent: Bond dissociation energies in simple molecules, **1970**, Gaithersburg (MD), National Institute of Standards and Technology (NIST)

[139] R. Walsh: Bond dissociation energy values in silicon-containing compounds and some of their implications, **1981**; *Acc. Chem. Res.*, 14 - 8, 246-252

[140] N.E. Stankova, P.A. Atanasov, R.G. Nikov, R.G. Nikov, N.N. Nedyalkov, T.R. Stoyanchov, N. Fukata, K.N. Kolev, E.I. Valova, J.S. Georgieva and S.A. Armyanov: Optical properties of polydimethylsiloxane (PDMS) during nanosecond laser processing, **2016**; *Appl. Surf. Sci.*, 374 - 96-103

[141] A. Dessler: The Chemistry and Physics of stratospheric Ozone, **2000**, London, Academic Press

[142] J. Genzer, A.E. Ozcam, J.A. Crowe-Willoughby and K. Efimenko: Silicone Surface Science - *Creating Functional Materials by Chemical and Physical Functionalization of Silicone Elastomer Networks*, **2012**, In: M.J. Owen and P.R. Dvornic, editor, Dordrecht: Springer Publishing; 59 - 94

[143] J. Sui, J. Chen, X. Zhang, G. Nie and T. Zhang: Symplectic Analysis of Wrinkles in Elastic Layers With Graded Stiffnesses, **2018**; *J. Appl. Mech.*, 86 - 1, 011008-011008-8

[144] J. Song, D. Tranchida and G.J. Vancso: Contact Mechanics of UV/Ozone-Treated PDMS by AFM and JKR Testing: Mechanical Performance from Nano- to Micrometer Length Scales, **2008**; *Macromol.*, 41 - 18, 6757-6762

[145] B.A. Glatz, M. Tebbe, B. Kaoui, R. Aichele, C. Kuttner, A.E. Schedl, H.-W. Schmidt, W. Zimmermann and A. Fery: Hierarchical line-defect patterns in wrinkled surfaces, **2015**; *Soft Matter*, 11 - 17, 3332-3339

[146] T.M. Gross and R.E. Youngman: Flexible Glass - Enabling Thin, Leightweight, and flexible Electronics - *Low Modulus, Damage Resistant Glass for Ultra-Thin Applications*, **2017**, In: S.M. Garner, editor, Hoboken, NJ, USA: Wiley Publishing; 72 - 75

[147] E.P. Chan and A.J. Crosby: Spontaneous formation of stable aligned wrinkling patterns, **2006**; *Soft Matter*, 2 - 4, 324-328

[148] D. Bodas and C. Khan-Malek: Formation of more stable hydrophilic surfaces of PDMS by plasma and chemical treatments, **2006**; *Microelectron. Eng.*, 83 - 4, 1277-1279

[149] D. Bodas and C. Khan-Malek: Hydrophilization and hydrophobic recovery of PDMS by oxygen plasma and chemical treatment—An SEM investigation, **2007**; *Sens. Act. B Chem.*, 123 - 1, 368-373

[150] J. Zhou, A.V. Ellis and N.H. Voelcker: Recent developments in PDMS surface modification for microfluidic devices, **2010**; *Electrophoresis*, 31 - 1, 2-16

[151] M.-E. Vlachopoulou, G. Kokkoris, C. Cardinaud, E. Gogolides and A. Tserepi: Plasma Etching of Poly(dimethylsiloxane): Roughness Formation, Mechanism, Control, and Application in the Fabrication of Microfluidic Structures, **2013**; *Plasma Proc. Polym.*, 10 - 1, 29-40

[152] U.S. Inan and M. Golkowski: Principles of Plasma Physics for Engineers and Scientists, **2011**, Cambridge, United Kingdom, Cambridge Universtiy Press Publishing; 4 ff

[153] U. Stroth: Plasmaphysik - Phänomene, Grundlagen, Anwendungen, **2011**, Wiesbaden, Germany, Vieweg + Teubner Publishing; 275 - 310

[154] D. Merche, N. Vandencasteele and F. Reniers: Atmospheric plasmas for thin film deposition: A critical review, **2012**; *Thin Solid Films*, 520 - 13, 4219-4236

[155] K.H. Becker, K.H. Schoenbach and J.G. Eden: Microplasmas and applications, **2006**; *J. Phys. D: Appl. Phys.*, 39 - 3, R55

[156] R. Morent, N. De Geyter, J. Verschuren, K. De Clerck, P. Kiekens and C. Leys: Non-thermal plasma treatment of textiles, **2008**; *Surf. Coat. Technol.*, 202 - 14, 3427-3449

[157] J.D. Cobine: Gaseous Conductors - Theory and Engineering Applications, **1958**, 1st ed, Dover, United Kingdom, Dover Publications

[158] K.H. Schoenbach and K. Becker: 20 years of microplasma research: a status report, **2016**; *Eur. Phys. J. D*, 70 - 2, 29

[159] M. Radmilovic-Radjenovic, B. Radjenovic, A. Bojarov, M. Klas and S. Matejcik: The Breakdown Mechanisms In Electrical Discharges: The Role Of The Field Emission Effect In Direct Current Discharges In Micro gaps, **2013**; *Acta Physica Slovaca*, 63 - 3, 105-205

[160] Chalad Yuenyao: Low pressure DC-plasma system for the modification of polymeric membrane surfaces, **2017**, Penerbit Universiti Kebangsaan Malaysia

[161] Y. Chen: Electrical Breakdown of gases in subatmospheric pressure, **2016**, Auburn University Graduate School, Auburn University, Auburn, AL, USA, 11

[162] R.S. Dhariwal, J. Torres and M.P.Y. Desmulliez: Electric field breakdown at micrometre separations in air and nitrogen at atmospheric pressure, **2000**; *IEE Proc. Sci. Meas. Technol.*, 147 - 5, 261-265

[163] E. Hourdakis, B.J. Simonds and N.M. Zimmerman: Submicron gap capacitor for measurement of breakdown voltage in air, **2006**; *Rev. Sci. Instrum.*, 77 - 3, 034702

[164] F. Iza, G.J. Kim, S.M. Lee, J.K. Lee, J.L. Walsh, Y.T. Zhang and M.G. Kong: Microplasmas: Sources, Particle Kinetics, and Biomedical Applications, **2008**; *Plasma Proc. Polym.*, 5 - 4, 322-344

[165] S. Kurosawa, H. Harigae, H. Aizawa, K. Terashima and H. Suzuki: Gas Recognition Films Fabricated by Microplasma Technology, **2006**; *J. Photopolym. Sci. Technol.*, 19 - 2, 253-257

[166] S. Kurosawa, H. Harigae, H. Aizawa, J.-W. Park, H. Suzuki and K. Terashima: Synthesis and Characterization of Microplasma-Polymerized Styrene and Propargyl Alcohol Films, **2005**; *J. Photopolym. Sci. Technol.*, 18 - 2, 273-276

[167] M. Radmilović-Radjenović, B. Radjenović, Š. Matejčik and M. Klas: The Breakdown Phenomena in Micrometer Scale Direct-Current Gas Discharges, **2014**; *Plasma Chem. Plasma Process.*, 34 - 1, 55-64

[168] R.O. Ebewele: Polymer Science and Technology, **2000**, 1st ed, Boca Raton, USA, CRC Press

[169] A. Vashchuk, A.M. Fainleib, O. Starostenko and D. Grande: Application of ionic liquids in thermosetting polymers: Epoxy and cyanate ester resins, **2018**; *Exp. Pol. Lett.*, 12 - 898-917

[170] J. Zhao and G.N. Ghebremeskel: A Review of Some of the Factors Affecting Fracture and Fatigue in SBR and BR Vulcanizates, **2001**; *Rubber Chem. Technol.*, 74 - 3, 409-427

[171] V. Heinrichs, S. Dieluweit, J. Stellbrink, W. Pyckhout-Hintzen, N. Hersch, D. Richter and R. Merkel: Chemically defined, ultrasoft PDMS elastomers with selectable elasticity for mechanobiology, **2018**; *PLOS ONE*, 13 - 4, e0195180

[172] R. Seghir and S. Arscott: Extended PDMS stiffness range for flexible systems, **2015**; *Sens. Act. A Phys.*, 230 - 33-39

[173] B.A. Glatz and A. Fery: The influence of plasma treatment on the elasticity of the in situ oxidized gradient layer in PDMS: towards crack-free wrinkling, **2019**; *Soft Matter*, 15 - 1, 65-72

[174] K.U. Claussen, M. Tebbe, R. Giesa, A. Schweikart, A. Fery and H.-W. Schmidt: Towards tailored topography: facile preparation of surface-wrinkled gradient poly(dimethyl siloxane) with continuously changing wavelength, **2012**; *RSC Advances*, 2 - 27, 10185-10188

[175] R.A. Benkeser and J. Kang: The composition of Speier's catalyst, **1980**; *J. Organomet. Chem.*, 185 - 1, C9-C12

[176] B. Marciniec, H. Maciejewski, C. Pietraszuk and P. Pawluc: Hydrosilylation - A Comprehensive Review on Recent Advances, **2009**, Heidelberg, Germany, Springer Publishing; 159 ff

[177] A. Ainla: PDMS Preparation, 12.06.2013, **2013**, http://www.ims.ut.ee/~alar/microtech/Ch1_5/

[178] N.P. Cheremisinoff: Elastomer Technology Handbook, **1993**, Taylor & Francis

[179] R. Keller: Practical Guide to Hydrogenated Nitrile Butadiene Rubber Technology, **2012**, Smithers Information Limited

[180] G. Markovic and V.P. M: Rubber Nano Blends: Preparation, Characterization and Applications, **2016**, Springer International Publishing

[181] K. Nagdi: Rubber as an engineering material : guideline for users, **1993**, Munich, Germany, Hanser Publishing

[182] L.W. McKeen: Fatigue and Tribological Properties of Plastics and Elastomers, **2016**, Elsevier Science

[183] D.D. Elastomers and T. Industries: Ethylene Propylene Rubber (EPM, EPDM), **Retrieved: 24.01.2019**, http://www.matweb.com/search/datasheet.aspx?matguid=f8e3355cc2c541fbb0174960466819c0&n=1

[184] S. Sahli, Y. Segui, S. Ramdani and Z. Takkouk: R.f. plasma deposition from hexamethyldisiloxane-oxygen mixtures, **1994**; *Thin Solid Films*, 250 - 1, 206-212

[185] K. Li, O. Gabriel and J. Meichsner: Fourier transform infrared spectroscopy study of molecular structure formation in thin films during hexamethyldisiloxane decomposition in low pressure rf discharge, **2004**; *J. Phys. D: Appl. Phys.*, 37 - 4, 588-594

[186] G.R. Nowling, M. Yajima, S.E. Babayan, M. Moravej, X. Yang, W. Hoffman and R.F. Hicks: Chamberless plasma deposition of glass coatings on plastic, **2005**; *Plasma Sources Sci. Technol.*, 14 - 3, 477-484

[187] H. Zhang, Z. Guo, Q. Chen, X. Wang, Z. Wang and Z. Liu: Deposition of silicon oxide coatings by atmospheric pressure plasma jet for oxygen diffusion barrier applications, **2016**; *Thin Solid Films*, 615 - 63-68

[188] C. Huang, S.-Y. Wu, C.-Y. Tsai and W.-T. Liu: The growth of organosilicon film using a hexamethyldisilazane/oxygen atmospheric pressure plasma jet, **2013**; *Thin Solid Films*, 529 - 292-295

[189] M.R. Alexander, R.D. Short, F.R. Jones, W. Michaeli and C.J. Blomfield: A study of HMDSO/O2 plasma deposits using a high-sensitivity and -energy resolution XPS instrument: curve fitting of the Si 2p core level, **1999**; *Appl. Surf. Sci.*, 137 - 1, 179-183

[190] A.C. Ritts, C.H. Liu and Q.S. Yu: SiOx plasma thin film deposition using a low-temperature cascade arc torch, **2011**; *Thin Solid Films*, 519 - 15, 4824-4829

[191] M. Bashir and S. Bashir: Hydrophobic–Hydrophilic Character of Hexamethyldisiloxane Films Polymerized by Atmospheric Pressure Plasma Jet, **2015**; *Plasma Chem. Plasma Process.*, 35 - 4, 739-755

[192] C. Huang and Q. Yu: Deposition of silicon oxide hard coatings by low-temperature radio-frequency plasmas, **2010**; *J. Appl. Polym. Sci.*, 116 - 1, 245-251

[193] R.A.M. Carvalho, R.R. Lima, A.P. Nascimento Filho, M.L.P. Silva and N.R. Demarquette: Plasma polymerized TEOS films for nanochannels formation and sensor development, **2005**; *Sens. Act. B Chem.*, 108 - 1, 955-963

[194] J.I. Goldstein, D.E. Newbury, J.R. Michael, N.W.M. Ritchie, J.H.J. Scott and D.C. Joy: Scanning Electron Microscopy and X-Ray Microanalysis, **2017**, Springer New York

[195] B. Fultz and J.M. Howe: Transmission Electron Microscopy and Diffractometry of Materials, **2012**, Springer Berlin Heidelberg

[196] E. Suzuki: High-resolution scanning electron microscopy of immunogold-labelled cells by the use of thin plasma coating of osmium, **2002**; *J. Microscopy*, 208 - 3, 153-157

[197] H. Sawada, N. Shimura, F. Hosokawa, N. Shibata and Y. Ikuhara: Resolving 45-pm-separated Si–Si atomic columns with an aberration-corrected STEM, **2015**; *Microscopy*, 64 - 3, 213-217

[198] S.-W. Kim and G.-H. Kim: Thickness-profile measurement of transparent thin-film layers by white-light scanning interferometry, **1999**; *Appl. Opt.*, 38 - 28, 5968-5973

[199] J.C. Wyant: White light interferometry, **2002**, SPIE

[200] A. Gruber, A. Dräbenstedt, C. Tietz, L. Fleury, J. Wrachtrup and C.v. Borczyskowski: Scanning Confocal Optical Microscopy and Magnetic Resonance on Single Defect Centers, **1997**; *Science*, 276 - 5321, 2012-2014

[201] W.B. Amos and J.G. White: How the Confocal Laser Scanning Microscope entered Biological Research, **2003**; *Biol. Cell*, 95 - 6, 335-342

[202] K. Kitagawa: Surface and thickness profile measurement of a transparent film by three-wavelength vertical scanning interferometry, **2014**; *Opt. Lett.*, 39 - 14, 4172-4175

[203] E. Betzig and R.J. Chichester: Single Molecules Observed by Near-Field Scanning Optical Microscopy, **1993**; *Science*, 262 - 5138, 1422-1425

[204] R.C. Dunn: Near-Field Scanning Optical Microscopy, **1999**; *Chem. Rev.*, 99 - 10, 2891-2928

[205] G. Binnig, C.F. Quate and C. Gerber: Atomic Force Microscope, **1986**; *Phys. Rev. Lett.*, 56 - 9, 930-933

[206] C.D. Frisbie, L.F. Rozsnyai, A. Noy, M.S. Wrighton and C.M. Lieber: Functional Group Imaging by Chemical Force Microscopy, **1994**; *Science*, 265 - 5181, 2071-2074

[207] U. Hartmann: Magnetic Force Microscopy, **1999**; *Annu. Rev. Mater. Sci.*, 29 - 1, 53-87

[208] D. Rugar, R. Budakian, H.J. Mamin and B.W. Chui: Single spin detection by magnetic resonance force microscopy, **2004**; *Nature*, 430 - 329

[209] U. Rabe and W. Arnold: Acoustic microscopy by atomic force microscopy, **1994**; *Appl. Phys. Lett.*, 64 - 12, 1493-1495

[210] U. Rabe, S. Amelio, M. Kopycinska, S. Hirsekorn, M. Kempf, M. Göken and W. Arnold: Imaging and measurement of local mechanical material properties by atomic force acoustic microscopy, **2002**; *Surf. Interface Anal.*, 33 - 2, 65-70

[211] M. Nonnenmacher, M.P. O'Boyle and H.K. Wickramasinghe: Kelvin probe force microscopy, **1991**; *Appl. Phys. Lett.*, 58 - 25, 2921-2923

[212] G. Haugstad: Atomic Force Microscopy: Understanding Basic Modes and Advanced Applications, **2012**, Hoboken, NJ, USA, Wiley Publishing

[213] B. Pittenger, N. Erina and C. Su: Nanomechanical Analysis of High Performance Materials - *Mechanical Property Mapping at the Nanoscale Using PeakForce QNM Scanning Probe Technique*, **2014**, In: A. Tiwari, editor, Dordrecht: Springer Netherlands; 31-51

[214] © Bruker: Principles of Tapping Mode AFM, **2019**

[215] M. Radmacher, J.P. Cleveland, M. Fritz, H.G. Hansma and P.K. Hansma: Mapping interaction forces with the atomic force microscope, **1994**; *Biophys. J.*, 66 - 6, 2159-2165

[216] M.E. Dokukin and I. Sokolov: Quantitative Mapping of the Elastic Modulus of Soft Materials with HarmoniX and PeakForce QNM AFM Modes, **2012**; *Langmuir*, 28 - 46, 16060-16071

[217] A. Rosa-Zeiser, E. Weilandt, S. Hild and O. Marti: The simultaneous measurement of elastic, electrostatic and adhesive properties by scanning force microscopy: pulsed-force mode operation, **1997**; *Meas. Sci. Technol.*, 8 - 11, 1333

[218] H.-U. Krotil, T. Stifter, H. Waschipky, K. Weishaupt, S. Hild and O. Marti: Pulsed force mode: a new method for the investigation of surface properties, **1999**; *Surf. Interface Anal.*, 27 - 5-6, 336-340

[219] B. Foster: New Atomic Force Microscopy(AFM) Approaches Life Sciences Gently, Quantitatively, and Correctively, **2012**; *Am. Lab.*, 4 - 24 - 28

[220] H. Hertz: Ueber die Beruehrung fester elastischer Koerper, **1881**; *Journal fuer die reine und angewandte Mathematik*, 92 - 156 - 171

[221] H.-J. Butt, B. Cappella and M. Kappl: Force measurements with the atomic force microscope: Technique, interpretation and applications, **2005**; *Surf. Sci. Rep.*, 59 - 1, 1-152

[222] B.V. Derjaguin, V.M. Muller and Y.P. Toporov: Effect of contact deformations on the adhesion of particles, **1975**; *J. Colloid Interface Sci.*, 53 - 2, 314-326

[223] V.M. Muller, B.V. Derjaguin and Y.P. Toporov: On two methods of calculation of the force of sticking of an elastic sphere to a rigid plane, **1983**; *Coll. Surf.,* 7 - 3, 251-259

[224] J.A. Greenwood: On the DMT theory, **2007**; *Tribology Letters*, 26 - 3, 203-211

[225] B. Derjaguin: Untersuchungen über die Reibung und Adhäsion, IV, **1934**; *Kolloid-Zeitschrift*, 69 - 2, 155-164

[226] L. Johnson Kenneth, K. Kendall, A.D. Roberts and D. Tabor: Surface energy and the contact of elastic solids, **1971**; Proc. Roy. Soc. A: Math. Phys. Sci., 324 - 1558, 301-313

[227] M. Ciavarella, J. Joe, A. Papangelo and J.R. Barber: The role of adhesion in contact mechanics, **2019**; *J. Roy. Soc. Interf.*, 16 - 151, 20180738

[228] D. Tabor: Surface forces and surface interactions, **1977**; *J. Colloid Interface Sci.*, 58 - 1, 2-13

[229] D. Maugis: Adhesion of spheres: The JKR-DMT transition using a dugdale model, **1992**; *J. Colloid Interface Sci.*, 150 - 1, 243-269

[230] J. Adamcik, C. Lara, I. Usov, J.S. Jeong, F.S. Ruggeri, G. Dietler, H.A. Lashuel, I.W. Hamley and R. Mezzenga: Measurement of intrinsic properties of amyloid fibrils by the peak force QNM method, **2012**; *Nanoscale*, 4 - 15, 4426-4429

[231] F.S. Ruggeri, J. Adamcik, J.S. Jeong, H.A. Lashuel, R. Mezzenga and G. Dietler: Influence of the β-Sheet Content on the Mechanical Properties of Aggregates during Amyloid Fibrillization, **2015**; *Angew. Chem. Int. Ed.*, 54 - 8, 2462-2466

[232] E. Barthel: Adhesive elastic contacts: JKR and more, **2008**; *J. Phys. D: Appl. Phys.*, 41 - 16, 163001

[233] C. Heu, A. Berquand, C. Elie-Caille and L. Nicod: Glyphosate-induced stiffening of HaCaT keratinocytes, a Peak Force Tapping study on living cells, **2012**; *J. Struct. Biology*, 178 - 1, 1-7

[234] A. Voss, C. Dietz, A. Stocker and R.W. Stark: Quantitative measurement of the mechanical properties of human antibodies with sub-10-nm resolution in a liquid environment, **2015**; *Nano Research*, 8 - 6, 1987-1996

3. Synopsis

“All knowledge and all multiplication of our knowledge does not end with a point, but with a question mark.”

Herrmann Hesse

3.1. Outline

After in chapter 1 an introduction to the topic of micro- and nano-structuring was given, in chapter 2 the theoretical and experimental fundamentals necessary to understand the key challenges in wrinkling of two- and multi-layer materials were explained in detail. The focus was on the formation of defects in in wrinkled surfaces, on preparation methods as well as on the material and size variability. A second focus was given to the fundamentals of mechanical testing via wrinkling. Fig. 17 gives a schematic overview over the work and the four chapters presented hereinafter. This specific chapter will present the experimental findings made in preventing defect formation, upscaling and mechanical testing, as well as interpret and discuss the same.

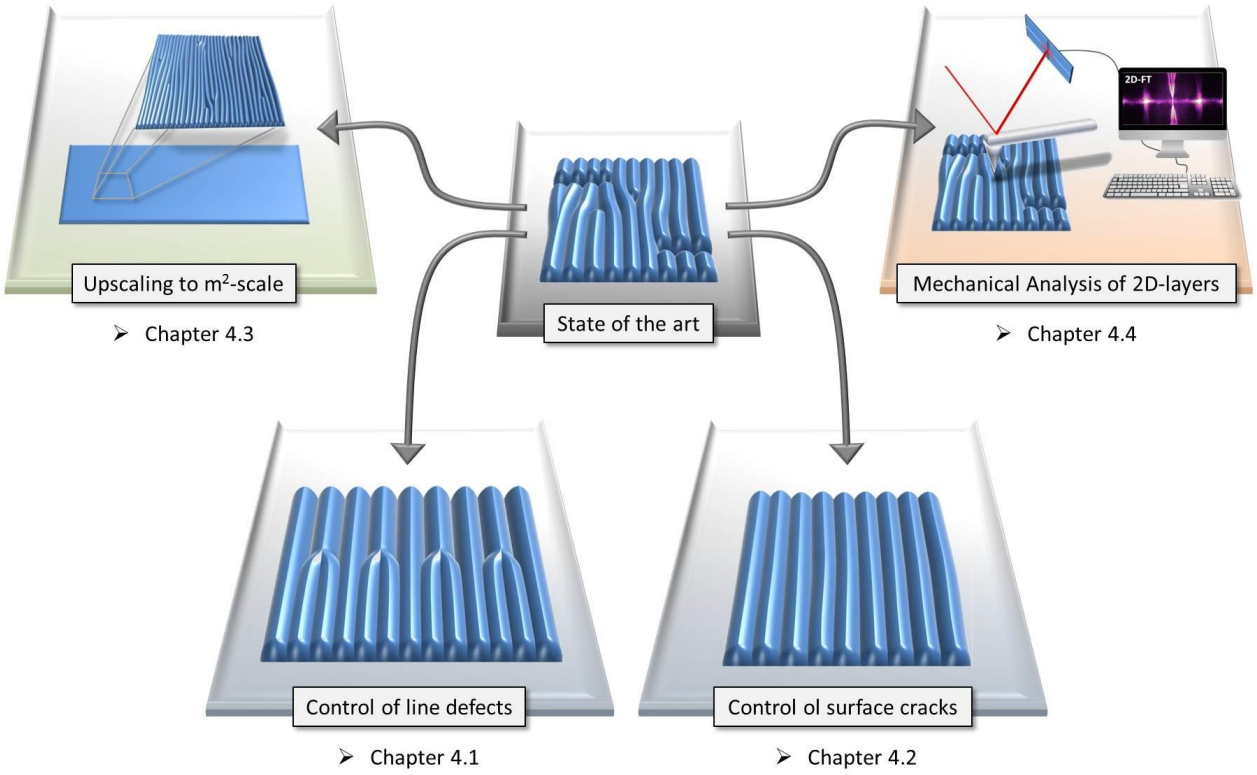

Figure 17 | Overall structure of this thesis, grouped in three main parts: In the first part the control of defect structures in state-of-the-art systems, so line defects and surface cracks, are investigated; in the second part upscaling of state-of-the-art systems to m^2-scales is achieved, and in the third part wrinkling is applied for measuring the mechanical properties of a molecular 2D-polymer layer via SIEBIMM

The chapter is divided into four parts, starting with the prevention of defects in the first two sections, continuing with methods to scale up existing wrinkling systems in the third section, and eventually finishing with the application of wrinkling for the mechanical testing of ultrathin 2D-layers in the fourth section. On the following

pages a brief overview of each chapter will be given, from the perspective of contemplating the individual chapters in the overall concept of this thesis. Furthermore, in chapter 3.2. the individual contribution of each author to each publication will be explained in brief.

3.1.1. Hierarchical line-defect patterns in wrinkled surfaces

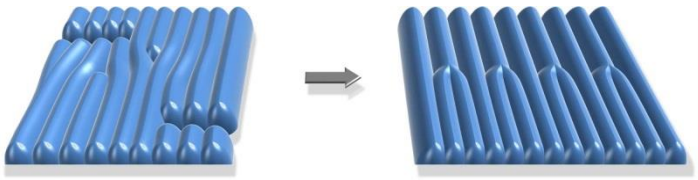

The main aim of chapter 4.1. is the investigation of line defects and their properties in a wrinkled bilayer, with an emphasis on density and position of those. From literature it is known that line defects occur in various different wrinkling processes, [1, 2] however neither the reasons for their appearance nor opportunities to control or prevent them have been described or discussed before. The only fact that seems certain is the interdependence of crack- and line-defect-density that may be influenced by the release rate of an applied pre-strain to the bilayer system. [3] The likely causes of line defect appearance in nominally uniform systems are versatile. On the one hand local property changes, such as stiffness variations in the Young's Modulus of thin layer or substrate or slight thickness changes in the layer are likely factors. On the other hand global variances such as non-uniform in-plane-stress fields along the layer-substrate-interface may be causative as well. Within this work the line defect appearance is investigated, namely the local property changes. Unlike to random line defect formation, the property changes are induced intentionally. For this purpose PDMS is used as a common substrate in soft lithographical methods, however in two different constitutions with divergent degrees of elasticity. By casting both together at a distinct interface, a leap in elasticity is achieved. On another side the thin top layer is created using UVO, which is known for producing wrinkles in the µm-range. [3, 4] This is deliberately chosen in order to take advantage of the optical visibility of such wrinkles. It enables not only the simple determination via optical microscopy, but also *in-situ*-analysis of the wrinkle- and defect-formation as well by video-caption – which is one of the major issues within this work.

Resultantly this work shows first of all the different critical strains to induce wrinkling for the divergent constitution of PDMS. The soft PDMS of E_S = 0.2 MPa with a 5 µm thick glassy layer starts to wrinkle at ε = 9 % strain release, while hard PDMS with E_S = 1.85 MPa begins at ε = 15 %. In between these values, the wrinkles on soft PDMS protrude along the common interface into the hard, unwrinkled PDMS surface, where they act as crystallization nuclei for the emerging wrinkles. Since the wrinkles on hard PDMS form shorter repeating wavelengths, the nucleation sites act in the following as places where line defects occur as well. For most elasticity ratios of soft-to-hard, the line defects along the interface form facing towards the soft part, mostly in a random manner. Nevertheless, at certain spots along the elasticity gradient interface, repetitive line-defect

patterns are observed. Consequently, these spots are recreated in MatLab to compare the theoretical model based on the Swift-Hohenberg-equation with the experimental findings. In case the parameters in the simulation are chosen as whole number ratios from large-to-small waves, an exceedingly good consistency of simulation and experiment is achieved. Furthermore, at most spots along the interface the localized line defects accumulate the local peak loads, and so are able to keep the surrounding area at a certain spacing line defect free. Fig. 18 shows the experimental results as well as the MatLab-simulations for the hard end of the gradient.

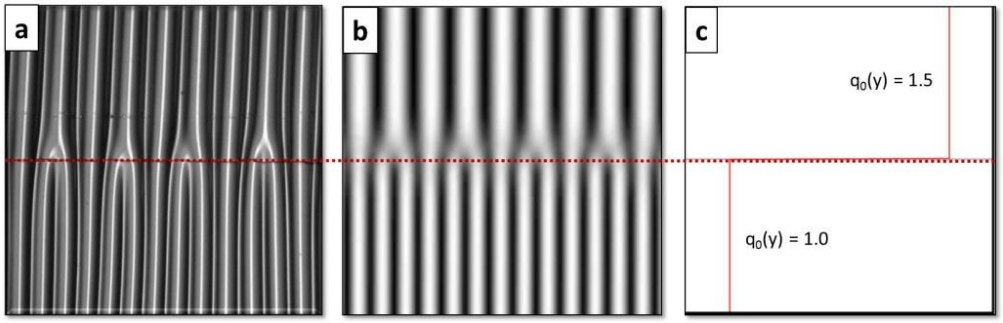

*Figure 18 | (**a**) Forced arrangement of line defects in a repetitive crossover pattern, found at the interface of the hard-to-soft crossover that lies under the in-situ oxidized layer; validated by MatLab simulations (**b**) and (**c**) via a planar Swift-Hohenberg-equation.*

Resultantly the conclusion of this work is: It is possible to control the positions and numbers of line-defects, when interfering in the system by inducing local material property fluctuations. If the fluctuations are chosen in a distinct soft-to-hard ratio, it is even possible to provoke the formation of repetitive line defect patterns. Furthermore, in places where the step gradient is pronounced, the surrounding area along the gradient interface can be kept line-defect free.

3.1.2. The influence of plasma treatment on the elasticity of the in situ oxidized gradient layer in PDMS: towards crack-free wrinkling

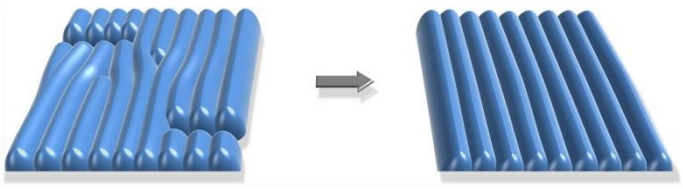

This work in chapter 4.2 follows from the question posed in chapter 4.1, whether line defects in wrinkled surfaces can be controlled or even avoided. As a follow-up to the topic, this paper deals with a directly related topic: Whether it is possible to control cracks or even to avoid them in the same manner. Though there has been elaborate studies on thin plain layers cracking on thick substrates, [5-9] potential strategies to avoid cracking have not been studied intensively yet. Just very recently works have been published that investigate crack prevention

strategies for bilayer systems. [10, 11] Furthermore the behavior of cracking in thin patterned layers on thick substrates is not investigated systematically so far.

Cracking takes place because of the differences in mechanical properties of two adjacent layers. For example, if a compound material gets heated or cooled, the materials of the composite expand to different extents due to the differing coefficients of thermal expansion. Consequently a mechanical tension occurs at the interface of two layers. In case this tension exceeds the adhesive forces between the two layers, cracks form at the conjointly interface. According to theory of mechanics the cracks will always be on the side of the stiffer participative material, so in case of wrinkling it will generally happen in the thin layer. Another familiar fact from literature is that layers with identical properties but varying thickness will show a higher absolute amount of cracks with decreasing layer thickness, [7, 12] whereas the absolute size and length of each crack grows with increasing layer thickness. [13, 14] Yet there are also crack-free layers reported that have a smooth, gradient shape instead of a rigid interface to its neighbor. So far it is only demonstrated that this approach potentially provides crack-free layers, though the phenomenon has not been fundamentally investigated yet.

The key question of this work is therefore whether it is possible to gain control over the formation of cracks by selectively introducing such a gradient-shaped mechanical layer. This is realized by plasma oxidation of PDMS via oxygen. Two main parameters of a low-pressure plasma-process are screened from the smallest to the largest technically feasible value, while all other parameters are kept constant: The nominal power of the plasma cleaner as well as the pressure inside the plasma chamber that again is controlled via the oxygen flow rate. In both screenings a perceptible variation of wavelength and amplitude is obtained, and more importantly both generate cracked as well as crack-free wrinkles within their individual parameter range. This enables the determination of the cracking limit from two independent parameters, and so a double-checked value with higher reliability in the end. Every gradient is made in two pathways: One time under a huge pre-strain in order to obtain and determine the wrinkle- and crack-patters, and another time with no pre-strain to analyze the mechanical gradient via PF-QNM. The first part provides the information of parameters, which result in cracked or non-cracked layers. The second part derives an individual and an average layer thickness for both screenings. Additionally each gradient is reconstructed in a mechanical FEM simulation in order to determine the individual peak tension with the gradient. Eventually, with a pre-strain of $\varepsilon = 60\ \%$ and a measured average layer thickness of $t_L = 100$ nm, the critical cracking tension can be specified to be $\sigma_c = 14$ MPa. Incidentally, the FEM simulations furthermore show that this is only 50 % of the comparable tension, which a single-step layer with equal thickness and equal average elasticity would have. Fig. 19 shows exemplarily two resulting wrinkled surfaces as well as the according PF-QNM layer analysis.

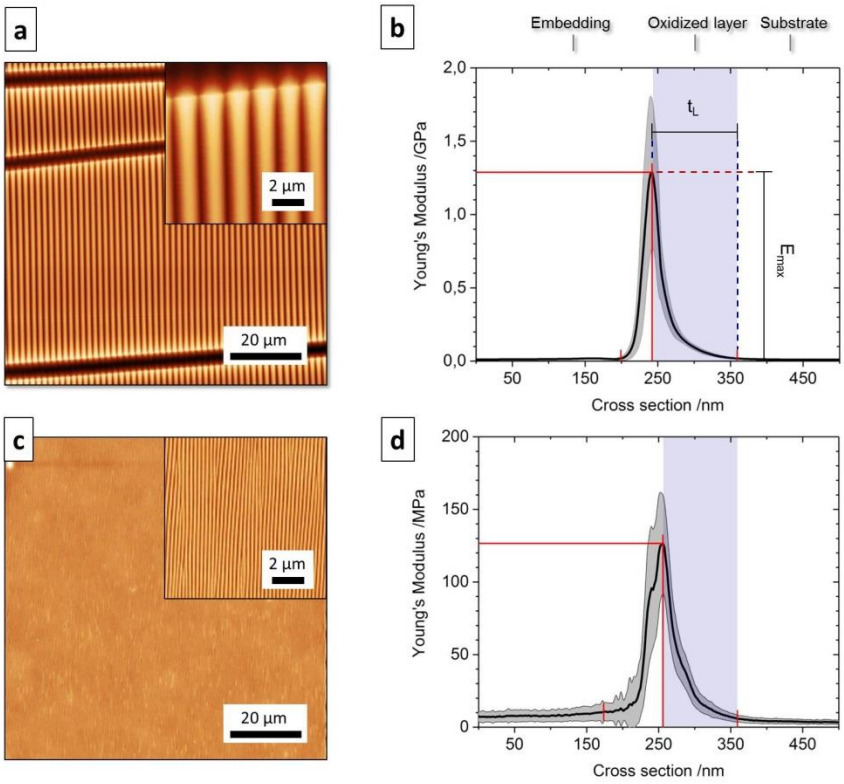

*Figure 19 | (**a**) Topographical AFM image at a chamber pressure of p = 0.05 MPa (resulting λ = 1703 nm), with corresponding PF-QNM cross section (**b**); (**c**) and (**d**): Respective AFM and PF-QNM images for a chamber pressure of p = 1.2 mbar (λ = 198 nm).*

To sum up, this work for the first identifies the in-plane-tension along the interface of mechanically pre-strained wrinkled surfaces, wherefore no comparative values can be found yet in literature. It furthermore shows that a mechanical gradient distinctly improves the resilience compared to single-step layers. In conclusion, this work suggest the implementation of a gradient for all wrinkled surface that shall be non-cracked.

3.1.3. Surface-structured polymer bodies and method for the fabrication thereof

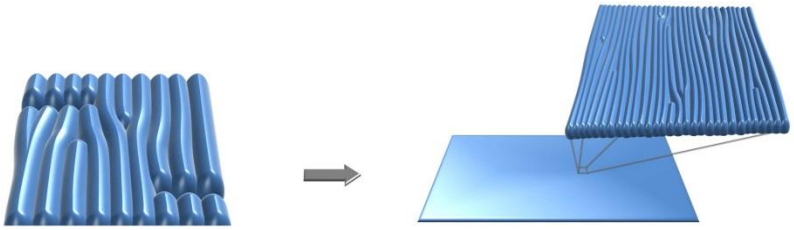

<u>Preliminary remark:</u> Since the original patent application consists only of technical descriptions and demarcations to other patents, figures to schematically describe the processes that are to be patented, are added. Moreover, in the application-examples-section results in the form of AFM analysis are added as well.

A lot of processes in literature that produce wrinkled surface in bilayer systems, already show the capability for up-scaling, but none of them has been converted to large areas yet. Therefore chapter 4.3 deals with reasons and first and foremost the solution to this challenge. The most spacious systems published to date remain in the lower cm^2 scale, [15, 16] even though the technical feasibility of larger areas was pointed out more than 10 years ago. [17] The reasons for that can only be conjectured.

This work in the form of a patent pending presents several solutions at once to this question. First of all, it is able to avoid the problem that arises when *in-situ* oxidation of silicones is carried out in a low-pressure plasma chamber, which is both poorly scalable and can only be converted into a continuous process under great technical difficulties and near-vacuum conditions. The simple trick is to switch from low-pressure plasmas to atmospheric plasmas that are able to operate under much simpler environmental conditions. This allows for continuous processes such as roll-to-roll treatment. Next, this patent presents two approaches for in-situ-plasma oxidation of silicone-like rubbers such as PDMS under ambient conditions. Both are already put into practice: On the one side there is treatment via Dielectric Barrie Discharge (DBD) and on the other side via Plasma Jet. In both methods an air-plasma is ignited at normal pressure, and pre-strained PDMS is shifted through the plasma discharge, leading straightforward to a glassification of it. Moreover, both methods in use offer the possibility to insert glass-forming precursor molecules to the plasma nozzle that become ionized and polymerized in the discharge. They are able to form a glass layer independently of silicone, so other elastomeric materials can be treated with this approach as well. Within this patent the elastomers EPDM and NBR are chosen as application examples, however others are processable likewise. The sole requirement to every elastomeric material within these processes is to offer the feasibility of covalently or adhesively bonding with the glass-forming molecule. On the other side, TEOS, HMDSO and TMDSO are used as glass-forming molecules for the thin layer. Altogether the different elastomers and precursor molecules offer numerous possibilities for material combinations, and furthermore DBD allow for large and uniform areas that shall be coated and wrinkled quickly, while Plasma Jets can be applied for the treatment of 3D-structures with high complexity. Fig. 20 shows the roll-to-roll setup and a resulting large-scale foil.

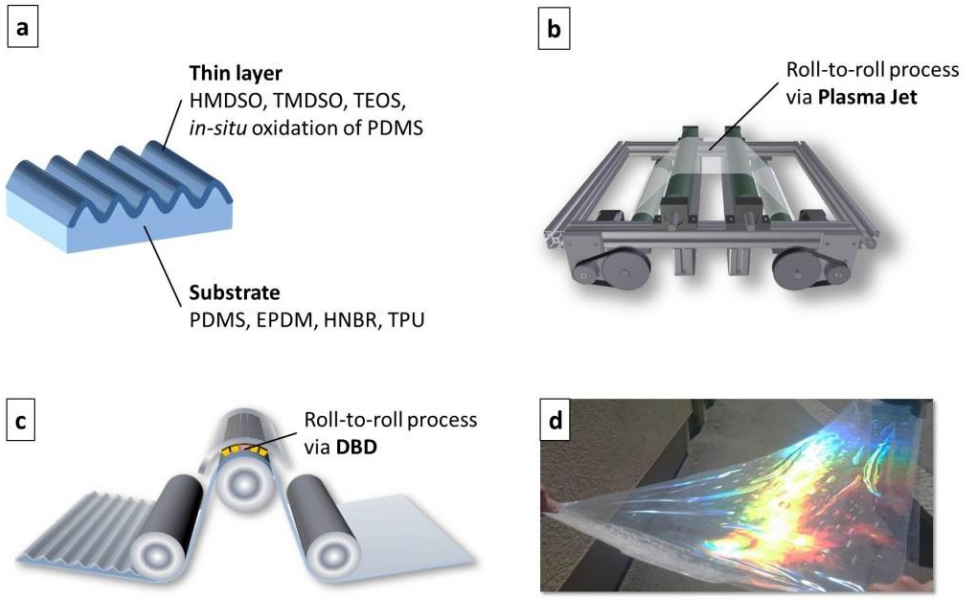

*Figure 20 | (**a**) Schematic of a wrinkled surface and the according layer and substrate materials that are applied within this work; (**b**) Schematics of plasma jet as well as DBD (**c**), showing the applied setups for atmospheric plasma treatment; (**d**) Image of DBD-treated, in-situ oxidized PDMS foil that was stretched for ε = 10 % in a continuous roll-to-roll process.*

In conclusion this patent and its application examples show two things: The up-scaling of wrinkles is demonstrated successfully. Via DBD as described above to a PDMS sheet of > 1m^2 is wrinkled entirely and uniformly, with a Plasma Jet sizes are slightly smaller in the upper dm^2-range.

3.1.4. Wafer-sized multifunctional polyimine-based two-dimensional conjugated polymers with high mechanical stiffness

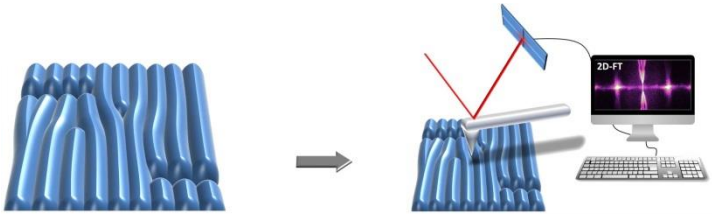

In chapter 4.4 the focus is on the mechanical characterization of 2D-polymer layers with the help of wrinkling. The topic of SIEBIMM is somehow known from literature, though it has been developed for comparably thick layers. However, it is not excluded that this procedure could be applied for thin layers down to the molecular level as well, since the fundamental physics are valid in that size range as well. Therefore, in this work the validity of SIEBIMM for ultra-thin 2D-polymer layers is checked and proofed.

This work presents a comprehensive analysis of the recently synthesized polymer. This includes optical and atomic force microscopy to rate the surface morphology, UV-Vis spectroscopy to determine its chemical consumption, selected area diffraction (SAED) to investigate the crystallinity, density functional theory (DFT)

calculations to calculate the electronic bandgap structure of the conjugate system, hydrogen evolution reaction (HER) in order to test its suitability as semiconductors, and eventually mechanical measurements via wrinkling (SIEBIMM) to investigate the in-plane-stiffness of the polymer – that thematically fits well into this dissertation.

First of all, 2D-polymers with molecular thickness are known since a long time, nevertheless the synthesis and characterization of such has attracted attention only lately. Especially the synthesis of covalently bonded 2D-polymers, so-called covalent organic frameworks, is still challenging. The 2D-polymer presented herein is a conjugate imine system synthesized from an amine and a planar aldehyde. Both monomers are kinetically and thermodynamically stable and flow on an air-water-interface, so the synthesis is rather simple at first. And secondly, the mechanism is basically a Schiff' base condensation reaction that sets free H_2O, so the equilibrium is on the right side of the reaction. In a nutshell, the synthesis is rather robust and simple.

Secondly and in the particular part of mechanical characterization, the main challenge is to establish a good bond between 2D-polymeric layer and PDMS substrate. With the use of diluted aqueous HCl, the CH_3-sidegroups within the PDMS network become reversibly hydrophilized by forming C-OH-groups. Consequently, these act as covalent binding sites for the highly polar conjugated polyimine. Both become connected by lifting up the PDMS substrate from a water bath through the freshly formed 2D-polymer that flows on the water-air-interface. In a next step, the bilayer system becomes strained in a custom-made stretching device, and in this state analyzed via AFM topographical analysis. The obtained data are evaluated via 2D-FT and PSD to find the peak maxima and width, which can be recalculated to the dominant wavelength and standard deviation. Eventually the measured wavelength allows for the determination of the in-plane-Young's Modulus of the polyimine layer. To check the validity of the method, a reference sample of known mechanical properties [18] is prepared alike, analyzed via SIEBIMM as well, and eventually the results are compared. They show a good correspondence with the literary value (16 ± 3 GPa via SIEBIMM in comparison with 13 ± 3 GPa via Nano-Indentation). Reproduced samples deliver comparable results. Fig. 21 shows the experimental setup as well as the results.

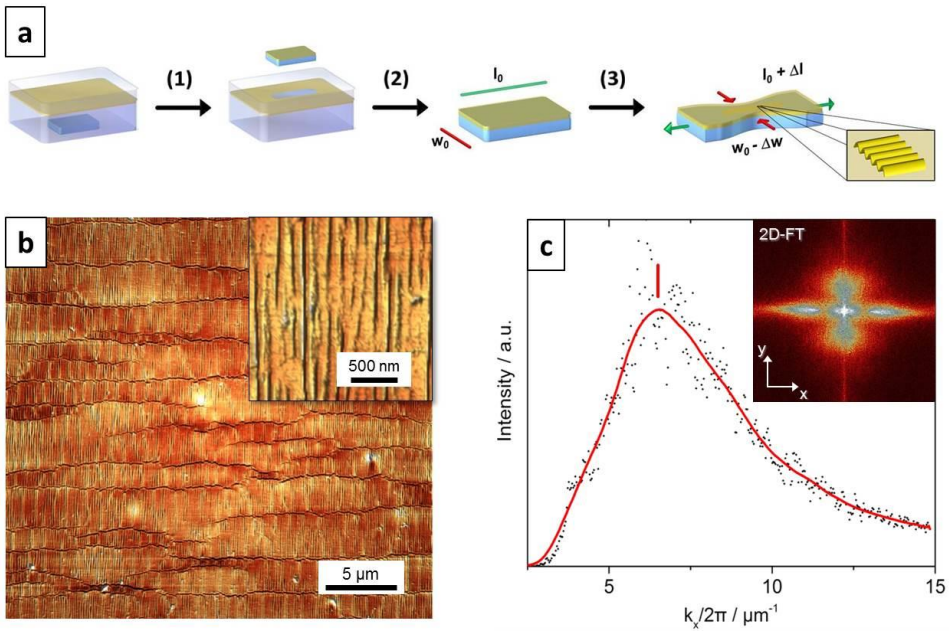

*Figure 21 | (**a**) Schematic of the transfer process: A PDMS slab is placed in a water bath, on which the 2D-polymer floats. By lifting the slab up and through the 2DP (**1**), the transfer is done resulting in the bilayer sample (**2**). By straining this (**3**), wrinkles occur that eventually become measured via AFM and determined via 2D-FT and PSD. (**b**) Topographical AFM image of wrinkled 2DP on PDMS substrate; (**c**) 2D-FT-analysis of (b) giving a peak maximum for λ = 152 nm with a resulting 2DP Young's Modulus of El = 267 ± 30 GPa*

This work therefore shows clearly the applicability of SIEBIMM even for 2D-polymers of molecular thickness < 1 nm.

3.2. Individual contribution to joint publications

Chapter 4.1

This work is published in *Soft Matter*, **2015**, 11 – 17, 3332 – 9 under the title:

"Hierarchical line-defect patterns in wrinkled surfaces"

by B.A. Glatz, M. Tebbe, B. Kaoui, R. Aichele, C. Kuttner, A.E. Schedl, H.W. Schmidt, W. Zimmermann and A. Fery

I performed all experiments except the gradient casting, and I accomplished the FEM simulations. Furthermore I wrote most of the manuscript. R. Aichele, B. Kaoui and W. Zimmermann accomplished the wrinkling simulations and the according part of the manuscript. A.E. Schedl and H.W. Schmidt synthesized the PDMS gradients. M. Tebbe helped with scientific discussions about the topic and with writing the manuscript, while A. Fery conceived the topic, helped with discussion as well, and corrected the manuscript eventually.

Chapter 4.2

This work is published in *Soft Matter*, **2019**, 15 – 1, 65 – 72 under the title:

"The influence of plasma treatment on the elasticity of the in situ oxidized gradient layer in PDMS: towards crack-free wrinkling"

by B.A. Glatz and A. Fery

I performed all experiments as well as the FEM simulations, and wrote the manuscript together with A. Fery, who helped to conceive the topic and the manuscript.

Chapter 4.3

This work is a patent application published under the numbers DE 10 **2017** 218 363 A1, EP 3470 456 A1 as well as US **2019**/0111610 A1 under the title:

"Surface-structured polymer bodies and method for the fabrication thereof"

by B.A. Glatz, A. Knapp and A. Fery

I performed all experiments, together with A. Knapp, and designed the topic, together with A. Fery. Furthermore, I and A. Knapp wrote the invention disclosure corrected by A. Fery, on which the underlying patent document is based.

This patent application is based on an invention disclosure that was prepared by myself with the help of A. Knapp and A. Fery within the Leibniz Institute of Polymer Research Dresden. The original patent application as presented in here was prepared by Rauschenbach Patentanwälte GbR, Dresden, Germany, naming me, A. Knapp and A. Fery as the inventors in the sense of the law. Legally speaking, the patent application belongs to the Leibniz Institute of Polymer Research Dresden.

Chapter 4.4

This work is published in *Nature Communications,* **2016**, 7 – 13461 under the title:

> **"Wafer-sized multifunctional polyimine-based two-dimensional conjugated polymers with high mechanical stiffness"**

by H. Sahabudeen, H. Qi, B.A. Glatz, D. Tranca, R. Dong, Y. Hou, T. Zhang, C. Kuttner, T. Lehnert, G. Seifert, U. Kaiser, A. Fery, Z. Zheng and X. Feng

H. Sahabudeen synthesized the 2D-polymer, while H. Qi, T. Lehnert and U. Kaiser performed TEM and SAED experiments. I performed the mechanical measurements via SIEBIMM, and did AFM as well as 2D-FT and PDS post-analysis with the help of A. Fery. D. Tranca and G. Seifert performed the DFTB calculations, Y. Hou the HER analysis and T. Zhang AFM and Raman spectroscopy. R. Dong and C. Kuttner helped with discussion, while Z. Zheng and X. Feng designed the topic and wrote most of the manuscript.

References

[1] C.J. Rand, R. Sweeney, M. Morrissey, L. Hazel and A.J. Crosby: Fracture-induced alignment of surface wrinkles, **2008**; *Soft Matter*, 4 - 9, 1805-1807

[2] A. Schweikart and A. Fery: Controlled wrinkling as a novel method for the fabrication of patterned surfaces, **2009**; *Microchimica Acta*, 165 - 3, 249-263

[3] K. Efimenko, M. Rackaitis, E. Manias, A. Vaziri, L. Mahadevan and J. Genzer: Nested self-similar wrinkling patterns in skins, **2005**; *Nat. Mat.*, 4 - 293

[4] J. Rodríguez-Hernández and A. del Campo: Fabrication of hierarchical wrinkled morphologies through sequential UVO treatments, **2015**; *J. Appl. Polym. Sci.*, 132 - 17,

[5] M.S. Hu and A.G. Evans: The cracking and decohesion of thin films on ductile substrates, **1989**; *Acta Metall.*, 37 - 3, 917-925

[6] A.G. Evans, M. Rühle, B.J. Dalgleish and P.G. Charalambides: The fracture energy of bimaterial interfaces, **1990**; *Mat. Sci. Eng. A,* 126 - 1, 53-64

[7] J.L. Beuth: Cracking of thin bonded films in residual tension, **1992**; *Int. J. Sol. Struct.*, 29 - 13, 1657-1675

[8] M. Yanaka, Y. Tsukahara, N. Nakaso and N. Takeda: Cracking phenomena of brittle films in nanostructure composites analysed by a modified shear lag model with residual strain, **1998**; *J. Mat. Sci.*, 33 - 8, 2111-2119

[9] P.A. Gruber, E. Arzt and R. Spolenak: Brittle-to-ductile transition in ultrathin Ta/Cu film systems, **2011**; *J. Mater. Res.*, 24 - 6, 1906-1918

[10] Z. Liu, D. Qi, P. Guo, Y. Liu, B. Zhu, H. Yang, Y. Liu, B. Li, C. Zhang, J. Yu, B. Liedberg and X. Chen: Thickness-Gradient Films for High Gauge Factor Stretchable Strain Sensors, **2015**; *Adv. Mater.*, 27 - 40, 6230-6237

[11] J. Sui, J. Chen, X. Zhang, G. Nie and T. Zhang: Symplectic Analysis of Wrinkles in Elastic Layers With Graded Stiffnesses, **2018**; *J. Appl. Mech.*, 86 - 1, 011008-011008-8

[12] T. Sakorikar, M.K. Kavitha, P. Vayalamkuzhi and M. Jaiswal: Thickness-dependent Crack Propagation in Uniaxially Strained Conducting Graphene Oxide Films on Flexible Substrates, **2017**; *Sci. Rep.*, 7 - 1, 2598

[13] Z.C. Xia and J.W. Hutchinson: Crack patterns in thin films, **2000**; *J. Mech. Phys. Sol.*, 48 - 6, 1107-1131

[14] T. Qasim, C. Ford, M. Bongué-Boma, M.B. Bush and X.-Z. Hu: Effect of coating thickness on crack initiation and propagation in non-planar bi-layers, **2006**; *Mat. Sci. Eng. A,* 419 - 1, 189-195

[15] L. Zhong, Z. Shen, Z. Pengfei, Y. Dayong, J. Gang and M. Hongwei: Surface initiated polymerization from integrated poly(dimethylsiloxane) enables crack-free large area wrinkle formation, **2012**; *Polym. Adv. Technol.*, 23 - 9, 1240-1245

[16] J. Xie, X. Han, C. Zong, H. Ji and C. Lu: Large-Area Patterning of Polyaniline Film Based on in Situ Self-Wrinkling and Its Reversible Doping/Dedoping Tunability, **2015**; *Macromol.*, 48 - 3, 663-671

[17] H.-L. Zhang, T. Okayasu and D.G. Bucknall: Large area ordered lateral patterns in confined polymer thin films, **2004**; *Eur. Polym. J.*, 40 - 5, 981-986

[18] Z. Zheng, C.S. Ruiz-Vargas, T. Bauer, A. Rossi, P. Payamyar, A. Schütz, A. Stemmer, J. Sakamoto and A.D. Schlüter: Square-Micrometer-Sized, Free-Standing Organometallic Sheets and Their Square-Centimeter-Sized Multilayers on Solid Substrates, **2013**; *Macromol. Rapid Commun.*, 34 - 21, 1670-1680

4. Publications and Patents

"Touch a scientist and you touch a child."

Ray Bradbury

4.1. Publication - Hierarchical line-defect patterns in wrinkled surfaces

4.1.1. Abstract

We demonstrate a novel approach for controlling the formation of line-defects in wrinkling patterns by introducing step-like changes in the Young's modulus of elastomeric substrates supporting thin, stiff layers. Wrinkles are formed upon treating the poly(dimethylsiloxane) (PDMS) substrates by UV/Ozone (UVO) exposure in a uniaxially stretched state and subsequent relaxation. Line defects such as minutiae known from fingerprints are a typical feature in wrinkling patterns. The position where these defects occur is random for homogenous substrate elasticity and film thickness. However, we show that they can be predetermined by using PDMS substrates consisting of areas with different cross-linking densities. While changing the cross-linking density is well known to influence the wrinkling wavelength, we use this parameter in this study to force defect formation. The defect formation is monitored in situ using light microscopy and the mechanical parameters/film thicknesses are determined using imaging AFM indentation measurements. Thus the observed wrinkle-wavelengths can be compared to theoretical predictions. We study the density and morphology of defects for different changes in elasticity and compare our findings with theoretical considerations based on a generalized Swift–Hohenberg-equation to simply emulate the observed pattern-formation process, finding good agreement. The fact that for suitable changes in elasticity, well-ordered defect patterns are observed is discussed with respect to formation of hierarchical structures for applications in optics and nanotechnology.

4.1.2. Introduction

Wrinkling is a mechanical instability phenomenon of thin films. Wrinkles form, if a laminar system consisting of a stiff, thin layer in strong adhesive contact with a soft, macroscopic elastomer is subject to in-plane compression. Under these conditions, the well-known buckling instability results in periodic surface corrugations. Due to its generic nature, wrinkling can be found in biological, [1, 2] geomorphological [3, 4] as well as artificial structures. [5, 6] In the framework of surface patterning and structuring, controlled formation of wrinkles has been investigated and characterized intensively in the last two decades. [7-12] Importantly, permanent wrinkle patterns can be formed, if the thin layer is created while an elastomeric substrate is under strain and subsequently relaxed. Possible preparation methods are in situ oxidation of poly(dimethylsiloxane) (PDMS) substrates by treatment with plasma, [13, 14] UVO, [15-17] wet chemicals [18] or coating of these substrates with metals [19] and polymers, [20] respectively. Besides, other methods are employed, e.g. the utilization of distortion effects of elastomers at an water–substrate-interface that lead to sinusoidal bending [21] or the coating of an elastomer with a UV-curable material instead of attaching two layers to each other. [22]

Wrinkle patterns display always deviations from an ideal structure, even in the simplest case of uni-axial strain, yielding parallel oriented wrinkles. These defects can be classified into two categories, cracks and line defects, respectively. Most work has been done on the investigation of cracks, which are mechanically induced film fractures. [23-25] Recently, some publications report on specific applications of thin-film-cracking where the evolving channels are filled with metals and consequently utilized as conducting 2D-networks. [26, 27] In contrast our work focuses on the second defect type – the line defects that are known as minutiae in fingerprints. Their evolution in random fingerprint-like structures with defects has been simulated lately. [28] Line defects are characterized by two adjacent ridges emerging into one single ridge or by a termination of a ridge, as illustrated in Fig. 22 for fingerprints, where the term minutiae is used for the line defects, and for wrinkle patterns formed using the method presented in this study.

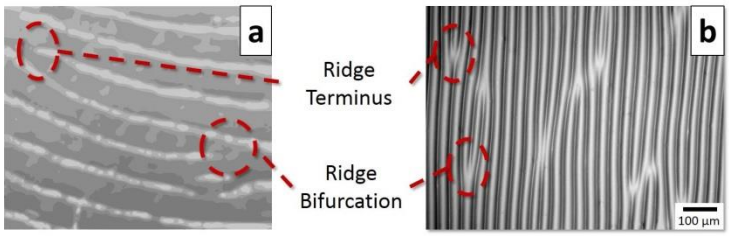

*Figure 22 | Comparison of a human fingerprint (**a**) and a wrinkled PDMS sample (**b**). Line defects as ridge termini and bifurcations are found in both cases. However the size differs from the millimeter-range on human hands down to the micrometer and nanometer-range for artificially wrinkled samples.*

For ideal homogenous, infinite systems line defect nucleation is a homogenous nucleation process. However, in real systems line defects are frequently found to nucleate at heterogeneities in elastic constants or film thicknesses or at boundaries. In many applications, these line defects are considered a nuisance since they appear stochastically and thus limit the structural perfection and long range order of wrinkling patterns. However, they as well present an interesting example of symmetry breaking and harnessing the position at which line defects occur might pave the road to control symmetry breaking and formation of complex hierarchical structures.

Following this rationale, we present a method to generate patterned defects in a controlled fashion. We introduce a novel method for the preparation of PDMS with steep local changes in the Young's modulus and study permanent wrinkle formation in these systems. We investigate the mechanical properties of the system using nanomechanical AFM techniques. Furthermore, we employ light microscopy for in situ investigation of wrinkle and line-defect formation. These studies are the basis to elucidate the underlying structure formation mechanism. We investigate the spatial distribution of line defects and long range ordering effects. Finally, we discuss potential applications in optics, particle alignment or microfluidics. [29, 30]

4.1.3. Results and Discussion

Wrinkled samples were prepared from commercially available PDMS system Sylgard 184 (Dow Corning Ltd., Midland, USA). PDMS samples were treated with UVO in uni-axially stretched state to induce wrinkle formation upon relaxation. A buckling instability caused by mechanical mismatch between the applied thin oxide layer and the elastic substrate leads to wrinkle formation perpendicular to the strain direction (see Fig. 2). The resulting wavelengths of the buckling instability can be calculated for small strains according to the well-known Eq. 4.1 – 4.3 [31, 32]

$$\varepsilon_c = \frac{1}{4}\left(\frac{\bar{E}_s}{3\bar{E}_f}\right)^{2/3} \tag{4.1}$$

$$\lambda = 2\pi h\left(\frac{\bar{E}_f}{3\bar{E}_s}\right)^{1/3} \tag{4.2}$$

with

$$\bar{E} = \frac{E}{1-\nu^2} \tag{4.3}$$

Herein, ε_c represents the critical uniaxial strain necessary to induce wrinkling, while λ describes the wavelength of the buckling instability, h is denoted as layer thickness and $\bar{E}_f$ and $\bar{E}_s$ are the plane-strain-moduli of the layer and substrate respectively that can be calculated with the according Poisson's ratio ν. Modifying the ratio of the pre-polymer to curing-agent results in a stiffness variation of the resulting silicone from 0.24 MPa to 1.82 MPa. To create a sample that features two different wrinkling wavelengths and a small, defined crossover area in between, we combined these materials displaying large differences in stiffness.

Sample preparation

The samples were prepared sequentially in three steps: (1) a matrix containing the highest cross-linker content was prepared, (2) fluid soft PDMS being discrete or gradient-like was cast into the matrix presenting one side and (3) the matrix was cross-linked thermally, ensuring a covalent linkage between both phases. The process is depicted in the Supporting Information (chapter 4.1.5) schematically in Fig. 28. Thus, PDMS of adjustable Young's modulus was embedded in a matrix of hard PDMS. Consequently, the interface between both materials displayed a sharp mechanical transition between the different phases of PDMS. According to Eq. 4.2 a change of substrate elasticity is directly correlated with a change in wavelength for constant film elasticity and thickness. To investigate wrinkling of substrates with different Young's moduli focusing on the defect formation process two different sample types were prepared (Fig. 23). One sample type was prepared casting soft PDMS into a mold consisting of only hard PDMS (Fig. 23 **a**) giving a composite consisting of two pure materials. The other sample

type was prepared by casting a soft- to-hard-gradient into a mold of hard PDMS using a modified method of Claussen et al. [33] (Fig. 23 **b**).

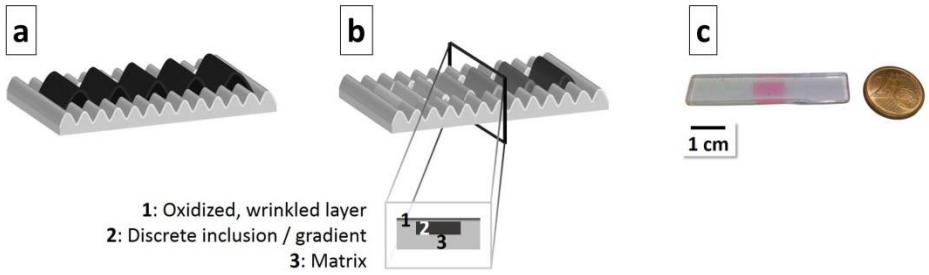

*Figure 23 | Schematic illustration of the two sample types: a soft, discrete (**a**) and a soft-to-hard gradient, both embedded in a hard matrix (**b**) with a cross profile of the sample. In (**c**) a typical sample of type (**a**) is shown scaled with a 2 €-cent coin. It consists of the hard, transparent matrix that includes the soft, red dyed inner part.*

The line-defects are expected to preferentially nucleate at the interface of hard-to-soft material. This is due to a difference in substrate stiffness, which forces a local change of preferred wavelength that goes along with formation of line branches. Additionally, the speed of relaxation has an impact on their number and shape, [34] that is why the samples were allowed to relax with highest possible rate after oxidation to create as many line defects as possible. Furthermore, according to Eq. 4.1 the wrinkle evolution is not simultaneous in both phases, but will occur when the critical strain ε_c is reached, depending on the respective Young's moduli. In order to analyze this predicted behavior, we used a custom-built in situ setup (see also Fig. 29) based on optical microscopy to study wrinkle and defect formation along the stiffness modification lines.

Qualitative analysis

The stretched and oxidized samples were released with a defined speed. The wrinkle evolution was tracked in situ via reflected light microscopy focused at the oxidized surface layer in order to capture changes in the surface morphology. Fig. 24 shows representative results for a homogeneous sample with a discrete step in substrate elasticity: After focusing the interface between hard and soft polymer the wrinkle evolution was induced by slowly decreasing the strain from an elongation of $\varepsilon = 50\%$ (15 mm initial sample length and 22.5 mm strained state) with $6.1\ \frac{mm}{min}$. For a ε of 41% the first wrinkles can be observed in the soft phase (Fig. 24 **b**). They were entirely shaped at a ε of 39% (Fig. 24 **c**), meaning the amount of waves and line-defects remains constant. For a ε of 35% buckling is induced within the hard phase (Fig. 24 **d**). The wrinkle evolution is completed at a ε of 30% resulting in a fully wrinkle-covered surface (Fig. 24 **e**). The corrugations on the soft phase slightly protrude into the unwrinkled hard phase (Fig. 24 **c**).

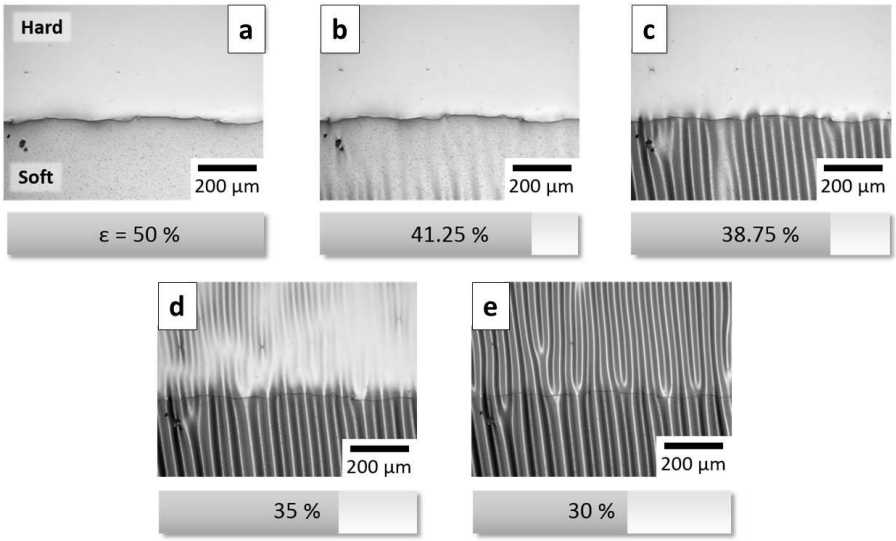

*Figure 24 | Same-spot in situ observation of the release process, focused on the crossover line from hard to soft PDMS. The soft discrete inclusion is present at the bottom each, the hard at the top. In the beginning the substrate is pre-strained to 50% of its initial length (**a**), the oxidized layer on top is unstrained. Upon strain release wrinkles do form first within the soft inclusion (**b** and **c**) followed by the hard matrix (**d** and **e**). For a video capture of this process, see Electron Supporting Information.*

It is caused by different boundary conditions of the two phases which results in a singularity within the interphase that consequently induces line-defect formation close to the interface. Here the critical strain as well as the final wavelength changes dramatically. Thus, line defects caused by singularity are pinned to the interface transition or nucleate in close proximity. Further strain release afterwards only leads to a compression of the waves, which results in increasing amplitudes and reduced wavelengths. The underlying wrinkle formation process can be divided into two different steps. First the waves emerge within domains with sizes of a few buckling periods, followed by a rapid growth with decreasing strain resulting in wrinkle joining. The latter is accompanied by the appearance of line-defects. [35] Furthermore, the buckling period depends on the stiffness (Young's modulus) of the underlying substrate following a third root law, in consistence with Eq. 4.2. The results observed for low strains are shown in Fig. 24 **e**. As expected a large wavelength is obtained on substrates with low stiffness values.

Quantitative parameter analysis

To compare our experimental results with theory we quantitatively determined all relevant parameters. According to Eq. 4.2 the required parameters are the Young's moduli $\bar{E}_s$ and $\bar{E}_f$ respectively, and the layer height h_F of homogenous (nonembedded) hard and soft PDMS. The data for the substrate moduli of hard and soft phase were taken from Claussen et al. [33] They determined 1.82 ± 0.04 MPa for hard and 0.24 ± 0.01 MPa for soft PDMS. Additionally, we performed indentation measurements to check for the mechanical uniformity of the individual

phases. Therefore the samples were analyzed prior to oxidation with a sapphire sphere (400 mm radius) along the line of previous publications. [15, 36] For statistical reasons every sample was measured five times on different spots. For hard PDMS the averaged Young's modulus was determined to be 2.9 ± 0.31 MPa and for soft 0.65 ± 0.14 MPa. These results are higher compared to the data taken from Claussen et al. obtained for bulk measurements. [33] Other groups showed that this effect is due to general differences between the mechanical testing setups. [37-39] Consequently we relied on the data of bulk tensile tests for further calculations. However, based on the performed indentation measurements we could not identify any stiffness gradient at the interface between soft and hard phase, as the modulus abruptly changes.

Next peak force tapping atomic force microscopy (AFM) allows for quantitative nanomechanical mapping (QNM) at nanometer lateral resolutions. [40-42] Consequently, this technique was applied to determine the Young's modulus and thickness of the oxide layer present on PDMS after UVO treatment. UVO-oxidized surfaces are assumed to show a vertical gradient in stiffness from the hard film to the soft substrate. Consequently, there is no distinct borderline but a declining interphase between layer and substrate. [43] This method enabled us to map areas of 20 µm x 20 µm at the interphase of bulk and oxidized PDMS. For this we took an oxidized and wrinkled sample and cut a cross profile at the layer edge from the sample middle with a scalpel. Afterwards a cryo-microtome was used to smoothen the surface (subsequent roughness: ~ 5 nm) followed by PF-QNM measurements (for detailed sample preparation see SI). The local maxima of Young's moduli for both hard and soft oxidized PDMS are found to be in the range of 90–100 MPa (Fig. 25). The effective layer thickness of the oxide-films was determined as the intersection of a linear fit of the gradient slope (green lines in Fig. 25) and the baseline of the profile (red lines). The resulting film thickness was determined to be 4.9 mm for hard and 5.7 mm for soft PDMS, respectively. Averaging the elastic constants allowed for estimation of the wrinkling wavelengths of the UVO oxidized samples. The averaging was performed by calculating the arithmetic mean of all Young's moduli from the layer top to its bottom. Doing so the average Young's modulus was determined to be 54.0 MPa for the oxidized layer on hard PDMS and 55.3 MPa on soft PDMS, respectively, which is compatible with the range found in literature. [44] The linear-like slope of hard PDMS is slightly steeper for soft PDMS. Most likely the less dense polymer network facilitates the ozone to penetrate deeper into the substrate. In general UVO results in a low degree of oxidation compared to plasma treated PDMS (0.4 GPa < E < 7.1 GPa) [44] or to glass (E ~ 73 GPa). [45]

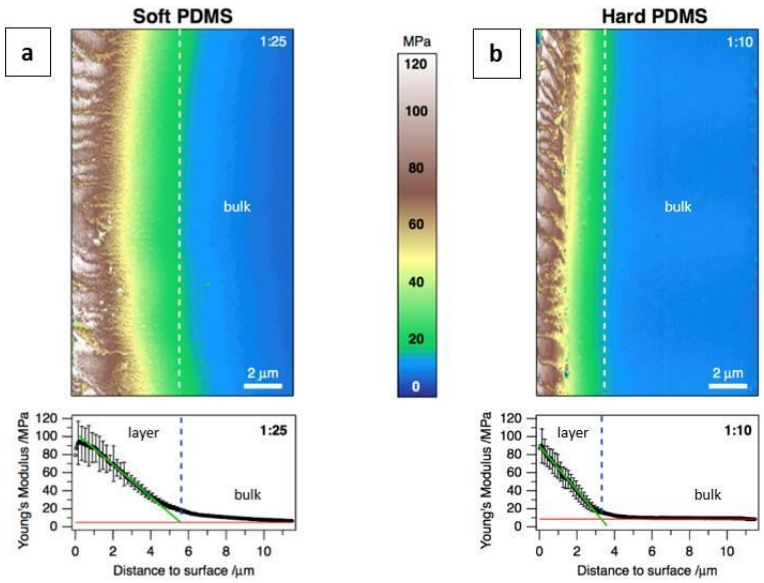

*Figure 25 | Peak Force QNM analysis: the terrain images are nanomechanical mappings of the Young's modulus at the bulk/oxide layer interphase of soft (**a**) and hard PDMS (**b**). Below are the according cross section profiles that were averaged over the whole image size consisting of 469 lines.*

Wrinkled surfaces were analyzed using a profilometer in order to determine the wavelengths of λ_{hard} = 46 µm and λ_{soft} = 72 µm. From the above discussed values the theoretical wavelength for the homogeneous samples were calculated according to Eq. 4.2 (in first order approximation) and compared to the experimentally determined wavelengths. Besides all known variables the Poisson's ratios used in 4.3) were set to 0.5 for PDMS and 0.17 for the oxidized, glassy film. Here, theory predicts wavelengths that are 30 % above our experimental results. Furthermore, we performed calculations based on a higher order approximation introduced by Jiang et al. [46] (Table 1). This approach also considers the effect of the applied strain on the wrinkle wavelength and amplitude as described in Eq. 4.4. Wrinkles always evolve at the same compression, if the stiffness values of layer and substrate are not modified. Nevertheless, further compression reduces the wavelength and increases the amplitude.

$$\lambda = \frac{\lambda_c}{(1+\varepsilon)\left(1+\frac{5\varepsilon(1+\varepsilon)}{32}\right)^{1/3}} \qquad (4.4)$$

Calculations based on Eq. 4.4 yields wavelengths of 39 mm for hard and 90 mm for soft PDMS (Table 2). In comparison to the simple approximation (Eq. 4.2), which significantly overestimates the wavelength, Eq. 4.4 yields wavelengths that are slightly reduced compared to the values determined experimentally. Thus the measured data are in better agreement with higher order approximation. We assume that the applied strain is

well-above the critical value resulting in creeping at least for the hard PDMS, causing better agreement with the Jiang's equation (Eq. 4.4).

Sample	$E_{Substrate}$ /MPa	$\lambda_{experiment}$ /µm	λ_1 (eqn. 2) /µm	σ /%	λ_2 (eqn. 4) /µm	σ /%
Hard PDMS	1.82 ± 0.04	46.00 ± 1.28	60.63	+ 31.80	38.96	- 15.30
Soft PDMS	0.24 ± 0.01	72.89 ± 6.05	139.67	+ 91.62	89.74	- 23.12

Table 1: Comparison of experimental findings and theoretical predictions for hard and soft PDMS samples

	$\lambda_{theoretical,homogenous}$ /µm	$\lambda_{heterogeneous}$ /µm	σ /%
Matrix (hard PDMS)	38.96	35.26 ± 0.96	- 9.50
Discrete Inclusion (soft PDMS)	89.74	45.60 ± 2.63	- 49.19

Table 2: Comparison of hard and soft PDMS calculations with the heterogeneous sample from Fig. 2

After this complete analysis of homogenous PDMS systems, we applied the results to the more complex embedded situation as sketched in Fig. 23. Table 2 compares the calculations according to Jiang and the values of elastic constants and layer thicknesses determined for the homogenous samples and experimental results performed for the composite sample. Both, hard matrix and discrete inclusion show smaller wavelengths (35 mm and 45 mm, respectively) than the equally stiff homogenous materials. However, the deviation in the hard matrix is not as pronounced as for the soft discrete inclusion. This difference is mainly caused by the complex stress/strain situation in the embedded sample: for the homogenous sample, the strain can be considered to be homogenous and directly related to the elongation of the sample in stretching direction. As defined by Hook's law stress is directly related to strain. The composite nature of the embedded sample however causes heterogeneity of the stress and strain. Neither can the local strain be inferred from the elongation of the sample, nor can stress be considered to be homogenous.

To gain a more quantitative picture of the stress/strain situation, mechanical finite element modelling was performed to understand the underlying mechanisms and distortions of the composite sample compared to homogenous PDMS. In a block of homogenous hard or soft PDMS the stress upon compression is distributed homogenously within the sample, as depicted in Fig. 26 **a**. In contrast the stress is not uniformly distributed for soft PDMS embedded in hard PDMS. The stress within the soft discrete inclusion is much lower than for the surrounding hard PDMS (Fig. 26 **a** and **c**). Furthermore, the stress within the hard matrix is focused at the sides of the inclusion leading to an increase from ~ 1.6 MPa (Fig. 26 **b**) to ~ 2.4 MPa (Fig. 26 **c**).

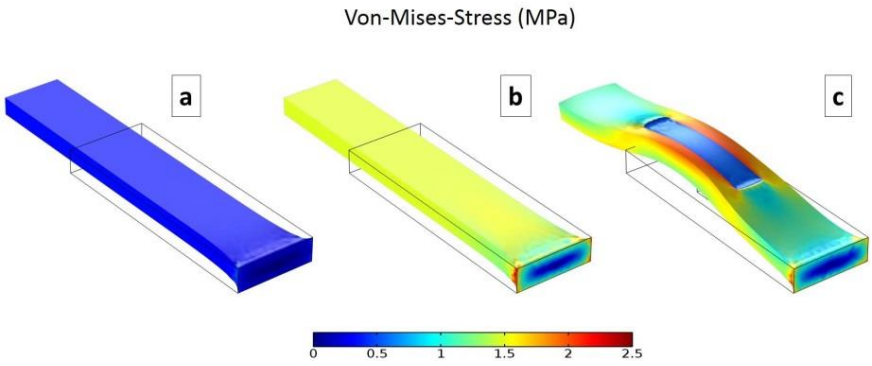

*Figure 26 | Mechanical simulations of neat, soft (**a**) respectively hard PDMS block (**b**) and a composite of soft block in a hard matrix (**b**). In all cases the initial dimensions of the outer block were set to 30 x 10 x 3 mm^3 indicated by the black box, in (**c**) the inner block is sized 10 x 5 x 1.5 mm^3, positioned lateral in the middle of the outer block, vertical on the upper side of it. The applied strain ε is set for all simulations to 50%. von-Misesstress distribution was modeled using COMSOL multiphysics with the same parameters as before except v_s, which was set to 0.499*

Stress and strain correlate over the Young's modulus according to $= \frac{\sigma}{E}$, as a consequence an increase of the applied stress leads to smaller wrinkle wavelengths when considering Eq. 4.4. This finding fits to our experimentally found data. Nevertheless it does not explain the shrinkage in wavelength for the soft PDMS. We identified two other potential reason for this observation: (1) an inhomogeneous stress distribution within the asymmetric matrix of soft PDMS (from all sides but one) causes a vertical distortion of the compressed sample, (2) changes in sample composition have however larger effects. Indentation measurements on unwrinkled composite substrates revealed differences in the Young's modulus compared to the neat samples. The soft phase is hardened from 0.65 to 0.8 MPa while at the same time the hard phase is slightly weakened from 2.9 to 2.5 MPa. These changes are most likely caused by diffusion of the Pt-catalyst from the hard into the soft phase either while gelation at room temperature and during thermal curing, respectively. In combination with the increase of stress within the matrix that is indicated by simulations the drastic changes in wavelength for both matrix and inner part can be explained.

Defect formation in gradient structures

The observed effects at the border between discrete inclusion and surrounding revealed that defects preferentially nucleate in close proximity to the mechanical transition. In order to study the underlying processes in more detail we substituted the discrete soft inclusion with a lateral, defined gradient in Young's modulus [33] and embedded it as before in a matrix of hard PDMS. Thus, the crossover from inclusion to matrix within this composite material is no longer at a fixed ratio between two stiffness values but changes gradually along the

substrate. The initial Young's modulus ratio is 1 : 5 and it decreases to a ratio of 1 : 1 at the hard end. At the interface bearing a Young's modulus ratio of 1 : 1 a similar wrinkle wavelength developed in both areas and no line-defects were observed (see Fig. 28 **a**). For the other cases, we defined a defect density by counting the number of waves in both areas from one to the next defect (Eq. 4.5). Dividing the counted number derived from the gradient by this of the matrix gives a defect density ratio σ_d defined by the number of waves in one repetitive unit n_i for the gradient and n_m for the matrix.

$$\sigma_d = \frac{n_i}{n_m} \qquad (4.5)$$

So at the center of the composite material the defect density from microscopy images is 0.83 (5 gradient waves divided by 6 matrix waves), with a measured modulus ratio of 1 : 2 (Fig. 28 **b**). The measured difference in wavelength by profilometry at the sample middle is as high as 43 ± 3 µm to 56 ± 2 µm, giving an average ratio of 0.77, so slightly lower. For the soft end however the defect density was determined to be 0.66 (Fig. 28 **c**) compared to 0.67 for profilometry, so in perfect agreement. These values are directly correlated with the change in wavelength and consequently the branching period. Furthermore, a drastic but uniform change of wavelength again indicates that no stiffness gradient perpendicular to the interface is present. Using numerical simulations for samples with a step-like transition function recover the same features and pinning of the line defects to the interface as observed experimentally. Fig. 28 **d** – **f** show patterns obtained by solving a generalized version of the Swift–Hohenberg equation [47] that includes both anisotropy [48] and a spatially periodic inhomogeneity (Eq. 4.6) [49] using the pseudo-spectral method and considering a flat surface with small noise as initial condition.

$$\partial_t u = [\varepsilon - (q^2(y) + \Delta)^2]\, u - W\, \partial_x^2\, \partial_y^2\, u - c\, \partial_y^4\, u - u^3 - 2\big(\partial_y u\big)\partial_y[q^2(y)] - u\, \partial_y^2[q^2(y)] \qquad (4.6)$$

u mimics the local height of the surface, *ε* is the dimensionless strain and the parameters *W* and *c* control the anisotropy of the system. We chose *W = 1* and *c = 0.5*. The spatially varying "natural" wavelength was set to be $\frac{2\pi}{q(y)}$. Perfectly aligned straight wrinkles (Fig. 28 **d**) are obtained for constant natural wavenumber *q* (Fig. 28 **g**). For a steep transition in wavenumber (Fig. 28 **h**) branching defects emerge (Fig. 28 **e**). The periodicity of these line-defects is further decreased resulting in higher branching density (Fig. 28 **f**) for increased values of the wavenumber jump (Fig. 28 **i**). Here, all the branching-defects are stationary and emerge spontaneously along the contact line between the two domains with different preferred wavenumbers. Those correspond well to the ratios determined experimentally at the middle end the soft end of the gradient, respectively.

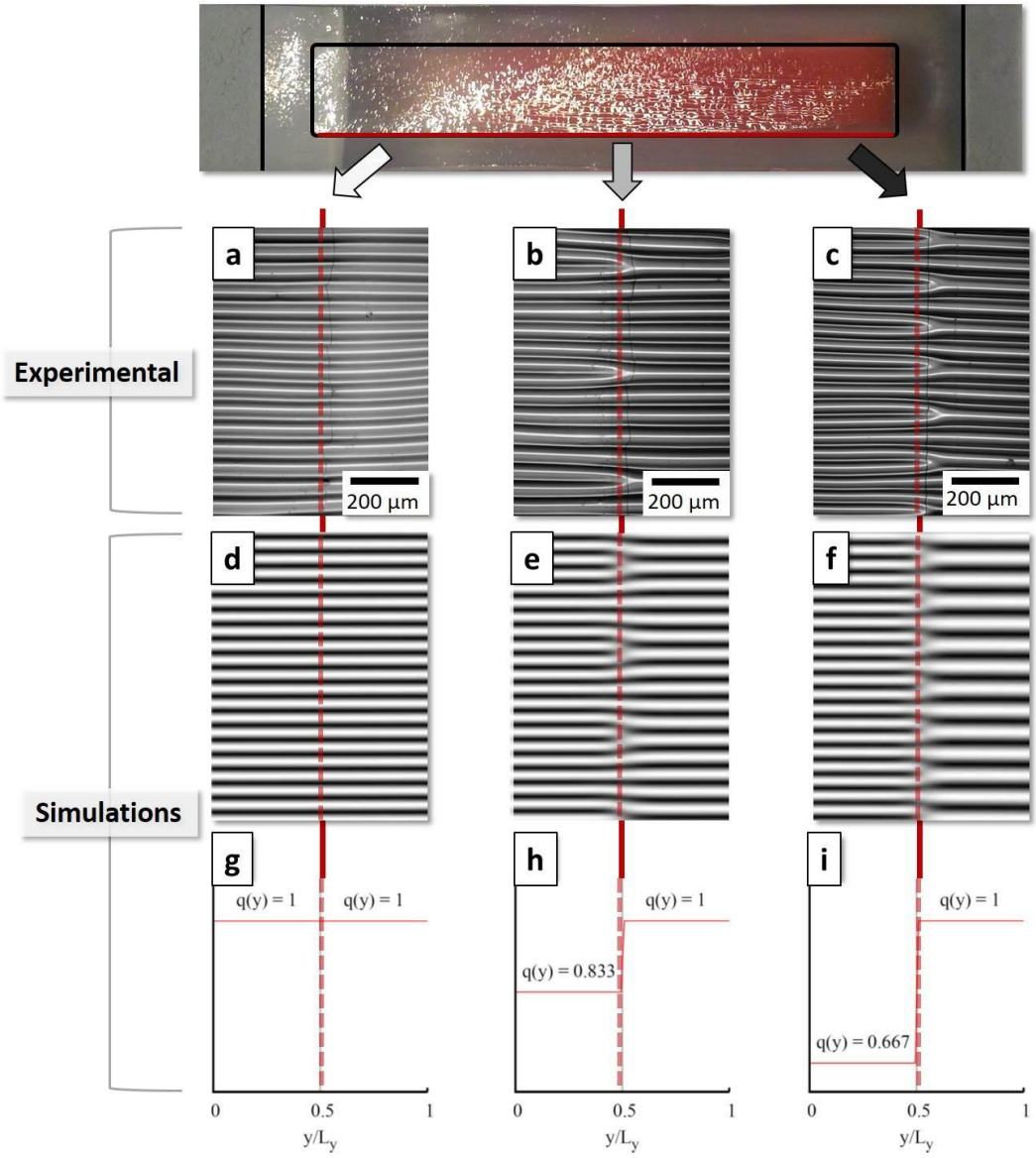

*Figure 27 | Branching points ordered along the gradient borderline with a jump in elasticity and wavenumber, respectively; (**a–c**) show experimental results, (**d–f**) the according simulations that are based on predetermined step-functions (**g–i**).*

The presented method has high potential for the systematic production of gradients and so not only for the aimed generation and understanding of ordered line branching structures. Beyond this the presented results might find application within the field of particle alignment. Controlled induction of line-defects can be used to break the symmetry within particle assemblies by generating Y-shaped particle lines. Furthermore, microfluidics might benefit from well-defined size- and angle-tunable channel junctions.

4.1.4. Conclusion

The objective of this work was the investigation of line defects observed in wrinkled substrates. Composite PDMS samples consisting of two covalently attached PDMS phases with different mechanical properties were prepared, wrinkled and analyzed. The predetermined change of substrate stiffness along the phase border resulted in different wavelengths caused by the buckling instability and so reinforced the wrinkles to branch more frequently here. Consequently the branches had a main orientation at the border, pointing from the soft side with large waves to the hard side, where shorter waves were found. The gradient sample showed an interesting behavior of oriented, patterned defects. We concluded that the stiffness difference of both substrate phases did match a value here that induced a whole-number ratio of the buckling instability. This was not observed in the sample with discrete, soft PDMS in the inclusion. In order to confront empirical wrinkling theories with our results, we had to measure h_F and E_F of the UVO-oxidized layer. Via Peak Force QNM we gained values of h_F = 4.9 – 5.7 µm and E_F = 54.0 MPa and 55.3 MPa, respectively. Wavelengths and amplitudes of the wrinkles were determined via profilometry resulting in 46 µm and 73 µm for the homogeneous samples, 35 µm and 45 µm in the heterogeneous system with just hard and soft PDMS respectively 51 µm and 63 µm in the gradient system. A mechanical stress simulation revealed an increase in the surface stress distribution around the embedded discrete inclusion that induces a wave shortage. In the wider dimensioned gradient sample this problem was less pronounced. Summarized the system presented in this paper has a high potential for ordering defects in a patterned way and beyond to keep the adjacent wrinkled areas defect-free.

Our findings increase the understanding of the formation of defects in controlled wrinkling systems. One application that may use line defects of adjustable number and direction is the generation of size- and angle-tunable channel junctions for microfluidic devices. Two waves terminating into one act as the micro-channel junction that may be sealed on top with another layer of PDMS or glass. Another application might be the organization of nanoparticles onto well-defined, equi-distant Y-shaped templates. Stamping these assemblies onto a flat substrate creates lines of particles that split on predefined positions. This might be useful for light management in nanophotonics.

Acknowledgements

We thank M. Lehmann for Peak Force QNM measurements as well as M. P. Neubauer for indentation measurements. Also we thank the European Research Council for financing this work within the Starting Grant Project ERC-2012-StG 306686 METAMECH. M. Tebbe was supported by the Elite Network Bavaria in the frame of the Elite Study Program “Macromolecular Science” and funded via a grant for PhD candidates according to Bavarian elite promotion law (BayEFG).

4.1.5. Supporting Information

Experimental

PDMS solution

The substrates were prepared with commercially available Sylgard 184 PDMS by Dow Corning Ltd, Midland, USA. A well-dispersed and degassed mixture of 20 g pre-polymer and 2 g curing agent was used for 1:10 ratio as well as 25 g pre-polymer with 1 g curing agent for 1:25 ratio.

Homogeneous samples

1:10 and 1:25 PDMS were cast each in a 10 cm x 10 cm Polystyrene (PS)-mold, set for 24 h at RT (48 h, respectively) and subsequently cured for 4 h at 80 °C. Stripes of 4.5 cm x 1 cm x 0.16 cm (resp. 0.17 cm) were cut out, ultrasonicated in Milli-Q H_2O for 10 min and dried with N_2.

1:25 Inclusion in 1:10 matrix

A 1:10 stripe from the homogeneous sample preparation was punched out in the size of 1 cm x 0.5 cm right in the middle. The hole was filled with 1:25 PDMS solution just to level out with the surrounding matrix and allowed to set for 48 h at RT. Afterwards another 1:10 layer of 0.1 cm thickness was cast on top, set for 24 h at RT and then cured at 80 °C for 5 h. Eventually the stripe was ultrasonicated in Milli-Q H_2O for 10 min and dried with N_2.

Gradient inclusion in 1:10 matrix

1:10 PDMS was cast into a 14 cm diameter glass petri dish to fill it up for 2 mm. It was allowed to set for 24 h. A 7 cm x 1 cm hole was punched out from the middle and filled with a slightly modified gradient of Claussen et al. [33] with halved casting speed to reach a doubled layer thickness. After setting at RT for 48 h another layer of 1:10 was cast on top of gradient and matrix with a height of 1 mm. It was allowed to set for 24 h at RT followed by curing at 80 °C for 4 h. Afterwards the gradient with surrounding matrix was cut out to give a sample of 11 cm overall length and 3 cm overall width, so 2 cm of protruding matrix on the long sides respectively 1 cm on the short sides. The sample was ultrasonicated in Milli-Q H_2O for 10 min and dried with N_2.

Wrinkle generation

The stripes from the above described preparation were attached to a custom-made stretching device, strained by 50 % and placed in a UV/Ozone (UVO)-cleaner (Novascan PSD-UV 8, Novascan Technologies, Ames, USA) for 90 min. All samples were oxidized at their contact face with the glass petri dish. This was to ensure a levelled

interface of inclusion and matrix and for reproducibility. The stress then was released instantaneously and wrinkles did form immediately. For the wrinkling process all samples were oxidized at their bottom sides.

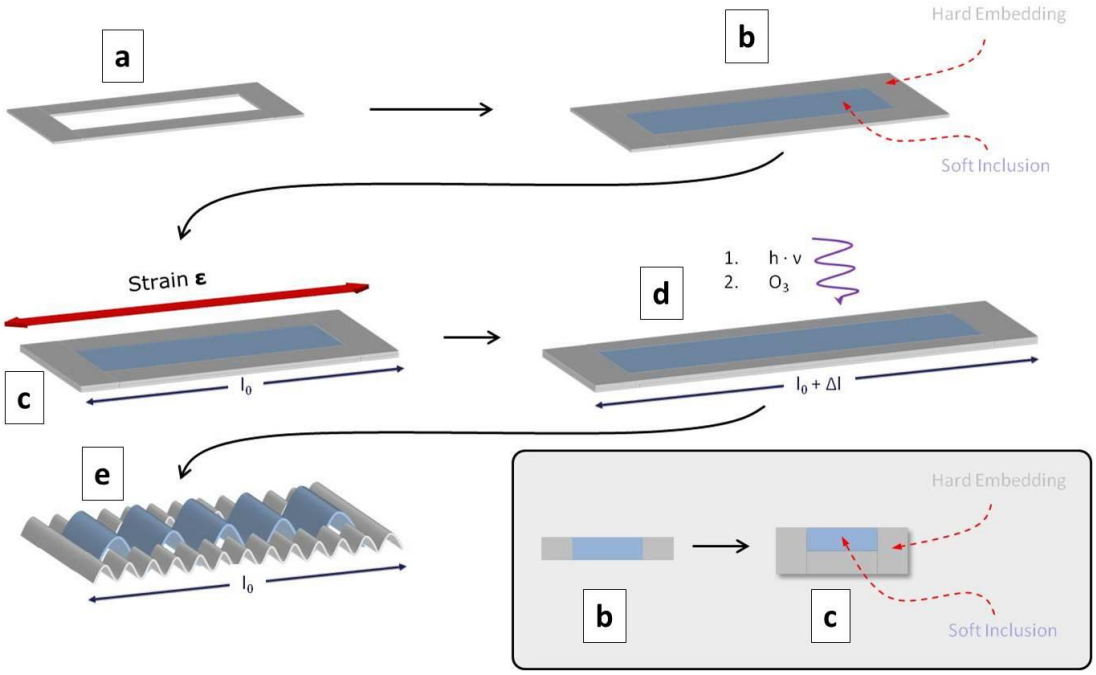

*Figure 28 | Heterogeneous sample preparation for a soft inclusion into a hard matrix. (**a**) RT-set, hard PDMS becomes punched out and filled with soft PDMS (**b**), followed by a cover layer over hard and soft (**b** → **c**). The sample then is strained (**c**), UVO-oxidized (**d**) and strain-released (**e**) to form wrinkles.*

Characterization

Three different qualitative and quantitative methods were used for characterizing the formed morphologies as well as mechanical properties, namely reflected light microscopy, profilometry and Peak Force QNM.

Optical microscopy

Optical microscopy was performed with Axiovert 200, Carl Zeiss GmbH (Jena, Germany), equipped with a Plan-Apochromat 10x / 0.25 lens, a Axiomcam ERc 5s computer-controlled camera and AxioVision V. 4.8.2.0 (2010, Carl Zeiss MicroImaging GmbH, Jena, Germany) analysis software.

Profilometry

Measurements were done with a Dektak 150 Profilometer from Veeco (Plainview, USA) with following boundary conditions: stylus force = 1 mg for 1:10 and 0.05 mg for 1:25, a stylus radius of 2.5 µm (N-Lite sensor) and a scan length of 500 µm for each measurement.

Peak-Force QNM

Layer thickness and nano-mechanical measurements were performed with a Dimension V Icon AFM (Bruker, Karlsruhe, Germany) with Peak-Force QNM software on a 20 µm x 20 µm area with 512 samples / line, Peak-Force set point = 0.15 V, driving amplitude = 150 V and tip radius = 5 nm.

Simulations

Wrinkling and branching property simulations were performed by solving a modified Swift-Hohenberg-Equation with initial surface noise.

Microscopy setup for in-situ analysis

In-situ measurements were accomplished with a custom-made stretching setup that allows control over strain and relaxation speed of the sample, respectively. It is schematically depicted in Fig. 29. In order to ensure that a fixed section of the sample's surface may be observable throughout all the relaxation process, both ends of the clamping device were designed to move uniformly. This requires thoroughly focusing on the sample middle. An exemplary recorded video is also available within the ESI.

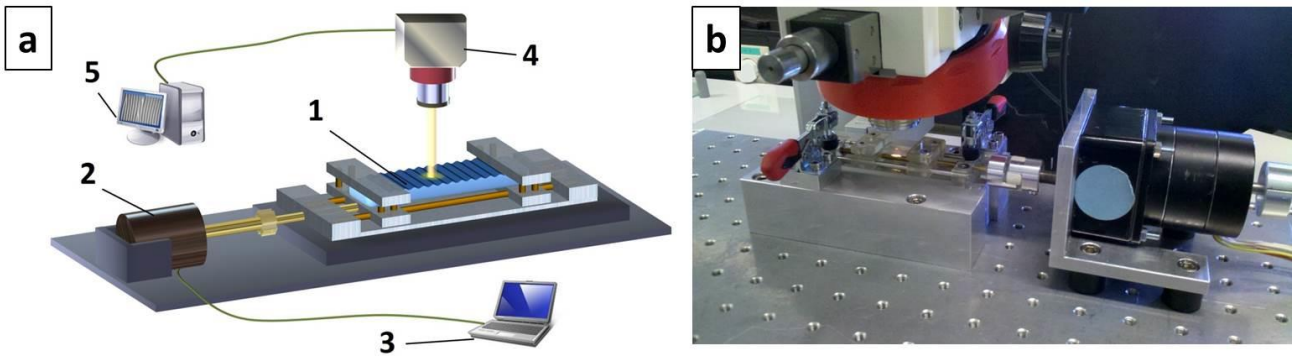

*Figure 29 | Reflected Light Microscopy setup for in-situ observations of the wrinkle formation schematically (**a**) and real (**b**). (**1**) custom-made stretching device with UVO-oxidized sample, (**2**) step motor to adjust the relaxation speed, (**3**) computer control for step-motor , (**4**) reflected light microscope with attached video camera, (**5**) computer control for microscope and camera*

During the relaxation process the speed is set to 6.1 mm/min at an initial clamping length of 15 mm respectively 22.5 mm for the stretched state (ε = 50%). The samples were not strain released back to the initial length to avoid cracking of the film or bulging of the sample. For the latter also the focus would have been lost. In most cases impurities on the PDMS surface were used to focus. Only in few cases it was possible without.

Peak Force QNM

For Peak-Force the UVO-oxidized and wrinkled samples were prepared in the following way: In step 1 a cross profile at the layer edge was cut from the sample middle with a scalpel. For step 2 a cryomikrotome was used to smoothen surface (subsequent roughness: ~ 5nm). In the final step 3 the surface was analyzed with Peak-Force QNM and optical microscopy.

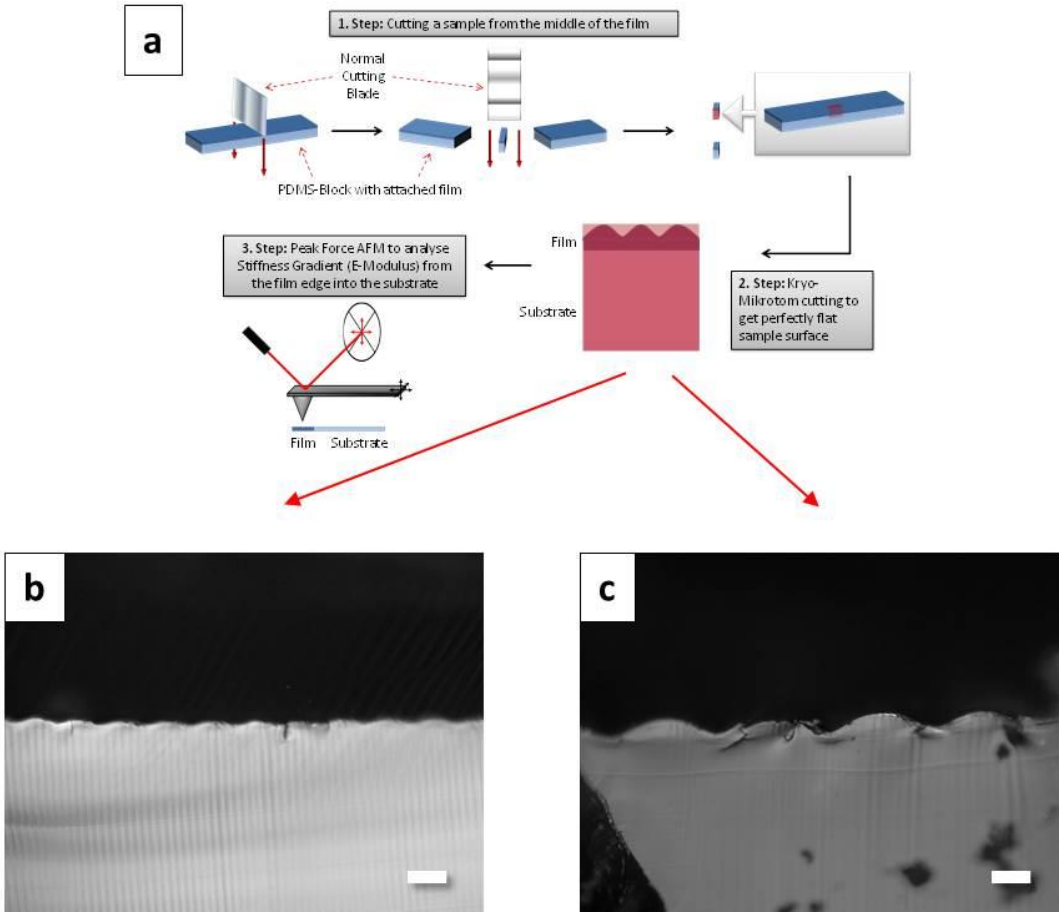

*Figure 30 | (**a**) Preparation of a UVO-oxidized and wrinkled sample for Peak-Force QNM analysis. (**b**) and (**c**): optical microscopy images of the cross profiles from hard (**b**) and soft PDMS (**c**); scale bar length is 100 µm.*

Wrinkling with a lateral gradient

As for pure PDMS and the composite sample we also performed profilometry measurements to compare given Eq. 1 – 4 with experimental data. The wrinkles show an exponential increase that can be explained by the process of gradient preparation where hard and soft PDMS tend to diffuse into each other. [33] The results fit well to theoretical predictions, especially when compared to the samples with a neat soft inclusion. Fig. 31 shows the results of wavelength and amplitude variation from the gradient's hard end (left, 1 cm) to its soft end (right, 6 cm). A slight increase of λ and A is recognizable that were fitted with exponential growth functions.

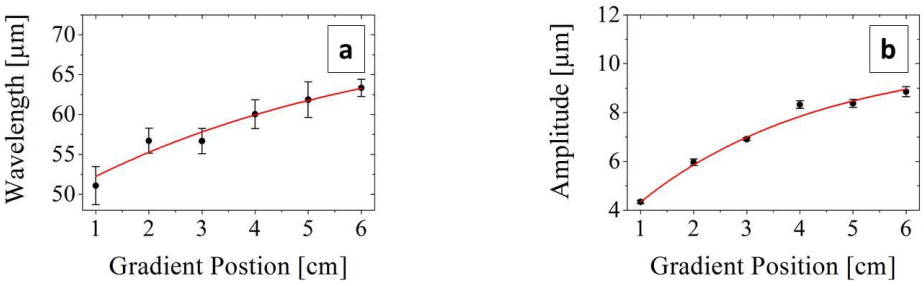

*Figure 31 | Modification of λ (**a**) and A (**b**) along the gradient*

Gradient Position	Theoretical λ /µm	λ on Gradient /µm	Deviation /%
1 cm	44.90	51.07 ± 2.40	+ 13.74
6 cm	76.91	63.34 ± 1.07	- 17.64

Table 3 | Comparison of theoretical values for λ (derived from Table 2) with the gradient's hard left and soft end right, respectively; the applied strain is ε = 20 %.

Those slighter deviations can be explained with the different sizes of the samples, as the gradient has distinctly larger dimensions of 90 mm x 40 mm x 3 mm compared to 30 mm x 10 mm x 3 mm for the two-phase-system. It is also the reason, why only 20 % strain were applied: Strain and stress within the sample are connected over $= \frac{\varepsilon}{A}$, where A is larger in the gradient than in the composite (12 mm^2 respectively 2.7 mm^2). A strain of 50 % would therefore have led to a rupture of the sample.

Double gradient along the soft-to-hard-crossover

In contrast to distinct interfaces as shown in the paper itself a few number of sample areas showed diffuse transition between both composite materials, where the transition spreads over several 100 µm. This is due to a partially tilted cut during the sample preparation. Soft and hard PDMS may flow underneath each other and create a blurred stiffness interface. It generates a second gradient, however rectangular to the first and in a much shorter length scale. It features interesting effects, as within these regions the line-defect formation between hard and soft phase took place in a quantized manner, meaning defects did not occur randomly along the short gradient but in bands lateral to the wrinkling direction (Fig. 32 **a**). We also employed numerical simulations on this behavior, where (y) was used to generate an imposed wavenumber (Fig. 32 **c**) that increases linearly along the short gradient. Simulations revealed a similar behavior in branching (Fig. 32 **b**), which allowed only few, quantized wavelengths for different gradient slopes and heights. Thus, simulations performed for distinct jumps in the wavelength are in good agreement with the experimentally determined values with slight deviations in the branch positions and step widths.

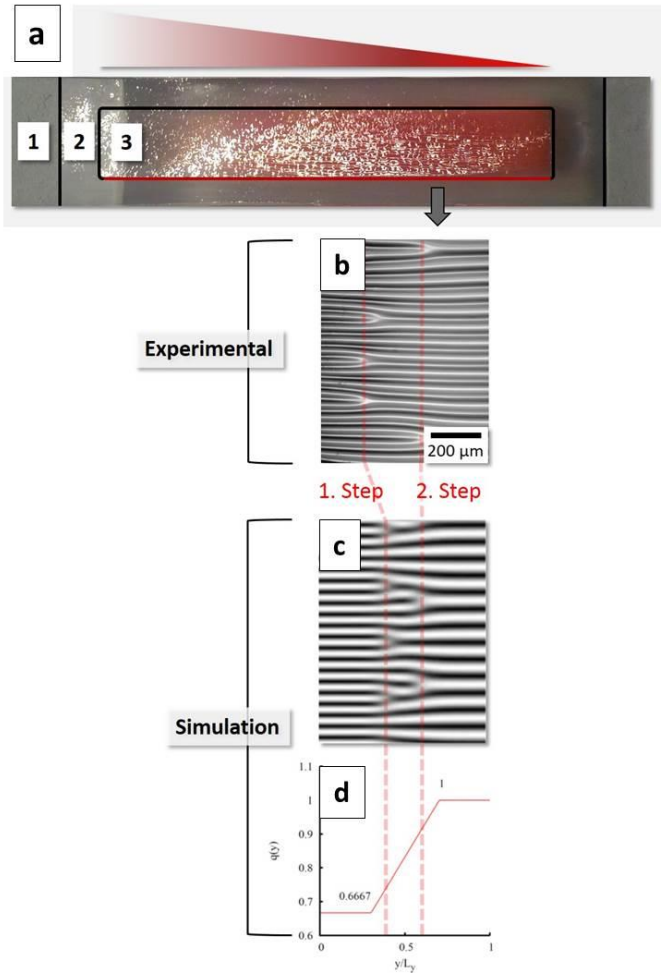

*Figure 32 | (**a**) Photo of the gradient sample; (**1**) shows the unwrinkled matrix, where the sample was clamped for stretching, (**2**) the wrinkled matrix and (**3**) the gradient with a stiffness decrease from left (translucent) to right (red dyed). (**b**) Microscopy image of disordered branching over two steps, (**c**) numerical simulation (**d**) with a predetermined linear increase of q(y) over a given gradient length L_y*

Specific wrinkling

A side aspect of heterogeneous substrates is the ability of specifically wrinkling just one of the participating PDMS phases. According to $\varepsilon_c = \frac{\sigma_c}{\bar{E}_f} = \frac{1}{4}\left(\frac{\bar{E}_s}{3\bar{E}_l}\right)^{2/3}$ the Young's moduli of layer and substrate influence the critical strain required for wrinkling. Providing that both hard and soft PDMS get oxidized equally and so $\bar{E}_f$ is constant, their difference in $\bar{E}_s$ can be measured directly. In this experiment the strain was set to ε = 10%, with plain strain moduli of the soft substrate being $\bar{E}_{sS}$: 0.3 MPa and for the hard substrate $\bar{E}_{hS}$: 2.5 MPa. The film's modulus $\bar{E}_f$ had to be determined in a subsequent measurement and was roughly estimated to 25 MPa. According to this a hard substrate starts to wrinkle not before ε_c = 10.9%, while the soft one buckles already at a critical strain ε_c of 2.5%. We found the expected wrinkling behavior (Fig. 33), with a well-defined crossover from the hard, unwrinkled to

the soft and wrinkled PDMS. The surface corrugations at the boundary of soft and hard substrates induce a stress-field in the hard elastomer. Initial waves form close to the crossover, though they completely flatten out in a range of ~ 50 µm. The result is a chemically homogeneous surface, which is in parts mechanically modified.

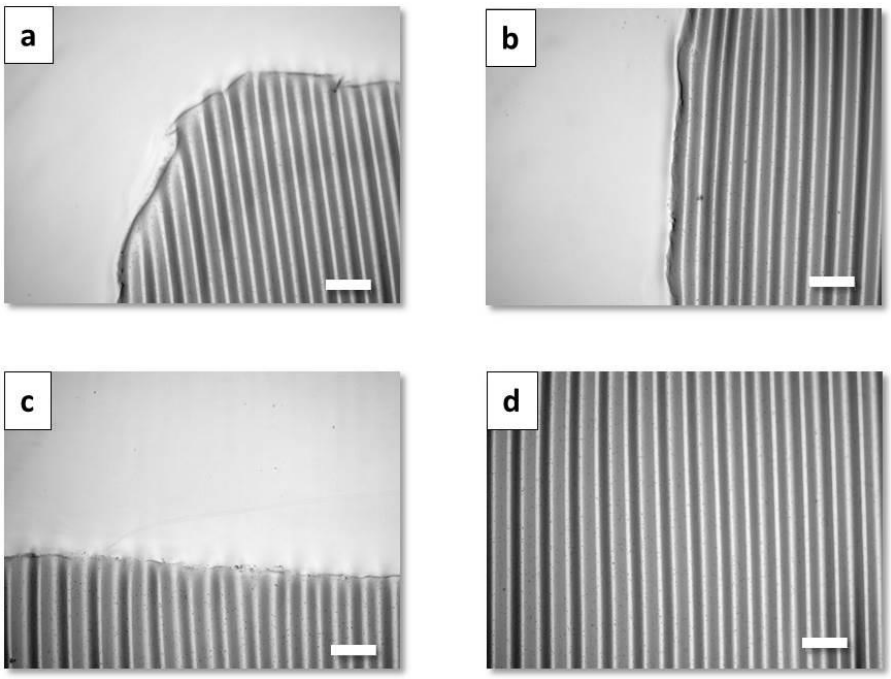

*Figure 33 | Wrinkled soft inclusion surrounded by an unwrinkled hard matrix; at the inclusion edge (**a**), the vertical and horizontal boundary lines (**b** and **c**) and inside the inclusion (**d**) with an average wavelength of 65 µm and an amplitude of 3 µm; scale bar length is 100 µm.*

References

[1] P. Yamato, B.J.P. Kaus, F. Mouthereau and S. Castelltor: Dynamic constraints on the crustal-scale rheology of the Zagros fold belt, Iran, **2011**; *Geology*, 39 - 9, 815-818

[2] B. Prüm, H. Florian Bohn, R. Seidel, S. Rubach and T. Speck: Plant surfaces with cuticular folds and their replicas: Influence of microstructuring and surface chemistry on the attachment of a leaf beetle, **2013**; *Acta Biomater.*, 9 - 5, 6360-6368

[3] C.D. Reuther: Grundlagen der Tektonik: Kräften und Spannungen der Erde auf der Spur, **2018**, Springer Berlin Heidelberg

[4] A. Mohamed: Die Krusten der Ränder der Fayoum-Depression – Geomorphologische Untersuchungen (Band 1), **2003**, Faculty of Geological Sciences, Ludwig-Maximilian-University Munich, Munich, Germany

[5] M. Berneburg, H. Plettenberg and J. Krutmann: Photoaging of human skin, **2000**; *Photoderm. Photoimm. Photomed.*, 16 - 6, 239-244

[6] H. Vandeparre, M. Piñeirua, F. Brau, B. Roman, J. Bico, C. Gay, W. Bao, C.N. Lau, P.M. Reis and P. Damman: Wrinkling Hierarchy in Constrained Thin Sheets from Suspended Graphene to Curtains, **2011**; *Phys. Rev. Lett.*, 106 - 22, 224301

[7] J. Genzer and J. Groenewold: Soft matter with hard skin: From skin wrinkles to templating and material characterization, **2006**; *Soft Matter*, 2 - 4, 310-323

[8] C. Jiang, S. Singamaneni, E. Merrick and V.V. Tsukruk: Complex Buckling Instability Patterns of Nanomembranes with Encapsulated Gold Nanoparticle Arrays, **2006**; *Nano Lett.*, 6 - 10, 2254-2259

[9] D.-Y. Khang, J.A. Rogers and H.H. Lee: Mechanical Buckling: Mechanics, Metrology, and Stretchable Electronics, **2009**; *Adv. Funct. Mater.*, 19 - 10, 1526-1536

[10] A. Schweikart and A. Fery: Controlled wrinkling as a novel method for the fabrication of patterned surfaces, **2009**; *Microchimica Acta*, 165 - 3, 249-263

[11] S. Singamaneni and V.V. Tsukruk: Buckling instabilities in periodic composite polymeric materials, **2010**; *Soft Matter*, 6 - 22, 5681-5692

[12] C.J. Young, N.A. J. and S.C. M.: Surface Wrinkling: A Versatile Platform for Measuring Thin-Film Properties, **2011**; *Adv. Mater.*, 23 - 3, 349-368

[13] M. Pretzl, A. Schweikart, C. Hanske, A. Chiche, U. Zettl, A. Horn, A. Böker and A. Fery: A Lithography-Free Pathway for Chemical Microstructuring of Macromolecules from Aqueous Solution Based on Wrinkling, **2008**; *Langmuir*, 24 - 22, 12748-12753

[14] F.A. Bayley, J.L. Liao, P.N. Stavrinou, A. Chiche and J.T. Cabral: Wavefront kinetics of plasma oxidation of polydimethylsiloxane: limits for sub-µm wrinkling, **2014**; *Soft Matter*, 10 - 8, 1155-1166

[15] K. Efimenko, M. Rackaitis, E. Manias, A. Vaziri, L. Mahadevan and J. Genzer: Nested self-similar wrinkling patterns in skins, **2005**; *Nat. Mat.*, 4 - 293

[16] C.J. Rand, R. Sweeney, M. Morrissey, L. Hazel and A.J. Crosby: Fracture-induced alignment of surface wrinkles, **2008**; *Soft Matter*, 4 - 9, 1805-1807

[17] J. Rodríguez-Hernández and A. del Campo: Fabrication of hierarchical wrinkled morphologies through sequential UVO treatments, **2015**; *J. Appl. Polym. Sci.*, 132 - 17,

[18] M. Watanabe and K. Mizukami: Well-Ordered Wrinkling Patterns on Chemically Oxidized Poly(dimethylsiloxane) Surfaces, **2012**; *Macromol.*, 45 - 17, 7128-7134

[19] H. Vandeparre, J. Léopoldès, C. Poulard, S. Desprez, G. Derue, C. Gay and P. Damman: Slippery or Sticky Boundary Conditions: Control of Wrinkling in Metal-Capped Thin Polymer Films by Selective Adhesion to Substrates, **2007**; *Phys. Rev. Lett.*, 99 - 18, 188302

[20] D.U. Ahn, Z. Wang, R. Yang and Y. Ding: Hierarchical polymer patterns driven by capillary instabilities at mobile and corrugated polymer–polymer interfaces, **2010**; *Soft Matter*, 6 - 19, 4900-4907

[21] G. Miquelard-Garnier, A.B. Croll, C.S. Davis and A.J. Crosby: Contact-line mechanics for pattern control, **2010**; *Soft Matter*, 6 - 22, 5789-5794

[22] Y. Xuan, X. Guo, Y. Cui, C. Yuan, H. Ge, B. Cui and Y. Chen: Crack-free controlled wrinkling of a bilayer film with a gradient interface, **2012**; *Soft Matter*, 8 - 37, 9603-9609

[23] W.P. Lee and A.F. Routh: Why Do Drying Films Crack?, **2004**; *Langmuir*, 20 - 23, 9885-9888

[24] S. Frank, U.A. Handge, S. Olliges and R. Spolenak: The relationship between thin film fragmentation and buckle formation: Synchrotron-based in situ studies and two-dimensional stress analysis, **2009**; *Acta Mater.*, 57 - 5, 1442-1453

[25] J.Y. Chung, J.-H. Lee, K.L. Beers and C.M. Stafford: Stiffness, Strength, and Ductility of Nanoscale Thin Films and Membranes: A Combined Wrinkling–Cracking Methodology, **2011**; *Nano Lett.*, 11 - 8, 3361-3365

[26] J. Gao, K. Pei, T. Sun, Y. Wang, L. Zhang, W. Peng, Q. Lin, M. Giersig, K. Kempa, Z. Ren and Y. Wang: Metallic Nanowire Networks: Transparent Nanowire Network Electrode for Textured Semiconductors (Small 5/2013), **2013**; *Small*, 9 - 5, 732-732

[27] B. Han, K. Pei, Y. Huang, X. Zhang, Q. Rong, Q. Lin, Y. Guo, T. Sun, C. Guo, D. Carnahan, M. Giersig, Y. Wang, J. Gao, Z. Ren and K. Kempa: Uniform Self-Forming Metallic Network as a High-Performance Transparent Conductive Electrode, **2014**; *Adv. Mater.*, 26 - 6, 873-877

[28] N. Stoop, R. Lagrange, D. Terwagne, P.M. Reis and J. Dunkel: Curvature-induced symmetry breaking determines elastic surface patterns, **2015**; *Nat. Mat.*, 14 - 337

[29] A. Ahmadivand and S. Golmohammadi: Comprehensive investigation of noble metal nanoparticles shape, size and material on the optical response of optimal plasmonic Y-splitter waveguides, **2014**; *Opt. Comm.*, 310 - 1-11

[30] C.P. Ody, C.N. Baroud and E. de Langre: Transport of wetting liquid plugs in bifurcating microfluidic channels, **2007**; *J. Colloid Interface Sci.*, 308 - 1, 231-238

[31] N. Bowden, W.T.S. Huck, K.E. Paul and G.M. Whitesides: The controlled formation of ordered, sinusoidal structures by plasma oxidation of an elastomeric polymer, **1999**; *Appl. Phys. Lett.*, 75 - 17, 2557-2559

[32] R. Huang: Kinetic wrinkling of an elastic film on a viscoelastic substrate, **2005**; *J. Mech. Phys. Sol.*, 53 - 1, 63-89

[33] K.U. Claussen, M. Tebbe, R. Giesa, A. Schweikart, A. Fery and H.-W. Schmidt: Towards tailored topography: facile preparation of surface-wrinkled gradient poly(dimethyl siloxane) with continuously changing wavelength, **2012**; *RSC Advances*, 2 - 27, 10185-10188

[34] P. Ball: Branches: Nature's patterns: a tapestry in three parts, **2009**, OUP Oxford

[35] L. Zhong, Z. Shen, Z. Pengfei, Y. Dayong, J. Gang and M. Hongwei: Surface initiated polymerization from integrated poly(dimethylsiloxane) enables crack-free large area wrinkle formation, **2012**; *Polym. Adv. Technol.*, 23 - 9, 1240-1245

[36] C.M. Stafford, C. Harrison, K.L. Beers, A. Karim, E.J. Amis, M.R. VanLandingham, H.-C. Kim, W. Volksen, R.D. Miller and E.E. Simonyi: A buckling-based metrology for measuring the elastic moduli of polymeric thin films, **2004**; *Nat. Mat.*, 3 - 545

[37] A. Mata, A.J. Fleischman and S. Roy: Characterization of Polydimethylsiloxane (PDMS) Properties for Biomedical Micro/Nanosystems, **2005**; *Biomed. Microdevices*, 7 - 4, 281-293

[38] C.C. White, M.R. VanLandingham, P.L. Drzal, N.-K. Chang and S.-H. Chang: Viscoelastic characterization of polymers using instrumented indentation. II. Dynamic testing*, **2005**; *J. Polym. Sci., Part B: Polym. Phys.*, 43 - 14, 1812-1824

[39] J.-H. Seo, K. Sakai and N. Yui: Adsorption state of fibronectin on poly(dimethylsiloxane) surfaces with varied stiffness can dominate adhesion density of fibroblasts, **2013**; *Acta Biomater.*, 9 - 3, 5493-5501

[40] B. Foster: New Atomic Force Microscopy(AFM) Approaches Life Sciences Gently, Quantitatively, and Correctively, **2012**; *Am. Lab.*, 4 - 24 - 28

[41] P. Trtik, J. Kaufmann and U. Volz: On the use of peak-force tapping atomic force microscopy for quantification of the local elastic modulus in hardened cement paste, **2012**; *Cem. Concr. Res.*, 42 - 1, 215-221

[42] C. Kuttner, M. Tebbe, H. Schlaad, I. Burgert and A. Fery: Photochemical Synthesis of Polymeric Fiber Coatings and Their Embedding in Matrix Material: Morphology and Nanomechanical Properties at the Fiber–Matrix Interface, **2012**; *ACS Appl. Mat. Interf.*, 4 - 7, 3484-3492

[43] C. Kuttner, A. Hanisch, H. Schmalz, M. Eder, H. Schlaad, I. Burgert and A. Fery: Influence of the Polymeric Interphase Design on the Interfacial Properties of (Fiber-Reinforced) Composites, **2013**; *ACS Appl. Mat. Interf.*, 5 - 7, 2469-2478

[44] S. Béfahy, P. Lipnik, T. Pardoen, C. Nascimento, B. Patris, P. Bertrand and S. Yunus: Thickness and Elastic Modulus of Plasma Treated PDMS Silica-like Surface Layer, **2010**; *Langmuir*, 26 - 5, 3372-3375

[45] S. Inaba, S. Fujino and K. Morinaga: Young's Modulus and Compositional Parameters of Oxide Glasses, **1999**; *J. Am. Ceram. Soc.*, 82 - 12, 3501-3507

[46] H. Jiang, D.-Y. Khang, J. Song, Y. Sun, Y. Huang and J.A. Rogers: Finite deformation mechanics in buckled thin films on compliant supports, **2007**; *Proc. Nat. Acad. Sci.*, 104 - 40, 15607-15612

[47] J. Swift and P.C. Hohenberg: Hydrodynamic fluctuations at the convective instability, **1977**; *Physical Review A*, 15 - 1, 319-328

[48] W. Pesch and L. Kramer: Nonlinear analysis of spatial structures in two-dimensional anisotropic pattern forming systems, **1986**; *Zeitschrift für Physik B Condensed Matter*, 63 - 1, 121-130

[49] B. Kaoui, A. Guckenberger, A. Krekhov, F. Ziebert and W. Zimmermann: Coexistence of stable branched patterns in anisotropic inhomogeneous systems, **2015**; *New J. Phys.*, 17 - 10, 103015

4.2. Publication – The influence of plasma treatment on the elasticity of the in situ oxidized gradient layer in PDMS: towards crack-free wrinkling

4.2.1. Abstract

Controlled surface wrinkling is widely applied for structuring surfaces in the micro- and nano-range. The formation of cracks in the wrinkling process is however limiting applications, and developing approaches towards crack-free wrinkles is therefore vital. To understand crack-formation, we systematically characterized the thickness and mechanics of thin layers formed by O_2-plasma-oxidation of polydimethyl siloxane (PDMS) as a function of plasma power and pressure using Atomic Force Microscopy Quantitative Nano-mechanical Mapping (AFM-QNM). We found a nearly constant layer thickness with simultaneously changing Young's moduli for both power and pressure screenings. We determined the respective crack densities, revealing conditions for crack-free wrinkling. Thus we could identify correlations between the intensity of plasma treatment and the cracking behavior. The primary cause for crack-suppression is a continuous elasticity gradient starting within the soft bulk PDMS, and rising up to several hundred MPa at the oxidized layer's surface. With mechanical simulations via the Finite Elements Method (FEM) we were able to demonstrate a noticeable difference in maximal stress intensity σ_{max} between a comparable, but theoretical single layer and a gradient interface. A threshold in tensile stress of σ_{crit} = 14 MPa distinguishes between intact and cracked layers.

4.2.2. Introduction

Nano-structured surfaces have recently made great impact on scientific and industrial applications, such as, e.g., adaptive surfaces for improved heat transfer [1] or friction reduction. [2] These structures share the ability to enhance the properties of existing surface systems, [3] or to even create desired properties which an unstructured surface could not exhibit. [4] The approaches to fabricate nano-structured surfaces are diverse, such as physical or chemical vapor deposition, chemical etching and photolithography. Photolithography in particular offers high order parameters and low defect densities; nevertheless the method is accompanied by disadvantages such as size limitations, elaborate setups and slow and expensive production. [5] Therefore soft-lithographic methods have attracted great interest, as diverse approaches to pattern surfaces are accessible, such as micro-contact-printing, [6] laser-interference-lithography, [7] or controlled wrinkling, with the last approach being the focus of the present paper. [8] Wrinkles develop if a strained elastomer is in strong adhesive contact with a comparably thin, stiff layer. When the bilayer system is subjected to in-plane compression, wrinkles will form as a consequence of the mechanical mismatch between the thin layer and the thick substrate. Wrinkle assisted pattern formation is cheap, has low instrumentation requirements and is well scalable. Wrinkles can be formed unordered or – by applying a defined stress-field – ordered as well, with well-defined wavelengths. [8-12] Wrinkle-structured surfaces have found applications in micro-fluidic devices, [13] stretchable electronics, [14] optics for micro-lens arrays, [15] or

templates for the self-assembly of particles. [16, 17] Controlled surface wrinkling however is accompanied by defect structures, such as line defects and surface cracks. While line defects can in some cases be used for introducing hierarchical patterning, [18-23] in most cases especially cracking is undesired and several groups have reported protocols for reducing crack formation. Fig. 34 schematically shows the fabrication of wrinkles, with two possible outcomes: as cracked surfaces (upper path) or uncracked surfaces (lower path).

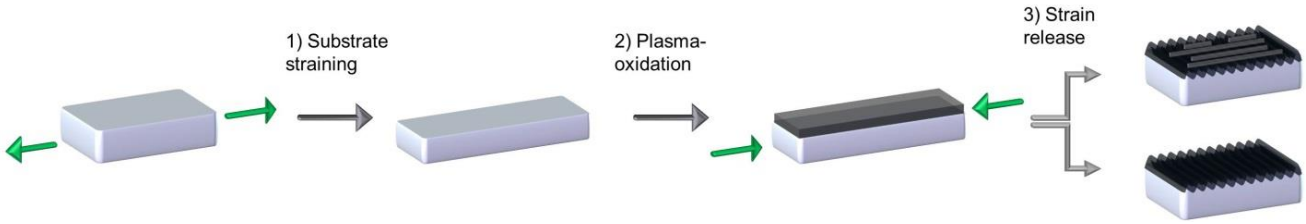

Figure 34 | Schematic description of the wrinkling process. In step 1 the elastomeric substrate becomes stretched to a pre-defined strain, followed by the in situ plasma oxidation in step 3. In the final step 3 wrinkles are formed and – in case a critical mechanical tension in the interface of layer and substrate is exceeded – cracks form as well.

For cracking defects, methods have been presented that are able to avoid such defects, e.g. with UV-curable systems. Xuan et al. synthesized a UV-curable acrylated polydimethylsiloxane with an acrylate cross-linker, [24] Park et al. used tetraethylene glycol diacrylate and tetraethylene glycol bis(4-ethenyl-2,3,5,6-tetrafluorophenyl) as the UV-curable polymer, [25] and other groups utilized similar systems. [26-29] Another approach via chemical treatment of PDMS-surfaces with acids was presented by Watanabe et al. [30] For plasma-treated PDMS, Béfahy et al. found crack-free conditions for oxygen plasma treatment on PDMS in a comparable screening setup to ours, [31] while Rhee et al. used CHF_3 instead of O_2. [32] Li et al. used initiator-integrated PDMS (iPDMS) to generate the stiff layer in grafting-from polymerization, leading to a stiff film consisting of dense polymer brushes on top of the comparably soft iPDMS. [33] However, so far, crack-free wrinkles were achieved by semi-empirical optimization rather than based on structure–property relationships. Initial pointers to the existence of a vertical gradient within the layer were found by Efimenko et al. by assuming a slight modification shift in UVO oxidized PDMS slabs, since this impedes the electron reflectivity on interfaces in near-edge X-ray fine structures (NEXAFS). [34] Other hints to a nonlinear slope have been found by various groups using X-ray photoelectron spectroscopy (XPS), [35-37] simple specular X-ray reflectivity (XR), [34, 38] energy-dispersive X-ray analysis (EDXA), [39] attenuated total reflection mode FT-IR (ATR-FTIR), [34, 37] sum frequency generation spectroscopy (SFG) [40] or Auger electron spectroscopy (AES). [41] All these methods offer the possibility to analyze the physical or chemical modifications of PDMS inside the oxidized layer, but not the mechanical modifications in deep-reaching cross section profiles. Chan et al. were the first to introduce a mechanical model system based on Ultraviolet/Ozone-(UVO) treated

PDMS. They postulated a composite layer consisting of a moderately converted intermediate layer topped by a thin, dense silica film. [42] The Young's modulus within the intermediate layer is defined as a square function of the local position z on the gradient, resulting in an overall effective Young's modulus $E_{eff} = \phi(z) \cdot E_{Silica}$. In addition, Sui et al. suggest an exponential decay function to describe the z-change in elasticity over a time-dependent system. [43] In this contribution, we correlate for the first time directly the nanostructure and nano-mechanical properties with crack densities for plasma-oxidized PDMS, the most widely used wrinkle-system. We compare our findings to finite element modelling and identify gradient formation in the surface layer as key to crack-free wrinkling. In general, the process to gain crack-free wrinkles can be utilized in all wrinkled surfaces that are desired to be uniform, which is relevant to most practical applications. Those are for example the template-assisted self-assembly (TASA) system as used by us, [16, 44] grating structures for photons, [45] anti-fouling surfaces [46-48] as well as surface films that additionally act as barrier layers for the surrounding media.

4.2.3. Experimental

PDMS preparation

PDMS was prepared by mixing the pre-polymer and curing agent of a Dow Corning Sylgard 184 PDMS Kit in 5 : 1 ratio, curing it at RT for 24 h followed by a thermal treatment of 4 h at 80 °C under ambient conditions. Slabs of 4.5 × 1.0 cm were cut out, cleaned with Milli-Q water and dried with nitrogen.

Plasma oxidation

Samples for wrinkling: The slabs were clamped in a custom-made stretching-device and strained uniaxially to 60% of their initial length. Afterwards the slabs were placed in a plasma chamber and irradiated for 300 s at a time under varying conditions.

Samples for QNM cross section analysis: The slabs were placed on a polyether-ether-ketone (PEEK) block inside the chamber and oxidized under the same conditions as for the wrinkling procedure. Afterwards they were left for 48 h in order to let the surface reverse to a hydrophobic state. Then they were placed in a PS mold with the glass surface facing upwards, and overcast with a perylene dye-doped second layer of PDMS under the same conditions as described above.

AFM topographical analysis

Oxidized and wrinkled slabs were analyzed in tapping mode (cantilever nominal spring constant $= 5\frac{N}{m}$, nominal resonance frequency = 290 kHz) using a Bruker Dimension Icon as well as a Bruker Dimension FastScan, both running with NanoScope 9.3 Software. Image sizes were 90 × 90 µm with 4096 px resolution and 35 × 35 µm with 1024 px resolution.

QNM analysis

Samples were cut in half in the middle. A small section was cut out, clamped in an AFM-holder, and the sample was smoothened along the three-layer-axis with a Cryo-Microtome. The smoothened surfaces were analyzed in QNM-in-air-mode with the same cantilevers and AFMs as described before. Image sizes were 1 × 1 µm with a resolution of 512 px. Every cantilever was calibrated in terms of spring constant, deflection sensitivity and tip radius.

4.2.4. Results and discussion

The cracks on the surface usually occur at locations that experience the highest stress intensities, or at points with reduced mechanical properties. In the case of wrinkling, a mechanical mismatch between the layer and the substrate is the reason for periodic deformations of the bilayer system. Nevertheless, this mismatch also is always accompanied by high in-plane stress at the interface between the layer and the substrate, due to the strongly differing mechanical properties of the layer and the substrate. [49] This stress concentration at the interface is most probably the reason for cracking of wrinkled surfaces. [50] We therefore investigate such interfaces in our model system of plasma-oxidized and wrinkled PDMS stripes, and discuss reasons thereof. We use Dow Corning's Sylgard 184 in a 1 : 5 ratio for the substrate, resulting in a Young's modulus measured via indentation of 3.5 ± 0.7 MPa. This is slightly higher than the comparable results from the literature, measured via tensile testing. [51]

First, we systematically tune the intensities of oxygen plasma via two parameters: the nominal power of the plasma cleaner and the oxygen pressure inside the plasma chamber, while all other parameters but the studied one are kept constant. We investigate the effect on the wrinkle size and crack density on pre-strained and wrinkled PDMS stripes as shown in Fig. 35. We strain the samples by 60% – a comparatively large strain – and subsequently plasma-treat them in order to achieve a high mechanical in-plane stress in the freshly formed bilayer system. In the eventual pre-strain relaxation step, wrinkles form as well as surface cracks. The wrinkles then are analyzed via 2D-Fourier Transformation (2D-FT) as schematically described in Fig. 35 **a**, showing a broad distribution of accessible wavelengths. Interestingly, the power screening showed a moderately pronounced increase of wavelength with a coincident rise of applied plasma power from 198 to 500 nm (Fig. 35 **b**). At the same time the pressure screening generates a strongly pronounced increase of wavelength from 263 to 1703

nm, with a steep increase especially for very low pressures <0.2 mbar (Fig. 35 **c**). To check the validity of the 2D-FT analysis, we furthermore performed Power Spectral Density (PSD) analysis. The detailed procedures and results of both 2D-FT and PSD can be found in the SI (Fig. 38 - Fig. 41 as well as Table 4 – Table 5).

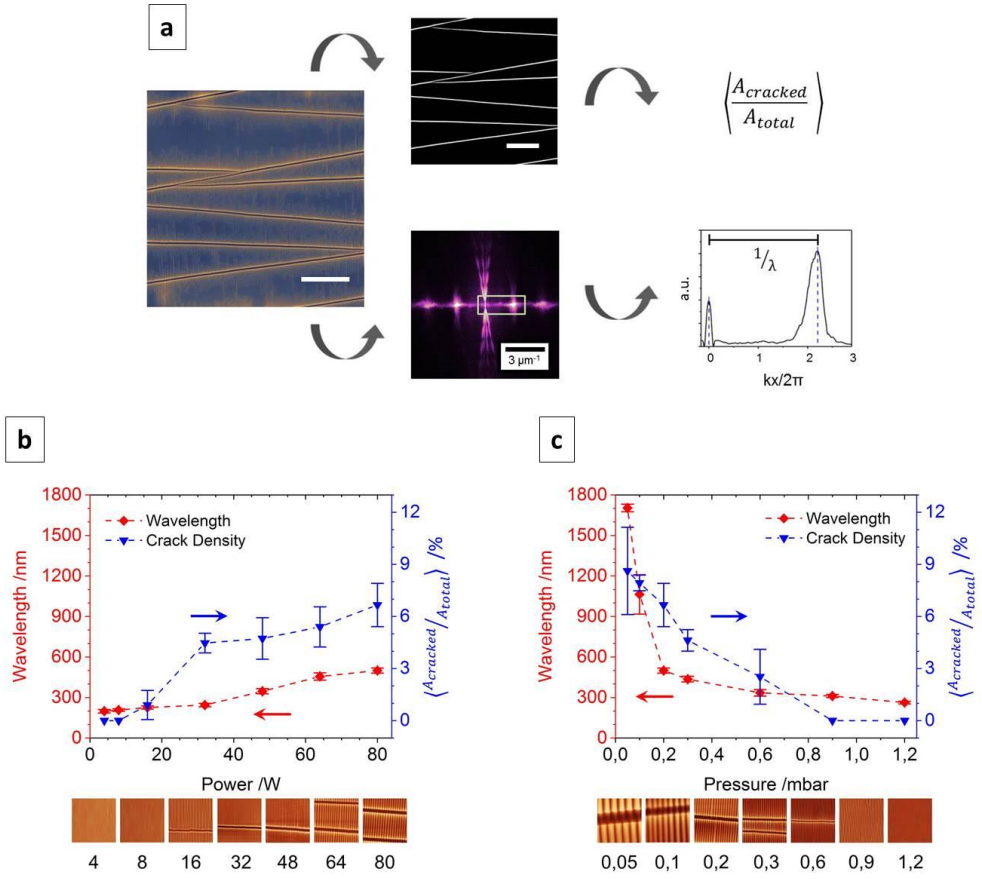

*Figure 35 | (**a**) Scheme of data evaluation of wrinkled surfaces: for crack density analysis (top), first a threshold was set for each image, and afterwards the cracked surface area was assessed. Wavelength analysis (bottom) was accomplished via a 2D-Fourier transformation; the scale bar is 20 mm. Results for power (**b**) and pressure (**c**) screening, considering crack density and wavelength results; the image size is 10 mm each.*

For both screenings we find a parameter window near the technically achievable extreme values, in which we are able to generate crack-free wrinkles. In the case of the power screening this window stretches from 0 to 8 W (0–10% of the nominal plasma cleaner power), while for the pressure screening it ranges from 0.9 to 1.2 mbar. Both windows cover the smallest feasible wrinkle wavelengths for each screening, and furthermore within these crack-free windows only slight changes in wavelength are obtained – being 198 nm to 207 nm for power screening, and 263 nm to 311 nm for pressure screening.

In order to correlate the observed crack densities with the structural properties of the film, we repeat the screenings under the same conditions for un-strained PDMS stripes. These allow for cross-section analysis of the interfacial region via QNM to determine the thickness and mechanical properties of the thin layer at the nanometer scale. The unstrained samples have equal geometries to those in the first part; furthermore they are treated with the same parameters as before. By this we ensure to fabricate compliant layers that are un-cracked and un-wrinkled due to the missing mechanical pre-strain. In a subsequent step we cast a dye-doped embedding consisting of another batch of 1 : 5 PDMS on top of the oxidized layer, and cut eventually out cross section profiles. The embedding step is necessary, as the analysis will be performed by the contact analysis QNM method. This essentially needs continuous surfaces to measure reliable values. The QNM analysis then is performed crosswise to the thin, oxidized layer, showing a three-layer-system consisting of the post-cast and dye-doped PDMS embedding/thin, plasma-oxidized layer/elastic PDMS substrate (Fig. 36 **a**). The results of both power and pressure screenings are depicted in Fig. 36 **b** and **c**. Here the elasticity always just represents the maximum stiffness of the layer. It gradually transits from hard to soft, and may be considered as a grouping of innumerable, infinitesimally thin layers with decreasing stiffness. We can identify two regions within the thin, plasma-oxidized layer – on the one hand a steep incline to the maximum Young's modulus, and on the other hand a gentler slope from the modulus' maximum down to the elasticity value of the elastic bulk material (Fig. 36 **a**). The first region appears due to the overcasting of the oxidized layer with the PDMS embedding. This is due to a gentle thermal curing of the three-layer-system, in order to guarantee a good covalent bonding to the plasma-oxidized layer for the QNM analysis. Therefore the thin oxidized layer also blurs slightly into the embedding, resulting in a broadened layer appearance. Nevertheless, only the second region represents the original plasma-oxidized layer.

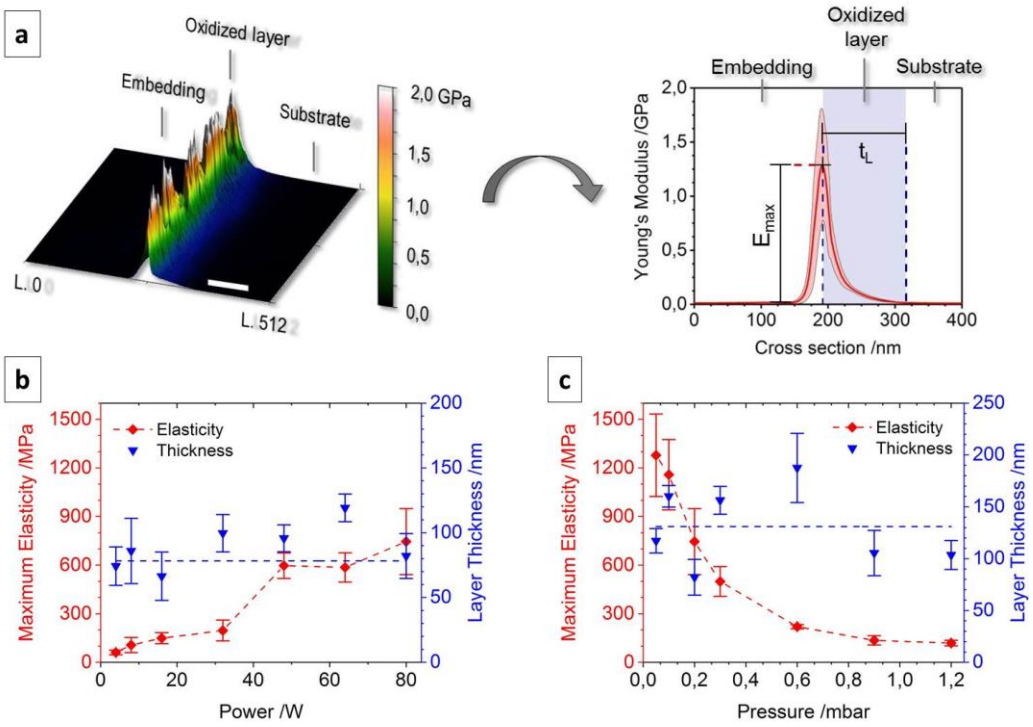

*Figure 36 | (**a**) AFM data evaluation: to exemplify the 0.05 mbar-sample from the pressure screening is depicted. First the modulus channel of the QNM measurement is converted to a 3D-data-matrix (left) and eventually averaged line by line over the whole image size of 512 rows (right); the scale bar is 100 nm. Results for power (**b**) and pressure (**c**) screening, regarding the maximum elasticity and layer thickness.*

We clearly identify an increase in elasticity from the substrate to the layer with decreasing chamber pressure and increasing nominal chamber power. As can be seen in Fig. 36 **b** and **c**, in the power screening the incline reaches from 61 MPa to 745 MPa (see also Fig. 42, SI), and in the pressure screening it is even more pronounced (Fig. 43, SI), reaching from 119 MPa to 1278 MPa. This is in good agreement with previously measured screenings for comparable setups. [31] Nevertheless, at the same time the thickness of the layer remains relatively constant with values fluctuating around 78 nm for the power screening and 131 nm for the pressure screening (Fig. 36 **b** and **c**). Within the power screening the deviations from the average layer thickness value are smaller compared to the ones in the pressure screening. The fluctuations can mainly be explained by the difficulty of deciding where the borderline from the PDMS substrate to the elasticity gradient is situated. We set a very low threshold for this crossover in order not to accidently cut the flat parts of the gradient out of the analysis. However, as not all layers show the same ideal gradient characteristics, in those analysis also parts of the PDMS substrate may be counted to the layer's gradient. Yet we see a reliable trend for the layer thickness, which does not rise or drop while changing the power or pressure of the process. The reasons for this nearly constant behavior can be found in the nature of plasma–surface interaction. The modification effect of a polymeric surface upon low pressure plasma treatment is, roughly, a superposition of two major pathways. The first is the impact of energetic ions: depending

on the type and energy distribution of ions hitting the surface, a collision cascade with a characteristic range develops. The second is the appearance of Vacuum Ultraviolet (VUV) absorption: the range of VUV photons depends on the wavelength of the plasma emission and the corresponding absorption coefficient of the exposed material. For the given system of plasma, one can assume that the crucial parameters for the interaction range, which are most likely ion energy and VUV wavelength, do not exhibit a pronounced variation across the screening intervals applied in this study. [52] So the variability of the excitation range is quite low, and furthermore self-bias effects close to the sample seem to be unlikely due to the very symmetric chamber geometry as well. [53] However, the flux of ions and VUV photons should vary significantly as a function of power or pressure. From that point of view the experimental evidence of surface modification with variable degree but constant range appears plausible. The order of magnitude observed for the overall range of the PDMS surface modification suggests that the major contribution arises via the VUV pathway, as bombardment ions penetrate only a few nm into the bulk material. [54, 55]

In order to clarify why the regime of crack-free samples correlates with the gradient nature of the hard layer, we carried out numerical simulations. For technical reasons, the continuous real gradient layers that have been measured are discretized into approximate stepwise gradient layer systems, as depicted in Fig. 4 **a**. Such a multilayered step gradient consists of many small intermediate layers of pre-defined steady thickness (blue curves), whose elasticity values are abstracted from the corresponding real gradient (black curve), while the corresponding Poisson ratio numbers have been estimated from materials with comparable Young's moduli. The Young's modulus of the PDMS substrate was set as E = 3.5 MPa. As a result, the real gradient now can be described via a multilayered step function. Secondly, a theoretical single layer is created, being the arithmetic mean of the experimentally determined Young's modulus along its total layer thickness (red dashed line). It represents the theoretical case, where the oxidized layer has no gradient-shaped interface to the bulk PDMS, and is also the most simple case of a bilayer system. The three different cases are also described schematically in Fig. 44 (SI). We test the real gradients with the cubic model systems of Chan [42] and the exponential system of Sui [43] (see Fig. 44 **b**, SI). We find both in very good agreement with the experimental data, where the exponential system is matching extremely well with a determination coefficient of $R^2 = 0.996$, while the cubic system is only slightly lower at $R^2 = 0.990$. In conclusion, both model systems appear to be suitable for the calculation and prediction of mechanical gradient layers.

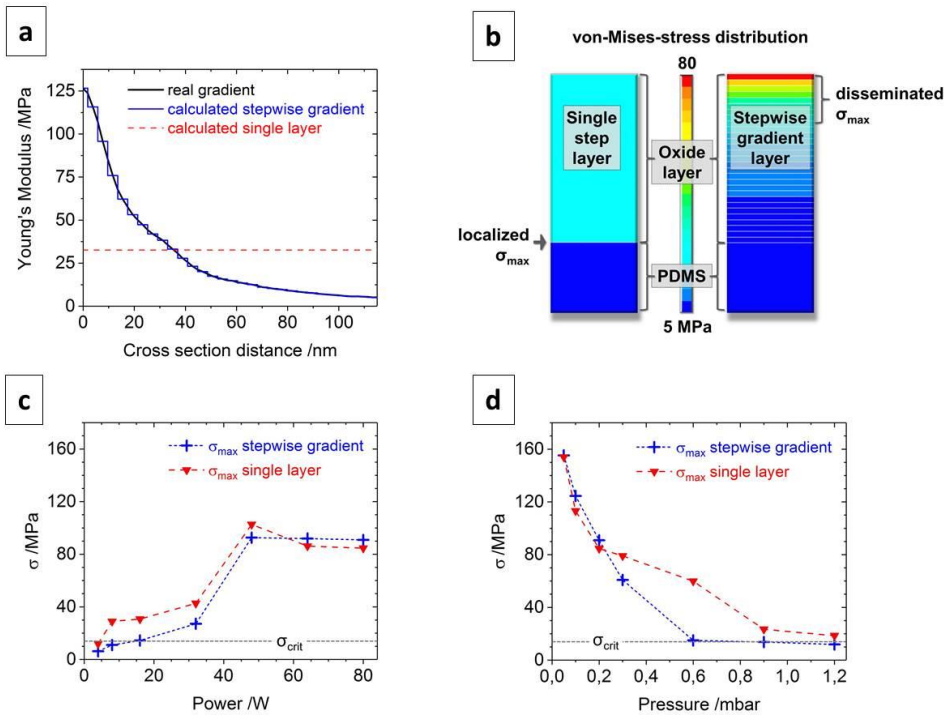

*Figure 37 | (**a**) The real gradient (black curve; 1.20 mbar-sample, taken from the pressure screening) is recalculated and overlaid by the stepwise gradient (blue curve) consisting of 30 steps, and eventually compared with the single step layer (red curve), whose stiffness represents the mean value of the real gradient. For the FEM simulation (**b**), the single layer (left) and also the stepwise gradient (right) are fixed on a quasi-infinite substrate underneath. Both are exposed to a simulated uniaxial strain of ε = 60%, and with equivalent boundary conditions. The results show the von-Mises-stress in both layers graphically, with a maximal stress intensity reaching from 5 to 80 MPa, indicated by the colored scale bar. (**c**) and (**d**) represent the simulated von-Mises-stress maxima for each sample, accomplished for the stepwise gradient (blue curve) as well as for the single layer (red curve). The critical stress (black dotted line) is calculated as σ_{crit} = 14 MPa.*

For our numerical simulations, both recreated layers are eventually calculated with mechanical ANSYS 19.1 FEM software (Fig. 37 **b**). Boundary conditions are chosen equally for all simulated samples. We define the left sample edge as the foundation, while the strain of ε = 60% is homogeneously applied to the right edge. The mesh size is created automatically, with a medium target range and a densification inside the layer. The results are obtained and displayed in the von-Mises-yield criterion. This allows for the estimation of tensile stress values in the real gradients. By doing so, we obtain two different maximal von-Mises-stress values – one for the stepwise gradient layer and one for the single layer. Plotting them against the according power (Fig. 37 **c**) or pressure (Fig. 37 **d**) values shows a trend similar to the corresponding wavelengths and crack densities in Fig. 35 **b** and **c**. Nevertheless, besides high power or low pressure values, the stepwise gradient always has a lower σ_{max} compared to its corresponding single layer value. When taking the experimentally derived crack density from

Fig. 35 **b** and c into account, we are able to determine a critical tensile stress σ_{crit}, up to which crack-free wrinkling under high mechanical pre-strains is possible. For the power screening, it can be found between 8 and 16 W, and for the pressure screening between 0.6 and 0.9 mbar. From Fig. 37 **c** and **d** we therefore conclude 13.7 MPa < σ_{max} < 14.4 MPa, so $\sigma_{crit} \sim$ 14 MPa. Thus it appears that the maximum stress of each single layer is higher, as the significant drop of elasticity between the hard layer and the soft substrate generates noticeably higher maximal stress values than within the corresponding gradient interface.

4.2.5. Conclusion

We measured the effect of the plasma device power and the plasma chamber pressure on highly strained elastomeric materials, in order to determine the emerging wrinkle wavelengths as well as the crack density. By this we identified a narrow parameter range for each, in which surface cracking does not occur. Based on these findings, we calculated the elasticity for every sample via two approaches: first as a theoretical single layer, and second as a stepwise gradient layer according to the corresponding experimental data. FEM simulations under mechanical strain were executed with both layers, resulting in the implication that the mechanical z-gradients cushioned the maximum tensile stress σ_{max} within the layer-to-substrate-interface. Therefore we could reduce σ_{max} for some parameters below a threshold of σ_{crit} = 14 MPa, where cracking of the surface did not occur. We therefore conclude that the production of crack-free wrinkles can be tuned via the implementation of a mechanical z-gradient in the hard, thin layer. The gradient slope nevertheless must not be too steep, since this leads to internal layer stress values that are higher than a theoretical corresponding single layer setup. For the generation of such gradients with PDMS, we therefore suggest systems that have a high penetration depth, but at the same time can be tuned to low plasma intensities. The insights of this paper can be used to develop crack-free wrinkled surfaces also for other applications, just as for particle assembly, optics, anti-bacterial, anti-cellular or anti-viral surfaces, etc., where disruptive features as cracks may obstruct the nano-structured functionality.

Acknowledgements

We thank Y. Brasse for preliminary work, as well as U. Reuter and A. Janke for assistance in AFM sample preparation. Also we thank L. Zybell for assistance in FEM simulations. This work was funded by the SAB 100333997 BIOS project.

4.2.6. Supporting Information

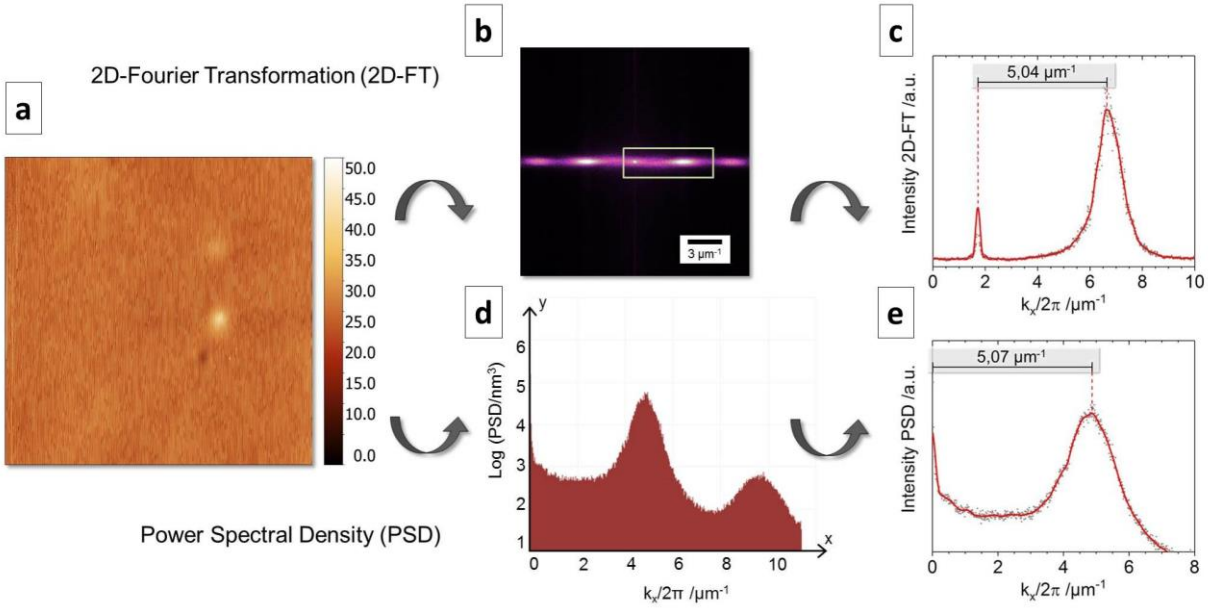

*Figure 38 | Evaluation process for topographical AFM images (**a**) via 2D-FT and PSD, exemplarily shown for one of the three samples used in the power screening at 4 W (5 % Plasma Cleaner power). For 2D-FT the AFM image is first transformed over a 2-Dimensional Fast Fourier Transformation (2D-FFT) to a FT-spectrum (**b**). In here, the area marked with the white box (including the FT-origin peak and the 1st order peak) is extracted as a profile. The data is fitted in Origin Pro with an FFT-filter (**c**) and the peak positions are subtracted from each other, resulting in the wavenumber k of the according corrugation length observed within the topographical AFM image. For PSD, the horizontal axis of the AFM image gets transformed in NanoScope Analysis software (**d**) and eventually the extracted profile is analyzed similar to 2D-FT (e), with the addition that the origin peak is automatically set to x = 0.*

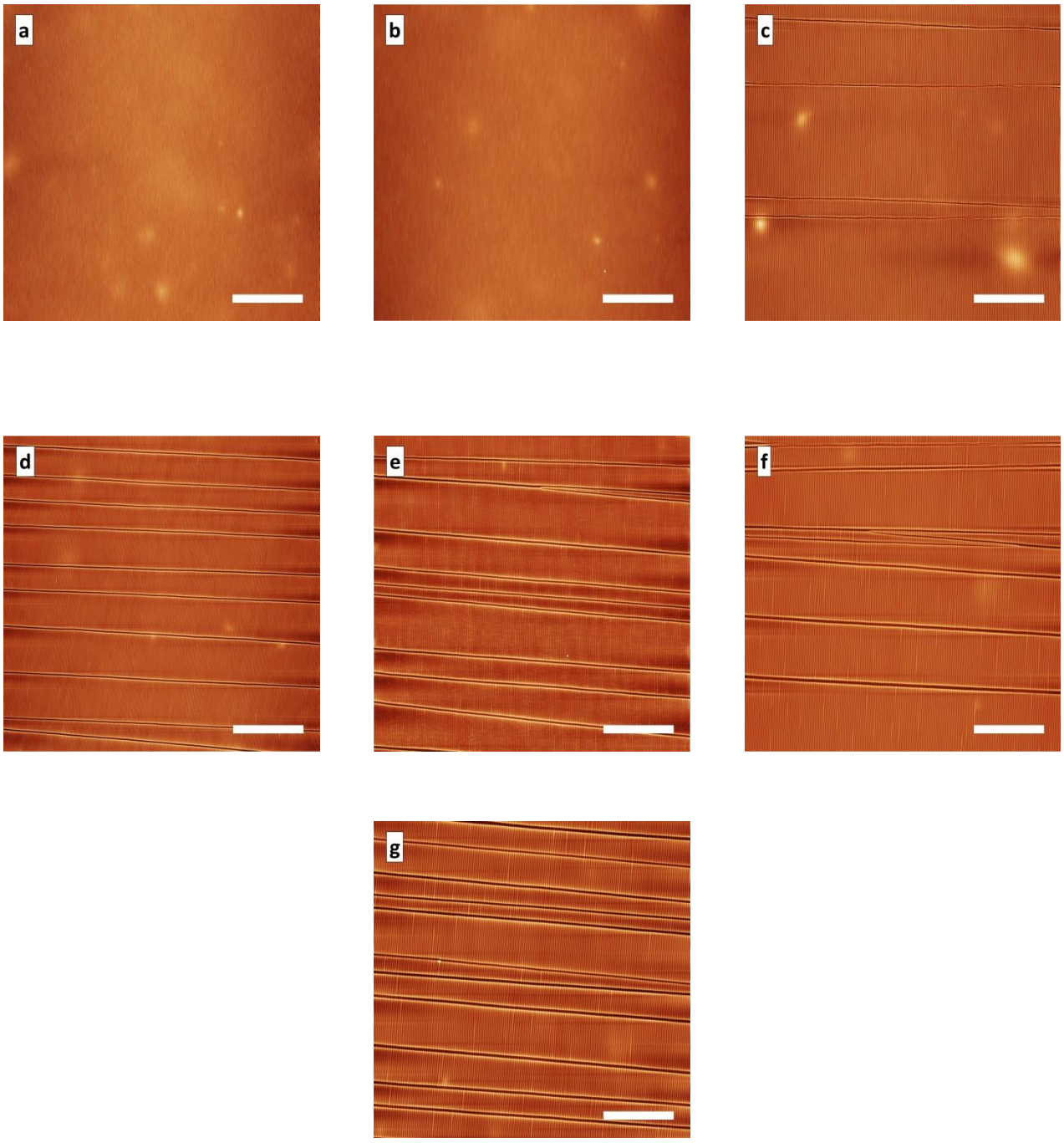

*Figure 39 | Topographical AFM images of the power screening, with (**a**) = 4 W, (**b**) = 8 W, (**c**) = 16 W, (**d**) = 32 W, (**e**) = 48 W, (**f**) = 64 W and (**g**) = 80 W. 10 x 10 µm cutouts are added to the power screening in Fig. 35 **b**. Scale bar is 20 µm.*

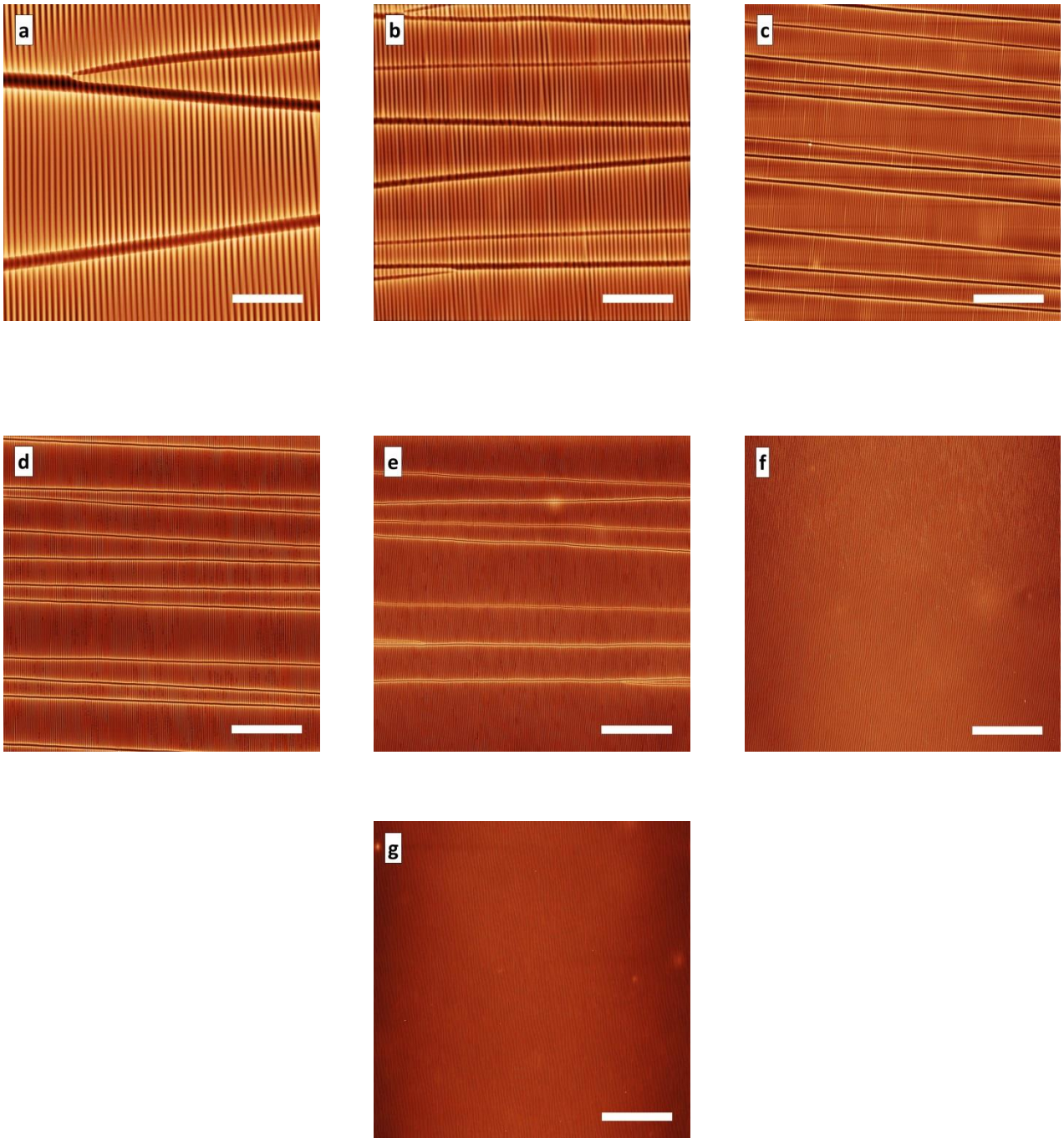

*Figure 40 | Topographical AFM images of the pressure screening, determined analogous to Fig. S2. With (**a**) = 0.05 mbar, (**b**) = 0.1 mbar, (**c**) = 0.2 mbar, (**d**) = 0.3 mbar, (**e**) = 0.6 mbar, (**f**) = 0.9 mbar and (**g**) = 1.2 mbar. 10 x 10 µm cutouts are added to the pressure screening in Fig. 35 **c**. Scale bar is 20 µm.*

Pressure	*PSD*				*2D-FT*				*Crack Density*		
	Individual		Ø		Individual		Ø		Individual	Ø	
mbar	λ	σ ±	λ	σ ±	λ	σ ±	λ	σ ±		**Area**	**σ ±**
	nm	**nm**	**nm**	**nm**	**nm**	**nm**	**nm**	**nm**	**Area %**	**%**	
	1730,8	121,0			1710,9	24,2			7,3		
0,05	1698,1	116,5	1698,5	123,8	1697,7	30,7	1703,3	28,0	11,5	8,6	2,5
	1666,7	121,4			1701,3	26,6			7,1		
	1216,2	87,3			1217,6	22,4			7,7		
0,10	1046,5	63,2	1070,0	153,1	1040,5	16,3	1063,4	145,6	7,7	7,9	0,5
	947,4	60,9			932,0	23,1			8,5		
	514,3	29,3			511,6	15,8			7,8		
0,20	494,5	29,7	499,3	32,1	494,9	14,1	499,8	18,6	6,8	6,7	1,2
	489,1	28,9			492,8	16,5			5,3		
	454,6	22,9			454,1	14,8			4,6		
0,30	422,5	23,4	434,5	30,3	426,7	12,2	436,1	20,8	4,0	4,6	0,6
	426,5	28,0			427,6	14,3			5,3		
	350,2	16,0			359,9	10,0			4,4		
0,60	312,5	17,1	325,8	26,6	317,8	9,9	334,8	24,1	1,7	2,5	1,6
	314,7	15,4			326,8	8,4			1,6		
	305,1	21,1			304,4	11,1			0,0		
0,90	314,7	16,5	311,5	19,9	316,6	8,1	311,1	11,6	0,0	0,0	0,0
	314,7	19,8			312,3	10,4			0,0		
	258,6	19,6			259,0	5,7			0,0		
1,20	255,7	16,7	258,6	18,9	262,8	9,5	262,6	9,8	0,0	0,0	0,0
	261,6	19,7			266,0	12,2			0,0		

Table 4 | Results of the pressure screening, displaying PSD (left columns), 2D-FT (middle) and the according crack density values at a time (right). For each data point, three samples were measured via AFM and analyzed with both PSD and 2D-FT. The results were averaged and the deviations summed up via Gaussian error propagation.

Power	PSD				2D-FT				Crack Density		
	Individual		Ø		Individual		Ø		Individual	Ø	
W	λ	σ ±	λ	σ ±	λ	σ ±	λ	σ ±	Area	Area	σ ±
	nm	nm	nm	nm	nm	nm	nm	nm	Area %	%	
	206,9	15,8			205,0	8,2			0,0		
5	197,4	15,9	197,4	18,6	202,6	9,8	198,5	12,9	0,0	0,0	0,0
	187,9	16,2			187,8	8,8			0,0		
	204,1	20,1			209,4	7,6			0,0		
10	211,3	16,8	205,3	18,1	209,5	8,5	207,1	9,0	0,0	0,0	0,0
	200,5	15,0			202,3	8,1			0,0		
	217,4	13,7			224,3	8,0			1,0		
20	239,0	16,2	225,4	19,2	235,2	8,0	225,8	12,2	0,0	0,9	0,8
	219,8	15,3			217,8	9,5			1,7		
	238,1	14,5			237,6	8,7			4,9		
40	250,7	14,6	244,4	17,1	251,1	7,7	244,3	12,6	4,1	4,5	0,6
	244,3	14,5			244,3	8,2			4,5		
	340,9	16,6			341,9	2,0			6,1		
60	326,1	18,4	344,3	27,7	331,6	12,2	346,2	19,0	4,4	4,7	1,2
	365,9	22,4			365,2	10,3			3,8		
	436,9	27,3			434,2	15,4			6,7		
80	471,2	28,4	455,0	32,2	476,1	15,7	455,9	27,2	4,6	5,4	1,2
	456,9	26,0			457,4	20,6			4,9		
	514,3	29,3			511,6	15,8			7,8		
100	494,5	29,7	499,3	32,1	494,9	14,1	499,8	18,6	6,8	6,7	1,2
	489,1	28,9			492,8	16,5			5,3		

Table 5 | Results of the power screening. The results were obtained analogous to Table 4.

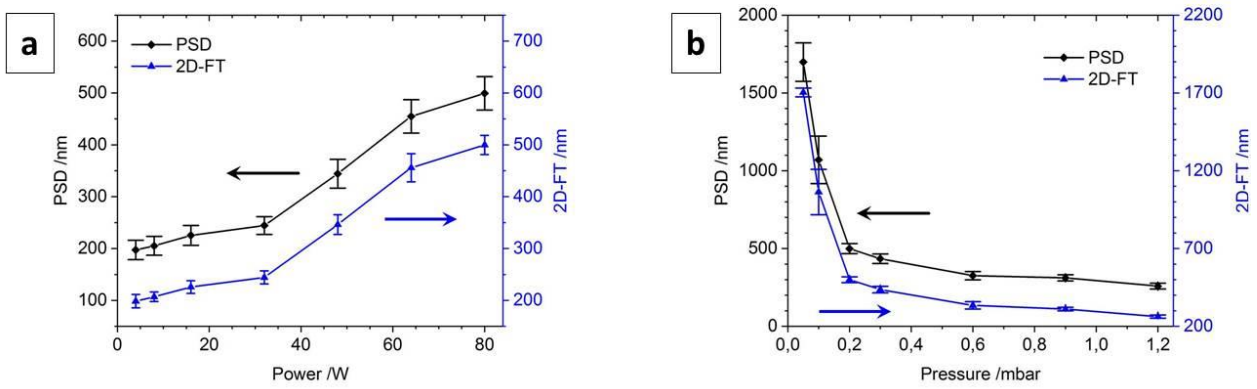

*Figure 41 | Wrinkle wavelengths for power (**a**) and pressure (**b**) screenings, determined via PSD (black curves) as well as 2D-FT (blue curves). PSD and 2D-FT are separated in both diagrams by a y-axis offset, since they superpose almost entirely when charting them on the same axis scale.*

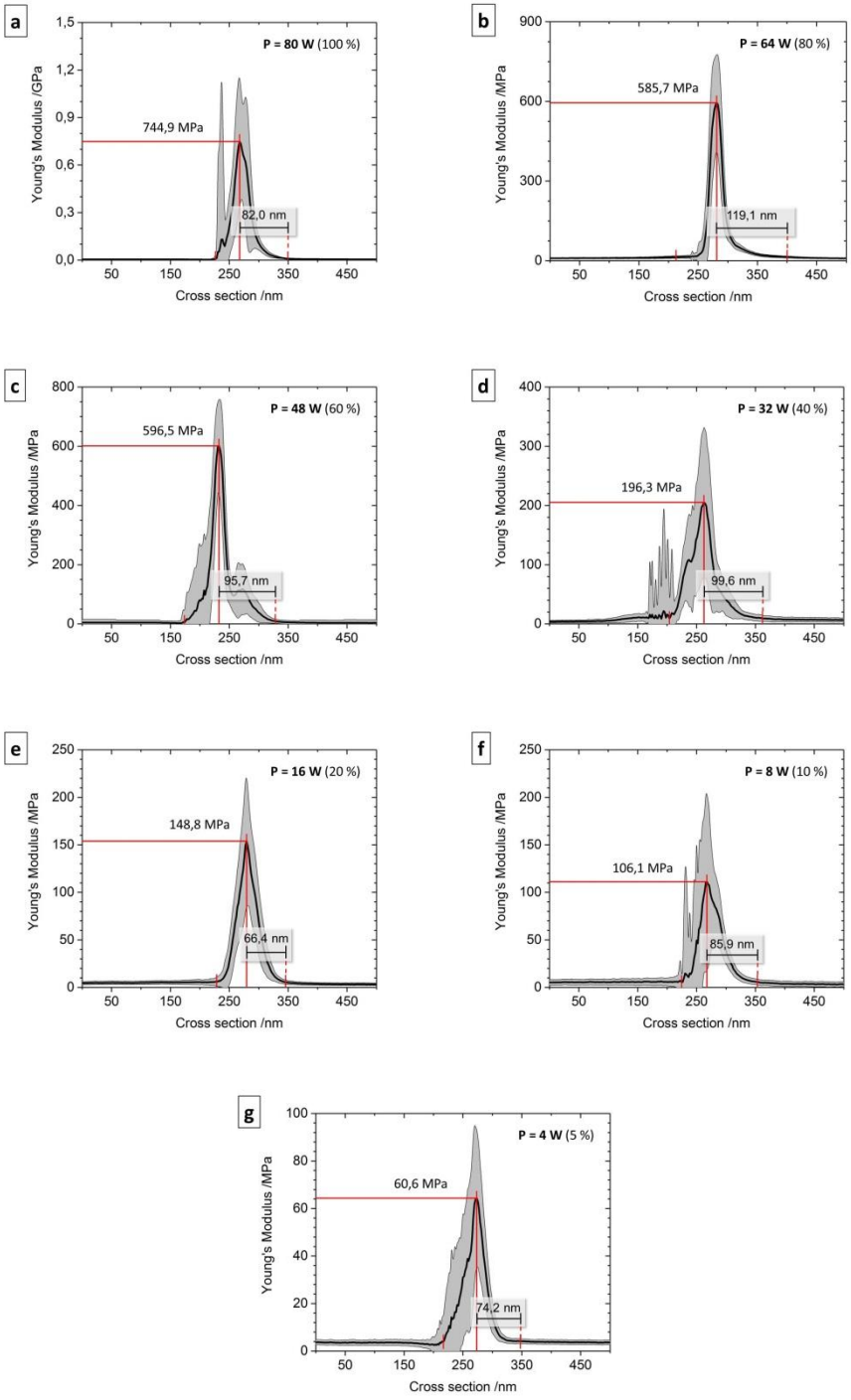

*Figure 42 | screening of the flat, unstrained samples, analyzed via QNM AFM method. The power range stretches from The highest accessible power at P_{max} = 80 W (**a**) to the lowest accessible power at P_{min} = 4 W (**g**). For every sample the maximum elasticity E_{max} as well as the average layer thickness t_l is denoted.*

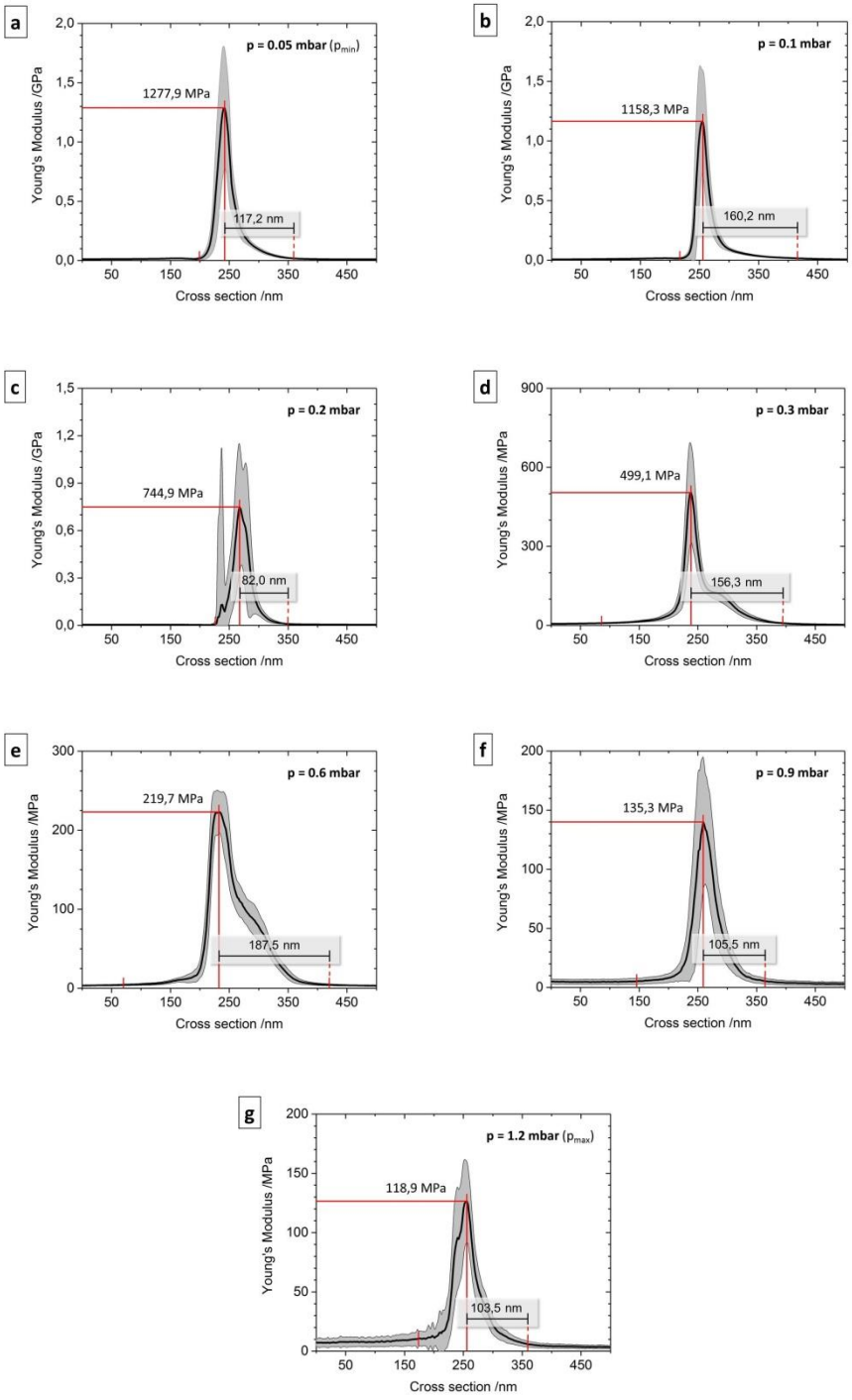

*Figure 43 | Pressure screening of the flat, unstrained samples, analyzed analogous to Fig. 42. The pressure range stretches from the lowest accessible pressure being p_{min} = 0.05 mbar (**a**) to the highest accessible at p_{max} = 1,2 mbar (**g**). For every sample the maximum elasticity E_{max} as well as the average layer thickness t_l is denoted.*

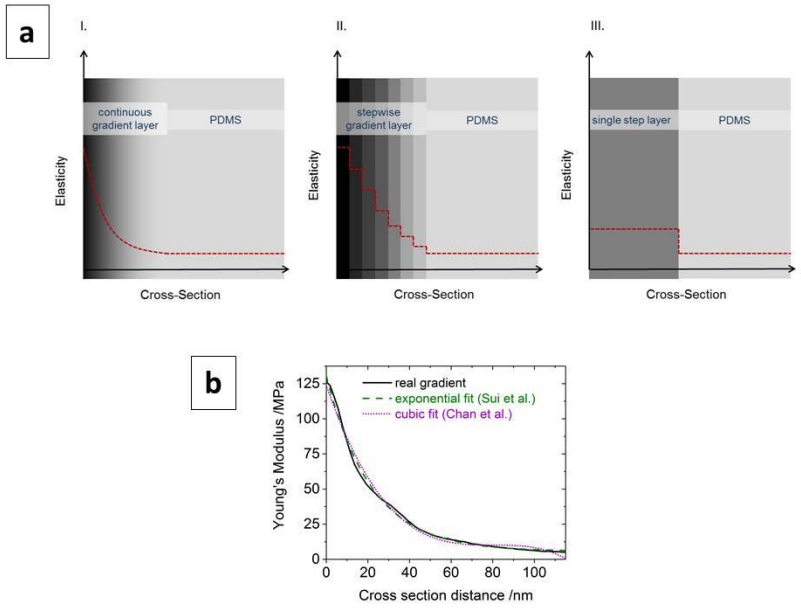

*Figure 44 | (**a**) Scheme of the calculated recreation of the gradient: The continuous gradient from I. is transferred into a corresponding multilayered stepwise gradient II. as well as a single step layer III. Below the corresponding stress diagrams for each layer-to-layer interface are shown schematically: For continuous (I.) and stepwise (II.) gradients a lower maximal von-Mises-stress σ_{max} than for the single step (III.) is simulated, due to the broader distribution of overall stress between layer and substrate when compared with the single layer. The critical stress σ_{crit} for cracking these layers indicates that for particular conditions $\sigma_{max,single\text{-}step} > \sigma_{crit} > \sigma_{max,gradient}$, so crack-free wrinkles can be achieved. In (**b**) the real gradient from Fig. 37 **a** is compared to two theoretical models; on the one hand the exponential model of Sui et al., [43] on the other hand the cubic model of Chan et al. [42] Both are in very good agreement with the experimental data, however the exponential model is even closer ($R_2 = 0.996$) than the cubic one ($R_2 = 0.990$).*

References

[1] L. Dong, X. Quan and P. Cheng: An experimental investigation of enhanced pool boiling heat transfer from surfaces with micro/nano-structures, **2014**; *Int. J. Heat Mass Transfer*, 71 - 189-196

[2] C. Muratore and A.A. Voevodin: Chameleon Coatings: Adaptive Surfaces to Reduce Friction and Wear in Extreme Environments, **2009**; *Ann. Rev. Mat. Res.*, 39 - 1, 297-324

[3] S. Veprek and M.J.G. Veprek-Heijman: Industrial applications of superhard nanocomposite coatings, **2008**; *Surf. Coat. Technol.*, 202 - 21, 5063-5073

[4] J.Y. Chung, J.P. Youngblood and C.M. Stafford: Anisotropic wetting on tunable micro-wrinkled surfaces, **2007**; *Soft Matter*, 3 - 9, 1163-1169

[5] M.J. Madou: Fundamentals of Microfabrication and Nanotechnology - Manufacturing Techniques for Microfabrication and Nanotechnology, **2011**, Boca Raton, USA, CRC Press Publisher; 2 ff

[6] T. Kaufmann and B.J. Ravoo: Stamps, inks and substrates: polymers in microcontact printing, **2010**; *Polym. Chem.*, 1 - 4, 371-387

[7] J. Bonse, R. Koter, M. Hartelt, D. Spaltmann, S. Pentzien, S. Höhm, A. Rosenfeld and J. Krüger: Femtosecond laser-induced periodic surface structures on steel and titanium alloy for tribological applications, **2014**; *Appl. Phys. A*, 117 - 1, 103-110

[8] A. Schweikart and A. Fery: Controlled wrinkling as a novel method for the fabrication of patterned surfaces, **2009**; *Microchimica Acta*, 165 - 3, 249-263

[9] K. Efimenko, M. Rackaitis, E. Manias, A. Vaziri, L. Mahadevan and J. Genzer: Nested self-similar wrinkling patterns in skins, **2005**; *Nat. Mat.*, 4 - 293

[10] J. Genzer and J. Groenewold: Soft matter with hard skin: From skin wrinkles to templating and material characterization, **2006**; *Soft Matter*, 2 - 4, 310-323

[11] H. Vandeparre, M. Piñeirua, F. Brau, B. Roman, J. Bico, C. Gay, W. Bao, C.N. Lau, P.M. Reis and P. Damman: Wrinkling Hierarchy in Constrained Thin Sheets from Suspended Graphene to Curtains, **2011**; *Phys. Rev. Lett.*, 106 - 22, 224301

[12] Q. Li, X. Han, J. Hou, J. Yin, S. Jiang and C. Lu: Patterning Poly(dimethylsiloxane) Microspheres via Combination of Oxygen Plasma Exposure and Solvent Treatment, **2015**; *J. Phys. Chem. B*, 119 - 42, 13450-13461

[13] J. Thiele, A.R. Abate, H.C. Shum, S. Bachtler, S. Förster and D.A. Weitz: Fabrication of Polymersomes using Double-Emulsion Templates in Glass-Coated Stamped Microfluidic Devices, **2010**; *Small*, 6 - 16, 1723-1727

[14] D.-Y. Khang, H. Jiang, Y. Huang and J.A. Rogers: A Stretchable Form of Single-Crystal Silicon for High-Performance Electronics on Rubber Substrates, **2006**; *Science*, 311 - 5758, 208-212

[15] C.E. P. and C.A. J.: Fabricating Microlens Arrays by Surface Wrinkling, **2006**; *Adv. Mater.*, 18 - 24, 3238-3242

[16] M. Tebbe, M. Mayer, B.A. Glatz, C. Hanske, P.T. Probst, M.B. Muller, M. Karg, M. Chanana, T.A.F. Konig, C. Kuttner and A. Fery: Optically anisotropic substrates via wrinkle-assisted convective assembly of gold nanorods on macroscopic areas, **2015**; *Faraday Discuss.*, 181 - 0, 243-260

[17] P.T. Probst, S. Sekar, T.A.F. König, P. Formanek, G. Decher, A. Fery and M. Pauly: Highly Oriented Nanowire Thin Films with Anisotropic Optical Properties Driven by the Simultaneous Influence of Surface Templating and Shear Forces, **2018**; *ACS Appl. Mat. Interf.*, 10 - 3, 3046-3057

[18] B.A. Glatz, M. Tebbe, B. Kaoui, R. Aichele, C. Kuttner, A.E. Schedl, H.-W. Schmidt, W. Zimmermann and A. Fery: Hierarchical line-defect patterns in wrinkled surfaces, **2015**; *Soft Matter*, 11 - 17, 3332-3339

[19] G. Miquelard-Garnier, A.B. Croll, C.S. Davis and A.J. Crosby: Contact-line mechanics for pattern control, **2010**; *Soft Matter*, 6 - 22, 5789-5794

[20] H. Vandeparre, S. Gabriele, F. Brau, C. Gay, K.K. Parker and P. Damman: Hierarchical wrinkling patterns, **2010**; *Soft Matter*, 6 - 22, 5751-5756

[21] Y. Ni, D. Yang and L. He: Spontaneous wrinkle branching by gradient stiffness, **2012**; *Phys. Rev. E*, 86 - 3, 031604

[22] S. Yu, Y. Ni, L. He and Q.-L. Ye: Tunable Formation of Ordered Wrinkles in Metal Films with Controlled Thickness Gradients Deposited on Soft Elastic Substrates, **2015**; *ACS Appl. Mat. Interf.,* 7 - 9, 5160-5167

[23] B. Kaoui, A. Guckenberger, A. Krekhov, F. Ziebert and W. Zimmermann: Coexistence of stable branched patterns in anisotropic inhomogeneous systems, **2015**; *New J. Phys.*, 17 - 10, 103015

[24] Y. Xuan, X. Guo, Y. Cui, C. Yuan, H. Ge, B. Cui and Y. Chen: Crack-free controlled wrinkling of a bilayer film with a gradient interface, **2012**; *Soft Matter*, 8 - 37, 9603-9609

[25] S.K. Park, Y.-J. Kwark, S. Nam, S. Park, B. Park, S. Yun, J. Moon, J.-I. Lee, B. Yu and K.-U. Kyung: Wrinkle structures formed by formulating UV-crosslinkable liquid prepolymers, **2016**; *Polymer*, 99 - 447-452

[26] D. Chandra and A.J. Crosby: Self-Wrinkling of UV-Cured Polymer Films, **2011**; *Adv. Mater.*, 23 - 30, 3441-3445

[27] J.M. Torres, C.M. Stafford and B.D. Vogt: Photoinitator surface segregation induced instabilities from polymerization of a liquid coating on a rigid substrate, **2012**; *Soft Matter*, 8 - 19, 5225-5232

[28] S.J. Ma, S.J. Mannino, N.J. Wagner and C.J. Kloxin: Photodirected Formation and Control of Wrinkles on a Thiol–ene Elastomer, **2013**; *ACS Macro Letters*, 2 - 6, 474-477

[29] S.K. Park, Y.-J. Kwark, J. Moon, C.W. Joo, B.G. Yu and J.-I. Lee: Finely Formed, Kinetically Modulated Wrinkle Structures in UV-Crosslinkable Liquid Prepolymers, **2015**; *Macromol. Rapid Commun.*, 36 - 22, 2019-2019

[30] M. Watanabe and K. Mizukami: Well-Ordered Wrinkling Patterns on Chemically Oxidized Poly(dimethylsiloxane) Surfaces, **2012**; *Macromol.*, 45 - 17, 7128-7134

[31] S. Béfahy, P. Lipnik, T. Pardoen, C. Nascimento, B. Patris, P. Bertrand and S. Yunus: Thickness and Elastic Modulus of Plasma Treated PDMS Silica-like Surface Layer, **2010**; *Langmuir*, 26 - 5, 3372-3375

[32] R. Dongjoon, L. Won-Kyu and O.T. W.: Crack-Free, Soft Wrinkles Enable Switchable Anisotropic Wetting, **2017**; *Angew. Chem. Int. Ed.*, 56 - 23, 6523-6527

[33] L. Zhong, Z. Shen, Z. Pengfei, Y. Dayong, J. Gang and M. Hongwei: Surface initiated polymerization from integrated poly(dimethylsiloxane) enables crack-free large area wrinkle formation, **2012**; *Polym. Adv. Technol.*, 23 - 9, 1240-1245

[34] K. Efimenko, W.E. Wallace and J. Genzer: Surface Modification of Sylgard-184 Poly(dimethyl siloxane) Networks by Ultraviolet and Ultraviolet/Ozone Treatment, **2002**; *J. Colloid Interface Sci.*, 254 - 2, 306-315

[35] H. Hillborg, J.F. Ankner, U.W. Gedde, G.D. Smith, H.K. Yasuda and K. Wikström: Crosslinked polydimethylsiloxane exposed to oxygen plasma studied by neutron reflectometry and other surface specific techniques, **2000**; *Polymer*, 41 - 18, 6851-6863

[36] M. Ouyang, C. Yuan, R.J. Muisener, A. Boulares and J.T. Koberstein: Conversion of Some Siloxane Polymers to Silicon Oxide by UV/Ozone Photochemical Processes, **2000**; *Chem. Mater.*, 12 - 6, 1591-1596

[37] A.E. Özçam, K. Efimenko and J. Genzer: Effect of ultraviolet/ozone treatment on the surface and bulk properties of poly(dimethyl siloxane) and poly(vinylmethyl siloxane) networks, **2014**; *Polymer*, 55 - 14, 3107-3119

[38] F.A. Bayley, J.L. Liao, P.N. Stavrinou, A. Chiche and J.T. Cabral: Wavefront kinetics of plasma oxidation of polydimethylsiloxane: limits for sub-μm wrinkling, **2014**; *Soft Matter*, 10 - 8, 1155-1166

[39] D.B.H. Chua, H.T. Ng and S.F.Y. Li: Spontaneous formation of complex and ordered structures on oxygen-plasma-treated elastomeric polydimethylsiloxane, **2000**; *Appl. Phys. Lett.*, 76 - 6, 721-723

[40] H. Ye, Z. Gu and D.H. Gracias: Kinetics of Ultraviolet and Plasma Surface Modification of Poly(dimethylsiloxane) Probed by Sum Frequency Vibrational Spectroscopy, **2006**; *Langmuir*, 22 - 4, 1863-1868

[41] J.-Y. Park, H.Y. Chae, C.-H. Chung, S.J. Sim, J. Park, H.H. Lee and P.J. Yoo: Controlled wavelength reduction in surface wrinkling of poly(dimethylsiloxane), **2010**; *Soft Matter*, 6 - 3, 677-684

[42] E.P. Chan and A.J. Crosby: Spontaneous formation of stable aligned wrinkling patterns, **2006**; *Soft Matter*, 2 - 4, 324-328

[43] J. Sui, J. Chen, X. Zhang, G. Nie and T. Zhang: Symplectic Analysis of Wrinkles in Elastic Layers With Graded Stiffnesses, **2018**; *J. Appl. Mech.*, 86 - 1, 011008-011008-8

[44] M. Mayer, M. Tebbe, C. Kuttner, M.J. Schnepf, T.A.F. König and A. Fery: Template-assisted colloidal self-assembly of macroscopic magnetic metasurfaces, **2016**; *Faraday Discuss.*, 191 - 0, 159-176

[45] J.B. Kim, P. Kim, N.C. Pégard, S.J. Oh, C.R. Kagan, J.W. Fleischer, H.A. Stone and Y.-L. Loo: Wrinkles and deep folds as photonic structures in photovoltaics, **2012**; *Nat. Phot.*, 6 - 327

[46] K. Efimenko, J. Finlay, M.E. Callow, J.A. Callow and J. Genzer: Development and Testing of Hierarchically Wrinkled Coatings for Marine Antifouling, **2009**; *ACS Appl. Mat. Interf.*, 1 - 5, 1031-1040

[47] M. Palacios-Cuesta, A. Cortajarena, O. García and J. Rodríguez-Hernández: Fabrication of Functional Wrinkled Interfaces from Polymer Blends: Role of the Surface Functionality on the Bacterial Adhesion, **2014**; *Polymers*, 6 - 11, 2845

[48] M. Guvendiren and J.A. Burdick: The control of stem cell morphology and differentiation by hydrogel surface wrinkles, **2010**; *Biomaterials*, 31 - 25, 6511-6518

[49] J.L. Beuth: Cracking of thin bonded films in residual tension, **1992**; *Int. J. Sol. Struct.*, 29 - 13, 1657-1675

[50] J.W. Hutchinson and Z. Suo: Advances in Applied Mechanics - *Mixed Mode Cracking in Layered Materials*, **1991**, In: J.W. Hutchinson and T.Y. Wu, editor, Elsevier; 63-191

[51] R.S. O'Connor, X. Hao, K. Shen, K. Bashour, T. Akimova, W.W. Hancock, L.C. Kam and M.C. Milone: Substrate Rigidity Regulates Human T Cell Activation and Proliferation, **2012**; *J. Immunol.,* 189 - 3, 1330-1339

[52] M.R. Wertheimer, A.C. Fozza and A. Holländer: Industrial processing of polymers by low-pressure plasmas: the role of VUV radiation, **1999**; *Nucl. Instr. Meth. Phys. Res. Sect. B Beam Interact. Mat. Atoms*, 151 - 1, 65-75

[53] D. Pasquariello, M. Lindeberg, C. Hedlund and K. Hjort: Surface energy as a function of self-bias voltage in oxygen plasma wafer bonding, **2000**; *Sens. Act. A Phys,* 82 - 1, 239-244

[54] V.A. Godyak, R.B. Piejak and B.M. Alexandrovich: Measurement of electron energy distribution in low-pressure RF discharges, **1992**; *Plasma Sources Sci. Technol.*, 1 - 1, 36

[55] V.A. Godyak, R.B. Piejak and B.M. Alexandrovich: Electron energy distribution function measurements and plasma parameters in inductively coupled argon plasma, **2002**; *Plasma Sources Sci. Technol.*, 11 - 4, 525

4.3. Patent – Surface-structured polymer bodies and method for the fabrication thereof

4.3.1. Abstract

The invention concerns the field of polymer chemistry and relates to surface-structured polymer bodies such as those which can, for example, be used in solar cells or as anti-fouling films in medical technology.

The object of the present invention is to specify surface-structured polymer bodies which have a high structuring accuracy with regard to the dimensions on the surface of the polymer bodies.

The object is attained by surface-structured polymer bodies in which polymer bodies with dimensions of at least ≥ 100 cm^2 are present, the surfaces of which are at least partially covered with at least one nano- to micrometer-thick layer, and the layers are physically and/or chemically coupled to the polymer bodies, and the surface of the polymer bodies with the layers is at least partially deformed, wherein the deformation is periodic within a deformation type and the arrangement of multiple different deformation types on a polymer body is anisotropic or isotropic, and wherein the elastic modulus of the material of the polymer body is less than the elastic modulus of the layer materials.

4.3.2. Patent application

The invention concerns the field of polymer chemistry and relates to surface-structured polymer bodies such as those which can, for example, be used in solar cells or as anti-fouling films in medical technology, for preventing the adhesion of viruses and/or bacteria, or for modifying tribological properties such as, for example, minimizing friction in industrial production processes, and to a method for the fabrication of said bodies.

Polymers are applied in numerous ways and in the most diverse areas of technology. It is thereby often helpful that bodies made of these polymers are surface-structured. This structuring can take place in a physical and/or chemical manner.

The controlled and targeted formation of wrinkles via mechanical processes at the nano and micro levels is known. This was published for the first time in 1998 by Bowden et al. [1]

Since then, there have been many reports about new possibilities for and ways of fabricating this system; emphasis was thereby almost always placed on the advantages of what is referred to as soft lithography over classical, radiation-based lithography, which advantages include mechanical wrinkling. In soft lithography, structures of the order of magnitude and precision of lithographic processes are achieved, but without etching and radiation. This almost always occurs via mechanical tensile and compressive processes with soft substrate

materials, hence the name soft lithography. [2] The two most important advantages are namely the expenditure of time and money and the potential scalability of wrinkling systems. The former point usually stands up to scrutiny, whereas it has not yet been possible to practically apply and demonstrate the latter.

The disadvantage of the known solutions for wrinkling processes is essentially that polymer surfaces can only be wrinkled on the lower end of the cm^2 scale.

Furthermore, from DE 10 2012 010 635 A1, [3] a method is known for the 3D structuring and shaping of surfaces made of hard, brittle, and optical materials. For this purpose, the surface of the materials is created using direct ablation by means of an ultrashort pulse laser, and the shaped surface is smoothed by means of a plasma jet.

According to WO2012/031201 A3, [4] a method for producing an anti-fouling surface with a micro- or nano-structured coating is also known. A substrate is thereby stretched, the surface of the stretched substrate is coated, and the stretching strain is then removed, so that the coated surface is compressed. The substrate can thereby be irradiated for the purpose of modification, and the coating of the substrate surface takes place solely be means of initiated chemical vapor deposition (iCVD).

With the known methods for fabricating surface-structured polymer bodies, these bodies can only be prepared with increased effort and inadequate structuring accuracy, and in particular only with an essentially isotropic arrangement of the structuring.

The object of the present invention is to specify surface-structured polymer bodies which have a high structuring accuracy with regard to the dimensions on the surface of the polymer bodies, and to specify a simple and cost-efficient method for the fabrication of said bodies.

The object is attained by the invention disclosed in the claims. Advantageous embodiments are the subject matter of the dependent claims.

In the surface-structured polymer bodies according to the invention, polymer bodies with dimensions of at least $\geq 100\ cm^2$ are present, the surfaces of which are at least partially covered with at least one nano- to micrometer-thick layer, and the layers are physically and/or chemically coupled to the polymer bodies, and the surface of the polymer bodies with the layers is at least partially deformed, wherein the deformation is periodic within a deformation type and the arrangement of multiple different deformation types on a polymer body is anisotropic or isotropic, and wherein the elastic modulus of the material of the polymer body is less than the elastic modulus of the layer materials.

Advantageously, polymer bodies with dimensions of 100 cm^2 to 100 m^2 are present. Fig. 45 as well as Fig. 46 show exemplarily the setup that is applied to form such polymer bodies.

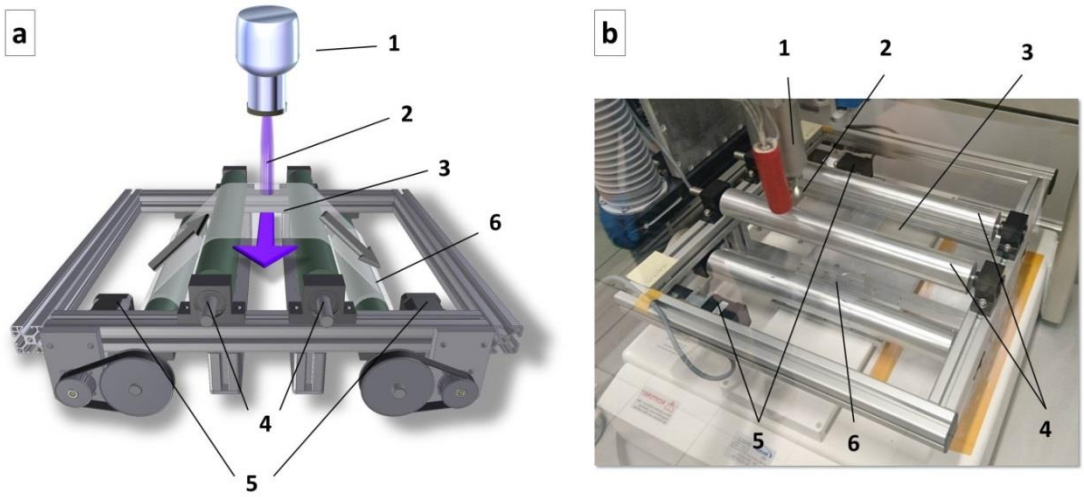

*Figure 45 | Schematic (**a**) and real setup (**b**) of large-scale wrinkling production via roll-to-roll process and in-situ-oxidation of PDMS with a plasma jet. The scheme shows the plasma nozzle (**1**) with the shout-out plasma jet (**2**) that hits the pre-strained PDMS foil (**3**). This is guided over two freely movable pulleys (**4**), which are propelled by two motor-driven and computer-controlled pulleys (**5**) mounted on a custom-made frame. The two grey arrows indicate the moving direction of the PDMS foil, which is slowly passed under the plasma jet. The purple arrow indicates the moving direction of the plasma jet that is permanently guided back and forth linearly between the two freely movable pulleys. The pre-strain is released between the third and fourth pulley (**6**), so that folds can form before winding up on the fourth pulley.*

Likewise advantageously, a layer having a layer thickness between 10 nm and 100 µm is present.

Also advantageously, the surfaces are coated with a layer composite of two to 10 layers on top of one another, wherein the total thickness of all layers is not more than 100 µm.

And also advantageously, the surface of a polymer body is completely or partially coated with a layer or a layer composite of different layer materials on top of or next to one another.

It is also advantageous if the physical coupling of the polymer bodies and layer or layer composite is achieved by mechanical interlocking or by means of van der Waals forces, and if the chemical coupling of the polymer bodies and layer or layer composite is achieved through chemical covalent bonds.

It is furthermore advantageous if the deformation within a deformation type on a polymer body is periodic and anisotropic.

It is likewise advantageous if, with the arrangement of multiple deformation types on a polymer body, the deformation within one arrangement is aligned in a periodic and isotropic manner and if the deformations among the different deformation types are aligned anisotropically to one another.

And it is also advantageous if the polymer bodies comprise multiple deformation types which differ in regard to the periodicity, dimensions, and/or shape of the deformations.

It is also advantageous if the materials of the polymer bodies are elastomers, thermoplastic elastomers, thermoplastics, and/or duromers, or if these materials are at least present on or contained in the polymer body surface that is to be coated.

It is furthermore advantageous if the layer or the layer composite is composed of metallic, polymeric, polymer-composite, ceramic, or vitreous materials.

It is also advantageous if the elastic modulus of the material of the polymer body is at least 1 order of magnitude less than the elastic modulus of the layer materials.

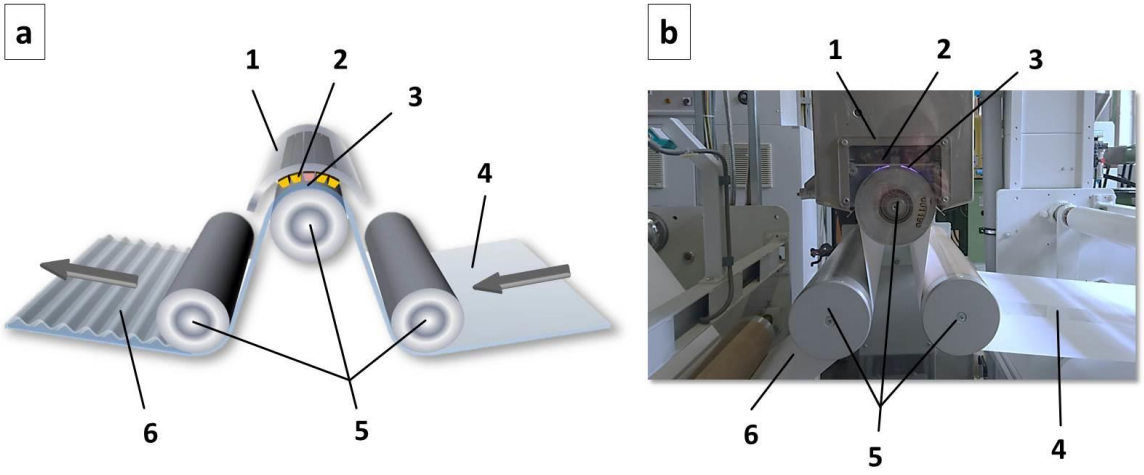

*Figure 46: Schematic (**a**) and real setup (**b**) of large-scale wrinkling production via roll-to-roll process and in-situ-oxidation of PDMS with a Dielectric Barrier Discharge (DBD). In the scheme a sheathing (**1**) covers the four high voltage electrodes (**2**), at which the silent discharge glow is generated homogeneously over a width of 50 cm (**3**). Through the discharge a PDMS foil that is piloted over a high-temperature stable paper sheet (**4**) is guided by diverse pulleys (**5**). After the second to last pulley the pre-strain is released, so that wrinkles can form (**6**) before winding up on the last roll (not visible in the scheme and real setup).*

In the method according to the invention for the fabrication of surface-structured polymer bodies, polymer bodies with dimensions of at least ≥ 100 cm^2 are subjected to a stretching strain in at least one direction at least

above the critical wrinkling stress and maximally up to below the fracture stress of the material of the polymer bodies, the surfaces of the polymer bodies are coated in the strained state with at least one nano- to micrometer-thick layer or layer composite by means of an atmospheric plasma or by means of printing or by means of knife coating, and the stretching strain of the polymer bodies is then released at least in sections, wherein the materials used in the polymer bodies have an elastic modulus which is less than the elastic modulus of the applied layer materials, and wherein the fabrication process is carried out continuously.

Advantageously, the critical wrinkling stress of the material of the polymer bodies is determined according to Eq. 4.7:

$$\sigma_c = \frac{F_c}{h\,w} = \left[\frac{9}{64}\left(\frac{E_s}{1-\nu_s^2}\right)\left(\frac{E_k}{1-\nu_k^2}\right)^2\right]^{1/3} \qquad (4.7)$$

Likewise advantageously, the layer application is carried out by means of atmospheric plasmas, for example, by means of plasma jet, by means of corona discharge, or by means of dielectric barrier discharge.

Also advantageously, precursor materials of the layer materials are used.

Also advantageously, the layer application is carried out by means of a plasma jet, the plasma activation cross-section of which is beam-shaped, in the shape of a rotating circle, and/or linearly flat.

With the solution according to the invention, it is for the first time possible to specify surface-structured polymer bodies which exhibit a high structuring accuracy in regard to the dimensions on the surface of the polymer bodies, and also to specify a simple and cost-effective method for the fabrication thereof.

This is achieved with surface-structured polymer bodies which, for example, are molded bodies such as injection molded parts or films that are two-dimensional with dimensions of at least ≥ 100 cm^2.

The materials of the polymer bodies used must thereby have at least the critical wrinkling stress as a minimum stretching strain. Only polymer materials of this type can be surface-structured according to the invention and can be present as surface-structured polymer bodies according to the invention.

The invention can be used in a particularly advantageous manner for a surface-structuring of polymer bodies with large dimensions of length and width compared to the thickness of said bodies, which dimensions are to be at least ≥ 100 cm^2, advantageously also 100 m^2 or even more.

Such large-area surface-structured polymer bodies that are scaled up from the polymer bodies from the prior art and have been fabricated in a continuous process are not yet known to date. Within the scope of the present invention, the scaling-up of the polymer bodies according to the invention is to mean that surface-structured

polymer bodies known from the prior art, the surface structuring of which corresponds to the deformation in the solution according to the invention, can be present and fabricated in significantly larger dimensions of length and width as a result of the solution according to the invention.

The surface-structured polymer bodies according to the invention comprise at least partially on their surface at least one nano- to micrometer-thick layer or one layer composite. The layer thickness of the layer or the layer composite is advantageously between 10 nm and 100 µm.

The length and width dimensions of the layer or the layer composite can be equal to or less than the maximum length and width dimensions of the polymer body, whereby the length and width dimensions of the layer or the layer composite can also be less than 100 cm^2.

In the case of a layer composite, this layer composite can advantageously be composed of two layers, but also up to 10 or 100 or several hundreds of layers on top of one another, wherein the total thickness of all layers is at least one order of magnitude smaller than the thickness of the polymer body.

The surface of the polymer bodies can also be completely or partially covered with one layer or one layer composite, wherein layers or layer composites made of different layer materials can also be arranged on top of and/or next to one another on a polymer body.

The layers or layer composites present according to the invention can, in addition to the surface structuring according to the invention, also comprise functional properties for the entire surface-structured polymer body, for example, they can be hydrophobic and/or oleophobic; electrically conductive or insulating; optically reflective, absorbent, or transmitting.

The layers or layer composites are physically and/or chemically coupled to the polymer bodies. The coupling of the layer materials to the polymer body material can, for example, be achieved by means of ionic bonding, van der Waals forces, chemical covalent bonds, or via mechanical interlocking.

The surface structuring of the polymer bodies takes place essentially through a deformation of the surface-proximate regions of the polymer bodies and the applied layers or layer composites. The surface of the polymer bodies with the layers is thereby at least partially deformed.

According to the invention, the deformation is periodic and advantageously also anisotropic within a deformation type, but can also be isotropic.

Within the scope of this invention, anisotropic deformation is to be understood as meaning that the deformation, at least in regard to the dimensions thereof in at least one direction, shows essentially identical deformations.

Within the meaning of the present invention, isotropic deformations are uneven and/or non-identical deformations, at least in regard to the dimensions thereof in multiple or all directions of the deformations.

Multiple different deformation types can also be arranged on a polymer body, in which types the deformation is isotropic or anisotropic. Advantageously, the deformation is also homogeneous within a deformation type, and is likewise advantageously sinusoidal, bisinusoidal, or quadrisinusoidal.

The periodicity can advantageously be 100 nm – 10 µm for a wrinkle-like deformation, for example.

The deformation in the case of multiple deformation types on a polymer body is advantageously also periodic and anisotropic within one deformation type, but among the multiple deformation types on a polymer body the different deformation types are also aligned anisotropically to one another or can also be aligned isotropically to one another.

The deformation types can thereby differ with regard to the periodicity, dimensions, and/or shape of the deformations.

Elastomers, thermoplastic elastomers, thermoplastics, and/or duromers can advantageously be present as materials for the polymer bodies, or they are at least present on the polymer body surface that is to be coated.

The layers or layer composites can be made of different polymer materials or metallic or ceramic, inorganic or organic layer materials, and of monolayers of molecules, particles or colloids of these materials.

The selection of the materials for the polymer bodies and layers which together form the surface-structured polymer body according to the invention takes place at least based on the elastic modulus of the respective materials, which is known for all usable materials or can be determined with little effort.

The elastic modulus of the material of the polymer body must thereby be at least 1 order of magnitude less than the elastic modulus of the layer materials.

In the method for the fabrication of surface-structured polymer bodies according to the invention, polymer bodies with dimensions of at least ≥ 100 cm^2 in two dimensions are subjected to a stretching strain in at least one direction, at least above the critical wrinkling stress and maximally up to below the fracture stress of the material of the polymer bodies.

At least the critical wrinkling stress of the polymer body material must be reached as a minimum stretching strain of the polymer bodies, which stress can be determined according to Eq. 4.7:

$$\sigma_c = \frac{F_c}{h\,w} = \left[\frac{9}{64}\left(\frac{E_s}{1-\nu_s^2}\right)\left(\frac{E_k}{1-\nu_k^2}\right)^2\right]^{1/3} \qquad (4.7))$$

Here, ε_c stands for the critical wrinkling stress, F_c for the corresponding critical force, h and w for the height and width of the polymer body being stretched, E_s and E_k for the respective elastic moduli of the materials of the polymer body and layer or layer composite, and ν_s and ν_f for the accompanying Poisson's ratios.

The stretching can thereby be carried out in at least one direction, or simultaneously in multiple directions. In this manner, multiple different deformation types can be produced at the same time on a polymer body, for example. By stretching the polymer body in only one spatial direction (uniaxial stretching strain), deformations can be produced in the shape of parallel wrinkles in two spatial directions positioned orthogonally to one another (biaxial stretching strain), referred to as herringbone or chevron patterns, which deformations are comparable to fishbone patterns. In addition, stretching strains of the polymer body in two or more directions that are not orthogonal to one another are also possible.

Stretching strains in a uniaxial as well as a biaxial direction also result in more complex deformations that can be composed of sinusoidal wrinkles, which are referred to as bisinusoidal and quadrisinusoidal wrinkles.

An important advantage of the solution according to the invention is that, according to the invention, deformations of this type can be achieved in a continuous process.

After achieving the stretching of the polymer bodies, the surfaces thereof are coated in the strained state with at least one nano- to micrometer-thick layer or a layer composite.

The coating of the polymer bodies thereby occurs by means of an atmospheric plasma, printing, or knife coating.

Advantageously, the coating occurs by means of atmospheric plasmas, for example, by means of plasma jet, by means of corona discharge, or by means of dielectric barrier discharge.

The layer materials or precursors of the layer materials can thereby be used as starting materials for the coating process. In particular, glass-forming precursors are used as precursors for the application by means of an atmospheric plasma. The precursors are thereby fragmented in the plasma during the plasma coating (ionized, radicalized, and at least pre-polymerized), and the layer on the surface is created by recombination.

Polydimethylsiloxane (PDMS), ethylene propylene diene monomer rubber (EPDM) or hydrogenated acrylonitrile butadiene rubber (HNBR), for example, can be used as materials for the polymer bodies, and hexamethyldisiloxane (HMDSO), hexamethyldisilazane (HMDSN), tetramethyldisiloxane (TMDSO), hexamethyltrisiloxane (HMTSO), tetramethyl orthosilicate (TMOS) or tetraethyl orthosilicate (TEOS), for

example, can be used as precursors for the coating. The elastic moduli of PDMS, EPDM, or HNBR are each less than the elastic moduli of HMDSO, HMDSN, TMDSO, HMTSO, TMOS, or TEOS.

Likewise, layers and layer composites can be formed directly in the material of the polymer body, that is, can be created in situ. For this purpose, polymeric materials such as silicones are required, which materials are characterized by their glass-forming property, for example, PDMS. By means of oxidation, radical formation, ionization, or reduction, the material undergoes a metamorphosis from a polymeric to a vitreous material. If this transformation takes place only in proximity to the surface, a layer, a layer-like film, or a layer composite is created as a result.

The use of atmospheric plasmas or printing or knife coating for the coating of polymer bodies and a subsequent deformation of at least the surface region and of the applied layer or layer composites is not previously known from the prior art.

Materials that can be fed into a plasma and processed under atmospheric conditions can be used as layer materials. For example, these can be metallic, polymeric, polymer-composite, ceramic, or vitreous materials.

The layer application can thereby take place in that the stretched polymer bodies are guided under the tools for the layer application, or the tools for the layer application are guided over the stretched polymer bodies.

Advantageously, the stretched polymer bodies are guided under the tools for the layer application, whereby very uniform activation cross-sections and a high structuring homogeneity are achieved.

For practical purposes, what are referred to as roll-to-roll processes are used for the layer application with the use of atmospheric plasmas, which processes comprise stretching devices for the polymer bodies that stretch the polymer bodies, that is, keep them under tension, and with which devices the polymer bodies are rolled up or unrolled under the constant stretching strain.

For the surface modification of polymer bodies according to the invention, polymer bodies are used in which the elastic modulus of the polymer body material is less, advantageously at least 1 order of magnitude less, than the elastic modulus of the applied layer materials.

Following the application of the coating to the polymer bodies, the stretching strain of the polymer bodies is removed at least in sections, that is, for example, the mechanical and/or thermal tension or tension due to swelling processes of the polymer bodies is released.

It is particularly important for the solution according to the invention that the fabrication process is carried out continuously.

Thus, according to the invention, large-area to very large-area surface-modified polymer bodies can be continuously fabricated in an ongoing production process, which had not been achieved previously according to the prior art.

With the method according to the invention, surface-structured polymer bodies according to the invention can be fabricated which exhibit a high structuring accuracy with regard to the dimensions on the surface of the polymer bodies. On the one hand, large areas of the polymer bodies up to the square-meter scale can thereby be surface-structured simultaneously and, with regard to the dimensions thereof and the shapes of the deformation, homogeneous structuring can thereby be achieved on the nm scale to the µm scale.

It is further advantageous that not only anisotropic structures can be fabricated, but also isotropic structures at the same time on a polymer body.

It is likewise an advantage of the solution according to the invention that the applied layer or the layer composite comprises functional properties, such as for example increased or reduced hydrophilicity, electrical conductivity or electrical insulation; increased or reduced optical activity, such as reflection, absorption or transmission; increased chemical and mechanical resistance; and increased or reduced static and kinetic friction; or that the properties of the applied layers or layer composites have been advantageously influenced by the parameters of the layer application.

In contrast to solutions from the prior art, anisotropic as well as isotropic structuring of the surface of polymer bodies can be achieved in a targeted manner with the solution according to the invention.

According to the invention, with the use of plasma-assisted methods for coating, monomers of the precursors can also be radicalized, applied to the surface, and polymerized. With the use of plasma-assisted methods, molecules can be used which can be polymerized not only radically or ionically. Here, additional physical and chemical processes play a role, which processes also take place via a fragmentation and recombination of molecules and thus allow other cross-links than merely polymerization processes.

The invention is explained below in greater detail with the aid of several exemplary embodiments.

4.3.3. Application examples

Example 1

A 100 x 20 x 0.025 cm film of polydimethylsiloxane (PDMS) with an elastic modulus of 2.5 MPa was stretched in a roll-to-roll stretching device. The stretching strain of the film was thereby set to a constant value of 10%. For the coating of the 70 x 20 cm effectively available area of the polymer film, the film was passed over by a punctiform plasma nozzle (PlasmaTreat GmbH, Steinhagen, Germany) with a diameter of 1 cm. The distance of the nozzle from the sample surface was 10 – 25 mm, the rated power of the plasma nozzle was 5.04 kW (280 V at 18 A), the travel speed of the nozzle over the sample was 100 mm/s.

As precursors for the layer deposition, tetraethyl orthosilicate (TEOS) with an elastic modulus of 450 MPa for the resulting layer was fed to the plasma nozzle. By means of the plasma nozzle, a homogeneous 100 nm-thick layer was deposited, which was composed of oligomeric, minimally cross-linked silicate following the deposition.

With the unrolling of the coated polymer film from the last roller of the roll-to-roll stretching device, the stretching strain was discontinued during the continuous process, and a surface-structured polymer film was present.

The surface structuring was composed of anisotropically arranged wrinkles with a periodicity of 1.5 µm and a structure height of 450 nm. The results are depicted in Fig. 47.

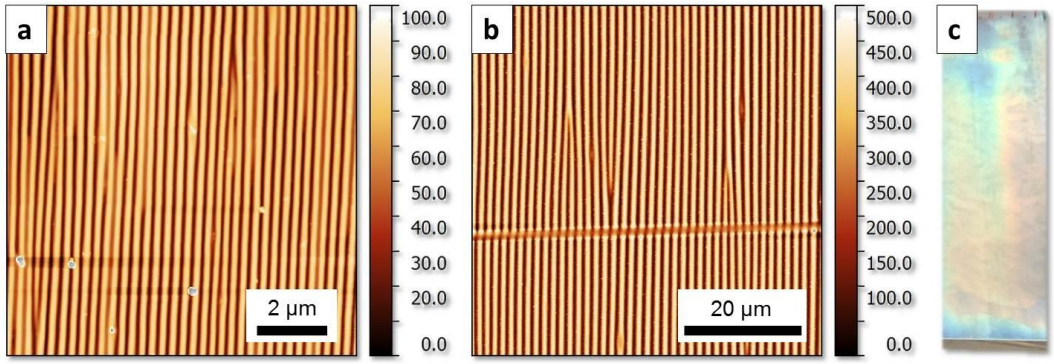

*Figure 47 | Wrinkled layer of TEOS on PDMS, prepared at a nozzle distance of 16 mm (**a**) resulting in λ = 300 nm, and at a distance of 10 mm (**b**) resulting in λ = 1.5 µm; (**c**) Image of a TEOS-coated and wrinkled PDMS-slab of 7 x 2 cm size.*

Example 2

A 100 x 20 x 0.1 cm film of acrylonitrile butadiene rubber (NBR) with an elastic modulus of 2.3 MPa was stretched in a roll-to-roll stretching device. The stretching strain of the film was thereby set to a constant value of 8%. The

for the coating of the 70 x 20 cm effectively available area of the polymer film, the film was passed over by a rotating plasma nozzle (PlasmaTreat GmbH, Steinhagen, Germany) with a diameter of 0.5 cm. The distance of the nozzle from the sample surface was 16 mm, the rated power of the plasma nozzle was 4.77 kW (265 V at 18 A), the travel speed of the nozzle over the sample was 100 mm/s.

As a precursor for the layer deposition, hexamethyldisiloxane (HMDSO) with an elastic modulus of 250 MPa for the resulting layer was fed to the plasma nozzle. The deposition rate of the precursor was varied between 4 and 120 g/h.

By means of the plasma nozzle, a layer of varying thickness between 5 and 200 nm was deposited, which was composed of oligomeric, minimally cross-linked silicate following the deposition.

With the unrolling of the coated polymer film from the last roller of the roll-to-roll stretching device, the stretching strain was discontinued during the continuous process, and a surface-structured polymer film was present.

The surface structuring was composed of anisotropically arranged wrinkles with a periodicity between 350 mm and 3.75 µm and a structure height of 100 nm and 1.15 µm nm. The results are depicted in Fig. 48.

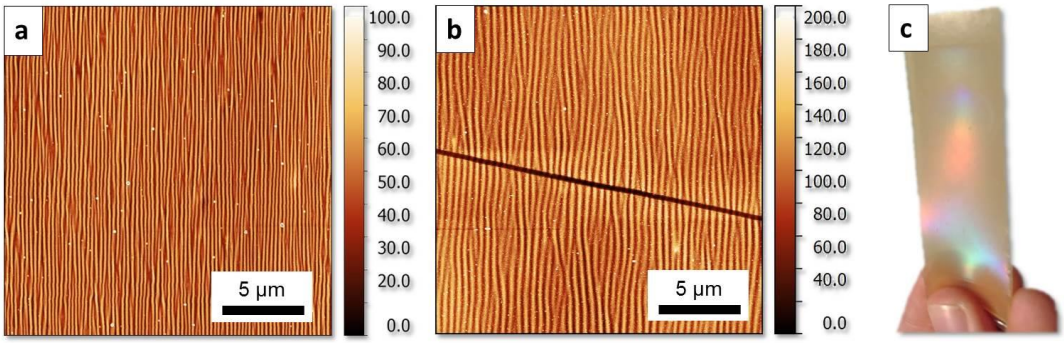

*Figure 48 | Wrinkled layer of HMDSO on NBR, prepared with a coating rate of (**a**) 4 g/h resulting in λ = 260 nm and with (**b**) ṁ = 40 g/h resulting in λ = 1.3 µm; (**c**) Image of a HMDSO-coated and wrinkled NBR-slab of 7 x 2 cm size.*

Example 3

A 100 x 50 x 0.0025 cm film of polydimethylsiloxane (PDMS) with an elastic modulus of 2.5 MPa was set out on a base paper with a longitudinal pre-strain of 15%. The 95 x 50 cm area of the polymer film effectively available for the coating was subjected to a plasma treatment with a dielectric barrier discharge (DBD) (4-part DBD - Fraunhofer IST, Braunschweig, Germany).

The distance of the electrode to the sample surface was set to 0.2 mm, the rated power of the DBD was 600 W, the unrolling and rolling-up speed was 0.5 m/min.

As a precursor for the layer deposition, tetramethyldisiloxane (TMDSO) with an elastic modulus of 300 MPa for the resulting layer was used. The deposition rate of the precursor was set to 7 L/m by means of a gas transport, which corresponds to a theoretical deposition rate of ~ 3 g/h.

After the unrolling of the coated polymer film from the last roller of the roll-to-roll DBD device, the stretching strain was discontinued, and a surface-structured polymer film was present.

The surface structuring was composed of anisotropically arranged wrinkles with a periodicity between 2.5 µm and 7 µm and a structure height between 450 nm and 2 µm. The results are depicted in Fig. 49.

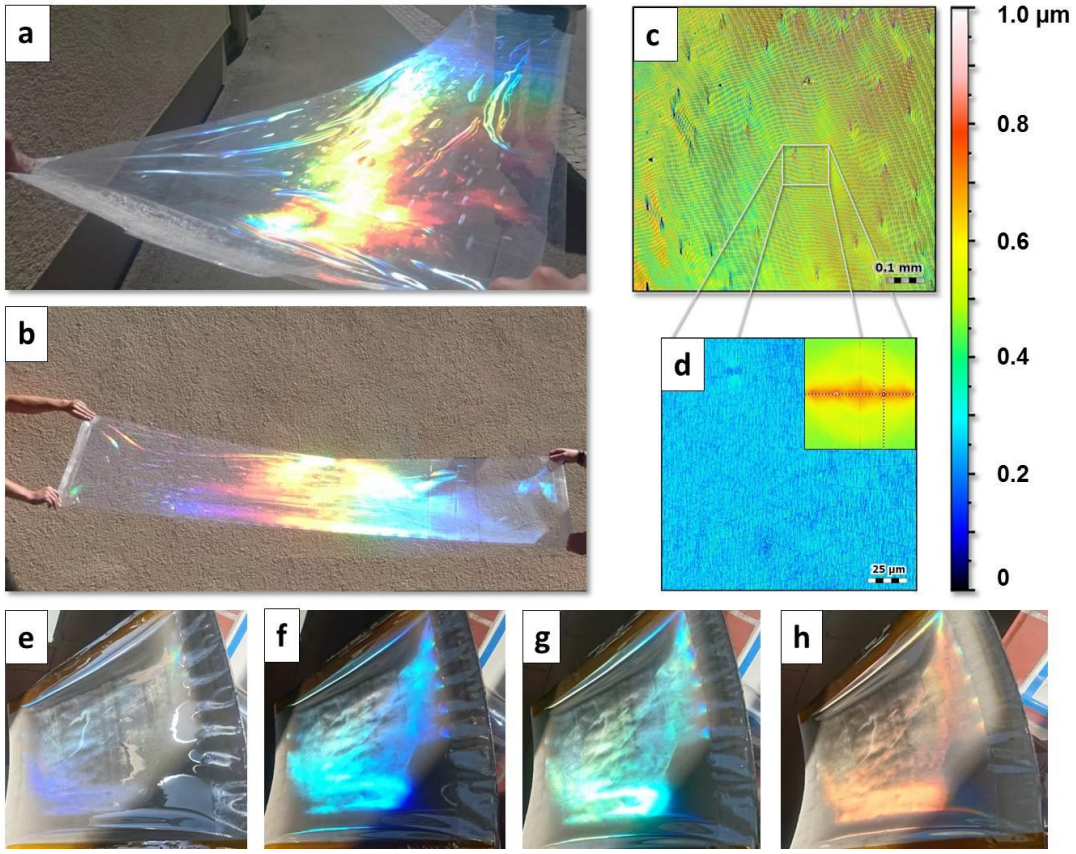

*Figure 49 | (**a**) and (**b**) wrinkled PDMS foil (wrapped in a protective PET foil from both sides) with dimensions of 2.5 x 0.5 m (1.25 m^2) x 0.25 mm, exhibiting an average wavelength of λ = 764 nm. (**c**) and (**d**): Optical confocal microscopy image at 10x (**c**) as well as 100x (**d**) magnification, the latter showing additionally a 2D-FT inset in which the 1st order scattering peak is marked with a dotted line. Confocal microscopy is chosen since the sample is too large to place it under the AFM. (**e**) – (**h**): PDMD wrinkled foil, prepared under the same conditions and additionally coated via PVD with a TiO_2-layer of 120 nm thickness; due to the enhanced refractive index of n_{TiO2} = 2., the lattice structure reveals maxima in the diffraction spectrum that are in the range of visible light, reaching over the whole spectrum from violet (**e**) over blue (**f**) and green (**g**) to red (**h**).*

Example 4

1) Bisinusoidal and quadrisinusoidal wrinkling

A 100 x 10 x 0.050 cm film of polydimethylsiloxane (PDMS) with an elastic modulus of 2.1 MPa was stretched in a roll-to-roll stretching device. The stretching strain of the film was thereby set to a constant value of 85%. For the coating of the polymer film, the film was passed over by a punctiform plasma nozzle (PlasmaTreat GmbH, Steinhagen, Germany) with a diameter of 1 cm. The distance of the nozzle from the sample surface was 10 mm,

the rated power of the plasma nozzle was 6.3 kW (350 V at 18 A), the travel speed of the nozzle over the sample was 25 mm/s.

The PDMS was oxidized in situ in order to thus create the layer. The layer obtained had a thickness of 180 nm at an average elastic modulus of 150 MPa for the resulting layer.

With the unrolling of the coated polymer film from the last roller of the roll-to-roll stretching device, the stretching strain was discontinued during the continuous process, and a surface-structured polymer film was present.

The surface structuring was composed of anisotropically arranged bisinusoidal wrinkles with a periodicity of 1.5 µm and a structure height of 550 nm for the deep amplitude and 350 nm for the flat amplitude (see Fig. 50 **a** and **c**).

If the film is stretched to 95%, anisotropically arranged quadrisinusoidal wrinkles are obtained with a periodicity of 2.5 µm and a structure height of 650 nm for the deep amplitude, 350 nm for the middle amplitude, and 100 nm for the flat amplitude. The results are depicted in Fig. 50.

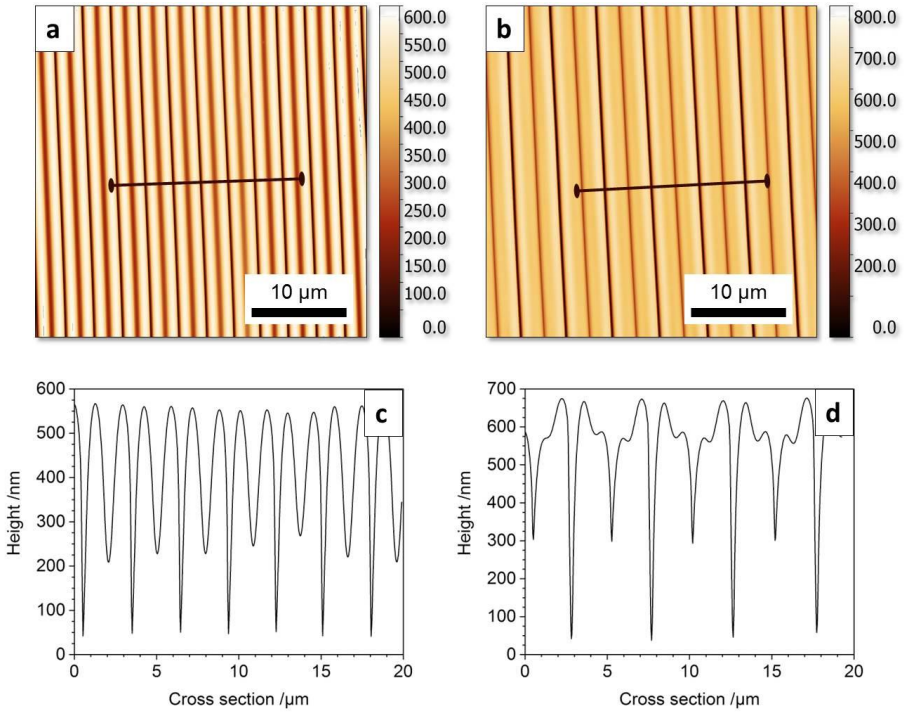

*Figure 50 | Topographical AFM images of (**a**) bi-sinusoidal and (**b**) quadro-sinusoidal wrinkles with the according cross section profiles of bi (**c**) and quadro (**d**).*

2) Biaxial stretching orthogonal to one another

A 100 x 10 x 0.125 cm film of polydimethylsiloxane (PDMS) with an elastic modulus of 2.0 MPa was stretched longitudinally in a roll-to-roll stretching device and, transversely thereto, in two sliding film stretchers made of polytetrafluoroethylene (PTFE). The stretching strain of the film was thereby set to a constant value of 5% in both directions orthogonal to one another. For the coating of the polymer film, the film was passed over by a circularly rotating plasma nozzle (PlasmaTreat GmbH, Steinhagen, Germany) with a diameter of 2.5 cm. The distance of the nozzle from the sample surface was 13 mm, the rated power of the plasma nozzle was 6.3 kW (350 V at 18 A), the travel speed of the nozzle over the sample was 50 mm/s.

The PDMS was oxidized in situ in order to thus create the layer. The layer obtained had a thickness of 110 nm at an average elastic modulus of 85 MPa for the resulting layer.

With the unrolling of the coated polymer film from the last roller of the roll-to-roll stretching device, the stretching strain was discontinued during the continuous process, and a surface-structured polymer film was present.

The surface structuring was composed of anisotropically arranged wrinkles that were directed orthogonally to one another in regular patterns, also referred to as a chevron or herringbone structure. A periodicity of 1.4 µm and a structure height of 80 nm were present in both spatial directions. The results are depicted in Fig. 51.

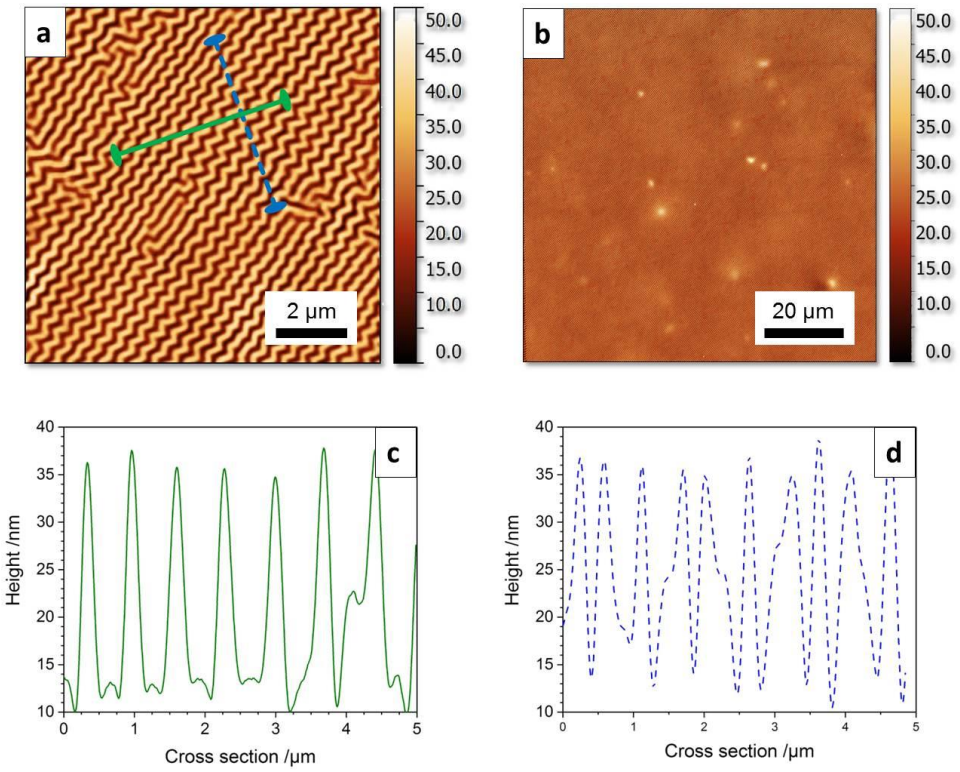

*Figure 51 | (**a**) and (**b**): Topographical AFM images of biaxial wrinkles, in which regularly patterns of orthogonally aligned waves are formed, also known as "Chevron" or "Herringbone" structures; The two cross section profiles (**c**) and (**d**) are extracted from (**a**) and demonstrate the biaxial, orthogonal repetitive character of the sample.*

4.3.4. Patent Claims

1. Surface-structured polymer bodies in which polymer bodies with dimensions of at least ≥ 100 cm^2 are present, the surfaces of which are at least partially covered with at least one nano- to micrometer-thick layer, and the layers are physically and/or chemically coupled to the polymer bodies, and the surface of the polymer bodies with the layers is at least partially deformed, wherein the deformation is periodic within a deformation type and the arrangement of multiple different deformation types on a polymer body is anisotropic or isotropic, and wherein the elastic modulus of the material of the polymer body is less than the elastic modulus of the layer materials.

2. The surface-structured polymer bodies according to claim 1 in which polymer bodies with dimensions of 100 cm^2 to 100 m^2 are present.

3. The surface-structured polymer bodies according to claim 1 in which a layer with a layer thickness between 10 nm and 100 µm is present.

4. The surface-structured polymer bodies according to claim 1 in which the surfaces are coated with a layer composite of two to 10 layers on top of one another, wherein the total thickness of all layers is not more than 100 μm.

5. The surface-structured polymer bodies according to claim 1 in which the surface of a polymer body is completely or partially coated with a layer or a layer composite of different layer materials on top of or next to one another.

6. The surface-structured polymer bodies according to claim 1 in which the physical coupling of the polymer bodies and layer or layer composite is achieved by mechanical interlocking or by means of van der Waals forces, and the chemical coupling of the polymer bodies and layer or layer composite is achieved through chemical covalent bonds.

7. The surface-structured polymer bodies according to claim 1 in which the deformation within a deformation type on a polymer body is periodic and anisotropic.

8. The surface-structured polymer bodies according to claim 1 in which, with the arrangement of multiple deformation types on a polymer body, the deformation within one arrangement is aligned in a periodic and isotropic manner and the deformations among the different deformation types are aligned anisotropically to one another.

9. The surface-structured polymer bodies according to claim 1 in which the polymer bodies comprise multiple deformation types which differ in regard to the periodicity, dimensions, and/or shape of the deformations.

10. The surface-structured polymer bodies according to claim 1 in which the materials of the polymer bodies are elastomers, thermoplastic elastomers, thermoplastics, and/or duromers, or these materials are at least present at or contained in the polymer body surface that is to be coated.

11. The surface-structured polymer bodies according to claim 1 in which the layer or the layer composite is composed of metallic, polymeric, polymer-composite, ceramic, or vitreous materials.

12. The surface-structured polymer bodies according to claim 1 in which the elastic modulus of the material of the polymer body is at least 1 order of magnitude less than the elastic modulus of the layer materials.

13. A method for the fabrication of surface-structured polymer bodies in which polymer bodies with dimensions of at least ≥ 100 cm^2 are subjected to a stretching strain in at least one direction at least above the critical wrinkling stress and maximally up to below the fracture stress of the material of the polymer bodies, the

surfaces of the polymer bodies are coated in the strained state with at least one nano- to micrometer-thick layer or layer composite by means of an atmospheric plasma or by means of printing or by means of knife coating, and the stretching strain of the polymer bodies is then released at least in sections, wherein the elastic modulus of the materials used in the polymer bodies is less than the elastic modulus of the applied layer materials, and wherein the fabrication process is carried out continuously.

14. The method according to claim 13 in which the critical wrinkling stress of the material of the polymer bodies is determined according to Eq. 4.7:

$$\sigma_c = \frac{F_c}{h\,w} = \left[\frac{9}{64}\left(\frac{E_s}{1-\nu_s^2}\right)\left(\frac{E_k}{1-\nu_k^2}\right)^2\right]^{1/3} \qquad (4.7))$$

15. The method according to claim 13 in which the layer application is carried out by means of atmospheric plasmas, for example, by means of plasma jet, by means of corona discharge, or by means of dielectric barrier discharge.

16. The method according to claim 13 in which precursor materials of the layer materials are used.

17. The method according to claim 13 in which the layer application is carried out by means of a plasma jet, the plasma activation cross-section of which is beam-shaped, in the shape of a rotating circle, and/or linearly flat.

References

[1] N. Bowden, S. Brittain, A.G. Evans, J.W. Hutchinson and G.M. Whitesides: Spontaneous formation of ordered structures in thin films of metals supported on an elastomeric polymer, **1998**; *Nature*, 393 - 146

[2] Y. Xia and G.M. Whitesides: Soft Lithography, **1998**; *Angew. Chem. Int. Ed.*, 37 - 5, 550-575

[3] G. Böhm, K. Zimmer, T. Arnold, H. Paetzelt and M. Ehrhardt: Three dimensional structuring or shaping of hard, brittle, and optical materials, comprises patterning surface of a hard, brittle and optical material with an ultra-short pulse laser, where surface of structure is smoothed by plasma jet, **2012,** DE102012010635, DE102012010635A1

[4] M.C. Boyce, D. Eggenspieler, K.K. Gleason and G. Ince: Fabrication of anti-fouling surfaces comprising a micro- or nano-patterned coating, **2010,** WO2012031201A3

4.4. Publication – Wafer-sized multifunctional polyimine-based two-dimensional conjugated polymers with high mechanical stiffness

4.4.1. Abstract

One of the key challenges in two-dimensional (2D) materials is to go beyond graphene, a prototype 2D polymer (2DP), and to synthesize its organic analogues with structural control at the atomic- or molecular-level. Here we show the successful preparation of porphyrin-containing monolayer and multilayer 2DPs through Schiff-base polycondensation reaction at an air–water and liquid–liquid interface, respectively. Both the monolayer and multilayer 2DPs have crystalline structures as indicated by selected area electron diffraction. The monolayer 2DP has a thickness of ∼ 0.7 nm with a lateral size of 4-inch wafer, and it has a Young's modulus of 267 ± 30 GPa. Notably, the monolayer 2DP functions as an active semiconducting layer in a thin film transistor, while the multilayer 2DP from cobalt-porphyrin monomer efficiently catalyses hydrogen generation from water. This work presents an advance in the synthesis of novel 2D materials for electronics and energy-related applications.

4.4.2. Introduction

Two-dimensional (2D) polymers (2DPs) that are laterally infinite, one atom- or monomer-unit thin, free-standing, covalent networks with long-range order along two orthogonal directions have attracted intense attention in recent years due to their wide applications in electronics, membrane and sensing. [1-4] A prototypical example of the 2DPs is graphene, a zero bandgap semiconductor consisting of an atomic layer of sp^2-carbons, which has demonstrated exceptional electron mobility, quantum Hall effect and ballistic charge carrier transport behavior. [5] However, if not provided by nature, the synthesis of graphene involves high-energy procedures, such as chemical vapour deposition (CVD), epitaxial growth and pyrolysis [6, 7] The harsh experimental conditions preclude molecular design of graphene on demand. As a first step to rationally synthesize 2DPs, 2D monolayers of porphyrin nanostructures and porous graphene on crystalline metal surfaces have been constructed through Ullmann coupling under ultra-high vacuum conditions. [8, 9] However, the synthesized 2D monolayers are limited to nanometers in size, and their release from original substrate is challenging. As an alternative approach, 2DPs have been recently achieved through ultraviolet initiated cycloaddition of anthracene-based monomers either in lamellar organic crystals followed by exfoliation into individual layers or at an air–water interface of a Langmuir-Blodgett (LB) trough. [10-13] The exfoliation method provides synthetic 2DPs with limited lateral size, typically ranging from a few hundred nanometers to several micrometers, which in the end are determined by crystal sizes. In contrast, the air–water interface method in principle offers 2DPs with unlimited lateral size, which is confined to that of irradiation spot for photochemical reaction. Despite the current progress, conjugation is missing in synthetic 2DPs, which impedes their applications in electronics and optoelectronics. Moreover, the mechanical property and functionality of synthetic 2DPs have not been explored so far. The future research and

application of this intriguing class of materials urgently call for the efficient synthesis of 2DPs with versatile methodology and structures.

Schiff-base condensation reaction, which forms a conjugated imine bond from an amine and an aldehyde group has been widely explored in the synthesis of covalent organic frameworks (COFs). [14, 15] Especially, intramolecular hydrogen bonds formed at the imine center can significantly enhance the structural rigidity, crystallinity and chemical stability of the synthesized COFs in aqueous solution. [16] Thus, we envision that such a reaction will be a promising methodology for the synthesis of large-area 2DPs at the water-containing interfaces. Although Schiff-base reaction without intramolecular hydrogen bond formation has been recently applied to obtain organic thin layers at an air–water interface, they have no proven crystallinity, which is a key feature regarding the synthesis and application of 2D layered materials. [17] Herein, we demonstrate the efficient synthesis of crystalline monolayer and multilayer 2DPs through Schiff-base condensation reaction between 5,10,15,20-tetrakis(4-aminophenyl)-21H,23H-porphine (monomer 1) or 5,10,15,20-tetrakis(4-aminophenyl)-21H,23H- porphyrin-Co(II) (monomer 2) and 2,5-dihydroxyterephthalaldehyde (monomer 3) at an air–water and water–chloroform interface, respectively. The resulting monolayer 2DP (4), which is as large as a 4-inch wafer, has demonstrated outstanding mechanical robustness with a Young's modulus of $\sim$ 267±30 GPa. Remarkably enough, the achieved monolayer 2DP (4) can function as an active semiconducting layer in a thin film transistor (TFT), whereas the multilayer 2DP (5) from cobalt-porphyrin monomer can efficiently catalyse the hydrogen generation from water.

4.4.3. Results

Synthesis and morphology of monolayer 2DP

Fig. 52 illustrates the interfacial synthesis of targeted 2DPs by Schiff-base polycondensation. A sub-monolayer of monomer 1 was first spread at an air–water interface of a LB trough from chloroform solution and compressed to a surface pressure of $10\ \frac{mN}{m}$, which promoted the formation of densely packed 1. Afterwards, monomer 3 was added to the subphase and diffused to the interface where 2D polymerization was triggered by the formation of imine bonds between amine and aldehyde groups in monomer 1 and 3, respectively. The interfacial reaction has been kept for more than four hours (vide infra) to promote the reaction conversion for the formation of the 2DP (4).

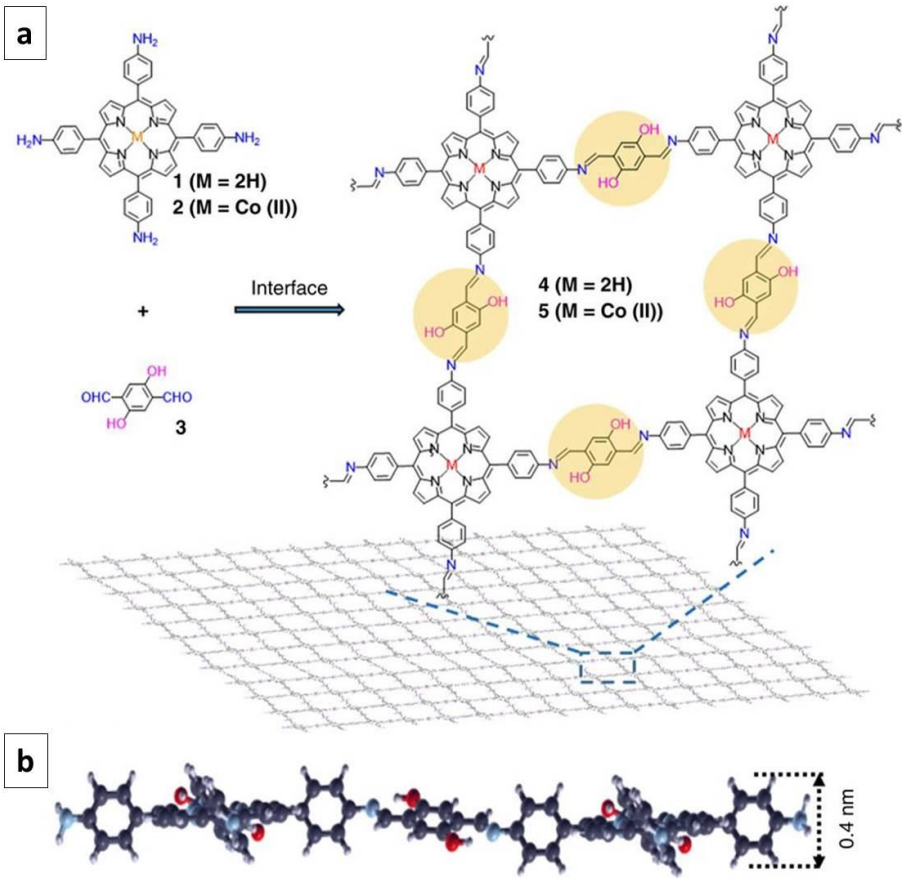

*Figure 52 | (**a**) Chemical structures of monomers (1, 2 and 3) and 2DPs (4 and 5). (**b**) Cross-sectional view of the molecular structure of a monolayer 2DP (4) suggested by DFTB.*

The resulting 2DP (4) can be readily transferred to any substrates. For instance, the horizontal transfer of the 2DP from the top of the water surface onto holey copper grid led to a freely suspended film over hexagonal holes with a slide length of ~ 20 µm (Fig. 53 **a**). A few cracks and folds were observed which are likely due to the mechanical stain caused during the transfer or/and drying process. Nevertheless, continuous film with an area of 1 mm^2 was typically obtained, suggesting high mechanical stiffness of the 2DP. Control experiments under the same experimental conditions for the synthesis of 2DP involving only monomer 1 or 3 failed to obtain a freestanding film.

After a vertical transfer of the 2DP onto 300 nm SiO_2/Si wafers, optical microscopy (OM) and atomic force microscopy (AFM) were performed to study the morphology of the 2DP. The OM image shows a macroscopically homogenous film with long straight edges (several hundred micrometers, Fig. 53 **b**), indicating that the 2DP breaks along a cleavage direction. The crack helps to locate an AFM tip to measure the film thickness, which amounts to ~ 0.7 nm (Fig. 53 **c**), thus suggesting the single-layer feature of the synthesized 2DP.

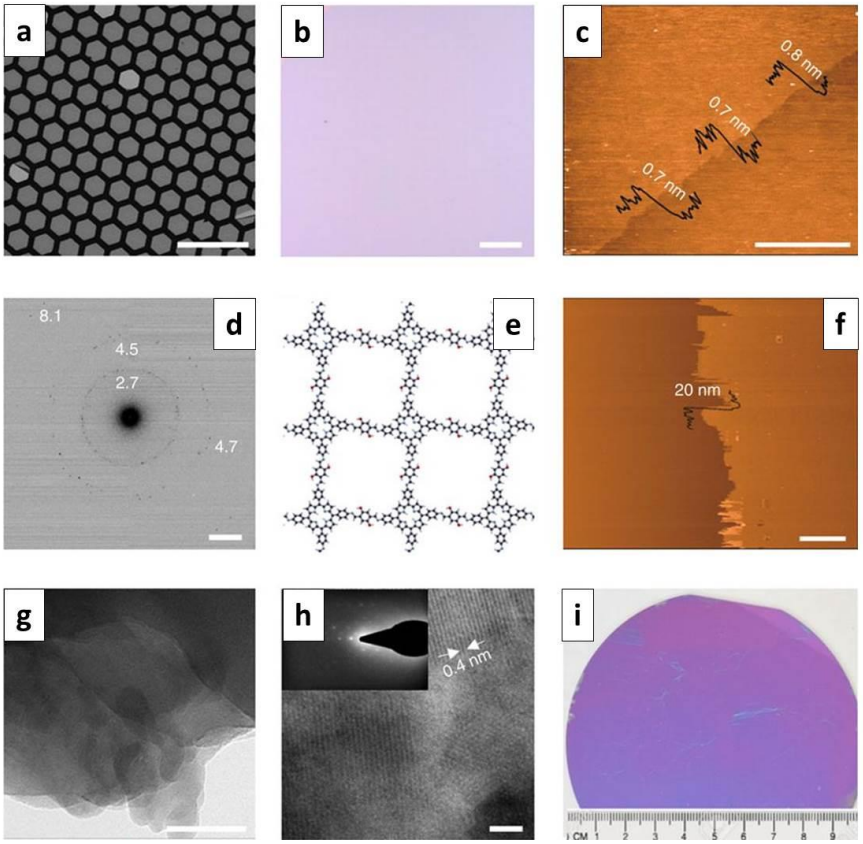

*Figure 53 | (**a**) Scanning electron and (**b**) optical microscopy images of monolayer 2DP suspended over a copper grid and deposited on 300 nm SiO_2/Si, respectively. (**c**) Atomic force microscopy (AFM) image of the monolayer 2DP on 300 nm SiO_2/Si. (**d**) Selected area electron diffraction (SAED) pattern of the monolayer 2DP sandwiched by two layers of graphene (G), G/2DP/G. (**e**) Molecular structure of the monolayer 2DP predicted by DFTB calculation. (**f**) AFM, and (**g,h**) TEM images of a multilayer 2DP synthesized at liquid–liquid interface. The insert in **h** is a SAED pattern of the multilayer. (**i**) Photographic image of monolayer 2DP on 4-inch 300 nm SiO_2/Si wafer. Scale bar, 100 µm (**a**); scale bar, 100 µm (**b**); scale bar, 3 µm (**c**); scale bar, 2 nm^{-1} (**d**); scale bar, 3 µm (**f**); scale bar, 50 nm (**g**) and scale bar, 3 nm (**h**), respectively.*

Structural characterization of mono- and multi-layer 2DPs

The internal structure of the monolayer 2DP was investigated by selected area electron diffraction (SAED) performed in a transmission electron microscope (TEM). However, due to the high electron beam sensitivity the freestanding 2DP was deteriorated rapidly and no diffraction pattern could be observed even under cryogenic condition (– 175 °C). To combat the negative effects of electron radiation, such as knock-on damage, electrostatic charging and chemical etching, a graphene encapsulation method was applied to enhance the radiation resistance of the 2DP. [18] To this end, a graphene-2DP-graphene sandwich structure was constructed using

graphene grown on copper foil by CVD at ~ 1,000 °C. In addition, low dose (below 0.05 e^{-} $Å^{-2}$ s^{-1}) diffraction technique was applied to better preserve the structure of the 2DP. Several rings composed of weak but clear diffraction spots were observed from the sandwich structures (Fig. 53 **d**). The diffraction spots at 4.7 and 8.1 nm^{-1} correspond well to the first and second order reflections of graphene. [19] The other diffraction spots originate from the 2DP, proving the existence of long-range order within the synthesized monolayer film. The diffraction spots at 2.7 nm^{-1} (~ 0.37 nm) and 4.5 nm^{-1} (~ 0.22 nm) are attributed to the cavity of the porphyrin units (~ 0.4 nm) and benzene and dihydroxylbenzene rings, respectively. This result suggests that the monolayer film consists of highly ordered arrangement of monomers 1 and 3, which agrees well with the structure of the 2DP based on density functional based tight binding (DFTB) calculation (Fig. 53 **e**). It is worth mentioning that the same diffraction rings has been repeatedly observed from different positions of the monolayer, which indicates high homogeneity of the polycrystalline 2DP on the unit-cell level.

AFM, TEM and SAED measurements have also been performed on a multilayer 2DP film, which was prepared at liquid–liquid interface using an aqueous solution of monomer 3 (upper phase, $1 \cdot 10^{-3} \frac{mol}{l}$) and a chloroform solution of monomer 1 (lower phase, $2 \cdot 10^{-4} \frac{mol}{l}$) with a reaction time of 10 days. The synthesized multilayer was fished onto 300 nm SiO_2/Si, which gave an AFM thickness of ~ 20 nm (**Fig.** 53 **f**). It could also be fished onto a copper grid, leading to a freely suspended film, and was further characterized with TEM and SAED. At the edge of the film, laminar structures were identified, suggesting that the synthesized 2DP had a multilayer feature (Fig. 53 **g**). High-resolution image of the film exhibits well-ordered lines due to the stacking of the layers. The layer distance is about 0.4 nm, pointing out the thickness of each layer, which is similar to that predicted by DFTB calculation (Fig. 52 **b**). When SAED was performed on the film, moiré fringes were observed, which indicated that the multilayer 2DP adopted slight interlayer offsets typical for stacked aromatic systems that have been observed within other layered materials, such as trilayer graphene and exfoliated 2D COFs. [20, 21] The shape of the moiré fringes is square (Fig. 53 **h**, inset), indicating the lattice geometry for the 2DP, which is in agreement with the structure derived from DFTB calculation (Fig. 53 **e**).

Spectroscopic characterization of 2DPs

To evaluate the chemical composition and homogeneity of the 2DP, the monolayer was horizontally transferred onto a quartz substrate and characterized by ultraviolet–visible spectroscopy. Ultraviolet–visible spectra of the monolayer shows the characteristic Soret (S) band at 442 nm and Q bands at 526, 571 and 656 nm, which correspond to porphyrin units, thereby further confirming their presence in the 2DP (Fig. 54 **a**). The S band of the 2DP red-shifts by 20 nm in comparison to that of the monomer 1, suggesting the existence of extended conjugation within the 2DP. Assuming that all the porphyrin moieties were lying parallel to the surface, the measured absorbance (~ 0.05) of the S band from the 2DP agrees well with calculated value of a monolayer with

100 % surface coverage. A multilayer 2DP was fabricated by repeated horizontal transfer of monolayers on a quartz substrate in a layer-by-layer fashion to evaluate the homogeneity of the 2DP and study the change in optical properties with controlled growth of layer thickness. Fig. 54 **b** shows a linear correlation between the absorbance value of the S band and the number of layers, following the Beer–Lambert law. The result clearly shows that the addition of each layer leads to the deposition of same amount of porphyrin units, which confirms the macroscopic homogeneity of the 2DP. The higher signal-to-noise ratio of the multilayer in comparison with that of monolayer also gives a more precise estimation of the optical band gap of the 2DP from the Q band of the absorbance spectra, which amounts to 1.4 eV. The electronic band gap of the 2DP is also computed by DFTB, and the corresponding projected density of states indicate a value of 1.3 eV (Fig. 54 **c**). Both the experimental and theoretical values are consistent with each other, which supports the semiconducting nature of the synthesized 2DP.

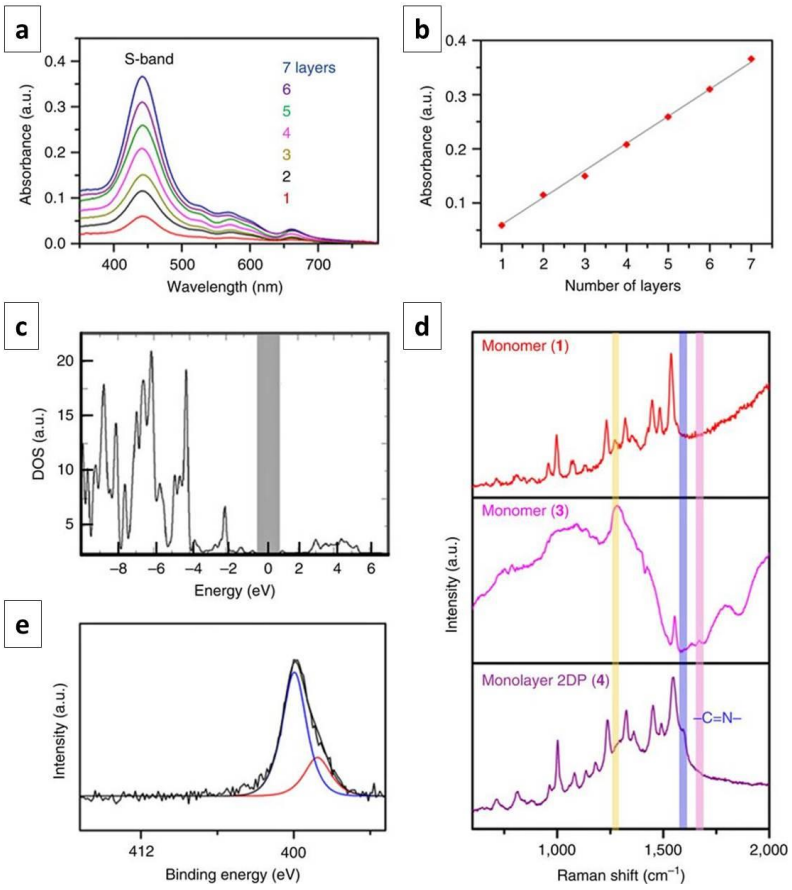

*Figure 54 | (**a**) Ultraviolet–Vis spectra of up to seven layers of 2DPs on quartz. (**b**) Plot of S band absorbance versus number of 2DPs. (**c**) Density of states (DOS) versus energy of the 2DP as calculated by DFTB. (**d**) Raman spectra of monomers (1, 3) and 2DP (4) on 300 nm SiO_2/Si. (**e**) X-ray photoelectron spectrum for N1s signal of monolayer 2DP on Au/Si. a.u., arbitrary unit.*

To gain insights into the chemical composition of the monolayer as well as the multilayer 2DPs, they were horizontally transferred onto 300 nm SiO_2/Si and Au/Si, and characterized by confocal Raman spectroscopy and X-ray photoelectron spectroscopy (XPS). Raman spectroscopy has been shown to have a sensitivity down to the single-molecule level and is capable of monitoring ions evolution in monolayer sheet, [22-24] which is vital for the characterization of 2DPs. Thus, we investigated the Raman spectra of monomers (1, 3) as well as the monolayer and multilayer 2DPs (4) by measuring variations in bands corresponding to the amine, aldehyde and imine groups (Fig. 54 **d**). The Raman spectra show the N-H bending band at 1,280 cm^{-1} for monomer 1 and the aldehyde C=O stretch at 1,675 cm^{-1} for monomer 3, respectively. [25, 26] Both bands disappear in the spectrum of the monolayer 2DP (4), revealing that the amine and aldehyde groups have been successfully transformed in 4. The spectra of the monolayer and multilayer 2DPs have similar features, indicating that there are no significant difference in their chemical bonding and compositions. In contrast to the monomers, a new band at 1,593 cm^{-1} characteristic for –C=N stretching is observed for 2DPs, highlighting the formation of imine bonds. The presence of this characteristic band provides a chance to use its intensity to qualitatively monitor the reaction time for the formation of the monolayer 2DP. In this aspect, time-dependent experiments were performed for the polycondensation reaction at the air–water interface with a period of 0.5, 1, 2, 4, 8 and 16 h. No significant change in the intensity of imine band was identified after 4 h, suggesting the efficient conversion for the formation of the 2DP.

The XPS spectra of the monolayer and multilayer 2DPs are similar to each other, further confirming no obvious difference in their chemical compositions. The N1s signal of the 2DP has two peaks with binding energies at 400 and 398.4 eV, which are attributed to pyrrole nitrogen (-NH-) and imine nitrogen with hydrogen bond (O-H···N=C) (blue), and imine nitrogen in porphyrin units (red), respectively (Fig. 54 **e**). [27] The ratio of intensities of the blue to red peaks at higher to that of lower binding energies is 3:1, which manifests that each porphyrin monomer 1 forms four imine bonds with monomer 3 in 2DP. The O1s signal is much stronger than expected from the chemical structure of 4, which is caused by the existence of large amount of water associated with interfacial synthesis. A quantitative analysis of the N1s and C1s signals suggests an $N/C_{aromatic}$ ratio (~ 15:100) similar to the expected chemical composition of 4 (N/C = 14:100). In conjunction with the Raman and XPS spectra, our results strongly validate the formation of imine 2DP with high efficiency at an air–water interface.

Lateral size of monolayer 2DP

The high reaction conversion for the formation of 2DP (4) triggers our curiosity to know how large its lateral size can be, which has been demonstrated by a horizontal transfer onto a 4-inch-sized 300 nm SiO_2/Si wafer partially covered by a piece of mica. Mica removal by tweezers breaks the monolayer and leads to a several cm^2-sized

crack within the 2DP, which gives obvious contrast and enables clear observation of the wafer-sized 2DP by the eyes or photography (Fig. 53 **i**).

Mechanical stiffness of monolayer 2DP

To determine the mechanical properties of the monolayer 2DP, a Strain-Induced Elastic Buckling Instability for Mechanical Measurements technique has been employed. [28] For the measurement, the monolayer was horizontally transferred onto an elastomeric support—polydimethylsiloxane (PDMS). Special care was taken to ensure a strong adhesion of the film on the elastomer, which was achieved by a drying process. The resulting sample was compressed, which led to the formation of a regular wrinkling pattern in the 2DP as recorded by AFM (Fig. 55 **a**,**b**). Perpendicular to the wrinkling pattern, elongated cracks were observed, which traced back to the pre-strain applied to the 2DP during the compression of the sample. These cracks did not affect the wrinkling periodicity and thus could be omitted in the mechanical analysis. Correlation between the wavelength of the wrinkling and thickness of the monolayer and the mechanical stiffness of the PDMS allows the evaluation of the Young's modulus for the 2DP (Supplementary Information on SIEIBIMM, chapter 4.4.5). [29, 30] A 2D Fourier-transformation and integration along wrinkling direction (k_x) were performed to estimate the wavelength of the wrinkling, which gave the first order peak at 6.57 μm^{-1} (Fig. 55 **c**). This value corresponds to a wavelength of 152 nm, which is similar to that obtained using a complementary analysis technique based on the power spectral density (Supplementary Fig. 58). Accepting the AFM height of 0.7 nm as the monolayer thickness, an average Young's modulus of E_{Young} = 267 ± 30 GPa is obtained (Supplementary Fig. 58 and Fig. 59). This value is comparable to the E_{Young} of other crystalline 2D sheets, such as graphene (1 TPa) [31] and graphene oxide (208 GPa), [32] and is much higher than E_{Young} of organic monolayers with ~ 66% reaction conversion, such as bis(terpyridine)-metal complex nanosheet (16 GPa) [33] and cycloaddition-induced anthracene nanosheet (11 GPa), [34] which reflect the high crystallinity and mechanical stiffness of the achieved monolayer 2DP in this work.

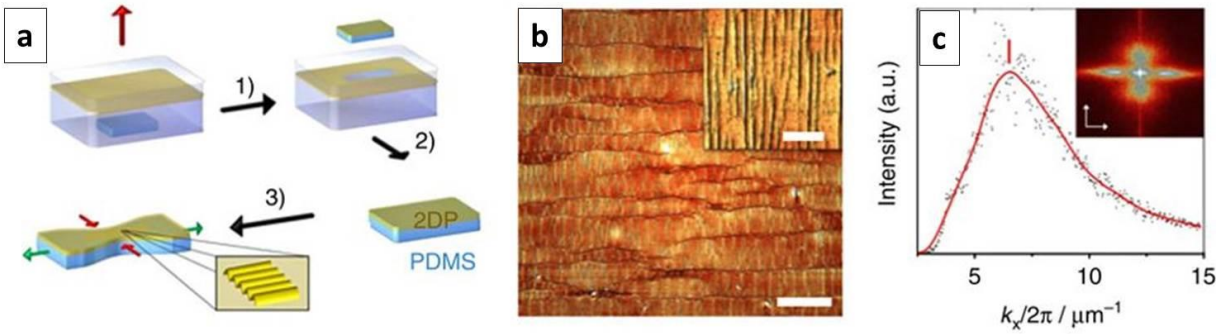

*Figure 55 | (**a**) Schematic depiction for the synthesis of the 2DP (1), transfer (2) onto a plain elastomeric substrate (PDMS), and transversal compression upon uniaxial lateral stretching of the 2DP on PDMS (3),*

*inducing wrinkling for the monolayer. (**b**) AFM topography image of the wrinkled 2DP. The insert in **b** shows an amplified image of the wrinkles. (**c**) Integrated intensity profile after 2D Fourier-transformation (see insert) along k_x direction revealing a mean periodicity of 152 nm. Scale bars in **b** and insert are 5 µm and 500 nm, respectively. a.u.*

Prototype applications of monolayer and multilayer 2DPs

Next, the monolayer 2DP has been integrated in a thin-film transistor for a proof-of-concept demonstration of the synthesized 2D materials as an active semiconducting layer. The 2DP was horizontally transferred onto an n-doped Si wafer with 300 nm SiO_2 (dielectric), on which 30 nm thick gold was deposited and used as bottom electrodes. From the transfer curve of the 2DP (Fig. 56 **a**), a mobility of $1.3 \cdot 10^{-6} \frac{cm^2}{V\,S}$ and an on/off ratio of 10^2 were obtained. When the 2DP was doped by I_2, the charge carrier mobility increased by a factor of more than two orders of magnitude and reached $1.6 \cdot 10^{-4} \frac{cm^2}{V\,S}$ (Fig. 56 **b**). These results clearly manifest that the synthetic 2DP has the potential to be used as semiconducting material for TFTs under ambient conditions.

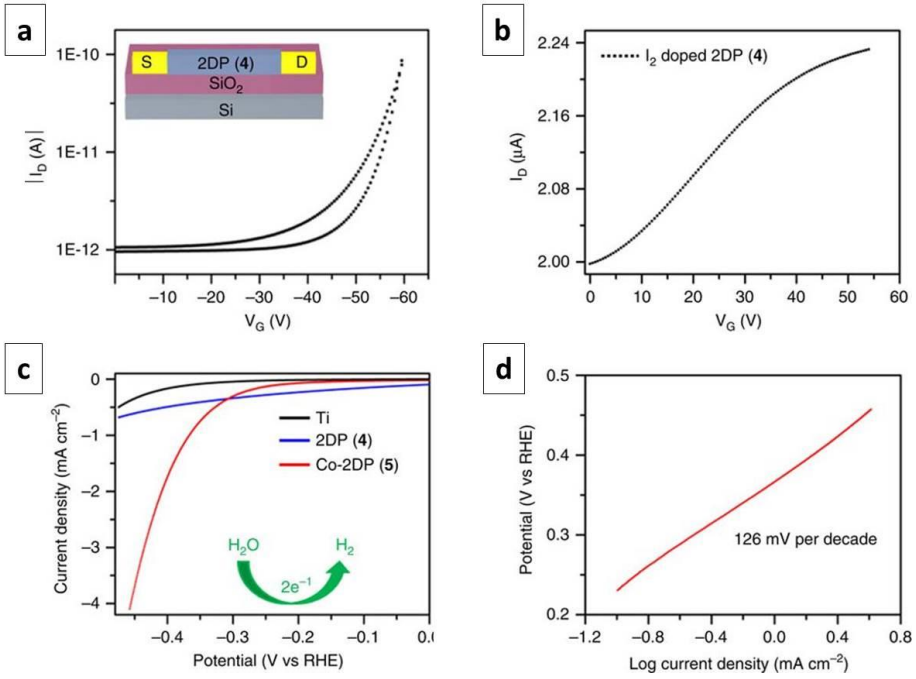

*Figure 56 | Transfer curve of a thin film transistor employing 2DP (4) as an active semiconducting layer at a source to drain voltage of −40 V (**a**) before and (**b**) after doping with iodine. (**c**) Hydrogen evolution reaction polarization plots of blank titanium foil (black), multilayer 2DP (4) (blue) and cobalt-2DP (5) (red) at a scan rate of 5 mV s^{-1} in 1.0 mol l^{-1} KOH. (**d**) Tafel plot of cobalt-2DP (5) with a slope of 126 mV $decade^{-1}$.*

Cobalt porphyrin in which a cobalt atom is coordinated with four nitrogen atoms (Co-N_4) can serve as active sites of molecular catalysts for electrocatalytic hydrogen evolution reaction (HER) [35] in aqueous solution. However, the molecular catalysts need to be immobilized onto electrode in a well-defined manner in order to avoid low catalytic activity and structural instability. [36, 37] Given that cobalt-porphyrin can be well-positioned in a large-area 2DP with high-density, the resulting film can be directly deposited onto an electrode surface thus functioning as a catalyst for HER. Hence, a multilayer 2DP (5) by reacting 5,10,15,20-tetrakis(4-aminophenyl)-21H,23H-porphyrin-Co(II) (2) with monomer (3) was constructed at water–chloroform interface. Subsequently, the as-synthesized Co-2DP was deposited onto a Ti electrode and explored as electrocatalysts for HER in 1.0 M aqueous KOH solution (Fig. 56 **c**) for a proof-of-concept application of the synthetic 2DP. The catalytic activity of the bare Ti electrode and cobalt-free 2DP (4) showed negligible HER activity. In contrast, the Co-2DP deposited on Ti substrate exhibited an excellent electrocatalytic activity for HER, suggesting the crucial active sites of Co-N_4 for HER. Specifically, the Co-2DP required an overpotential of about 367 mV to reach current density of $1.0\,\frac{mA}{cm^2}$; and an onset potential of 308 mV and a Tafel slope of $126\,\frac{mv}{decade}$ were derived from the polarization curve (Fig. 56 **d**). These values are superior to those of the previously reported cobalt complex based molecular HER catalysts, including diimine-dioxime cobalt catalysts, cobalt microperoxidase-11and porphyrin-cobalt embedded in graphene oxide sheets. [35, 38, 39]

4.4.4. Discussion

In summary, we have demonstrated the synthesis of wafer-sized, 2D conjugated polymer with a monolayer thickness of ~ 0.7 nm through Schiff-base polycondensation reaction at an air–water interface. The achieved monolayer 2DP has a Young's modulus of 267 ± 30 GPa, which is on the same order of graphene (200 – 1000 GPa). The 2DP has an optical band gap of 1.4 eV and can function as an active semiconducting layer in the TFT. Multilayer 2DP from cobalt-porphyrins catalyses hydrogen generation from water with a performance superior to those of cobalt-nitrogen (Co-N_4) coordination based molecular catalysts that grafted onto carbon nanotubes or immobilized in graphene oxide sheets. This work opens the door for interfacial synthesis of functional 2DPs using reversible polycondensation reaction, which may pave the way for the rational synthesis of 2D organic soft materials as promising candidates for next generation electronics and energy-related applications.

Methods

Materials:

5, 10, 15, 20-Tetrakis (4-aminophenyl) porphyrin (monomer 1) and 5, 10, 15, 20-Tetrakis (4-aminophenyl) porphyrin-Co(II) (monomer 2) were obtained from TCI Deutschland, GmbH (Germany) and Porphyrin

Laboratories GmbH (Germany), respectively. They were used as received. In all, 2, 5-dihydroxyterephthalaldehyde (monomer 3) was synthesized according to previously reported procedure. [40]

Synthesis of monolayer 2DP:

The monolayer 2DP was prepared at an air–water interface of a Langmuir-Blodgett trough (Minitrough, KSV NIMA, Finland). [33] The trough was equipped with a platinum Wilhelmy plate, a Taflon dipper and a pair of Delrin barriers. The substrates were immersed in to the subphase (water) and 30 µl of chloroform solution of monomer 1 ($1\,\frac{mg}{ml}$) were spread on the water surface. The solvent was allowed to evaporate for 30 min and the compression was then done at a rate of 1 mm min−1. When the surface pressure reached $10\,\frac{mN}{m}$, 2 ml of aqueous solution of monomer 3 ($4.4\,\frac{\mu mol}{l}$) was added to the subphase. The molar amount of monomer 3 was ~ 200-fold excess to that of monomer 1. After 16 h of polymerization, the single layer 2DP was horizontally transferred onto substrates with a rate of $1\,\frac{mm}{min}$. The samples were rinsed with chloroform and water and then dried in N_2 flow.

Synthesis of multilayer 2DP

The multilayer was synthesized on a custom made glass trough. [41] Fifteen millilitres of chloroform solution of monomer 1 or 2 ($1{,}2 \cdot 10^{-4}\,\frac{mol}{l}$) was provided in the glass trough, followed by overlaying 15 ml of an aqueous solution of monomer 3 ($1{,}0 \cdot 10^{-3}\,\frac{mol}{l}$). After the resulting interface was allowed to stay undisturbed for 10 days, the as-synthesized multilayer 2DP was fished onto substrates of interests for characterization.

Fabrication of graphene-2DP-graphene sandwich structure

CVD graphene flakes were transferred to a Quantifoil grid, followed by deposition of monolayer 2DP. In the next step, 2-3 µl of Milli-Q water was drop casted on the surface of the 2DP. Another Quantifoil grid with CVD graphene flakes was laid subsequently on top of the water droplet with the graphene flakes facing the 2DP. The grids were left in ambience for 24 h until the water was completely dried. As a result, a graphene-2DP-graphene has been constructed. Since the electron diffraction experiments were conducted under cryogenic conditions, a thin layer of gold (approx. 20 nm) was sputtered onto the other side of the Quantifoil grids to improve thermal conductance.

Preparation of PDMS

PDMS precursor (Dow Corning Sylgard 184) was mixed in a 10 : 1 mass ratio of oligomeric base to curing agent, degassed for 20 min and poured into 100 × 100 mm poly(styrene) molds. The precursor was allowed to harden at room temperature for 48 h on a tared table followed by a thermal curing at 80 °C for 4 h. Eventually the

hardened PDMS was cut in 55 × 10 × 5 mm slabs, washed carefully with Milli-Q-water and dried with N_2. The resulted PDMS has a Young's modulus and Poisson ratio of 1.85 MPa and 0.5, respectively. [42]

Preparation of monolayer 2DP on PDMS

The monolayer was lifted out of the air–water interface of a LB trough using slabs of PDMS that has been treated before with 10% HCl. The samples were dried at 50 °C for 30 min and stretched by a pre-determined strain of 20%. Measuring the necking at this pre-strain revealed a substrate compression of 8.48%.

2D Fourier transformation (2D-FT) analysis

The wrinkle periodicity, that is, the wavelength, was determined using 2D-FT. The 2D-FT transformed image was integrated perpendicular to the periodic structures (k_x). The central zero-order peak between 0 and 2.5 μm^{-1} was omitted. The information of the wrinkle periodicity was evaluated from the k_x range between 2.5 and 15 μm^{-1}. The integration in k_x resulted a peak maximum at 6.57 μm^{-1}, corresponding to a wavelength of 0.152 µm. Integration in k_y, that is, parallel to the wrinkles, yielded a shoulder at around 0.3 μm^{-1}, which most likely can be attributed to the average crack density of one crack per ~ 3.3 µm of wrinkled area.

Thin film transistor (TFT)

TFT structures on 230 nm SiO_2/Si with 30 nm thick Au patterns for source/drain contact were purchased from Fraunhofer IPMS, Germany. The length and width of the transistor channels are 20 and 500 µm, respectively. The single layer 2DP was horizontally transferred onto the substrate by Langmuir Schäfer method. Transfer curves of the TFT were characterized by a HP 4145B parameter analyser in a nitrogen glove box.

Hydrogen evolution reaction (HER)

All electrochemical measurements were carried out with an electrochemical workstation (CHI 760E, CH Instruments, USA) in a conventional three-electrode cell system using a Pt wire as the counter electrode and an Ag/AgCl electrode as the reference electrode. The Ti foil with thickness of 0.25 mm was used as substrate and the working electrode. The multilayer cobalt-2DP were horizontally transferred on to the surface of the Ti substrate (1 × 1 cm). All potentials in this study were relative to that of a reversible hydrogen electrode. The potential difference between Ag/AgCl and reversible hydrogen electrode was determined based on a calibration measurement in a H_2-saturated electrolyte. The polarization curves were obtained in an Ar-saturated 1.0 M KOH electrolytes with a scan rate of $5\frac{mV}{s}5$ at room temperature. The long-term durability was tested using chronopotentiometric and chronoamperometric measurements.

4.4.5. Supplementary Information on SIEBIMM

This supplementary information contains only the data regarding the mechanical characterization of the 2DP, accomplished via SIEBIMM. All other supplementary data regarding other methods, analysis and results can be found in the electronic supplementary information (ESI) of the original publication in *Nature Communications*.

Mechanical characterization

To determine the stiffness of the 2DP, we choose a simple and easy-to-handle metrology technique called Strain-Induced Elastic Buckling Instability for Mechanical Measurements (SIEBIMM) that is based on the buckling of thin films (wrinkling) on thick elastic supports. For this purpose, a thin film needs to be situated on top of a thick elastomeric substrate in strong adhesive contact. Compressing this system induces wrinkling of the film. Analysis of the wrinkling frequency allows for the precise evaluation of the in-plane moduli of the thin layer. The wrinkle periodicity can be correlated to the mechanical mismatch of the top and supporting materials as described in Eq. 4.8.

$$\lambda = 2\pi h_l \left[\frac{(1-{\nu_s}^2)E_l}{(1-{\nu_l}^2)E_s}\right]^{1/3} \tag{4.8}$$

where h_f being the film's thickness, ν_s and ν_f are Poisson ratios as well as E_s and E_f are Young's Moduli of substrate and the film, respectively. Solving for E_f gives the in-plane modulus of the thin layer for a corresponding wavelength, as described in Eq. 4.9.

$$E_l = \frac{3E_s(1-\nu_l^2)}{(1-\nu_s^2)}\left(\frac{\lambda}{2\pi h_l}\right)^3 \tag{4.9}$$

This buckling based metrology method has been investigated and applied to a variety of other thin films and 2D materials (see Table 6). As can be seen, it is valid for a broad range of layer thicknesses as well as mechanical constants of both layer and substrate.

Sample	Layer thickness /nm	Periodicity /nm	In-Plane-Modulus /GPa	Reference
PS / Silica on PDMS (varying thicknesses)	150 – 250 nm	8 – 13 µm	3,4 GPa	[28]
Nanofibrillated cellulose on PEI (varying thicknesses)	35 – 75 nm	1 – 3 µm	1,5 GPa	[43]
Hectorite on PDMS	0,96 nm	149 nm	143 GPa	[44]
Graphene Oxide on PDMS	0,7 nm	89 nm	110 GPa	[45]

		138 nm	420 GPa	
Aluminium chlorohydrate on PDMS (while drying)	~ 5 nm	40 – 70 µm	10 – 190 MPa	[46]

Table 6 | Overview of SIEBIMM applications from literature

In the case investigated in this manuscript, we performed two sets of SIEBIMM experiments on identically prepared samples. After transfer of the 2D-layers onto the elastomer special care was taken to ensure strong adhesive contact, since weak adhesion will result in slippage and consequently an underestimation of Young's modulus. To avoid such a delamination, the transferred layer is dried cautiously over night at 50 °C, as it carries along a thin water layer from the LB-bath preparation. This hinders the adhesion of layer and elastomer, so the sample is not strained before any water has been evaporated. Subsequently it becomes clamped into a custom-made stretching-device and gets pulled longitudinally causing a laterally compression of both elastomer and layer. At a certain compression periodic wrinkle corrugations of the layer show up. For sample 1, the critical compression ε_c is at 8 %, for sample 2 we got 9 %. Subsequently the corrugations are imaged via AFM. For each set of experiments several 1024 x 1024 px high resolution AFM images of the wrinkled film in different states of compression were obtained, as shown in Fig. 57. Wrinkles and cracks perpendicular to the wrinkles can be clearly identified and areas which are not covered by the 2D-layer are wrinkle-free.

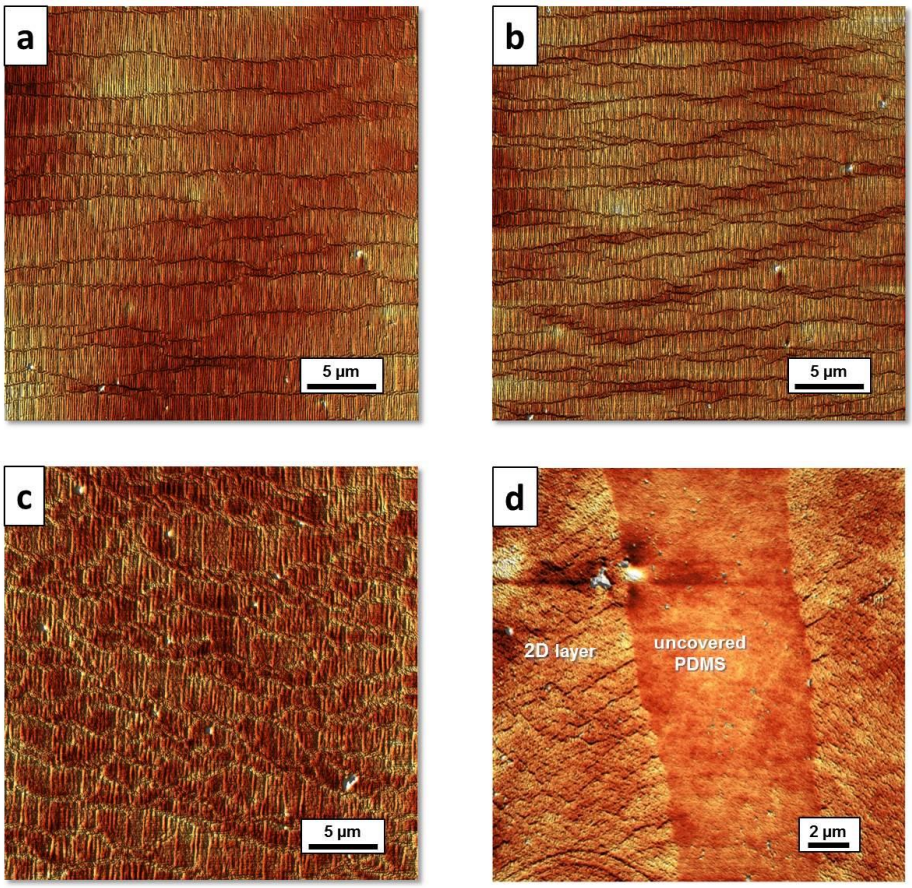

*Figure 57 | AFM z-senor images (**a**) 2DP layer, sample 1 (**b**) 2DP layer, sample 2 (**c**) reference sample and (**d**) unstrained 2DP layer at its interface to an uncovered region. All images have been made in 1024 x 1024 px high resolution to ensure statistical relevance.*

To statistically average our results, we performed two independent averaging methods, 2D-Fast Fourier Transformation (2D-FFT) and Power Spectral Density (PSD) analysis, which yield good agreement. 2D-FFT was performed by transferring the raw data into a 2D-FT image in Gwyddion 2.43 SPM analysis software. By choosing the relevant area, an angle correction of the data was performed simultaneously. The extracted cross-section then was load into Origin 2015 software and peak picking was performed. For PSD the integrated tool of Bruker NanoScope 1.6 software was used, which transfers and integrates the relevant area at the same time. Eventually the maximum peak is picked. Nevertheless, this method does not have angle correction of the raw data, wherefore larger values for the wrinkle periodicities are observable. We prevented this by only taking images into account that are already very close to a 90°-angle referring to the transfer direction. Fig. 58 shows a typical result for a representative sample. One can clearly identify a peak corresponding to the wrinkle wavelength.

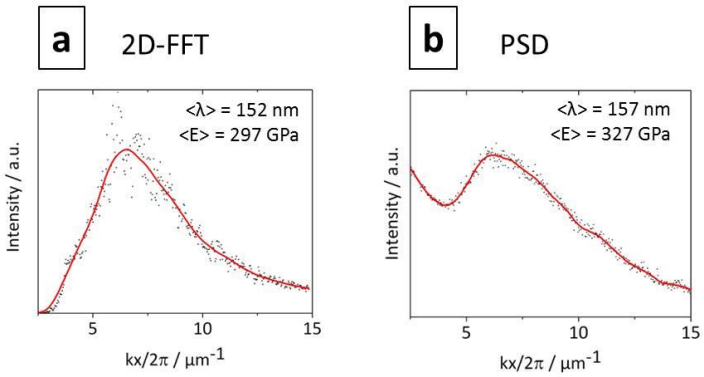

*Figure 58 | Wavelength estimation of the 1st sample in 2DP wrinkling (**a**) by 2D Fast-Fourier-Transformation (2D-FT) and (**b**) by Power spectral density (PSD) methods. Red lines correspond to integration perpendicular to the wrinkle direction.*

An average over all samples resulted in wavelength of 146 nm (2D-FFT) and 150 nm (PSD). This corresponds to Young's moduli of 267 ± 30 GPa (2D-FFT) and 287 ± 40 GPa (PSD). Since generally 2D-FFT showed the periodicity more precisely due to its angle indepency, but also clearly with a narrower peak, showed best agreement with literature in the reference experiments (see below) and is used in most studies in the literature, we report 267 ± 30 GPa in the manuscript.

Application of the method to a reference system

In an additional experiment we verified the data by wrinkling and measuring a thin 2DP film material that is very similar in the preparation, transfer of the film and adhesion treatment of the film and which has been previously characterized by an independent method (AFM force spectroscopy). [33] Here, SIEBIMM analysis results a Young's Modulus of 16 GPa (2D-FFT) and 13 GPa (PSD). Both values are in very good agreement with the primal AFM Nano-indentation result of 16 GPa, altogether proving the reliability of our investigation.

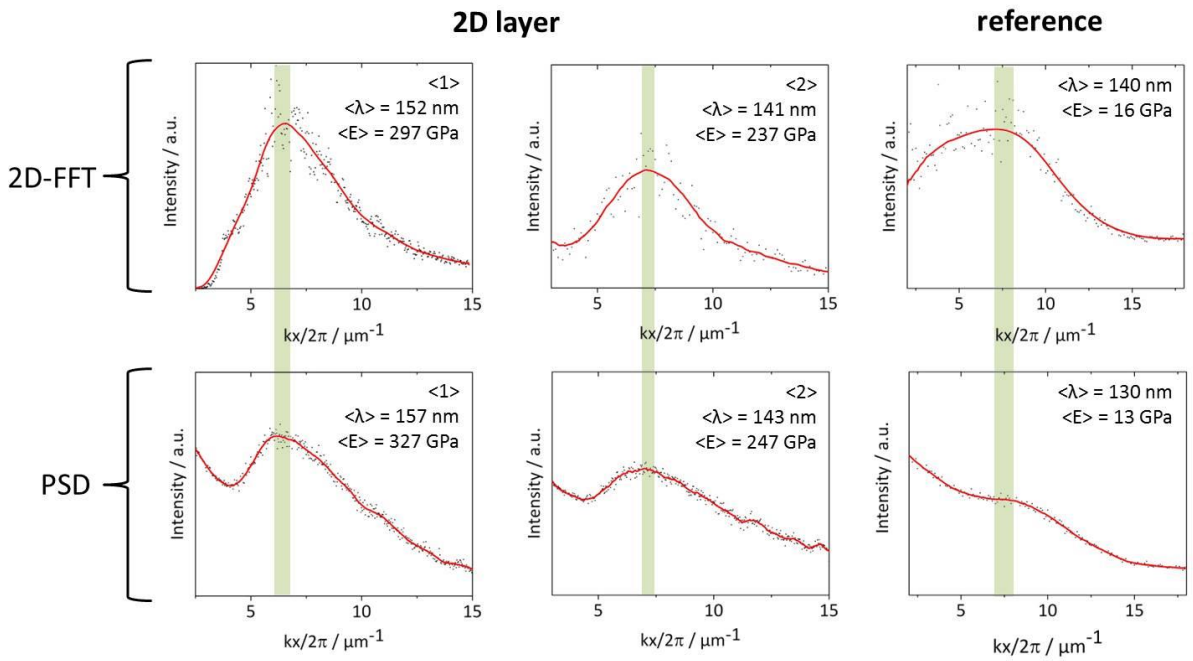

Figure 59 | Wavelength estimation of 2D layer (left) and bis(terpyridine)-metal complex nanosheet (right) [33] *wrinkling by 2D Fourier-transformation (2D-FT) and Power spectral density (PSD) methods. Red lines correspond to integration perpendicular to the wrinkle direction. For the 2D layer, a spectral analysis perpendicular to the wrinkles by 2D-FT and PSD exhibited a wavelength of 0.141 µm to 0.152 µm (top, left) and 0.143 µm to 0.157 µm (bottom, left), respectively. Both techniques are in close agreement for the wrinkle periodicity. While 2D-FT gives a Young's modulus E_{Young} of 237 – 297 GPa, PSD provides a value of 247 – 327 GPa. In average, the E_{Young} of the 2DP is 277 ± 37 GPa. For the bis(terpyridine)-metal complex nanosheet (E_{Young} = ∼ 16 GPa from AFM nanoindentation reported by Zheng et al.), a wavelength of 140 nm (top, right) and 130 nm (bottom, right) for 2D-FT and PSD, which gives a Young's modulus of ∼ 16 GPa and 13 GPa, respectively.*

References

[1] K.S. Novoselov, V.I. Fal'ko, L. Colombo, P.R. Gellert, M.G. Schwab and K. Kim: A roadmap for graphene, **2012**; *Nature*, 490 - 192

[2] A.C. Ferrari, F. Bonaccorso, V. Fal'ko, K.S. Novoselov, S. Roche, P. Bøggild, S. Borini, F.H.L. Koppens, V. Palermo, N. Pugno, J.A. Garrido, R. Sordan, A. Bianco, L. Ballerini, M. Prato, E. Lidorikis, J. Kivioja, C. Marinelli, T. Ryhänen, A. Morpurgo, J.N. Coleman, V. Nicolosi, L. Colombo, A. Fert, M. Garcia-Hernandez, A. Bachtold, G.F. Schneider, F. Guinea, C. Dekker, M. Barbone, Z. Sun, C. Galiotis, A.N. Grigorenko, G. Konstantatos, A. Kis, M. Katsnelson, L. Vandersypen, A. Loiseau, V. Morandi, D. Neumaier, E. Treossi, V. Pellegrini, M. Polini, A. Tredicucci, G.M. Williams, B. Hee Hong, J.-H. Ahn, J. Min Kim, H. Zirath, B.J. van Wees, H. van der Zant, L. Occhipinti, A. Di Matteo, I.A. Kinloch, T. Seyller, E. Quesnel, X. Feng, K. Teo, N. Rupesinghe, P. Hakonen, S.R.T. Neil, Q. Tannock, T. Löfwander and J. Kinaret: Science and technology roadmap for graphene, related two-dimensional crystals, and hybrid systems, **2015**; *Nanoscale*, 7 - 11, 4598-4810

[3] J. Sakamoto, J. van Heijst, O. Lukin and A.D. Schlüter: Two-Dimensional Polymers: Just a Dream of Synthetic Chemists?, **2009**; *Angew. Chem. Int. Ed.*, 48 - 6, 1030-1069

[4] X. Zhuang, Y. Mai, D. Wu, F. Zhang and X. Feng: Two-Dimensional Soft Nanomaterials: A Fascinating World of Materials, **2015**; *Adv. Mater.*, 27 - 3, 403-427

[5] K.S. Novoselov, A.K. Geim, S.V. Morozov, D. Jiang, Y. Zhang, S.V. Dubonos, I.V. Grigorieva and A.A. Firsov: Electric Field Effect in Atomically Thin Carbon Films, **2004**; *Science*, 306 - 5696, 666-669

[6] R. Muñoz and C. Gómez-Aleixandre: Review of CVD Synthesis of Graphene, **2013**; *Chem. Vap. Deposition*, 19 - 10-11-12, 297-322

[7] W. Yang, G. Chen, Z. Shi, C.-C. Liu, L. Zhang, G. Xie, M. Cheng, D. Wang, R. Yang, D. Shi, K. Watanabe, T. Taniguchi, Y. Yao, Y. Zhang and G. Zhang: Epitaxial growth of single-domain graphene on hexagonal boron nitride, **2013**; *Nat. Mat.*, 12 - 792

[8] L. Lafferentz, V. Eberhardt, C. Dri, C. Africh, G. Comelli, F. Esch, S. Hecht and L. Grill: Controlling on-surface polymerization by hierarchical and substrate-directed growth, **2012**; *Nat. Chem.*, 4 - 215

[9] M. Bieri, M. Treier, J. Cai, K. Aït-Mansour, P. Ruffieux, O. Gröning, P. Gröning, M. Kastler, R. Rieger, X. Feng, K. Müllen and R. Fasel: Porous graphenes: two-dimensional polymer synthesis with atomic precision, **2009**; *Chem. Commun.*, - 45, 6919-6921

[10] P. Kissel, R. Erni, W.B. Schweizer, M.D. Rossell, B.T. King, T. Bauer, S. Götzinger, A.D. Schlüter and J. Sakamoto: A two-dimensional polymer prepared by organic synthesis, **2012**; *Nat. Chem.*, 4 - 287

[11] P. Kissel, D.J. Murray, W.J. Wulftange, V.J. Catalano and B.T. King: A nanoporous two-dimensional polymer by single-crystal-to-single-crystal photopolymerization, **2014**; *Nat. Chem.*, 6 - 774

[12] M.J. Kory, M. Wörle, T. Weber, P. Payamyar, S.W. van de Poll, J. Dshemuchadse, N. Trapp and A.D. Schlüter: Gram-scale synthesis of two-dimensional polymer crystals and their structure analysis by X-ray diffraction, **2014**; *Nat. Chem.*, 6 - 779

[13] D.J. Murray, D.D. Patterson, P. Payamyar, R. Bhola, W. Song, M. Lackinger, A.D. Schlüter and B.T. King: Large Area Synthesis of a Nanoporous Two-Dimensional Polymer at the Air/Water Interface, **2015**; *J. Am. Chem. Soc.*, 137 - 10, 3450-3453

[14] Y. Jin, Y. Zhu and W. Zhang: Development of organic porous materials through Schiff-base chemistry, **2013**; *Cryst. Eng. Comm.*, 15 - 8, 1484-1499

[15] M.E. Belowich and J.F. Stoddart: Dynamic imine chemistry, **2012**; *Chem. Soc. Rev.*, 41 - 6, 2003-2024

[16] S. Kandambeth, D.B. Shinde, M.K. Panda, B. Lukose, T. Heine and R. Banerjee: Enhancement of Chemical Stability and Crystallinity in Porphyrin-Containing Covalent Organic Frameworks by Intramolecular Hydrogen Bonds, **2013**; *Angew. Chem. Int. Ed.*, 52 - 49, 13052-13056

[17] W. Dai, F. Shao, J. Szczerbiński, R. McCaffrey, R. Zenobi, Y. Jin, A.D. Schlüter and W. Zhang: Synthesis of a Two-Dimensional Covalent Organic Monolayer through Dynamic Imine Chemistry at the Air/Water Interface, **2016**; *Angew. Chem. Int. Ed.*, 55 - 1, 213-217

[18] G. Algara-Siller, S. Kurasch, M. Sedighi, O. Lehtinen and U. Kaiser: The pristine atomic structure of MoS2 monolayer protected from electron radiation damage by graphene, **2013**; *Appl. Phys. Lett.*, 103 - 20, 203107

[19] J.C. Meyer, A.K. Geim, M.I. Katsnelson, K.S. Novoselov, T.J. Booth and S. Roth: The structure of suspended graphene sheets, **2007**; *Nature*, 446 - 60

[20] L. Brown, R. Hovden, P. Huang, M. Wojcik, D.A. Muller and J. Park: Twinning and Twisting of Tri- and Bilayer Graphene, **2012**; *Nano Lett.*, 12 - 3, 1609-1615

[21] D.N. Bunck and W.R. Dichtel: Bulk Synthesis of Exfoliated Two-Dimensional Polymers Using Hydrazone-Linked Covalent Organic Frameworks, **2013**; *J. Am. Chem. Soc.*, 135 - 40, 14952-14955

[22] Z. Zheng, L. Opilik, F. Schiffmann, W. Liu, G. Bergamini, P. Ceroni, L.-T. Lee, A. Schütz, J. Sakamoto, R. Zenobi, J. VandeVondele and A.D. Schlüter: Synthesis of Two-Dimensional Analogues of Copolymers by Site-to-Site Transmetalation of Organometallic Monolayer Sheets, **2014**; *J. Am. Chem. Soc.*, 136 - 16, 6103-6110

[23] S. Nie and S.R. Emory: Probing Single Molecules and Single Nanoparticles by Surface-Enhanced Raman Scattering, **1997**; *Science*, 275 - 5303, 1102-1106

[24] L. Opilik, P. Payamyar, J. Szczerbiński, A.P. Schütz, M. Servalli, T. Hungerland, A.D. Schlüter and R. Zenobi: Minimally Invasive Characterization of Covalent Monolayer Sheets Using Tip-Enhanced Raman Spectroscopy, **2015**; *ACS Nano*, 9 - 4, 4252-4259

[25] H. Wang, J. Xu, J. Wan, Y. Zhao and X. Zheng: Excited State Structural Dynamics of Tetra(4-aminophenyl)porphine in the Condensed Phase: Resonance Raman Spectroscopy and Density Functional Theory Calculation Study, **2010**; *J. Phys. Chem. B*, 114 - 10, 3623-3632

[26] R.A. Yadav, Ramakant, P.C. Mishra and I.S. Singh: Raman and infrared spectra of tere-phthalaldehyde, **1982**; *Pramana*, 18 - 4, 311-315

[27] M. Lu, B. Chen, T. He, Y. Li and J.M. Tour: Synthesis, Grafting, and Film Formation of Porphyrins on Silicon Surfaces Using Triazenes, **2007**; *Chem. Mater.*, 19 - 18, 4447-4453

[28] C.M. Stafford, C. Harrison, K.L. Beers, A. Karim, E.J. Amis, M.R. VanLandingham, H.-C. Kim, W. Volksen, R.D. Miller and E.E. Simonyi: A buckling-based metrology for measuring the elastic moduli of polymeric thin films, **2004**; *Nat. Mat.*, 3 - 545

[29] N. Bowden, W.T.S. Huck, K.E. Paul and G.M. Whitesides: The controlled formation of ordered, sinusoidal structures by plasma oxidation of an elastomeric polymer, **1999**; *Appl. Phys. Lett.*, 75 - 17, 2557-2559

[30] B.A. Glatz, M. Tebbe, B. Kaoui, R. Aichele, C. Kuttner, A.E. Schedl, H.-W. Schmidt, W. Zimmermann and A. Fery: Hierarchical line-defect patterns in wrinkled surfaces, **2015**; *Soft Matter*, 11 - 17, 3332-3339

[31] C. Lee, X. Wei, J.W. Kysar and J. Hone: Measurement of the Elastic Properties and Intrinsic Strength of Monolayer Graphene, **2008**; *Science*, 321 - 5887, 385-388

[32] J.W. Suk, R.D. Piner, J. An and R.S. Ruoff: Mechanical Properties of Monolayer Graphene Oxide, **2010**; *ACS Nano*, 4 - 11, 6557-6564

[33] Z. Zheng, C.S. Ruiz-Vargas, T. Bauer, A. Rossi, P. Payamyar, A. Schütz, A. Stemmer, J. Sakamoto and A.D. Schlüter: Square-Micrometer-Sized, Free-Standing Organometallic Sheets and Their Square-Centimeter-Sized Multilayers on Solid Substrates, **2013**; *Macromol. Rapid Commun.*, 34 - 21, 1670-1680

[34] P. Payamyar, K. Kaja, C. Ruiz-Vargas, A. Stemmer, D.J. Murray, C.J. Johnson, B.T. King, F. Schiffmann, J. VandeVondele, A. Renn, S. Götzinger, P. Ceroni, A. Schütz, L.-T. Lee, Z. Zheng, J. Sakamoto and A.D. Schlüter: Synthesis of a Covalent Monolayer Sheet by Photochemical Anthracene Dimerization at the Air/Water Interface and its Mechanical Characterization by AFM Indentation, **2014**; *Adv. Mater.*, 26 - 13, 2052-2058

[35] D. Huang, J. Lu, S. Li, Y. Luo, C. Zhao, B. Hu, M. Wang and Y. Shen: Fabrication of Cobalt Porphyrin. Electrochemically Reduced Graphene Oxide Hybrid Films for Electrocatalytic Hydrogen Evolution in Aqueous Solution, **2014**; *Langmuir*, 30 - 23, 6990-6998

[36] E.S. Andreiadis, P.-A. Jacques, P.D. Tran, A. Leyris, M. Chavarot-Kerlidou, B. Jousselme, M. Matheron, J. Pécaut, S. Palacin, M. Fontecave and V. Artero: Molecular engineering of a cobalt-based electrocatalytic nanomaterial for H2 evolution under fully aqueous conditions, **2012**; *Nat. Chem.*, 5 - 48

[37] R. Dong, M. Pfeffermann, H. Liang, Z. Zheng, X. Zhu, J. Zhang and X. Feng: Large-Area, Free-Standing, Two-Dimensional Supramolecular Polymer Single-Layer Sheets for Highly Efficient Electrocatalytic Hydrogen Evolution, **2015**; *Angew. Chem. Int. Ed.*, 54 - 41, 12058-12063

[38] N. Kaeffer, M. Chavarot-Kerlidou and V. Artero: Hydrogen Evolution Catalyzed by Cobalt Diimine–Dioxime Complexes, **2015**; *Acc. Chem. Res.*, 48 - 5, 1286-1295

[39] Y. Sun, C. Liu, D.C. Grauer, J. Yano, J.R. Long, P. Yang and C.J. Chang: Electrodeposited Cobalt-Sulfide Catalyst for Electrochemical and Photoelectrochemical Hydrogen Generation from Water, **2013**; *J. Am. Chem. Soc.*, 135 - 47, 17699-17702

[40] T. Kretz, W. Bats Jan, H.-W. Lerner and M. Wagner. 2,5-Diformylbenzene-1,4-diol: A Versatile Building Block for the Synthesis of Ditopic Redox-Active Schiff Base Ligands, *Zeitschrift für Naturforschung B*, **2007**, 66

[41] M. Pfeffermann, R. Dong, R. Graf, W. Zajaczkowski, T. Gorelik, W. Pisula, A. Narita, K. Müllen and X. Feng: Free-Standing Monolayer Two-Dimensional Supramolecular Organic Framework with Good Internal Order, **2015**; *J. Am. Chem. Soc.*, 137 - 45, 14525-14532

[42] K.U. Claussen, M. Tebbe, R. Giesa, A. Schweikart, A. Fery and H.-W. Schmidt: Towards tailored topography: facile preparation of surface-wrinkled gradient poly(dimethyl siloxane) with continuously changing wavelength, **2012**; *RSC Advances*, 2 - 27, 10185-10188

[43] E.D. Cranston, M. Eita, E. Johansson, J. Netrval, M. Salajková, H. Arwin and L. Wågberg: Determination of Young's Modulus for Nanofibrillated Cellulose Multilayer Thin Films Using Buckling Mechanics, **2011**; *Biomacromol.*, 12 - 4, 961-969

[44] D.A. Kunz, J. Erath, D. Kluge, H. Thurn, B. Putz, A. Fery and J. Breu: In-Plane Modulus of Singular 2:1 Clay Lamellae Applying a Simple Wrinkling Technique, **2013**; *ACS Appl. Mat. Interf.,* 5 - 12, 5851-5855

[45] D.A. Kunz, P. Feicht, S. Godrich, H. Thurn, G. Papastavrou, A. Fery and J. Breu: Space-resolved in-plane moduli of graphene oxide and chemically derived graphene applying a simple wrinkling procedure, **2013**; *Adv. Mater.*, 25 - 9, 1337-41

[46] G.L. Ferretti, M. Nania, O.K. Matar and J.T. Cabral: Wrinkling Measurement of the Mechanical Properties of Drying Salt Thin Films, **2016**; *Langmuir*, 32 - 9, 2199-2207

5. Acknowledgements

So, eventually the PhD-time is over. This time seemed to be flying by (at least, most of the time) – and, honestly, it was about time! It's time to go, time to say goodbye – and time to say "thank you" to some people.

First of all, there is my boss, Prof. Fery: Thank you Andreas for giving me the chance to proof myself in the field of physics, where I'm still a bit stranger! Luckily, I also had some chemistry in there, and beyond that you gave me the freedom to implement some engineering in it as well. Altogether you anyways gave me the chance to freely develop my skills and interests in the topic, without following a fixed, inflexible roadmap. I still highly appreciate that since this "freedom in mind and acting" helped me a lot to develop the ideas and experiments about crack-free wrinkling, bi-sinusoidal wrinkling, upscaling etc – so a major part of my thesis topics. I rarely had the feeling of being stuck in a dead end (which probably inevitably happens during a PhD thesis). But when I got stuck, you had an open ear and an idea how to get out.

Next, I would like to thank Dr. Christoph Hanske and Dr. Moritz Tebbe, who several years ago introduced me to the topic of bilayer wrinkling back in Bayreuth. Your manner and patience have paved the way for me to this thesis - because you have given me the scientific and collegial basis for this work.

A big thank you also goes to my colleagues and cooperation partners in Dresden, namely Dr. Mirko Nitschke, Prof. Sven Wießner, André Knapp, Lutz Zybell and Mathias Ullrich from IPF, Dr. Frauke Junghans from FILK Freiberg and Hafeesudeen Sahabudeen, Dr. Zhikun Zheng and Prof. Xinliang Feng from TU Dresden. Your continuous support with your wisdom certainly helped me to develop my topics and to expand my knowledge. And of course, a thank you goes to my fellow colleagues who worked with or for me, namely Anik Kumar Ghosh, Ellen Häußler, Himanshu Patel, Juanjuan Wang and Sebastian Stelzner.

Coming back to Bayreuth, I would like to thank Sybille Zimmermann for being the fairy godmother of PCII in Bayreuth. Furthermore, I say thank you to all my cooperation partners there, namely Andreas Erich Schedl, Prof. Hans-Werner-Schmidt, Dr. Badr Kaoui, Prof. Walter Zimmermann, and of course also to my PCII-colleagues that supported me during my time there, namely Markus Hund, Petra Zippelius, Carmen Kunert, Dr. Wolfgang Häfner and Prof. Georg Papastavrou.

Eventually, and importantly – my family: Thank you Mom and Dad, Stefan and Rebecca, for always believing in me! And that you have never stopped believing that that one day I'd be finished after all. I think I can say: Finally it came true!

Last but foremost: Thank you Anja for being my backing and support, in high and low!

6. Eidesstattliche Versicherungen & Erklärungen / Declaration of Authorship

Hiermit versichere ich eidesstattlich, dass ich die Arbeit selbstständig verfasst und keine anderen als die von mir angegebenen Quellen und Hilfsmittel benutzt habe (vgl. Art. 64 Abs. 1 Satz 6 BayHSchG). (§ 8 Satz 2 Nr. 3 PromO Fakultät)

Hiermit erkläre ich, dass ich die Dissertation nicht bereits zur Erlangung eines akademischen Grades eingereicht habe und dass ich nicht bereits diese oder eine gleichartige Doktorprüfung endgültig nicht bestanden habe. (§ 8 Satz 2 Nr. 3 PromO Fakultät)

Hiermit erkläre ich, dass ich Hilfe von gewerblichen Promotionsberatern bzw. –vermittlern oder ähnlichen Dienstleistern weder bisher in Anspruch genommen habe noch künftig in Anspruch nehmen werde. (§ 8 Satz 2 Nr. 4 PromO Fakultät)

Hiermit erkläre ich mein Einverständnis, dass die elektronische Fassung der Dissertation unter Wahrung meiner Urheberrechte und des Datenschutzes einer gesonderten Überprüfung unterzogen werden kann. (§ 8 Satz 2 Nr. 7 PromO Fakultät)

Hiermit erkläre ich mein Einverständnis, dass bei Verdacht wissenschaftlichen Fehlverhaltens Ermittlungen durch universitätsinterne Organe der wissenschaftlichen Selbstkontrolle stattfinden können. (§ 8 Satz 2 Nr. 8 PromO Fakultät)

Dresden,

…….

Bernhard Glatz